Medical Image Analysis for the Detection, Extraction and Modelling of Vascular Structures

By

Iván Macía Oliver

Dissertation presented to the Department of Computer Science and Artificial Intelligence in partial fulfillment of the requirements for the degree of

Doctor of Philosophy

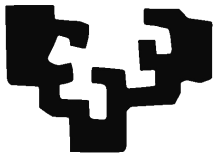

PhD Advisor:

Prof. Dr. Manuel Graña Romay

At

The University of the Basque Country
Donostia - San Sebastián
2012

Para Maider y Daniela

Para papá y mamá

Universidad del País Vasco Euskal Herriko Unibertsitatea

AUTORIZACION DEL/LA DIRECTOR/A DE TESIS

PARA SU PRESENTACION

Dr/a. _____con N.I.F._____

como Director/a de la Tesis Doctoral: _____

_____

_____

realizada en el Departamento _____

_____

por el Doctorando Don/ña. _____ ,

autorizo la presentación de la citada Tesis Doctoral, dado que reúne las condiciones necesarias para su defensa.

En _____a _____de _____de _____

EL/LA DIRECTOR/A DE LA TESIS

Fdo.: _____

Universidad del País Vasco Euskal Herriko Unibertsitatea

CONFORMIDAD DEL DEPARTAMENTO

El Consejo del Departamento de _____

_____

en reunión celebrada el día ____ de _____ de _____ ha acordado dar la conformidad a la admisión a trámite de presentación de la Tesis Doctoral titulada: _____

_____

_____

dirigida por el/la Dr/a. _____

_____

y presentada por Don/ña. _____

ante este Departamento.

En _____a _____de _____de _____

Vº Bº DIRECTOR/A DEL DEPARTAMENTO SECRETARIO/A DEL DEPARTAMENTO

Fdo.: _____ Fdo.: _____

Universidad del País Vasco Euskal Herriko Unibertsitatea

ACTA DE GRADO DE DOCTOR

ACTA DE DEFENSA DE TESIS DOCTORAL

DOCTORANDO DON/ÑA. _____

TITULO DE LA TESIS: _____

_____

_____

El Tribunal designado por la Subcomisión de Doctorado de la UPV/EHU para calificar la Tesis Doctoral arriba indicada y reunido en el día de la fecha, una vez efectuada la defensa por el doctorando y contestadas las objeciones y/o sugerencias que se le han formulado, ha otorgado por_____la calificación de:

unanimidad ó mayoría

Idioma/s defensa: _____

En _____a _____de _____de _____

EL/LA PRESIDENTE/A, EL/LA SECRETARIO/A,

Fdo.: Fdo.:

Dr/a: _____ Dr/a: _____

VOCAL 1º, VOCAL 2º, VOCAL 3º,

Fdo.: Fdo.: Fdo.:

Dr/a: _____Dr/a:_____Dr/a:_____

EL/LA DOCTORANDO/A,

Fdo.: _____

Acknowledgements

My special thanks to my advisor, Prof. Manuel Graña. Without knowing me he had confidence in me from the very first moment, that day he met a tall guy that filled his blackboard with formulas. He has given me some freedom when I needed it, and helped me when it was necessary to advance. I hope we can collaborate in the future.

Thanks to Dr. Luis Kabongo, my internal supervisor at Vicomtech. He had always time for advice when needed. We are part of a great team.

This thesis was developed with the support of Vicomtech-IK4. Thanks to Vicomtech Directors, Julián, Jorge, Shabs, Edurne and Céline. They had confidence in me and gave me the necessary time and resources I needed for this thesis.

Thanks to Prof. Karl Krissian for his warm welcome in Gran Canaria and his advice about the contents of this thesis.

Thanks to Mariano de Blas Bravo MD and his team at the Interventional Radiology and Vascular Surgery Units of Hospital Donostia for his explanations and for providing the necessary information for the validation of the aortic aneurysm experiments. Our work in the bioengineering field would not make sense without their implication.

Thanks to Dr. Antonio Salterain. He was the person who introduced me into the research world and he always thought what was the best for me even against his own advantage. There is some mathematical stuff in this thesis I am sure he will enjoy. On that time I also met Dra. María Teresa Linaza, now in Vicomtech, to whom I would also like to thank her support these years.

To my new family. To my wife Maider, if it wasn't for her support this thesis would not be possible. She is the best thing that happened to me in life together with my little girl Daniela. We are the present, she is the future.

To my parents, because I would not be what I am if it wasn't for them and because they always wanted the best for me without asking for anything in return.

To my brothers and sisters, Idoia, Rubén, Hugo, Leti, they were also an important part of my education and they are always there when needed. Also to my in-laws, that have treated me as one more of them and have taken care of Daniela.

To my workmates at Vicomtech, specially to those at the Biomedicine Area. Thanks for your support and for the exceptional environment we enjoy. Iñigo, María, Isabelle, Aitor, Beñat, thanks for the support and for helping my in the review of this thesis. To my current and former workmates at Vicomtech, specially David, for putting up with my complaints so many times while drinking some beers. Also to my mates at the university, they have treated me as one more of them.

To my friends, because after the family they are the best in life and I am lucky to have so many good friends.

To all who have helped me to be here.

To all of them thank you.

Iván Macía

Agradecimientos

Mi agradecimiento especial para mi director, Profesor Manuel Graña. Sin apenas conocerme confió en mí desde el primer momento, aquel día que conoció a un chico alto que acabó llenándole la pizarra de fórmulas. Me ha dado libertad cuando la he necesitado y ayudado cuando había que tirar hacia adelante. Espero que podamos seguir colaborando en el futuro.

Gracias al Dr. Luis Kabongo, mi supervisor interno en Vicomtech. Siempre ha tenido tiempo para asesorarme cuando lo he necesitado. Somos parte de un gran equipo.

El desarrollo de esta tesis ha sido posible por el apoyo de Vicomtech. Gracias a mis jefes en Vicomtech, Julián, Jorge, Shabs, Edurne, Céline. Ellos confiaron en mí y me dieron el tiempo y los recursos necesarios que necesitaba para sacar esta tesis adelante.

Gracias al Prof. Karl Krissian por su cálida acogida en Gran Canaria y por sus consejos acerca del contenido de la tesis.

Gracias al Dr. Mariano de Blas Bravo y su equipo de la Unidad de Radiología Intervencionista y de Cirugía Vascular del Hospital Donostia por sus explicaciones y por facilitar la información necesaria para la validación de los experimentos en aneurismas de aorta. Nuestro trabajo en el ámbito de la bioingeniería no tendría sentido sin la implicación del equipo médico.

Gracias al Dr. Antonio Salterain. Él fue el que me introdujo en el mundo de la investigación y siempre pensó en lo que era mejor para mí por encima de su propio beneficio. En esta tesis hay alguna parte matemática que estoy seguro que le encantará. Por aquel entonces también conocí a la Dra. María Teresa Linaza, ahora en Vicomtech, a la que agradezco también su apoyo estos años.

A mi recién estrenada familia. A mi mujer Maider, si no fuera por su apoyo esta tesis no sería posible. Es lo mejor que me ha pasado en la vida junto con la pequeña Daniela. Nosotros somos el presente, ella es el futuro.

A mis padres, porque no sería lo que soy ahora si no fuera por ellos y siempre han buscado lo mejor para mí sin pedir nada a cambio.

A mis hermanos, Idoia, Rubén, Hugo, Leti, ellos también fueron parte importante de mi educación y siempre están ahí cuando se les necesita. También a mi familia política, que me ha recibido como uno más y cuidado de Daniela.

A mis compañeros de Vicomtech, especialmente a los del Área de Biomedicina. Gracias por vuestro apoyo y por el ambiente tan fenomenal del que disfrutamos. Iñigo, María, Isabelle, Aitor, Beñat gracias por el apoyo y por ayudarme con las revisiones. Al resto de compañeros de Vicomtech, los de ahora y los de antes, especialmente a David por aguantar tantas veces mis quejas entre caña y caña. También a mis compañeros de la uni, que me han recibido como uno más.

A mis amigos, porque después de la familia es lo mejor que uno tiene en la vida y yo soy afortunado de tener muchos buenos amigos.

A todos los que me han ayudado a llegar hasta aquí.

A todos ellos gracias.

Iván Macía

Medical Image Analysis for the Detection, Extraction and Modelling of Vascular Structures

Iván Macía Oliver

Submitted to the Department of Computer Science and Artificial Intelligence on May 30th, 2012, in partial fulfillment of the requirements for the degree of Doctor of Philosophy

Abstract

Vascular-related diseases are among the most important public health problems in developed countries. Recent advances in medical imaging provide high resolution 3D images of the vessels, allowing the generation of accurate patient-specific geometric vessel models. Image-based vessel analysis allows advanced computer-assisted diagnostic, intervention and follow-up of vascular-related diseases. It also provides valuable information for computer-assisted surgery planning and navigation, both to avoid damaging vital structures and to use vessels as anatomical landmarks.

From the modelling point of view, this thesis proposes a *Vessel Knowledge Representation* (VKR) model in the area of blood vessel analysis. It allows reusability of software pieces through appropriate abstractions, facilitating the development of innovative methods, procedures and applications. The VKR model is designed for an easy integration with existing medical imaging and visualization software platforms.

Regarding 3D vascular detection algorithms in medical imaging, we provide a detailed analysis of some well-known *vesselness* functions. We identify different types of scaling parameters in these detectors, and tests their individual influence and their relationship against synthetic and real datasets in order to establish some scale selection criteria. With respect to 3D vascular extraction methods on angiographic images, we propose an architecture and process model for the subset of vascular tracking methods called *Generalized Vascular Tracking* (GVT). We demonstrate how the different components and stages of the GVT model allow incorporating different modules into the system with increasing complexity. We also contribute with a novel method for optimized vascular section estimation during vessel tracking procedures.

As a real life application and a particular case of vascular analysis we provide a novel segmentation method for both the lumen and thrombus of abdominal aortic aneurysms on CTA images after endovascular intervention and a method for the automatic detection and quantification of endoleaks in the thrombus.

Finally, we developed the Image-based Vascular Analysis (IVAN) Toolkit, a set of software libraries for vascular detection, analysis and modelling in medical imaging. It implements many of the ideas proposed in this Thesis, and has been used and validated extensively in our experiments.

Contents

List of Figures

List of Tables

Chapter 1

Introduction

This chapter provides the general introduction to the Thesis intended to allow a quick appraisal of its contents, contributions, supporting publications and structure.

Section 1.1 provides the motivation behind this line of research. Section 1.2 enumerates the objectives set for the Thesis. Section 1.3 enumerates the contributions of this Thesis. Section 1.4 presents the general processing pipeline of vascular image analysis, Section 1.5 enumerates the publications obtained while working in this Thesis. Finally, Section 1.6 details the structure of the Thesis.

1.1 Motivation

Vascular-related diseases are among the most important public health problems nowadays. Heart and cerebrovascular diseases are respectively the first and third cause of death in 2006 in the U.S.A [62]. Malignant tumors are the second cause of death, and their growth is directly associated with vessel recruitment and angiogenesis [64]. Besides, vascular diseases are one of the principal causes of death and disability in people with diabetes [33]. These facts are justify the research efforts providing a better understanding of the structure of the vascular system and related processes and diseases, and leading to any improvement of diagnostic and intervention procedures.

The vessel structure of the blood circulatory system is one of the most complex structures of the body. Blood vessel anatomy has been studied from castings and in-vivo examinations in order to build models that provide valuable insight into the normal and variant circulatory anatomy, helping to understand the causes, evolution and outcome of several vascular-related diseases. However, many answers to simple questions about vascular morphology and angiogenesis remain open [154].

Recent advances in medical imaging technology provide high resolution 3D images of the vessel structures, so that the generation of accurate patient-specific geometric *in-vivo* vessel models [9] and related quantitative measurements has become feasible. This has resulted in the development of a wide range of new applications for computer-assisted diagnostic, intervention and follow-up of vascular-related diseases. Image-based vessel analysis provides valuable information for planning and naviga-

tion during surgical procedures, both to avoid damaging vital structures and to use vessels as anatomical landmarks for orientation and localization of structures of interest. Moreover, comprehensive image-based vascular analysis has opened new horizons in the discovery and understanding of the vascular structure and underlying processes, such as angiogenesis and blood circulation, that may help to understand the evolution of diseases in which vascular structures play an important role [17, 157].

In the recent years, a vast variety of methods and approaches has emerged dealing with vascular extraction, analysis and modelling with increasing complexity [97]. In order to accelerate the research in the area it is necessary to identify the constituting components or building blocks of the different methods, their individual influence, their relationship, and the influence and sensitivity of their parameters, so as to build robust and efficient methods that can be used in a clinical setup. Moreover, it is necessary to provide the scientific community with verified and well designed tools that allow comparing results obtained from different methods, replace some individual components and reproduce the experiments without investing extra efforts on the implementation.

From the modelling point of view, we have detected the lack of a widely accepted knowledge representation model for vascular networks allowing a structured storage of the information obtained from the extraction algorithms in such a way that it can readily be used in the clinical applications.

1.2 Objectives

1.2.1 General Objectives

- Develop a generic and versatile information model for storing and accessing information describing vascular structures.
- Develop methods for robust automated detection, extraction, quantification and analysis of vessels depicted in volumetric angiographic modalities, such as Computerized Tomography Angiography (CTA) or Magnetic Resonance Angiography (MRA).
- Perform a clinical validation of the accuracy, robustness and speed of the developed methods, to ensure that can be used in clinical practice.
- Develop specific methods for the automated analysis of Abdominal Aortic Aneurysms (AAA) after Endovascular Repair (EVAR) in CTA images for automated follow-up.
- Contribute to the field of vascular image analysis by providing insight into existing methods through critical review and replication of experimental results.

1.2.2 Operational Objectives

- Develop an information model for vascular structures which:

  - Accommodates easily the information obtained from the vascular structures by the extraction algorithms that take a vascular (angiographic) image as source.
  - Provides a versatile, intuitive and adequate structure for the development and practice of clinical applications of vascular image analysis.

- Study the underlying components and parameter setup of the most popular vascular detection algorithms:
  - Medialness functions, providing measures of the likelihood of an image point to be on the centerline.
  - We explore both differential and integral approaches.

- Propose a generic framework for vascular tracking algorithms that allows:
  - Mapping existing approaches into this framework.
  - Generating complex extraction schemes.
  - Studying the influence of components of the processing pipeline, both working individually or as a group, such as the choice of section estimation algorithm or vesselness function.

- Develop a novel method for the segmentation of AAAs after EVAR, with special focus on the thrombus segmentation. The method should be suitable for clinical routine, which implies that is fast, robust, has a small set of parameters easy to setup and with little sensitivity and allows for easy correction of the results.

- Build a free open source software toolkit for vascular image analysis, implementing relevant popular approaches to vascular detection and extraction in a consistent framework. It will ease independent comparison of different approaches in a simple way for scientific discovery and rapid prototyping of vascular applications.

1.3 Contributions of the Thesis

We have set a state of the art through an extensive review at all levels of vascular image processing, vascular morphology, vascular-related diseases, vascular imaging (aka angiographic) modalities, techniques for vascular extraction and analysis from these images and practical applications of vessel analysis. A detailed review of edge and ridge detection techniques in images and their relationship with the detection of curvilinear structures has been carried out.

The Thesis has been realized on implementations developed on the basis of or compatible with open source free software (such as the *Insight Toolkit* or the *Visualization Toolkit*), allowing for extensive diffusion of the software developed, reproducibility of the results by the research community, and contributing to building a platform that will allow quick deployment of working solutions.

1.3.1 General Contributions

- We propose a *Vessel Knowledge Representation* (VKR) model suitable for representing, in a compact and structured, manner the geometrical, topological and contextual information obtained from the vascular analysis. The VKR is proposed as the kernel for the development of systems with potential clinical application.
- We have developed a novel taxonomy of vessel attributes to be incorporated into high level information models for vessels.
- We provide a detailed analysis of the scales to be used when applying some relevant vascular detection functions (aka *vesselness* functions). We identify different types of scaling parameters in these detectors, and test their individual influence and their relationship against synthetic datasets with different noise levels, in order to establish some scale selection criteria for these detectors in real datasets.
- We propose an architecture for a specific class of vessel extraction methods: the vascular tracking processes, namely the *Generalized Vascular Tracking (GVT) Framework*. We demonstrate how the different components and stages of the GVT process model provides a systematic approach to vascular tracking that incorporates different components into the system with increasing complexity.
- We propose a novel method for vascular section estimation during tracking procedures, incorporating an optimization stage that uses specific modified vascular detectors as cost functions, in order to obtain accurate vascular sections when the direct detection approach fails. This new approach is validated on real datasets.

1.3.2 Technical Contributions

- Detailed analysis and additional insight into existing ideal cylinder shape models for vascular image analysis, on the cylinder and toroid models. Providing alternative reference frames and studying the behaviour of the principal image curvatures both theoretically and experimentally.
- A new Helix shape model allowing to study the influence of both, the geometric shape curvature and torsion, in the image curvatures.
- Study of different section profiles for the shape models, allowing to infer conclusions about scale selection in the image analysis of real tubular shapes.
- A software for the generation of synthetic tubular shape images for their use in the validation of the detection and extraction algorithms.

1.3.3 Real Life Application

The Thesis contains a real life application of most of the ideas developed, towards the final implementation of a complete system for vascular image analysis. It also deals

with the problem of image analysis of large vessels in the presence of abnormalities. Specifically, the Thesis includes results on the image processing of AAA after EVAR obtained on data provided by the medical specialists from the Hospital Donostia, in a close collaboration which is leading to improved results and products that may end up in clinical application. The main contributions in this field consist of:

- A novel segmentation method for both the lumen and thrombus of AAAs after EVAR on Computed Tomography Angiography (CTA) images.

- A method for the automatic detection and quantification of endoleaks in AAA thrombus as depicted in CTA images. To the best of our knowledge, there were no previous works in the literature addressing this specific problem.

1.3.4 Technological Contributions

The main technological contributions of this Thesis are implemented in the Image-based Vascular Analysis (IVAN) Toolkit, which is a set of C++ software libraries for vascular detection, analysis and modelling in medical imaging developed using concepts of generic programming. Due to its design, this toolkit is intended to provide the scientific community with an important tool to accelerate discovery and encourage reproducibility in the field of vascular image analysis. The IVAN toolkit provides the following specific technological contributions:

- An implementation of the VKR model whose design allows for extension by inclusion of new concepts.

- A repository of *vesselness* detectors which includes several popular approaches in the literature, designed to be easily extended by incorporation of new methods or modification of existing ones.

- An implementation of the GVT Framework whose design allows for the exchange of components or the addition of different stages so as to provide flexibility in the design of complex vascular tracking methods. This provides a way of testing the influence of the different components both individually and in conjunction.

- A means of generating synthetic models of ideal shapes as volumetric images, such as the cylinder, toroid or helix models described in Appendix A, with different cross-sections, shape and image parameters and noise levels.

- A means of reproducing the experiments developed in this Thesis.

Another technological contribution is the implementation of a set of N-dimensional discrete Gaussian derivative kernels, that have become part of the *Insight Toolkit* [118].

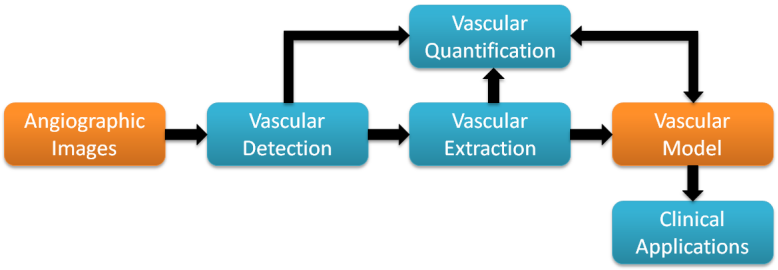

Figure 1.1: Vascular Analysis Pipeline

1.4 Vascular Image Analysis Pipeline

The *Vascular Image Analysis Pipeline*, depicted in Figure 1.1, represents, in a very compact manner, the different sources of information (in orange) and processes (in blue) involved in the development of a clinical application of vascular image analysis.

The first stage of detection or enhancement of vascular structures is performed on the source angiographic images. This stage is usually followed by an extraction stage which isolates the vascular structures obtaining additional geometric, topological or contextual information. Depending on the approach, the detection and extraction stages may be considered as a single operation. The information resulting from the extraction process is stored in an information model of vascular structures so it can be used efficiently by the clinical applications. The quantification stage involves obtaining quantitative or qualitative information on the vascular structures and, depending on the operation performed, can follow the detection or extraction stages or may only require the information stored in the model. In all cases, the information obtained in this stage is also stored in the model.

The information from the model may be used by the clinical applications in different ways. For example, 3D models of vessels may be obtained for navegation purposes during interventional procedures; information from the quantification stage may be used directly or feed into a classification engine, providing advanced vascular diagnostic information; other examples include patient-specific blood flow simulation [10], clinical studies of vascular morphometry [28] or intra-operative registration of pre-operative images using vessels as landmarks [124], among others. This image analysis pipeline can be used also for the study of other anatomical structures of similar geometry and shape, such as airway trees.

Despite the direction of the processing pipeline is from left to right, the requirements are usually built the other way. The clinical application determines which information is needed and in turn, this determines the imaging examination to be performed on the patient. Subsequently, this determines the most suited detection and extraction methods methods used to obtain the necessary information for the clinical applications.

1.5 Publications

- Ivan Macia, Manuel Graña, Celine Paloc. Knowledge Management in Image-based Analysis of Blood Vessel Structures. *Knowledge and Information Systems* 30(2):457-491, 2012.

- Iván Macía, Manuel Graña. Vascular Section Estimation in Medical Images Using Combined Feature Detection and Evolutionary Optimization. *In Proc. Hybrid Artificial Intelligent Systems* (HAIS), 503-513, 2012.

- Ivan Macia, Maria Arenas, Jon Haitz Legarreta, Isabelle Robin, Manuel Graña, Sabarinath Rajasekharan. Fast Segmentation of Abdominal Aortic Aneurysms for Endovascular Repair Planning and Follow-up. *In Proc. 1st Int. MICCAI Workshop on Computer Assisted Stenting*, 2012 (accepted).

- Ivan Macia, Manuel Graña, Josu Maiora, Celine Paloc, Mariano de Blas. Detection of Type II Endoleaks in Abdominal Aortic Aneurysms After Endovascular Repair. *Computers in Biology and Medicine* 41(10): 871-880, 2011.

- I. Macia, M. Graña, and C. Paloc. Towards a Proposal for a Vessel Knowledge Representation Model. R. Setchi et al. (Eds.): *In Proc. Knowledge Based and Intelligent Information and Engineering Systems* (KES) , Part IV, LNAI 6279, 80-87. Springer Heidelberg, 2010.

- Legarreta, J., Boto, F., Macía, I., Maiora, J., García, G., Paloc, C., Graña, M., de Blas, M. Hybrid Decision Support System for Endovascular Aortic Aneurysm Repair Follow-up. *In Proc. Hybrid Artificial Intelligence Systems* (HAIS), 500-507, 2010.

- Maiora, J., García, G., Macía, I., Legarreta, J., Boto, F., Paloc, C., Graña, M., Abuín, J. Thrombus Volume Change Visualization after Endovascular Abdominal Aortic Aneurysm Repair. *In Proc. Hybrid Artificial Intelligence Systems* (HAIS), 524-531, 2010.

- Maiora, J., Garcia, G., Tapia, A., Macia, I., Legarreta, J.H., Paloc, C., De Blas, M. & Grana, M. Thrombus Change Detection After Endovascular Abdominal Aortic Aneurysm Repair. *Int. J. of Computer Assisted Radiology and Surgery*. Springer-Verlag, Vol. 5 (Suppl 1), pp. S15, 2010.

- Iván Macia Oliver, Jon Haitz Legarreta, Céline Paloc, Manuel Graña, Josu Maiora, Guillermo García. Segmentation of Abdominal Aortic Aneurysms in CT Images using a Radial Model Approach. *In Proc. Intelligent Data Engineering and Automated Learning* (IDEAL), Emilio Corchado, Hujun Yin (eds) LNCS 5788, Springer Verlag, 2009.

- I. Macía, J.H. Legarreta, F.Boto, C.Paloc, M. Graña, G. García, J. Maiora, M. de Blas. Segmentación de Aneurisma Abdominal de Aorta en Imágenes CT Mediante un Modelo Radial: Estudio Preliminar. *In Proc. XXVIII Congreso Anual de la Sociedad Española de Ingeniería Biomédica*(CASEIB), 2009.

- Josu Maiora, Guillermo García, Arantxa Tapia, Iván Macía, Jon Haitz Legarreta, Manuel Graña. Stent Graft Change Detection after Endovascular Abdominal Aortic Aneurysm Repair. *In Proc. Intelligent Data Engineering and Automated Learning* (IDEAL), Emilio Corchado, Hujun Yin (eds) LNCS 5788, Springer Verlag, 2009.

- I. Macía. Generalized Computation of Gaussian Derivatives Using ITK. *The Insight Journal*. Jul-Dec 2007.

1.6 Structure of the Thesis

The structure of this Thesis follows the vascular image analysis pipeline depicted in Figure 1.1. Following this scheme, *Chapter 2* introduces the general problem of vascular image analysis, describing the clinical applications and the anatomical and algorithmic information that is used to build the vascular information model that is proposed in *Chapter 3*. *Chapter 4* introduces some concepts about image analysis of edge, ridge and curvilinear structures. *Chapter 5* focuses on the detection of vascular structures, with special emphasis on the parameter and scale selection of some popular vesselness functions. *Chapter 6* postulates a framework for vascular tracking for direct vascular centerline extraction whose utility is tested experimentally on synthetic and real datasets. *Chapter 7* deals with the specific clinical application of analysis of AAA after EVAR. Due to the size of the vascular structures involved (the aorta), the shape of the abdominal aneurysm (which is a blob-like structure) and the endoleaks (which can be regarded as amorphous), this problem is treated separately since it requires specific methods of analysis that are not described in the previous chapters. Complementarily, *Appendix A* describes and analyzes some ideal shape models and section intensity profiles of vascular structures that are used in the detection and extraction stages and *Appendix B* describes the IVAN library.

Chapter 2

Overall review

In this chapter we review some background ideas of the ensuing chapters of this Thesis. To set the stage, we review Vascular Morphology and some facts of vascular related diseases which serve as an introduction for the main applications in the field of modelling and visualization of vessel structures. Next, we provide an overview of the angiographic modalities for image-based diagnostic of vascular-related diseases, as well as the applications and vessel information which is considered relevant for diagnosis in the clinical practice. We will comment on the current computational techniques for vessel information extraction from the angiographic images. Finally we discuss the need for a Knowledge Representation Model in this area of medical image processing.

The structure of the chapter is as follows: Section 2.1 introduces some biological ideas about vascular morphology. Section 2.2 gives a short review of vascular diseases. Section 2.3 is referred to image based diagnosis information and tools. Section 2.4 introduces the algorithms for vessel extraction from angiographic images. Section 2.5 introduces the Vessel Knowledge Representation (VKR) Model.

2.1 Vascular Morphology

The efficient distribution and collection of nutrients requires a blood vessel branching tree structure, except at the level of the capillaries. Vascular networks are asymmetric tree structures, in which each parent branch, with diameter D_1, is bifurcated (except in very rare cases) into two branches with smaller diameters (D_2 and D_3). The tree may be also locally unbalanced regarding the diameters of child branches ($D_2 \neq D_3$) and the number of bifurcations along each path from the root to the leaves of the each subtree [76]. Geometric models for the description of vessel bifurcations were first proposed by Murray [128, 165] and later by Oka and Nakai [133] specifying relationships between vessel widths and angles based on physiological observations.

Recent studies [77, 208] have discovered that the construction of the vascular trees obeys to a set of scaling laws which minimize both, the energy cost of fluid transportation, which decreases as the diameters increase, and the energy cost of construction and maintenance of the vessel structure, which increases with larger diameters. These

scaling laws are morphometric relationships between the arterial volume, cumulative length, and diameter of a branch and its distal subtree. In particular, it can be seen that, in order to minimize the power needed to maintain the blood circulation operation over the network, the diameter relationship between a parent branch and its two child branches is:

$$D_1^k = D_2^k + D_3^k, \tag{2.1}$$

with average values of k typically between 2 and 3.

With respect to the vessel sections, in a simplistic approach the vessel sections can be assumed to be circular but, in fact, most of the times it has some smooth irregular round shape. The thickness of the vessel wall is non-negligible, but most imaging modalities only depict the vessel *lumen*, which is the space where the blood flows. Few imaging modalities, such as Intravascular Ultrasound (IVUS), can image the vessel wall.

In order to estimate the complexity and branching frequency of the human vascular trees [34, 168, 66, 68, 67, 69], several studies used and adapted the *Strahler order* of branching complexity [172], defined originally for hydrology studies but applicable to all branching, tree-like structures. The original Strahler ordering system assigns the order 1 for the smallest branches. When two vessels join into a confluent vessel, the order of the confluent vessel is increased by 1 if the two child vessels have the same order; otherwise the parent assumes the order of the highest order child. However, the use of the original order as defined by Strahler encountered the problem of diameter overlapping among vessels of consecutive orders in morphometry analysis of very large trees. In order to take into account the vessel radius, the *Diameter-defined Strahler Ordering System* [78] incorporated a new rule stating that: "When a vessel of order n meets another vessel of order $\leq n$, the confluent vessel is assigned order $n+1$ only if its diameter exceeds that of the lower order vessel by a certain amount, which is determined by the statistical distribution of the diameters of each order". In practice, threshold computation must be iterative, since the diameter distribution has to be recalculated when the order is assigned. Applied to haemodynamic studies, this enhanced ordering system provides a reasonable and systematic way to handle main arteries that vary considerably in diameter along their length, such as the main pulmonary artery. In a morphometric study of the human lung vasculature casts [69] it was found that, in pulmonary arterial and venous trees, the relationship between the order of a branch [78] and its diameter follows closely a logarithmic scale. They found a maximal order of 15 for both arterial and venous trees of the human lung.

In order to represent the connectivity of asymmetric branches and to distinguish serial and parallel branches of the same order, three new concepts were introduced in [78]: *Vessel Segment*, *Vessel Element* and *Connectivity Matrix*. A *Vessel Segment*, corresponding to a branch, is the portion of vessel between two bifurcations. A *Vessel Element* is defined as a set of serially connected segments of the same order. Statistical data of diameters and lengths are obtained for segments and elements. Haemodynamic flow circuits are composed of vessel elements. Ratios of segment/element can also be calculated for each order. The *Connectivity Matrix* is an upper triangular matrix, in which each element $C(m,n)$ is the ratio of the total number of elements of order m

whose parents are elements of order n divided by the total number of elements of order n.

The advent of new imaging techniques such as Microcomputed Tomography and advanced algorithms for vascular segmentation, quantification and analysis, has recently improved the possibility of performing detailed studies of vascular morphology, i.e. in the coronary [194], renal [131] and pulmonary trees [152], and the ability to perform comparisons in populations [202], enhancing the understanding of the vascular structure, and the physiology and pathology of the corresponding organs.

2.2 Vascular-related Diseases

Hemorrhages and embolisms are the two main types of vascular accidents, with a mortality of about 5% of the population over 65 years-old. Hemorrhages can be produced by vessel ruptures due to aneurysms. An *aneurysm* is a local growth of the vessel diameter due to weakening of the vessel wall that suffers increased local elasticity. Aneurysms occur most commonly in arteries at the base of the brain (circle of Willis) and in the thoracic and abdominal aorta. Embolisms and thrombosis are obturations of the vessels as a consequence of a progressive abnormal local reduction or the vessel diameter or *stenosis* (pl. stenoses). There are several causes or conditions that lead to stenosis such as atherosclerosis, birth defects, diabetes, infection, inflammation or ischemia among others. Atherosclerosis is a condition in which the arterial wall thickens, due to the accumulation of a mixture of substances such as calcium, cholesterol fibrin and macrophage blood cells, which causes stenosis or occlusion of the vessel or aneurysms due to excessive compensation by enlargement of the vessel. The possibility of performing early diagnoses of aneurysms, stenoses or other vascular accidents may avoid further complications and thus, will decrease the morbidity and mortality associated to vascular-related diseases. There exists evidence [10] that regions of the vessel wall exposed to disturbed flow, such as at bifurcations and regions of high curvature, are prone to the initiation and development of atherosclerosis. Identification of such regions by geometrical analysis may provide further insight into the development of this disease.

There are some pathological conditions for which blood vessels play an important role in their evolution. The most important case is the vascularization of malignant tumors. In order for the cancer cells to obtain appropriate nutrients to grow and to get rid of waste material, tumors need to be vascularized. Tumors achieve this by several methods such as cooption (recruitment of pre-existing vessels) and angiogenesis [64]. Furthermore, most of the conditions induce changes in vessels at different levels. Cancer induces the development of abnormal, tortuous vessels [50], that can be reverted by successful treatment [73]. Images of the retina may provide information on pathological changes caused by local ocular diseases and early signs of certain systemic diseases [7, 207, 29, 196]. Other examples may be hypertension and diabetes, which induce the narrowing of the arteries. For example, a recent study has shown that retinal vessel microvascular structure is associated to risk of mortality from ischemic heart disease and stroke [196].

2.3 Image-based Diagnosis

An introductory overview of medical imaging modalities is needed to understand their ability to produce images of the blood vessels, their possible application as tools in clinical and research studies, and the requirements that the image processing and knowledge representation techniques need to take into account. The diagnostic support provided by the vessel structure images is further made concrete by the specification of precise attribute measurements.

2.3.1 Angiographic Modalities

Nowadays, there are many medical imaging modalities and protocols devised specifically for the visualization of vessels, that are generally denoted with the term *angiography*. Some of them include the injection of a modality-specific contrast agent that enhances the visualization of blood vessels[1].

- *Digital Substraction Angiography* (DSA) is an evolution of the original *X-ray Angiography* (XA) technique, that digitally subtracts a pre-contrast image from a contrasted images obtained after injection of a contrast agent. Until recently, DSA has been considered the standard vessel imaging technique in many diagnostic and interventional procedures, such as assessment of renal and carotid artery stenosis, cerebral aneurysms, acute limb ischemia or arterio-venous malformations (AVMs) among others. The main advantage of DSA imaging is that it allows real-time, live visualization of very thin vessel structures, and thus can be used during interventional procedures. However, DSA involves radiation exposure, is a 2D modality and, more importantly, is an invasive procedure and thus, it has an associated risk of small complications. DSA is gradually being replaced by some non-invasive 3D imaging techniques, such as *Computerized Tomography Angiography* (CTA) and *Magnetic Resonance Angiography* (MRA).

- CTA images are standard Computerized Tomography (CT) images generated by contrast injection simultaneously with the image acquisition. Depending on the synchronization of the image acquisition with the flood flow, different contrasts may be obtained, such as those corresponding to the arterial phase, venous phase, post-constrast phase, etc., that depict several stages of the contrast inflow into the vessels. Some of the applications of CTA imaging are analysis of stenosis in renal arteries, aortic aneurysms, brain aneurysms or AVMs, atherosclerosis assessment and detection of vein clots in legs. The main drawback of the technique is the radiation dose that the patient receives during the scanning procedure. With the advent of multidetector technology and improved computational image reconstruction schemes, acquisitions have increasing spatial resolution obtained in faster times with less radiation dose.

[1] The first coronary *X-ray angiography* (XA) was performed accidentally by Sones and Shirey in 1958 [169]. While injecting contrast material in the right ventricle, the catheter slipped into the right coronary artery and for the first time discovered the advantages of imaging the vessels.

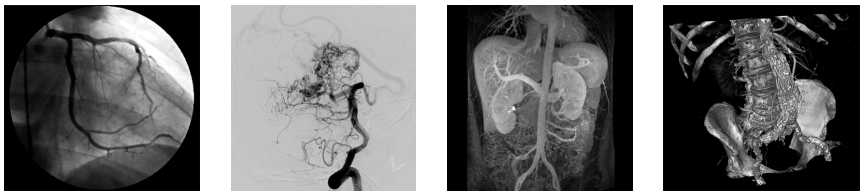

Figure 2.1: Examples of Angiographic Modalities. From left to right XA of the coronaries, DSA of the brain vessels, MRA in venous phase and CTA showing stent after endovascular aortic aneurysm repair.

- MRA comprises several techniques based on Magnetic Resonance Imaging (MRI). The techniques are based either on imaging flow effects or on using contrast agents, like in *Constrast-enhanced MRA* (CE-MRA). Vessel images can also be obtained by adequate pulse sequences without contrast. *Time-of-flight MRA* (ToF-MRA) uses a short echo time and flow compensation to enhance contrast of blood vessels. It is commonly used in the head and neck, where it gives very high resolution image, but has problems in areas of slow blood flow such as aneurysms. *Phase-contrast MRA* (PC-MRA) manipulates the phase of the MR signal providing both, the vessel image and the corresponding flow speed. PC-MRA has larger acquisition times, since the technique requires acquisitions in the three basic orientations (axial, sagittal and coronal). Recent MRI techniques include *Fresh Blood Imaging* (FBI) [127] and *Susceptibility Weighted Imaging* (SWI), also called *BOLD Venography* [151, 203]. The main advantage of MRA compared to CTA is the absence of radiation exposure while maintaining very high image quality, though spatial resolution is lower in MRA than in CTA. However, as acquisition times are larger, motion artifacts are more likely to appear.

- *Vessel Ultrasound* imaging is a non-invasive procedure that allows live blood vessel visualization. Combined with the technique of Doppler ultrasound, it also gives measures of blood flow. It can help the physician to visualize and assess stenoses, aneurysms, varicose veins and many other vessel accidents. The main problem is its low signal-to-noise ratio which gives poor image quality.

- *Optical* imaging can also be used to image vessels, as in *Retinal Fundu*s images, where vessel analysis is used in the assessment of retinopathy and as an early sign of systemic diseases [7]. Other recent techniques, such such as non-invasive *Near-infrared* (NIR) imaging can be used for visualizing vessels through the skin [56].

- *Intravascular Ultrasound* (IVUS) provides a means of imaging the vessel wall by using a catheter equipped an ultrasound transducer.

- A recent development is the study of the mechanic properties of vessel wall by *Magnetic Resonance Elastography* [198].

2.3.2 Applications of Vessel Analysis

As the technology of vessel imaging evolves, improving the quality and quantity of information about vessel structure that can be obtained, the applications have also flourished. Here we enumerate some of the current ones, that will motivate the knowledge representation and manipulation tools to be discussed below.

- Surgery:
  - Surgery planning: allows the surgeon to evaluate the alternative actions and prepare for the intervention [163].
  - Planning and navigation [182] during interventional therapy and biopsy : here vessel structures are critical by themselves, but also serve as spatial reference or anatomical landmarks for planning and navigation. It has strong real-time requirements, because the vessel structure may be changing during the intervention. Sometimes it requires fusion of diverse imaging modalities to improve the interaction.
  - Training of surgeons and interventional radiologists using annotated virtual reality systems [181], virtual atlases, etc.
- Cancer studies:
  - Non-invasive estimation of tumor malignancy and growth by vessel quantification and localization of abnormal vessel clusters [26, 27].
  - Simulation and study of vessel angiogenesis, which is an important factor in malignant tumor growth [50].
- Diagnosis of vessel-related diseases:
  - Characterization of retinal-related diseases such as diabetic retinopathy or retinopathy of prematurity by induced changes in vessel attributes such as diameter and tortuosity [29].
  - Quantification of stenosis and aneurysms [75].
  - Decision support systems [107] for vessel-related disease [94].
- Image registration using vessel as landmarks [124]. This is typically used in non-rigid registration [89].
- Studies of vessel morphometry [69] and haemodynamics [178]:
  - Construction of geometric models of vessel trees [76] which allow direct visual diagnosis and fast and interactive visualization and exploration, and provide by themselves a good understanding of the (patient-specific) vessel network structure and morphology.
  - Discovering of statistical properties of attributes of vessels in healthy and diseased populations [28].

- Performing comparative studies, possibly with the help of anatomical atlases, for assessment of vascular diseases, malformations and abnormalities [27].
- Simulation of arterial flow and pressure in organs that cannot be accessed by direct measurement [161], in aneurysms [185] or for detecting regions of turbulent flow prone to atherosclerosis, such as bifurcations and high-curvature regions [10].

2.3.3 Vessel Attributes

The main concern in this section is about measurements that can be somehow obtained from the images and used as a basis for diagnosis or any of the applications enumerated above. These measurements are the relevant attributes of the KRM proposed below for the feasible applications, therefore their identification from the literature survey is an important step in the KRM definition. We must also take into account the possibility that the user may specify some qualitative attributes, which are not the result of any quantitative model, though the user may base its observation on results from computational image processing. They are used by the clinician to perform diagnoses or intervention decision upon their direct inspection. Structural attributes refer to the morphological and structural description of the vessel network. They are mostly used for intervention planning and some diagnoses based on structural morphology and complexity, like angiogenesis. The quantitative description of each vessel branch and bifurcation are the bricks of the decision support and model building processes.

Qualitative Vessel Attributes

- *Vessel Shape*: provided by direct visualization of volumes containing (contrasted) vessels, or surface reconstructions of the vessel walls.
- *Vessel Section Shape*: needs some processing and abstraction from the image in order to obtain an adequate representation. It may include the vessel wall or not, depending on the imaging modality.
- *Anatomical Location*: more important than the absolute anatomical position of the vessels is the relative position of the vessels with respect to adjacent organs or structures of interest, specially pathological structures. It may require some image registration techniques to obtain the corrected relative location.

Structural Vessel Attributes

- *Vessel Network Topology*: the topological structure and interconnections of the vascular network.
- *Total Number of Branches*: when restricted to a space, it is a measure of vessel density.

- *Depth Level*: this is the level of a branch with respect to the root branch of the vessel network, that is, the minimum number of bifurcations that separate the current branch from the root branch.
- *Strahler Number*: a numerical measure of branching complexity [172, 78].
- *Branching Frequency*: the number of bifurcations and distance between them.
- *Ratios of Branch Radii*: several measures can be obtained as ratios of branch radii in a bifurcation. The *branching ratio* and the *area expansion ratio* are related to the portion of flux going into each branch in a bifurcation [6].

Quantitative Vessel Attributes

- *Diameter*: is an immediate indicative of an aneurysm or stenosis.
- *Length*: though the absolute length of a branch may not be significant by itself, and its significance is relative, it can be used to calculate other important properties such as tortuosity.
- *Size/Volume*: volume and size of the vessels in a region of interest provides quantitative measurements of vessel growth.
- *Tortuosity*: is a property of a curve being twisted, having many turns. There have been several attempts to quantify this property [192]. Tortuosity is a sign of vessel abnormality usually associated to disease. Bullitt *et al*. [28] distinguish three types of blood vessels tortuosity:
  - *Type 1*: where vessels elongate and become tortuous. This may occur in conditions such as retinopathy, prematurity, hypertension and aging.
  - *Type 2*: vessels that make frequent changes of direction and may appear as a "bag of worms", as occurs in arteriovenous malformations and within hypervascular tumors.
  - *Type 3*: high-frequency low-amplitude oscillations or 'wiggles', associated to the neovascularity of malignant tumors.
- *Surface Area*: as arteries bifurcate and convert into arterioles and capillaries, the total surface area for the same blood supply increases.
- *Section Area*: this is the area of the vessel cross-sections, which lie in the normal plane to the medial line or centerline.
- *Blood Velocity*: differences in blood velocity can be measured or simulated in order to find stagnancy regions or abnormal circulation patterns.
- *Elasticity*: of the vascular walls that may change due to plaque accumulation or the presence of aneurysms.

2.4 Vessel Extraction and Analysis in Angiographic Images

The literature on algorithms for vessel detection and extraction from angiographic images is huge [97, 136, 79, 18, 48]. The approaches differ in the assumptions made about the shape and structure of the physical vessels, the medical imaging modalities, the mathematical models describing the vessels, the image features used to detect them, and the algorithmic schemes to extract them. In a recent outstanding review [97], vessel lumen segmentation techniques are categorized according to the underlying models (assumptions on appearance and geometry of the real vessels as shown in the images) image features (quantitative image metrics used to detect the vessels), and extraction schemes, (the algorithm used to extract the vessels, according to the assumed models and defined image features), sometimes with the help of data mining algorithms [200]. We proceed to describe the most important angiographic image-based vessel modelling and extraction (segmentation) techniques, emphasizing the most salient elements that are explicitly modelled in our knowledge representation framework.

2.4.1 Vessel Models in Image-based Analysis

In image-based analysis of vascular networks, there are two main types of assumptions and models used for vessels: *photometric* models and *geometric* models. *Photometric* models deal with the generation of vessel images in the corresponding angiographic modalities. They are modality dependent, used for image processing, and outside the scope of this paper. On the other hand, *geometric* vessel models describe elements such as branches, corresponding cross-sections, bifurcations and relationships in the vessel tree. They are relevant to the definition of our knowledge-based model which is more influenced by geometrical considerations.

Surface-only models of vessels, defined by polygonal meshes, which may be obtained directly from vessel segmentations by polygonal reconstruction [51], are not relevant to our endeavor because they are rather difficult to manipulate and useless as the basis for structural analysis and representation.

Vessels are elongated structures, except in some very specific (pathological) cases. For this reason, one of the most common approaches is to use the centerline as the main shape descriptor. The centerline corresponds to the medial loci of the vessel [19], centered inside the lumen, and constituting the centroid of successive cross-sections. The centerline allows to describe objects in terms of a tree of "elemental figures" [144]. However, it is very sensitive to vessel boundary details, so there has been an extensive research in algorithms that obtain smoother centerlines, such as Voronoi skeletons [129], shock loci of reaction-diffusion equations [166], "cores" (height ridges of medialness functions) [143] and distance transforms [22].

From the vessel's centerline, the external contour can be modelled as a generalized cylinder [5], that is, a tubular shape with a curvilinear axis (the centerline) and varying width along its length, which is usually defined by the cross-sections along the centerline. Different shape descriptors can be used to define these cross-sections (see figure 3.4). Constraints can be imposed on the successive sections in order to maintain

spatial coherence when producing 3D models of vessels [132]. Sometimes the external surface of the vessel can be modelled explicitly [51] or implicitly [180, 10] from the vessel centerline. A mesh surface model of the vessel wall can also be obtained by sweeping the cross-sectional contours [81, 130].

The tree structure of vessel networks is naturally described in the form of a graph, more specifically as trees (directed acyclic graphs) [59, 25, 163, 4, 140, 125]. A vessel graph is obtained from the segmentation by skeletonization (see 2.4.2) and analysis of line structures. The graph description is useful for operations such as pruning, trimming, correcting and reconnecting of vessel branches via graph-based techniques after initial extraction. Graph-based representations can be mapped back into visual representations providing a better insight into the vascular structure by means of symbolic renderings [59] or surface reconstructions from centerline and section data [48].

2.4.2 Extraction Schemes

Because of its central importance, we dwell on the methods for centerline extraction found in the literature. Note that initial vessel volume segmentation can be obtained by techniques such as simple thresholding, region-growing [21], wave tracking [150] or vessel-adapted level-sets methods [110] among others.

Centerline Extraction by Skeletonization: Centerlines can be extracted by 3D skeletonization of an initial volume vessel segmentation. Thinning algorithms [139] are based on iteratively removing points on the border of the object that do not modify its topology (simple points). The remaining set of points is the topological skeleton. The problem is that they usually provide a centerline at a pixel/voxel level. Subvoxel accuracy may be obtained by other methods, such as flux of gradient vectors of distance functions [22].

Direct Centerline Extraction: In some cases, a rough estimation of each slice's centerline point is enough to provide an approximate segmentation of the vessel tree, that may be useful for a more refined segmentation. This can be done by obtaining complete surfaces from the centerline, or on a section-by-section basis, by fitting models of sections or by extracting the section image planes and obtaining the boundaries by segmentation as in [92] (Figure 3.4).

The first approach to centerline extraction is interactive manual selection of centerline points and interpolation with or without an underlying mathematical curve model, such as a B-spline. However, this method is not very precise, and automatic algorithms are desirable.

Direct centerline tracking algorithms start from a initial point or set of points, selected manually or automatically in the centerline or its vicinity, and try to iteratively extract consecutive vessel centerline points, usually by estimating vessel direction, until the end of the branch or tree is reached. Most of these methods also estimate the local vessel normal (section plane) and scale (approximate diameter) and differ mainly in the image features used for centerline tracking, in their ability to handle bifurcations and in their robustness to noise. We have found in the literature methods based on

tracking multi-scale *medialness*[2] features [11], analysis of connected components of spheres [31], Kalman filtering [199], moments of inertia [61] and Bayesian tracking [95] among others.

Centerlines can also be obtained as *minimum cost paths* (geodesic paths) between start and end points detected on a branch or on the whole vessel tree. The inverse of the features or metrics used to estimate *medialness* measures can be used in this case as cost functions [193], minimized by optimization algorithms such as Dijkstra's shortest paths [44], graph-based schemes [134, 193], or the Fast Marching algorithm [3] used in [43].

Global Centerline Detection: Centerlines can also be obtained by calculating vesselness or medialness features in the whole region of interest and by obtaining patches of centerlines by connected local maxima (ridges) of these features [147]. These patches are usually too wide and usually need to be skeletonized in order to obtain the medial representation that corresponds to the centerline. Other operations involve pruning, for removal of noisy branches, and reconnection of broken branches, as vessel features sometimes yield low values at bifurcations. For the reconnection, local strategies of the aforementioned minimum cost paths approaches can be used between candidate reconnection points.

2.4.3 Vascular Feature Models

Several vessel (disease-related) features can also be modelled. *Stenosis* are usually modelled as local diameter reductions [52, 99]. *Aneurysms* are more difficult to model and quantify due to their shape variability. Specific models have been proposed for cerebral [126] and aortic [116, 38] aneurysms. *Calcifications and stents* often appear as hyperintense structures. Recently, methods have been proposed that combine appearance and geometric models for the segmentation of these structures from CTA images [80, 184]. Recently, we proposed an automatic method for the detection of *endoleaks* after endovascular repair of aortic aneurysms [115].

2.5 Knowledge Representation Model

There are some examples of specialized vessel representation systems in the literature. The *Vascular Modelling Toolkit* [142] focuses on the geometric modelling of vascular structures in order to generate surface and mesh models suitable for structural and haemodynamic studies. Gerig *et al*. [59] proposed a symbolic model that encodes shape features and structure relationships of vessels obtained from segmentations of angiographic images, and applied it to the analysis of cerebral vasculature in MRA images. The hybrid model proposed by Puig *et al*. [148] provides information of the topological relationships of the vessels and incorporates vascular accidents such as aneurysms and stenoses as special vessel segments. It is organized in three

[2] A medialness function quantifies to which degree a point is part of the centerline

layers: global structure, which is a graph-based structure, vascular surface and volume model. The model is constructed from segmented MRA images with application in a computer-assisted neurovascular system. The model proposed here tries to overcome some limitations of these early models, through a general yet flexible knowledge representation of vascular systems.

Common elements, components and stages found in our experience and literature review.

- In most of the cases, it is valid the assumption that the vessels are elongated, tube-like objects, whose length is much larger than the diameter.
- Vessels appear as hyperintense[3] structures (sometimes hypo) in the vascular imaging modalities, brighter that their neighboring tissues, though sometimes we can find contrast agent inhomogeneity or imaging artifacts.
- Homogeneity in vessel size and photometric intensity is desirable, but usually it is necessary to deal with varying vessel widths and intensity inhomogeneities.
- The use of a vessel centerline, as a descriptor of the shape of the vessel and extraction and modelling of sections, is also a common element.
- Some schemes reuse well-known features, such as *medialness* functions, or intermediate representations, such as medial-based representations or skeletons.
- Some common processing stages can be identified in families of algorithms, for example, in vessel tracking procedures.

In fact, as emphasized in [97] many vessel algorithms rely on increasingly complex combinations of existing techniques, sometimes operating at different levels of abstraction. The identification of the building blocks that constitute the extraction schemes and the explicitation of some hidden assumptions and abstractions used in their conception is a crucial step for a better understanding of the underlying concepts for the improvement existing methods. This explicitation can be performed through the development of unified frameworks, which implement the most commonly used models, features and algorithms and identifying their appropriate settings.

In ensuing chapters of this Thesis, we propose a unified framework focused on the modelling of vascular vessel networks and related qualitative and quantitative information. The framework models the vessel network in such a way that is easy to be handled by extracting schemes based on image analysis, but also to be converted into other representations suitable in several applications (see Figure 3.1). Such a framework will allow:

- an increased automation of the processes, which, in turn, increases the reproducibility of the experiments and allows to perform large quantitative studies which would be impossible to tackle otherwise.

[3] Hypointense vessel can be converted to hyperintense just by inverting the image intensities.

- a quantitative comparison of the performance of different techniques under the same conditions and with known implementations, that may provide better insight into their behavior and that may lead to their optimization.
- an efficient reusability of components that will allow faster prototyping and more reproducibility in research studies.

Chapter 3

Vessel Knowledge Representation

We have detected the lack of a widely accepted knowledge representation model in the area of Blood Vessel analysis. We find that such a tool is needed for the future development of the field and our own research efforts. The model should accommodate the vascular information obtained from the image analysis stages in such a way that can be used efficiently in the clinical applications. It will allow easy reuse of software pieces through appropriate abstractions, facilitating the development of innovative methods, procedures and applications. After the identification of the key representation elements and operations, we propose a Vessel Knowledge Representation (VKR) model that would fill this gap. We give insights on its implementation based on standard Object Oriented Programming (OOP) tools and paradigms. The VKR would easily integrate with existing medical imaging and visualization software platforms.

The structure of the chapter is as follows: Section 3.2 describes the requirements for a Vessel Knowledge Representation (VKR) model. Section 3.3 gives details of the VKR. Finally, some conclusions are drawn in Section 3.5.

3.1 Introduction

The diversity of medical and biological applications and the availability of huge amounts of high-quality information for vessel analysis has raised the problem of vascular knowledge representation in its full multi-faceted complexity . Our purpose is to discuss appropriate knowledge representation and manipulation tools for vessel structures which could serve as a common ground for the development of compatible and reusable systems. We frame this study in the diversity of applications found in the literature, and in our actual research experience [115, 94, 120, 119, 116, 121, 117]. We contribute a *Vessel Knowledge Representation* (VKR) model that, due to its efficiency and versatility, may be used for a wide variety of image-based vessel extraction schemes and vessel analysis applications. This model aims to fill an information management gap that we

have detected in the literature dealing with vessel structures computerized extraction and analysis of vascular structures.

We have in mind two objectives when proposing the *Vessel Knowledge Representation* (VKR) *Model*:

1. to ease the definition of new algorithms, providing a kind of road map of tools and applications.

2. to allow the easy reuse of previously generated pieces of software, as building blocks of the image processing pipeline. This approach is common to some other medical imaging processes, like brain mapping.

3.2 Requirements of the Vessel Knowledge Representation (VKR) Model

The VKR model is being defined through a process of identification and abstraction of structural, geometrical and morphological properties of vessels in the literature and in our own research experience. This leads to the identification of data structures, operations and components used in the most common models and schemes for vessel extraction. This model can then be converted into an appropriate data representation, such as a mesh surface model, a refined segmentation or a symbolic visual representation. When rendered, these representations can be used for localization and for interactive exploration of the VKR model and underlying properties in some of the applications described above. Alternatively, these derived data representations can also be used, for example, for numerical studies, such as simulations of haemodynamics, structural analysis or other medical and research applications out of the scope of this thesis. The VKR model must include the geometry and topology of vessel trees with constituting branches, bifurcations and sections, as well as vascular accidents such as stenoses, aneurysms and abnormal regions, such as those feeding neighboring tumors. Models of these physical entities and related concepts used in vessel analysis applications must be devised and structured by using object-oriented design techniques.

We can make more precise some desired properties of our VKR model design:

- *Versatility*:
  - Modelling of low level entities, such as vessel centerlines or sections, without compromising higher level elements, such as the global graph-based model of the vessel tree and its traversal mechanisms.
  - Allowing several coexisting representations of the same vascular system, providing easy transformation among representations. This idea is illustrated in Figure 3.2 where different graph-based representation of the same vascular tree are shown.
  - Decoupling algorithms from underlying data structures. Abstract mechanisms must be provided for accessing, traversing and manipulating the data.

- *Efficiency*: as data amounts are huge in this kind of applications, and time requirements are increasingly tight, efficiency in terms of computational time and use of resources is highly desired.

- *Utility*: to be useful the VKR must take into account actual design practices and constraints from:

  - The actual state of the art vessel extraction algorithms (see section 2.4.2) that may have been used for generating the vessel data structure from the angiographic image data.
  - A broad range of clinical and research applications that will be increasing in complexity and response time requirements.

- *Complexity Hierarchy*: the framework should be able to provide different levels of complexity and abstraction in order to represent the vessel structures at different levels. The structures need to be represented at least at the tree, branch and section level and at each level geometric, topological and semantic information layers need to be managed.

- *Integration* : we require that the knowledge representation framework can be easily integrated with pre-existing frameworks which deal with certain specific models, processes and data structures efficiently, such as the *Insight Toolkit (ITK)* [204], for medical image segmentation, registration and analysis and the *Visualization Toolkit (VTK)* [159], for visualization of resulting vascular structures together with image data.

3.3 Model Description

3.3.1 The VKR Model in Context

The VKR model is the core of the diverse operations and functions related with vessel analysis techniques, as shown in the workflow diagram depicted in Figure 3.1. The boxes in this diagram correspond to data types of some kind, while the labeled arrows correspond to transformations or manipulations of the data. We have omitted the closed operations, such as branch pruning or image filtering. The VKR vessel representation can be obtained directly (see section 2.4.2) from the angiographic image or volume or indirectly from the results of an intermediate image segmentation process. In the latter case, the segmentation detects the image/volume regions corresponding to the vessels, from which the vessel representation can be obtained by skeletonization (see 2.4.2), to obtain the centerlines, followed by section or boundary estimation. Alternatively, a set of disconnected volume vessel regions can be obtained by a global detection process of vessel features, followed by pruning and/or reconnection of centerline patches (see section 2.4.2). We include in the diagram obvious storage and retrieval operation of the VKR to/from a file or database. The VKR model is the natural domain to perform measurements which can be added to it as an enrichment.

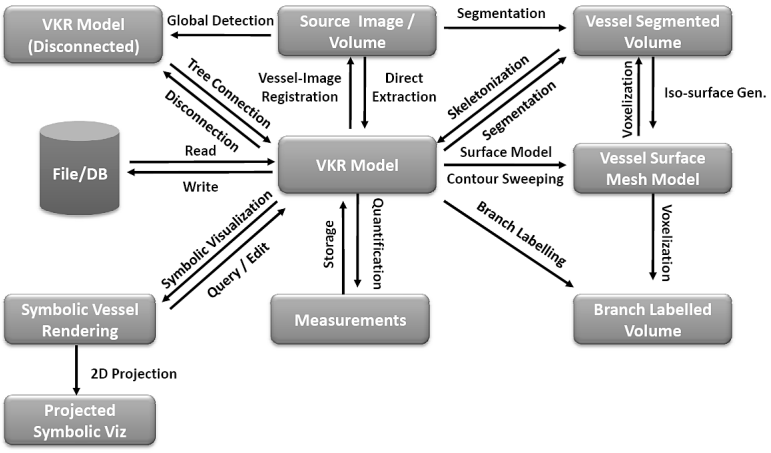

Figure 3.1: VKR Workflow Diagram

By assigning symbolic graphical representations or *glyphs* (such as lines, spheres, cones or more complicated shapes...) to the underlying components of the VKR model, a symbolic visual representation of the vessel tree can be obtained. This may be used as a roadmap, for agile exploration and interaction, or may be directly overlaid or projected onto the angiographic images, slices or volumes in order to provide visual cues.

The VKR model can be the basis to build up a surface mesh of the vessel boundaries[1] by several techniques such as contour sweeping of the cross-sections or by an explicit or implicit surface model as explained in 2.4.1. The VKR model can also be used to generate a mask or Region of Interest (ROI) on the CTA/MRA volume for further processes. The VKR data can be then converted into a mesh surface by iso-surface reconstruction [108]. Generated surface meshes can then be used for direct visualization and navigation, possibly mixed with other symbolic, surface, volume or slice renderings, in a kind of Augmented Reality computational environment. In the same spirit, the identified and labeled branches can be mapped into the CTA/MRA volume or mesh surface, allowing increased interaction via direct structure picking. The mapping can go both ways, allowing the access to the VKR model from the visualization of the CTA/MRA volume, and visualization of CTA/MRA data corresponding to VKR selections.

3.3.2 Data Structures

The data structures of the model are designed in order to describe qualitative (i.e. section shape, anatomical location, diagnostic annotations) and quantitative (section area,

[1] This is only feasible with volumetric angiographies, but the model is able to handle 2D representations too

curvature) information (Figure 3.5) in such a way that can be handled efficiently both by the extraction schemes and by the final applications while keeping a high degree of versatility. The data structures represent vessel information at different levels ranging from a complete vascular network to a vessel center or boundary point.

3.3.2.1 Vessel Graph

In general, we can consider the vessel network as a binary tree structure since in most cases bifurcations split a branch into two [69], with some exceptions like the Circle of Willis in the brain [161]. Since a tree is a subtype of graph, the latter can be used for the structural representation in the VKR, providing additional freedom for incorporating additional elements that cannot fit into a tree structure.

A graph typically consists of nodes, representing the modelled concepts, and edges, that connect the nodes and represent their relationships, which is in terms of parent/child for tree structured graphs. In our case, a *VesselNode* represents an abstraction of an element used for vessel representation and analysis at graph level. Such an element may be a vessel branch, bifurcation or vessel accident, among others. Anatomical vessel branches are modelled as nodes[2] (*BranchNode*) and if we need to assign properties to the bifurcations, we can also explicitly model them (*BifurcationNode*). In order to provide more modelling flexibility, we define also *Composite* nodes, which make use of the *Composite Pattern* [58] in order to group nodes. This way the group of nodes acts as a single entity, hiding their internal relationships and offering the possibility of building a hierarchy of several levels of abstraction complexity in the graph.

By inheritance of node objects we are also able to model conditions that occur in the branches themselves or in the surroundings (*FeatureNode*). We also allow nodes to model some abstract concepts, such as annotations that may be of interest in diagnostic applications. The properties of each node type are defined by specific attributes and operations and the use of OOP techniques such as polymorphism allow different behaviour with an unified interface for a set of operations.

Our graph-based model, however, is not restricted to a tree structure, to provide the flexibility in its definition, that is necessary in some applications. For example, the number of parents of a node is not limited to one, although anatomical branches in general have a single parent. This flexibility allows for several types of representation of the same vessel network. The structure of these representations is open, since nodes can be, in principle, arranged in any desired manner. However, our model was designed at least to support a few representations that have been found useful for many vessel analysis applications. We will proceed to describe these representations and introduce the node types involved.

Branch Vessel Graph Representation The *Branch Vessel Graph Representation* (BVG) is the simplest representation of a vessel network in VKR. It consists of a graph of interconnected nodes of type *BranchNode*. This type of node is the most conspicuous in VKR models, since it represents the geometry and properties of vessel branches, which are the main constituents of physical vessel networks. The rest

[2] This differs from other works where nodes are modelled as graph edges [148]

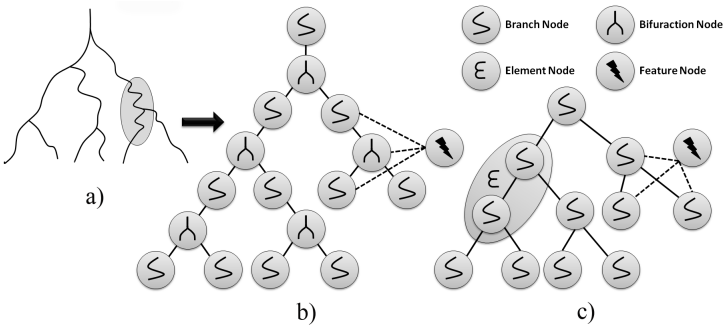

Figure 3.2: Vessel Graph Representations. a) Symbolic depiction of a vessel tree b) BVG rep. c) BBVG Rep and OEVG after incorporating an *Element* supernode.

of the vessel network is in fact an abstraction of the relationship of vessel branches (such as bifurcations), related features, groupings of branches, etc. The most important part of a *BranchNode* is the *Centerline Model* that is described in section 3.3.2.3. Several *BranchNode* instances can be connected in series, in order to divide a branch into different segments. This might be useful to model parts of a branch which require special attention, such as regions with stenosis or aneurysm, and separate them from the healthy regions.

Branch-bifurcation Vessel Graph Representation The *Branch-bifurcation Vessel Graph Representation* (BBVG) explicitly models the bifurcations using a *BifurcationNode*. In this case, the parent and children of a *BifurcationNode* needs to be a *BranchNode* or any subclass of it.

Ordered Element Vessel Graph Representation The *Ordered Element Vessel Graph Representation* (OEVG) is most suited for morphometric and haemodynamic studies, since serial branches of the same order, with the order defined according to the *Diameter-defined Strahler Ordering System* [78], are grouped into a *CompositeNode* called *ElementNode*. In an OEVG representation, *BranchNodes* that are not grouped can also be considered as *ElementNodes* since they also represent an element in Strahler's system. In haemodynamic circuits, a series of vessel branches of the same order are the equivalent of an electric circuit composed of resistances in series.

3.3.2.2 Vessel Branch

A virtual vessel branch is represented in VKR by a *BranchNode,* and it corresponds to the vessel segment that extends between consecutive bifurcations. A physical vessel branch may also be represented by several concatenated *BranchNode* instances. This would be useful when the user wants to make a difference between different parts along the length of a physical branch, for example by indicating that part of a branch

is stenosed. This is performed by associating corresponding accident node representations, such as the *StenosisModel*, to the *BranchNode*. This will be described in detail in section 3.3.2.7. The core of a vessel branch in our model is represented by the *Centerline Model* described next.

3.3.2.3 Centerline Model

The vessel centerline or medial loci [19] is an important part of our model, since it is a good descriptor of elongated objects. Compared to other descriptors, such as boundary descriptors, the centerline captures better the vessel shape and provides a straightforward way of obtaining the relationships between the different branches of the vessel tree [167], since the centerline can be easily converted into a graph structure. Furthermore, it serves as a reference for calculating and storing local properties, both inside and on the boundaries of vessels. For example, the vessel length is measured along the centerlines and diameters are measured over sections whose center is the centerline. Therefore, we provide an explicit, yet flexible and agile, representation of the centerline.

The *Centerline Model* is designed to provide several degrees of increasing representation complexity, as shown in Figure 3.3 left. The simplest level of representation complexity is to define a centerline by its point descriptors, where a point descriptor is anything that may identify the location of a geometrical point on the centerline. Examples of point descriptors may be geometrical points in physical coordinates, image pixel indexes, chain-codes, etc. The next level of complexity involves defining the vessel normal section that defines the cross-sectional planes. On a third level, we can define a section model, thus allowing further levels of flexibility and complexity.

Our point-based *Centerline Model* is independent from the mathematical model used to define the centerline curve, whose points need to be defined explicitly in our model. The reason is that the centerline curve needs to be discretized in order to store local quantitative properties of the vessel centerline and sections, and to localize vessel accidents or other features of interest that need to be referred to some point on the curve. However, this does not preclude the definition of an interpolation mathematical model that can be assumed to be a curve point generator. Examples of this could be a centerline curve defined as a B-spline by using control points. This can be implemented either by subclassing *Centerline* class or, as will be described in section 3.3.3.6, by decoupling the curve generation from its defining points, by providing an external generator by subclassing the *CenterlineAlgorithm* class.

Finally, the *Centerline Model* provides a placeholder for optionally storing local centerline metrics which may provide valuable quantitative information about the local shape of the centerline. The most common and useful local centerline metrics, that can be defined at every point of the centerline, are the curvature, torsion (3D) and Frenet frame of reference, which includes the tangent, normal and binormal vectors (Figure 3.3 right). We contemplate an implementation (*LocalCurveMetrics* class) that generalizes this reference system to N-dimensions.

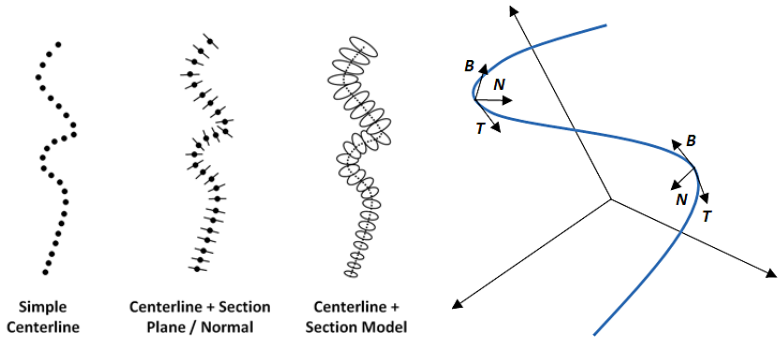

Figure 3.3: Centerline Models (left) and Frenet reference frame for a 3D curve (right).

3.3.2.4 Section Model

Vessel Sections are localized at centerline points and they are assumed to vary along the vessel length. This variability is reflected in the parameters that define the section, for example, the diameter.

As we can see in Figure 3.4, vessel sections, like centerlines, can also be defined at increasing levels of complexity. The simplest level is to define the section as a circle, giving its center and radius/diameter. Since our sections are defined at explicit centerline points, the center is already given. The next level of complexity is an elliptical shape. More advanced mathematical models include radial functions and B-spline contours. The section can also be implicitly defined by a segmentation mask image or by level-sets of a higher dimensional function, that can be obtained by the level-sets method, based on evolution of implicit curves or surfaces [137]. Another possibility is that a section may define more than one contour. This is for example the case when we want to model the shape of the external and internal vessel wall or when we want to model the lumen and the aneurysm contour in abdominal aortic aneurysms). In the latter special case, the section is modeled in such a way that it can be shared by at least two different branches (*SharedVesselSection*) since a single aneurysm contour may extend to both iliac arteries.

These are just a few examples that demonstrate the versatility of the model. In this sense, our section model does not impose any shape model, the only condition is that it can be referred to centerline points.

3.3.2.5 3D Surface and Voxel Models of Vessels

So far we have dealt with explicit modelling of cross-sections. Another possibility, when dealing with 3D image data, is to directly generate a 3D surface mesh from the centerline. If the 3D mesh is generated for the complete vessel tree, it can be referred to branches or even to centerline points (and thus to sections) of the VKR model by proximity to the corresponding centerline. This reference can be direct, by splitting the model into surface patches and keeping references to them, or indirect, simply by

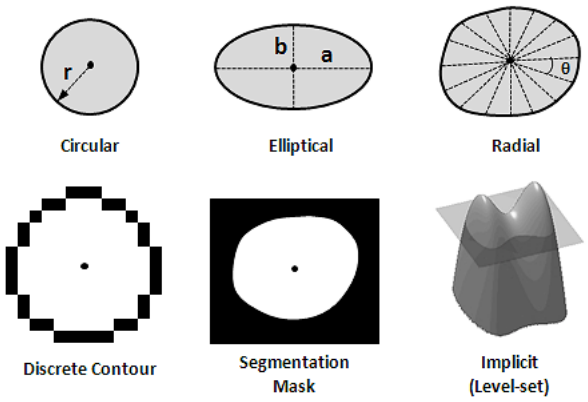

Figure 3.4: Section Models

associating a scalar value, acting as identifier, to the mesh points that corresponds to referred branches. This way a forth-and-back relationship may be kept between the VKR and surface models. Explicit sections may also be obtained by intersection with corresponding section planes.

If a segmentation is available, obtained either *a priori* or from the VKR model, it can be referred to corresponding branches by just labeling the mask pixels/voxels with corresponding branch identifiers. In this case, keeping references to separate volume "patches" seems to be more difficult to handle but it is a possibility that could be useful in cases where the source angiographic volumes are huge. The reason is that, in most software frameworks, only arrays corresponding to rectilinear volumes can be stored, and for sparse structures such as the vessels, sometimes many of these voxels are empty. Another possibility is to store these labeled voxels as sparse images.

3.3.2.6 Vessel Bifurcations

Bifurcations may be represented explicitly in the VKR model by means of the *BifurcationNode* object that defined at graph level. The use of this node type is optional (see BBVG representation in section 3.3.2.1), and may be required when special features of the bifurcation are to be modelled, when (quantification) operations need to be assigned to the bifurcation, such as estimation of branch angles, and when there may exist more than one parent branch.

3.3.2.7 Vessel Features

In the VKR model, vessel "features" (*FeatureNode*) represent special characteristics of the vessels that need to be highlighted. Their definition may include models for vessel accidents or simply comments used for diagnostic. A feature may affect or may be associated to a part of a branch, a whole branch or a set of branches, entirely or

partially. In order to make explicit these relationships, two mechanisms are devised:

1. *FeatureNodes* are assigned as children (or alternatively as parents) of affected *BranchNodes*. This is illustrated in Figure 3.2.

2. *FeatureNodes* keep a *VesselRegion* structure that indicates which vessel branches are affected and to which extent. This is achieved by keeping a set of *VesselBranch* node identifiers, and for each identifier, the starting and end indexes of the points in corresponding centerlines that comprise the area affected by the feature.

Since a feature may affect more than one branch, *FeatureNodes* are treated in a special manner and are not even visited when performing many operations that require traversal of the graph. In this sense, FeatureNodes can be treated as "hypernodes" and their relationship with *VesselBranch* nodes (or possibly other nodes) is not that of a parent-child relationship but merely a reference.

An example of use of a *FeatureNode* is to perform an annotation, such as a diagnostic remark in a application for computer aided vascular diagnosis. The clinician would choose the branches affected by a given feature, for example, those feeding a tumor or included in it, and assign to them the corresponding nodes comment. Another possibility is to assign specific models of vessel accidents or disease, such as a *StenosisModel*, to a *FeatureNode* which are described next.

3.3.2.8 Models of Vessel Accidents or Disease

The VKR model offers the possibility of providing representation models for vessel accident or disease. Examples of these models are the *StenosisModel* and *AneurysmModel*. These models contain the quantitative morphological measurements and other properties that are typical of a given vessel accident or related disease. We provide flexibility for defining application-specific models of this kind.

There are two main possibilities for incorporating these models in the vessel graph: in a *BranchNode* or in a *FeatureNode*. The first option is more suitable for cases in which the accident affects a whole branch or a part of it. In this case, the affected area is modelled by a subclass of BranchNode (for example *StenosisBranchNode* or *AneurysmBranchNode*) that is connected serially in both ends either to other *BranchNodes* or to *BifurcationNodes*. This configuration can be seen in Figure 3.6 and is further commented in section 3.3.3.6. Another possibility is incorporating the model into a *FeatureNode* as explained in the previous section. This is more appropriate in cases in which the accident affects more than one branch.

3.3.3 Supported Operations

Operations that can be performed on the VKR model data structures can be classified by their nature or by the type of object they operate on. For example, quantification operations can be performed at graph, branch, centerline or section level, among others. Based on their nature we distinguish the following types:

- *Access Operations*: abstract access mechanisms that allow performing other types of operations. For example, graph traversal is an operation that allows to access nodes on the vessel graph and perform other operations on them.
- *Edition Operations*: change the internal structure and properties of the model.
- *Quantification Operations*: evaluate quantitative measurements over different elements of the model.
- *Input/Output Operations*: load and save the model data.
- *Data Transformation Operations*: generate of the VKR model and transform it into another representation that can be useful for intended applications.
- *Model-specific Operations*: internal operations that are specific to certain elements of the model, such as centerlines or sections.

3.3.3.1 Access Operations

Graph Traversal The most important access operation is graph traversal. Graph traversal operations can be performed efficiently by using the *Visitor Pattern* [58] object-oriented technique (*GraphVisitor*). This pattern allows to decouple the structure of the graph and corresponding nodes from the operations performed of them. This is desirable because it constitutes and efficient manner of extending the framework with new operations. The visitor abstracts the mechanism of traversing the graph according to a set of rules that are defined by the user. For example the user may choose to visit only some specific types of nodes, such as bifurcations or may use node masks to enable/disable visiting specific nodes. Subclasses define specific traversal rules and the operation to be performed. Operations at any depth level that need to be performed on the whole vessel tree are implemented this way.

Model Picking Picking operations are those that allow to access structures of the VKR model by selecting them from a derived representation, either symbolic or geometric. They constitute the random access means to any part of the VKR.

Picking operations are based on established relationships between the target structures of the model (nodes, branches or sections) and their representation. This can be performed directly, by keeping references (pointers) to the structures on the model, or by assigning corresponding identifiers. Another possibility to establish this relationship is by proximity in terms of Euclidean distance. For example, a user could pick a point on the surface and the closest centerline point or section could be selected and its properties displayed.

3.3.3.2 Model Editing Operations

Most edition operations can be implemented in a straightforward manner by exposing the internal structure of the data after a picking operation. Of particular interest are graph editing operations, which alter the structure of the graph by changing the

relationships between nodes and insert or delete nodes on demand. Graph editing operations can be performed interactively by the user, i.e. to correct artifacts in VKR models produced during its extraction, or by autonomous algorithms, i.e. deleting noisy branches based on their absolute length or underlying image values.

3.3.3.3 Quantification Operations

Quantification operations can be performed once the initial graph structure of the vessels has been created. Some of these quantitative measurements are calculated and stored in the model on-the-fly, when they are part of the necessary calculations performed by the vessel extraction algorithms. Some other quantification operations are only performed on demand, on the whole vessel tree or on a part of it, since they may be computationally expensive. Whole tree calculations are performed via specific graph visitors. These visitors may incorporate other specific objects to perform quantification at deeper levels. For example, a *CenterlineMetricsCalculatorVisitor* object traverses the tree searching for centerlines of *BranchNodes*. At each centerline, a *CenterlineMetricsCalculator* object calculates local centerline metrics. If we want to calculate metrics for a single centerline, we can access it directly and use this latter object instead of using the visitor object.

Quantification can be performed at almost every level in the VKR model. A reference diagram of some of the attributes that can be measured is shown in Figure 3.5. The diagram shows the data model on which the operations are performed and the locality and type of measurement (i.e. geometrical, topological, image-based...) in a hierarchical manner. Some of the measurements are directly stored in the corresponding data structures or placeholders of the VKR model. Others can be obtained from the object that performs the operations.

3.3.3.4 Input/Output Operations

Input/Output (I/O) operations are intended to store/recover instances of the VKR model data structures. Two main types of I/O operations are initially considered: file and database I/O operations. The chosen format for file operations has been *GraphML* [24]. It is an XML-based format specifically designed for serializing graph information and that can be extended for custom needs. It allows to explicitly define the graph nodes, its relationships as edges[3]. Attributes can also be assigned to nodes and edges, allowing to store properties. Input/output of structures such as images or meshes is out of the scope of the model. As it may easily integrate with other toolkits, these operations are should be performed by third-party libraries. Other types of data may require the design of custom I/O routines, sometimes application specific. On the other hand, application-specific relational databases can be designed, mimicking the data structures of the VKR model, and allowing operations such as performing queries or keyword search of semantic qualitative attributes [141], or advances multimodal interfaces such as those described in [83].

[3] In our model, graph edges are implicitly defined as references or pointer to nodes

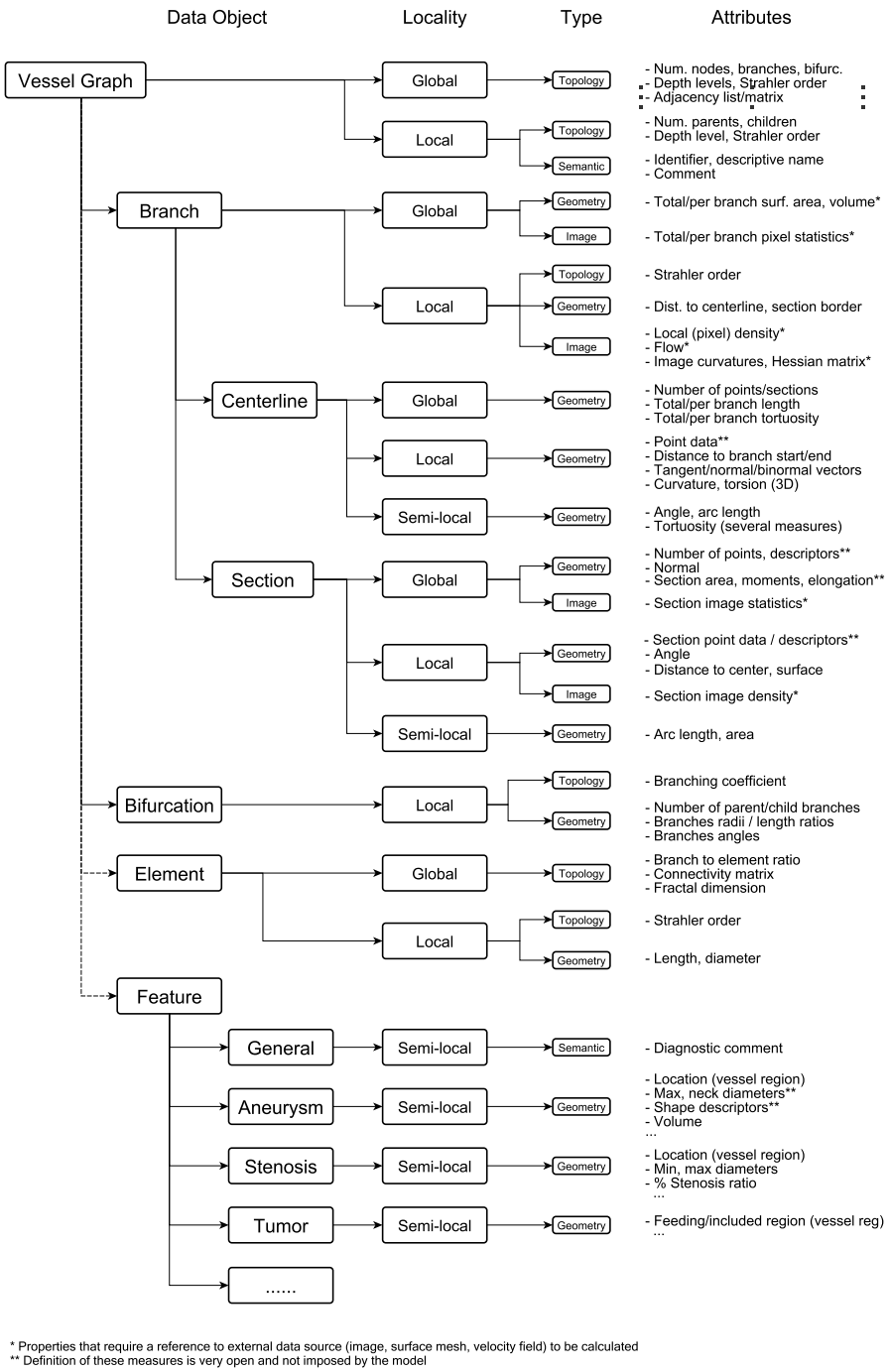

Figure 3.5: Quantitative and qualitative attributes

3.3.3.5 Data Transformation Operations

Data transformation operations involve conversions between high-order vessel representations and are summarized in the VKR workflow diagram in Figure 3.1. Except for graph-to-graph operations, they consist of generation of the VKR model from external image data and transformations to other types of data representations used in corresponding applications. Many of these external operations are not yet implemented, but for the sake of completeness, we describe some of these operations and important considerations here.

Graph-to-graph Operations These operations convert a vessel graph into another vessel graph in which the configuration of the nodes has changed. This is possible because the nature and openness of the graph representation in the VKR model allows the definition of different types of graphs and nodes, and thus, conversion operations between graph types. We do not include here operations that transform inner data structures only, such as the centerlines. Typical graph operations are conversions between vessel graphs representations.

Another operation of this type is converting a disconnected set of branches obtained by global detection algorithms into a vessel graph (see Figure 3.1). This is the equivalent of having a container of disconnected nodes which are organized into a complete graph by establishing the links.

Image-to-graph Operations These correspond to the VKR model construction from the image/volume by using vessel extraction schemes. Some schemes may use intermediate representations, such as a segmentation mask or a disconnected set of nodes (see Figure 3.1).

Graph-to-image Operations Sometimes it is necessary to convert the graph into a voxel representation (segmentation) that also involves branch labeling. This can be used, for example, for overlaying and blending this labeled segmentation on top of the original image and assigning a color to each label. These labels can also be used as region of interests, to limit further processing operations on the source image to corresponding branches.

Another set of graph to image operations is projection on 2D images (see Figure 3.1). A typical example is when we have a VKR model obtained from a 3D angiography (such as CTA or MRA) and we want to project part of the model, such as the centerline on a 2D X-ray angiography, in order to visualize the real paths of some vessels that may be occluded.

Graph-to-mesh Operations These operations convert a vessel graph into a surface mesh. The conversion depends on the actual representation of the graph. It can be obtained by contour sweeping or by using a predefined mesh model either explicitly or implicitly as described in section 2.4.1 among other techniques.

3.3.3.6 Model-specific Operations

We describe some model-specific operations that are not included in the previous classes of operations and that are exclusive of the corresponding representations.

Graph Operations We consider here operations that modify the attributes of common nodes only, because graph operations will be specified in terms of node operations and visitor patterns.

Graph Labeling is a straightforward operation that assigns unique labels to nodes. *Node Wrapping/Unwrapping* are operations that transform a vessel graph into another vessel graph in which some nodes are wrapped into a supernode (subclass of *CompositeNode*) and viceversa. Node wrapping may require specific rules by which nodes are merged into a single supernode. On the other hand, node unwrapping may work without setting any rules by simply restoring the underlying nodes. A specific wrapping operation is defined in order to convert a (B)BVG rep. into a OEVG rep. (see section 3.3.2.1) as defined in [69].

Branch Operations Operations that affect the branches as a whole are included here. A specific operation for branches is assigning them an *order* in the (modified) Strahler ordering system . This involves traversing all branches from the leaves to the roots. If the diameter-defined method is used, this requires iteratively assigning orders and calculating diameters.

Branch splitting is the operation of dividing a branch into several branches. This operation (see Figure 3.6) may be performed, for example, to mark a region of a branch as having a specific accident or disease model. *Branch merging* is the contrary operation, where several branch patches are merged into a single branch node. They can be also considered as edition operations (see section 3.3.3.2).

Section interpolation is an operation that needs to be considered at branch level, since it involves both, generation of new intermediate centerline points, that define the section location, and estimation of section normal and boundary according to the corresponding model.

Centerline Operations Centerline operations involve modification of the points that define a centerline. Centerline generation operations, such as centerline tracking or skeletonization (see section 2.4.2 and 2.4.2), lie in this group, but they are usually part of the vessel extraction schemes that explicitly deal with centerlines and are not considered here.

Centerline interpolation is the process of resampling an existing centerline, or one that is being created, following a given mathematical model of curve. For example, if the distance between centerline points is not uniform, a linear resampling may produce uniform sampling. Another possibility is to fit the centerline curve to a set of connected B-spline curves.

Centerline filtering may also be used to convert a rough, noisy centerline into a smoother centerline, by removal of points or by several types of smoothing filters, such as average, median or anisotropic diffusion filters that operate on centerline points.

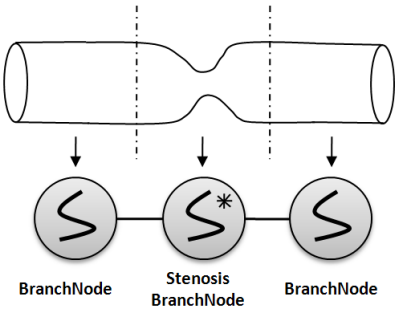

Figure 3.6: Example of branch splitting operation to indicate a stenosis. A single *BranchNode* is split into three serial nodes, where the middle node incorporates a *StenosisModel*.

Centerline registration is the process of converting a centerline into another centerline by applying a rigid or elastic transform to the points of the centerline. This transform is obtained by minimization of a cost function, that is usually based on image-values. Examples of centerline registration applications are comparison of vessel geometrical features between different patients [153] or quantification of aneurysms and stenosis [75].

Section Operations Section operations involve generally modification of the geometry of the section, or re-estimation of the section normal[4]. As in the previous case, these operations can be performed after or during the vessel extraction procedure. In the second case, section generation can be considered as an inherent part of the extraction schemes described in section 2.4.2 but, like in the case of the centerline, some of the algorithms can be applied at a post-processing stage.

Section interpolation can be performed in two ways, either by interpolating the section geometry according to its mathematical representation (resampling of points, etc.) or by interpolating sections by creating new intermediate sections. In the latter case, it also involves a modification of the centerline and as such, can be considered a branch operation (see section 3.3.3.6).

Section filtering involves geometric filtering of noisy boundaries. It is similar to centerline filtering and depends greatly on the section model.

3.4 Prototype Execution Example

We are currently developing several vascular applications that make use of our VKR model. As an example, a prototype is being developed to demonstrate some of the capabilities of the model. Once a 3D image is loaded, the user may trace the corresponding centerlines, branch by branch, by means of a set of control points. These points

[4]Re-estimation of the section center corresponds to a centerline operation

are interpolated by using a BSpline curve model by means of a Centerline operation (see Section 3.3.3.6). The integration of our model with the model/view framework of the user interface toolkit (Nokia Qt) is straightforward, and allows displaying several views of the defined model, being the tree view the most intuitive for exploration. Once a branch is selected in the tree, the properties of the corresponding sections may be displayed also.

In Figure 3.7 we can see an interactive definition of the hepatic vein branches in a 3D contrast-enhanced MRI of the liver. The projections of the resulting centerlines are displayed in 2D orthogonal views (the vessel segments in green lie on the current slice) and the corresponding 3D renderings are overlaid on a volume rendering of the dataset. This allows an intuitive exploration and visualization, by displaying branches in their real position and selecting them directly in the corresponding visualizations via picking operations. Local plane sections may be calculated from the centerline points, and the corresponding section images displayed. Furthermore, a curved planar reformatting may be obtained from the centerlines that displays the vessel along their whole length in a single plane. Obtained section images and curved reconstructions may be stored within the model if necessary by simply subclassing the section and centerline models, without modifying the existing algorithms, due to the adequate use of generic programming techniques.

Currently we are extending the capabilities of the prototype for allowing different types of sections and nodes, editing of branches and points, improved visualizations, etc. We are developing similar prototypes for other applications that require different models of sections, such as follow-up after aortic aneurysm repair, which requires a delineation both of the aorta lumen and aneurysm thrombus. As mentioned before, combining the definition of several types of vessel sections is eased by the versatility of the model.

3.5 Conclusions

The evergrowing applications and techniques of Blood Vessel Analysis have produced a complex landscape of algorithms and data representations that hinders the composition of procedures, the reuse of software and the comparative analysis in terms of computational efficiency and quality of final results (visualization, measurement, edition, and others). We have detected the need of proposing a foundational Vessel Knowledge Representation (VKR) model that may allow the exchange of data among applications and users. One of the goals of VKR is the reuse of software pieces, providing a ground functional layer that may serve as the basis for new developments, thus alleviating development efforts. The model can be used as an intermediate representation between image-based extraction schemes and clinical and research applications, to perform quantitative measurements on extracted vessel structures and to provide the necessary vessel representation and handling tools for the target applications. We have identified, from the literature and our own research work, the key knowledge representation items, as well as the key operations that are the building blocks for nowadays and future vessel analysis processes and applications.

VKR provides a versatile and efficient object-oriented representation of vessel struc-

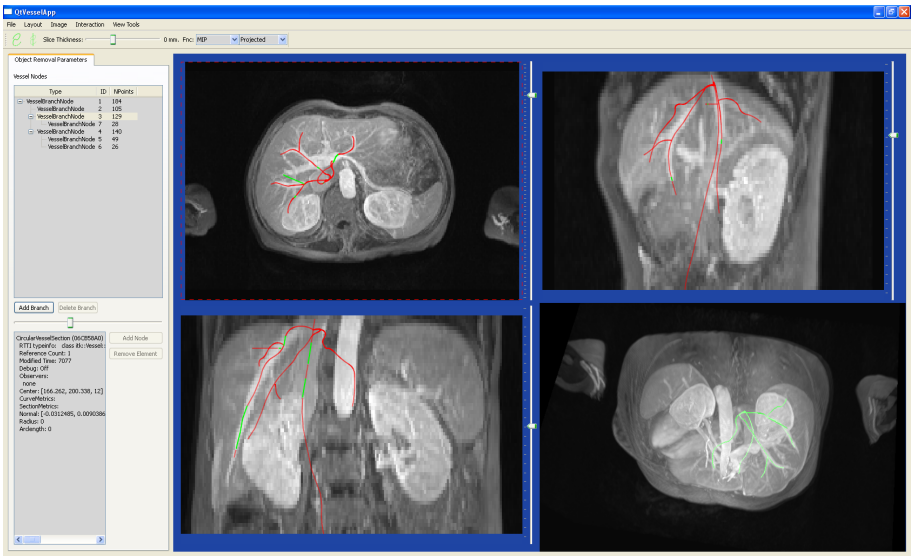

Figure 3.7: Screen capture of the visualization given by the modeling application under development. Lines correspond to vessel centerlines created interactively by a user over a liver CTA.

tures and associated algorithms and quantitative data. It contemplates flexible data representations for the vascular tree, underlying structures such as branches, bifurcations, centerlines and sections, as well as vessel features such as stenosis, aneurysms, etc. It also contemplates operations and algorithms that operate efficiently on corresponding data structures. Furthermore, the model is designed so it can be easily integrated with pre-existing frameworks. We are already applying the VKR model in vessel-related applications related to our current research areas [94, 120, 119, 117, 116, 115].

Chapter 4

Basic Differential Feature Detection

This chapter presents the concepts of edge and ridge detection, scale-space analysis, and their relationship with curvilinear structure detection. The objective of the chapter is to lay-off the basic concepts and tools that form the building elements of the blood vessel detection algorithms in medical images.

The structure of the chapter is as follows: Section 4.1 gives an introduction to the chapter. Section 4.2 discusses edges and ridges. Section 4.3 introduces the principles of edge detection. Section 4.4 introduces scale space image analysis. Section 4.5 introduces the principles of ridge detection. Section 4.6 introduces second order detectors based on the Hessian matrix. Section 4.7 discusses other features.

4.1 Introduction

Curvilinear structures, also known as line or tubular structures are small width elongated structures present in both 2D and 3D medical images[1]corresponding to either anatomical structures, such as blood vessels, bronchi, nerves, biliary ducts, etc. or artificial structures, such as catheters, electrodes, stents, etc.

The basic geometrical property describing a line structure is that its length exceeds by far its diameter; thus it can be considered as a 1D manifold in the 2D/3D embedding image space [84]. At every point of the line structure (with the exception of the end and bifurcation or branching points) we can associate a direction, corresponding to the direction of the centerline (aka medial axis/line [19]) of the line structure, and a section line (in 2D images) or plane (in 3D images), that is normal to the axis direction. The geometry of the line structure's section is almost circular for small vessels, tending to differ from the ideal circle for larger vessels or when clinical or anatomical anomalies are present, such as stenoses or aneurysms.

[1]The term line structure or line filtering is more used in the literature in the context of detection and the term tubular structure is more used in volumetric image analysis.

The typical intensity profile of a tubular structure measured on its section shows a central elevation. The 2D or 3D shape of this elevation may be modeled as a Gaussian, bar-like (also known as rectangular or boxcar), parabolic or roof cross-section [86, 170]. On the other hand, the intensity profile variation along the line direction is small, assuming that there is no blockage that prevents the diffusion of the contrast media. These hyperintensity properties are exploited by most detection methods.

The main goal of the vessel detection process is to detect curvilinear structures of, within some limits, arbitrary shape and size, regardless of the section intensity profiles [84]. Vessel detection methods are generally based on a '*vesselness*' measure, which can be calculated either locally or globally, estimating for each voxel the likelihood that it belongs to a blood vessel. If the vesselness measure is specially designed to detect the vessel centerlines, we call it *medialness* measure, as it refers to the medial line or medial axis of the curvilinear structure.

4.2 Edges, Ridges and Curvilinear Structures in Images

One approach to curvilinear structures detection is to consider their cross-sectional profiles as *double-sided edges* building detectors based on the image local derivatives.

Consider an ideal step edge along the y direction. Its cross-sectional profile in the x direction corresponds to an ideal unit step or Heaviside function[2]:

$$u(x) = \begin{cases} 1 & x > 0 \\ 0 & x \leq 0 \end{cases} \tag{4.1}$$

A double-sided edge can be represented ideally with a rectangular function (aka normalized boxcar, bar or pulse function), which can be expressed in terms of the ideal step edge or bar profile as follows:

$$f_b(x) = u(x + \frac{\omega}{2}) - u(x - \frac{\omega}{2}), \tag{4.2}$$

where ω is the width of the pulse. If we make the pulse narrower, by decreasing the value of ω we obtain an ideal line-like structure with a rectangular cross-sectional profile. In the limit, when $\omega \to 0$, we would obtain an ideal delta or Dirac pulse.

In real images, edge profiles are not sharp. Sometimes they can be approximated by Gaussian or other functions, with some kind of noise added. Let us consider the convolution of the previous ideal step functions with a Gaussian kernel in the x direction (Eq. 4.3). The effect of Gaussian convolution is to smooth the profiles so as to obtain an smooth transition as can be seen in Fig. 4.1. In the case of the ideal line with rectangular profile, the line in the middle corresponding to the maxima in the x direction is known as an *intensity ridge*.

An intensity ridge corresponds to local maxima of N-dimensional functions in N-1 principal directions [46]. If we think of a 2D image as a 3D surface map, where the

[2] An alternative definition is $u(x) = \int_x^\infty \delta(x)dx$ where $\delta(x)$ is the Dirac or delta function

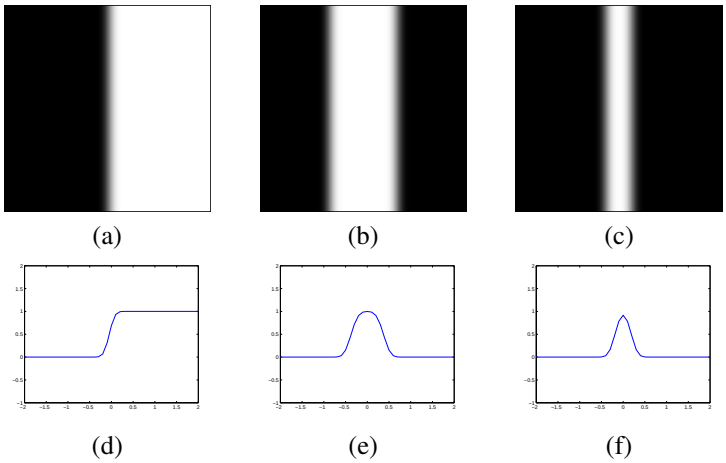

Figure 4.1: Different ideal edge images (top row) and profiles along x direction (bottom row) after smoothing with Gaussian convolution. Columns correspond to ideal unit step (left), rectangular function (center) and line-like profile (right)

height correspond to intensity, ridges correspond to the surface crests. On the other hand, valleys follow the dual definition considering local minima instead of maxima. Intensity ridges are important both in edge and linear structure detection, since they may be used for the detection and localization of the corresponding structures.

The concept of edges and ridges can easily be extended to 3D images. The case of the step edge is trivial and less interesting for our analysis and is simply a transition in one direction of a volume. For the case of the double-sided edge or ridge, a 3D ideal line can be represented by an ideal cylinder with rectangular, Gaussian or other types of cross-section.

Let us consider a ramp edge profile as depicted in Fig. 4.2 (a) and the corresponding first and second order derivatives in Figs. 4.2 (b) and 4.2 (c), respectively. The first derivative of this ramp is a pulse. Narrowing the ramp (Fig. 4.2, second row), we approximately have a line structure for the first derivative. Performing a Gaussian convolution on the ramp edge (Fig. 4.2 bottom row), we approximately obtain an intensity ridge for the first derivative.

From the previous analysis we can conclude that *the analysis of line structures is equivalent the analysis of the first derivative of standard single-sided edges of various profiles*. Thus, from the review of the main edge detection techniques, we can draw some conclusions important for the task of line detection.

As we have seen, there is a connection between the analysis of edges and the analysis of line structures and ridges, since the latter can be derived from special edge definitions and from the first-derivatives of single-sided edges.

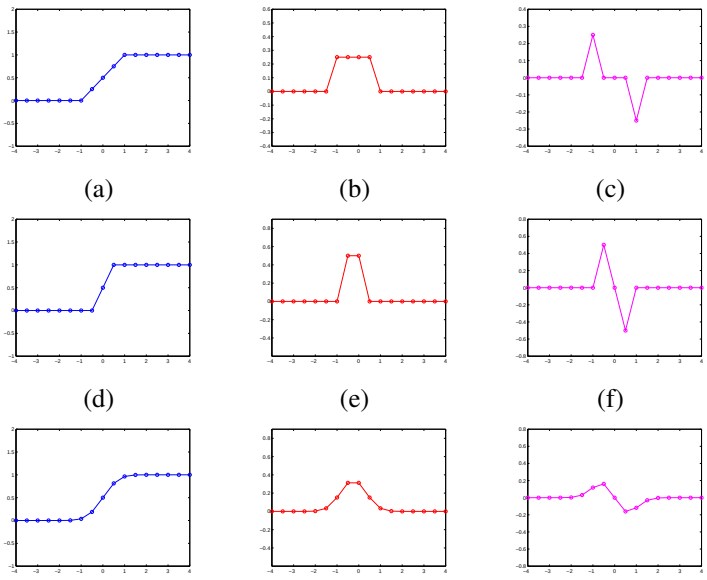

Figure 4.2: Several models of an ideal ramp edge (left column) and corresponding first (center column) and second (right column) derivatives. The first row corresponds to a wide edge, the second row to a narrow edge and the third row correspond to the narrow edge after Gaussian convolution (smoothing).

4.3 Principles of Edge Detection

4.3.1 The Problem of Edge Detection

The goal of edge detection methods is to find a set of curves that define the significant image edges that represent the boundaries of the objects of interest and reduce the amount of information to be processed [30]. Edge detection is affected by noise, illumination conditions, image resolution, contrast, etc.

One of the most common approaches for edge detection is to use detectors based on the local derivatives of the image, usually first- and second-order derivatives. In the analysis of first and second-order derivatives of ramp profiles in [60] (572-576) they conclude that:

- Edges can be detected by the magnitude of the first derivative.
- The second derivative gives two responses for a single peak, corresponding to the positive and negative image curvatures at each side of the edge. This is initially an undesirable property since we would like a single signed response.
- The second derivative gives two responses of different sign. Thus the edge can be detected by considering the zero-crossing of the second derivative.
- Derivative-based calculation is very sensitive to noise, and this effect is more evident in the second-derivative, since it is more sensitive to small variations in the signal.

When trying to detect a given profile using derivatives, there is a limit or scale of noise, from which the derivative values start degenerating considerably. The reason is that, when calculating derivatives we are not comparing any more the source, signal with noise, but local variations of the signal with noise. Depending on the scale at which these differences are observed, they may be small and they may become close to the magnitude of noise.

This led to think that some sort of scaling in the derivative calculations was necessary, so differences are taken into account only at the appropriate *scale or aperture* at which differences are meaningful. On the other hand, scale-selection implies removal of structures at coarser scales without introducing new spurious details [82] so scale-selection must be performed via some sort of smoothing which also removes noise. Conversely, by blurring images to remove noise what we do is to make measurements at larger scales above the scale of noise, where image entities are more meaningful.

To sum up, *in order to calculate derivatives robustly and coherently we must devise a way to calculate smoothed and scaled image derivatives*.

Gaussian filtering is widely used as a pre-processing step while calculating derivatives and also for *scale-space* image analysis (see Section 4.4). In image processing, it is achieved by convolving an input source image with discrete approximations of the continuous, normalized (unit integral) Gaussian function:

$$g(x;\sigma) = \frac{1}{\sqrt{2\pi}\sigma} e^{-\frac{x^2}{2\sigma^2}} \qquad (1D) \tag{4.3}$$

$$g(x,y;\sigma) = \frac{1}{2\pi\sigma^2} e^{-\frac{x^2+y^2}{2\sigma^2}} \qquad (2D) \tag{4.4}$$

$$g(x_1,x_2\ldots x_N;\sigma) = \frac{1}{\left(\sqrt{2\pi}\sigma\right)^N} e^{-\frac{\sum_{i=1}^{N} x_i}{2\sigma^2}} \qquad (ND) \tag{4.5}$$

The degree of smoothing is controlled by the aperture[3] σ of the Gaussian (the larger, the smoother). It has several important properties that makes it specially adequate in many circumstances. We can mention here a few:

- The Fourier transform of a Gaussian function in spatial domain is a Gaussian function in the frequency domain, usually centered at zero and with standard deviation $1/\sigma$, which corresponds to a low-pass filter . For a normalized 1D Gaussian function, its Fourier transform is:

$$G(\varpi) = e^{-\frac{\varpi^2\sigma^2}{2}} \tag{4.6}$$

- The Gaussian is the function that optimizes the localization in both the spatial and frequency domains. In Section 4.4.1 we will see that these both localization requirements are desirable for smoothing filters but are conflicting: localization in the spatial domain spreads the spectrum in the frequency domain and viceversa. This can easily be seen in formulas 4.3 and 4.6: if we decrease σ in the spatial domain it increases in the frequency domain. The Gaussian function optimizes this trade-off with respect to other types of filters.

- Gaussian convolution is linearly separable: this means that, instead of using one large 2D Gaussian kernel, one can use a 1D kernel and apply it successively in x and y direction, which is computationally much more efficient (unless applied for a single pixel). The same applies for a higher number of dimensions.

- Gaussian convolution has infinite support: theoretically one would need the whole image to compute the smoothed value for every pixel. However, in practice, the contribution of pixels at a distance of more than 3σ is usually negligible and kernels can be designed in order to obtain the desired accuracy within some limits, for example in terms of the unit integral [112] .

- The convolution of two Gaussians with standard deviations σ_1, σ_2 is another Gaussian with standard deviation $\sqrt{\sigma_1^2+\sigma_2^2}$. This can be easily proved in the frequency domain:

$$G_1(\varpi)G_2(\varpi) = \exp\left(-\frac{\varpi^2\sigma_1^2}{2}\right)\exp\left(-\frac{\varpi^2\sigma_2^2}{2}\right) = \exp\left[-\frac{\varpi^2\left(\sigma_1^2+\sigma_2^2\right)}{2}\right] \tag{4.7}$$

The problem remains of finding the desired edges by building an edge detector that uses these derivatives. An ideal edge detector should have the following properties [30]:

[3] The use of the term aperture is common in the computer vision literature when referring to the standard deviation of the Gaussian

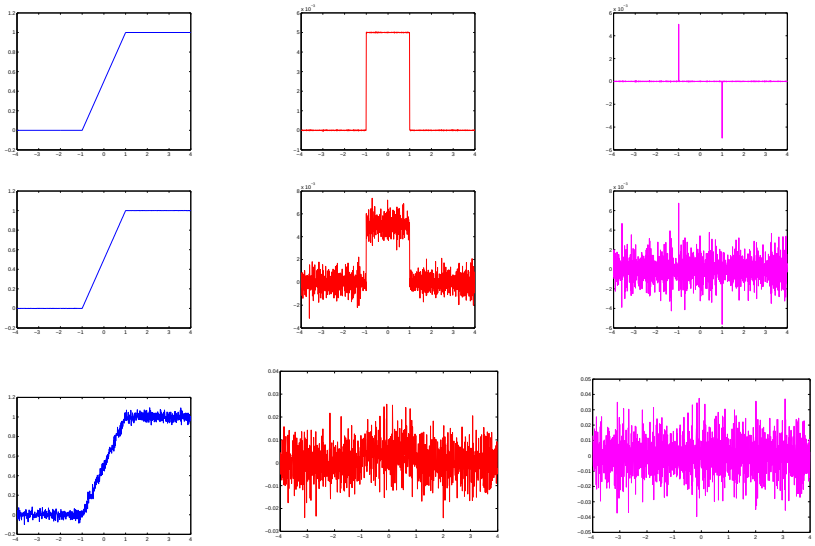

Figure 4.3: Ideal ramp edge (left column) and corresponding first (center column) and second (right colum) derivatives with increasing values of noise (from top to bottom SNR = 100, 65, 35).

- Good detection: the algorithm should find most edges of the image avoiding false edge detection. This criterion corresponds to maximizing the signal-to-noise ratio.
- Good localization: the algorithm should obtain edges close enough to the center of the true edges.
- Single response: ideally we would like to obtain a single response per edge (important for ideal centerline detection).

Edge detection algorithms must find a compromise between the two first requirements. If we are going to suppress noise by smoothing in order not to detect false edges, which is equivalent to increasing the scale or aperture by increasing the support of the filter, then we will blur the real edges obtaining a poorer localization. On the other hand, if we deal with small scales preserving all the details, we will localize better the true edges but will also detect noisy spurious details. In most cases, a single scale of analysis is not sufficient to detect all edges of the image and one must devise a way to obtain responses at different scales and integrate them into a single, *multiscale* representation. The same applies for the detection of ridges and other features.

4.3.2 First-order Derivative Methods

Most of first-order derivative edge detection methods are *search-based* methods. The idea is to compute a measure of edge strength, such as the gradient magnitude, and of

edge direction, such as the normal to the gradient vector. Then, the edge location can be found as the local maxima in the edge direction.

The components of the image gradient are the first order derivatives of the image f in each direction. For a 3D image:

$$\nabla f(x,y,z) = \frac{\partial f}{\partial x}i + \frac{\partial f}{\partial y}j + \frac{\partial f}{\partial z}k = f_x i + f_y j + f_z k \tag{4.8}$$

The *gradient magnitude* provides a measure of the edge strength:

$$|\nabla f(x,y,z)| = \sqrt{f_x^2 + f_y^2 + f_z^2} \tag{4.9}$$

and the unit vector in the direction of the gradient provides information about the edge orientation:

$$u_{\nabla f}(x) = \frac{\nabla f(x)}{|\nabla f(x)|} \tag{4.10}$$

where we have chosen the notation for the first derivatives $f_i = \frac{\partial f}{\partial x_i}$. When using higher order derivatives, we will use the notation $f_{ij} = \frac{\partial f}{\partial x_i \partial x_j}$. Derivatives in other directions can be calculated as the scalar product of gradient and the unit vector u in the desired direction:

$$f_u = \frac{\partial f}{\partial u} = \nabla f \cdot u \tag{4.11}$$

Since the gradient is a continuous function and we are dealing with digital images, it is necessary to compute discrete approximations of the gradient. Discrete derivatives in one dimension are computed using finite differences. In order to compute discrete image gradients, we must devise convolution kernels that may calculate derivatives in all possible image dimensions. The basic requirements that these kernels must meet are:

- The coefficients must sum to zero, in order to obtain zero response in constant regions (differently from smoothing kernels which must sum to one in order not to change constant regions).
- Obtain high absolute values in places of high contrast.
- Avoid the introduction of sampling artifacts and spurious details.

Numerous convolution kernels for derivative calculation can be found in the literature, such as the Prewitt, Sobel or Robert-Cross operators [60]. These kernels can be thought of as a rough approximation to the first order derivative of a Gaussian function which presents interesting properties for edge detection [30]. However, these kernels perform poorly when edges are blurred and noisy. Convolution and derivative operations

are commutative and associative. Take for example Gaussian filtering and derivative calculation on an image:

$$\frac{\partial}{\partial x}(f * g) = f * \frac{\partial g}{\partial x} \tag{4.12}$$

For our scaled derivative calculations used in tubular structure detection we have developed discrete implementations of the Gaussian derivatives using 1D kernels in different directions as explained in [112] where 1D kernels are calculated for desired order of derivatives and apertures and then applied in the corresponding directions.

If we obtain the gradient magnitude of an image, most of the edges resemble a line-like structure with some thickness. The corresponding profiles show in most cases a raising gradient magnitude, a peak, corresponding to the ridge, and a falling gradient magnitude. Thus, the problem of edge extraction with first-order derivative methods corresponds to the problem of finding the intensity ridges of the gradient magnitude images which leads to second-order derivative methods.

4.3.3 Second-order Derivative Methods

Second-order derivative methods try to find the maxima of the gradient magnitude directly, since they correspond to local maxima in the direction of the edge's normal, looking for points where the second derivative of the image becomes zero. As we have seen in 4.3.1, in the presence of an edge, the second derivative gives two responses of different sign and the *zero-crossing* of the second derivative is located, approximately, on the center of the edge. The problem of edge detection is stated as the problem of *finding the zero-crossings of the second derivative in the appropriate direction*. The advantages of finding zero-crossings is that they are easier to estimate than the maxima of the gradient magnitude and they always form closed contours.

In 2D/3D images, edges are not necessarily oriented in the main axes directions, and we need detectors that can cope with different edge orientations. One idea is to try to estimate the edge direction locally (corresponds to the orientation of the zero crossing) and then calculate the derivative of the gradient magnitude in that direction (directional second derivative). The orientation of the zero-crossing will have maximum slope under the assumption of *linear variation*, that is, when the intensity variation near and parallel to the line of zero-crossings is locally linear, which is approximately true for smoothed images [122].

The disadvantage of this approach is that it would require either multiple convolutions in different orientations, in order to search for the maximum response, or alternatively, an optimal estimation of the direction.

Another approach is to use some sort of detector valid for different edge orientations. The only rotationally-invariant second-order operator is the *Laplacian*, which is the scalar product of the gradient vector by itself:

$$\triangle f = \nabla^2 f = \nabla \cdot \nabla f = \frac{\partial^2 f}{\partial x^2} + \frac{\partial^2 f}{\partial y^2} + \frac{\partial^2 f}{\partial z^2} \tag{4.13}$$

Two different convolution kernels may be used typically to calculate the Laplacian:

$$\frac{1}{8}\begin{bmatrix} 0 & -1 & 0 \\ -1 & 4 & -1 \\ 0 & -1 & 0 \end{bmatrix} \qquad \frac{1}{16}\begin{bmatrix} -1 & -1 & -1 \\ -1 & 8 & -1 \\ -1 & -1 & -1 \end{bmatrix}$$

Figure 4.4: Laplacian convolution kernels in 2D.

The Laplacian operator is usually used in conjunction with a Gaussian operator for smoothing and scale selection because Laplacian zero-crossings are only effective in a band-limited situation. Again, due to the associative and commutative properties of the convolution, we can combine both operators

$$g_\sigma(x,y) = \frac{1}{2\pi\sigma^2}\, e^{-\frac{x^2+y^2}{2\sigma^2}} \tag{4.14}$$

$$\triangle\left[g_\sigma(x,y) * f(x,y)\right] = \triangle\left[g_\sigma(x,y)\right] * f(x,y) = LoG * f(x,y) \tag{4.15}$$

and obtain an expression for the new operator

$$LoG \triangleq \triangle\left[g_\sigma(x,y)\right] = \frac{\partial^2 g}{\partial x^2} + \frac{\partial^2 g}{\partial y^2} = \frac{x^2+y^2-2\sigma^2}{\sigma^4} g_\sigma \tag{4.16}$$

The resulting *LoG* operator, that depends on theσ scale parameter, is known as the *Laplacian of Gaussian* or *Marr-Hildreth* operator [122] and can be seen in Fig. 4.5, where we can also see the corresponding second derivative components. The scale, corresponding to the σ value of the Gaussian, should be chosen according to the size of the edge features to be detected. Discrete approximations may be obtained for each scale value by several methods, for example by approximating and truncating the Gaussian function (sampled Gaussian kernel) or by discrete derivative approximations using the *discrete Gaussian kernel*, which preserves scale-space properties [101].

Another second order approach is the *Difference of Gaussians (DoG)* operator [111]. From the fact that scale-space representation of an image $L(x,y;t)$ satisfies the diffusion equation [82]

$$\frac{\partial L(x,y;t)}{\partial t} = \triangle L(x,y;t) = L_x^2(x,y;t) + L_y^2(x,y;t) \tag{4.17}$$

also called Laplace equation, it follows that the *LoG* operator can be found as the limit of the difference between two Gaussian smoothed images:

$$\triangle L(x,y;t) = \lim_{\triangle t \to 0} \frac{2}{\triangle t}\left(L(x,y;t+\triangle t) - L(x,y;t)\right) \tag{4.18}$$

where $L(x,y;t) = f(x,y) * g(x,y;t)$ and $t = \sigma^2$.

Hence, subtracting two Gaussian smoothed images with different apertures we obtain an edge detector. The *DoG* operator is an approximation of the Laplacian of Gaussians but does not require complex second order derivative calculations which made its use quite popular.

Once the zero-crossings have been calculated, a magnitude can be assigned to them at each scale, as the slope of the second directional derivative taken perpendicular to the zero-crossing segment [122]. Another possibility is to simply use the gradient magnitude at the zero-crossing location.

The use of the *LoG* operator requires that the intensity variation along, but not necessarily near, the line of zero-crossings is approximately linear. Then the Laplacian zero-crossings will coincide with the local orientation line zero-crossings [122]. However, this operator exhibits severe localization errors in curved edges and other places where the intensity varies in a non-linear way [122, 164]. Moreover, it detects false edges corresponding to local minima of the gradient magnitude and it is difficult to combine the information obtained from the zero-crossings at different scales so it is not currently used in practice.

Extensive local second-order derivative information may be obtained by calculating the *Hessian matrix* at an image point. Its components are the image second-order spatial derivatives. A second-order Taylor expansion of a 2D image around a point x_0 is:

$$f(x_0+\triangle x, y_0+\triangle y) \backsimeq f(x_0,y_0) + \begin{bmatrix} \triangle x & \triangle y \end{bmatrix} \begin{bmatrix} f_x(x_0,y_0) \\ f_y(x_0,y_0) \end{bmatrix} +$$

$$+\frac{1}{2}\begin{bmatrix} \triangle x & \triangle y \end{bmatrix} \begin{bmatrix} f_{xx}(x_0,y_0) & f_{xy}(x_0,y_0) \\ f_{xy}(x_0,y_0) & f_{yy}(x_0,y_0) \end{bmatrix} \begin{bmatrix} \triangle x \\ \triangle y \end{bmatrix}$$

We obtain an expression which is valid for N-dimensional scalar images

$$f(x_0+hv) = f(x_0) + h\nabla f(x_0,y_0)\cdot v + \frac{1}{2}h v^T \mathscr{H}(x_0,y_0)\, v + O(h^3) \tag{4.19}$$

where $\mathscr{H}$ is the symmetric Hessian matrix, h is the step size and v is a unit vector in the direction of the step. The Hessian matrix $\mathscr{H}$ captures the second order local structure of the image in the vicinity of x_0, corresponding to the local image curvatures as it is described in more detail in section 4.6.

Different features may be obtained from the Hessian matrix. The Laplacian in eq. 4.13 corresponds to the trace of the Hessian matrix:

$$\triangle f = \nabla^2 f = \mathrm{tr}\,(\mathscr{H}(x)) \tag{4.20}$$

A more in-depth analysis of the Hessian matrix properties is performed later in section 4.6 in the context of line structure detection.

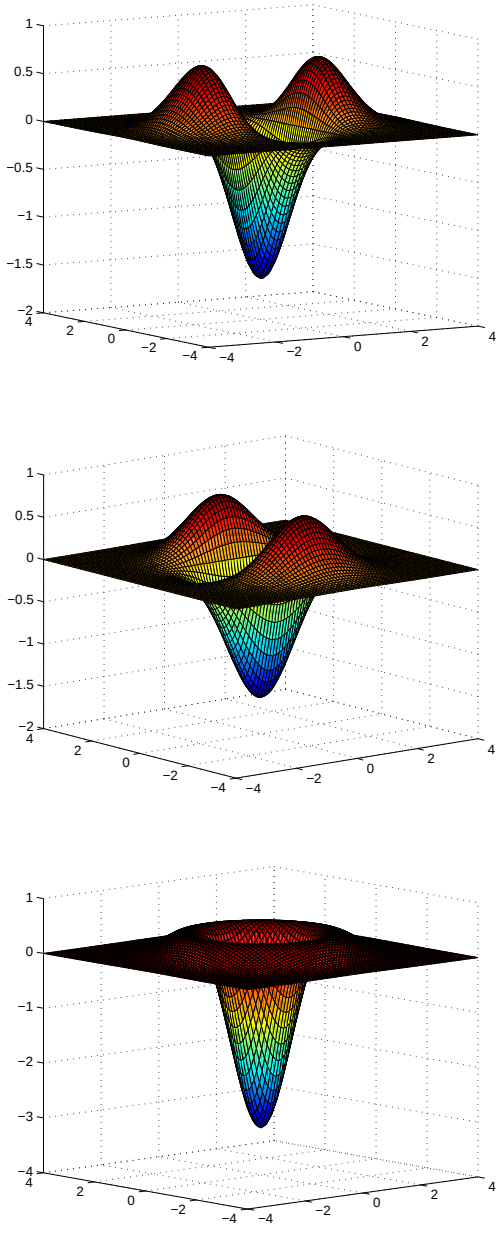

Figure 4.5: Surface plots of $\partial^2 g/\partial x^2$ (top) and $\partial^2 g/\partial y^2$ (middle) and Laplacian of Gaussian (bottom). All surfaces are calculated for $\sigma = 1.0$.

4.3.4 Advanced Edge Detection

Marr and Hildreth introduced important concepts such as some notion of scale, that was later conceptualized in the framework of *scale-space*, first introduced by Witkin [195], and Gaussian filtering as a means of scale selection [82]. However, early edge detectors such as the Marr-Hildreth operator exhibited several problems which led researchers to develop new strategies such as optimal edge detection, integration of information at multiple scales and non-linear filters. It is not our intention to make an extensive review on the subject of edge detection (see for example [138] or [15]) but rather focus on some interesting concepts useful for tubular structure detection.

4.3.4.1 Canny-like Edge Detectors

Canny [30] developed a computational theory of edge detection in order to find the optimal edge detector which maximized the criteria of detection, localization and single responseness (see Section 4.3.1). He showed that there is an uncertainty principle regarding detection and localization of noisy edges and that one must find a trade-off between these. He then derived an optimal detector which is the sum of four complex exponentials, but which can be approximated in practice by the first derivative of Gaussian functions, which is much more efficient to compute. Compared to the Marr-Hildreth operator, its 2D performance is better in terms of detection and localization due to its directional properties. Moreover, the amplitude of the response is a good estimate of edge strength and compared with the zero-crossings of the Laplacian, it can be thresholded adaptively to find local maxima.

Canny's edge detector finds the zero-crossings of the second-order image derivative in the edge direction n:

$$\frac{\partial^2}{\partial n^2} g * f \tag{4.21}$$

which correspond to the maxima of the derivative in the edge direction. First, an estimate of the local edge direction is computed using the gradient:

$$n = \frac{\nabla (g * f)}{|\nabla (g * f)|}$$

In practice, the direction can be rounded to one of four edge directions at angles of 0º, 45º, 90 and 135º.

Often the Canny algorithm computes the first directional derivative of Gaussian filtered image

$$\frac{\partial}{\partial n} g * f \tag{4.22}$$

performing later the non-maximum suppression in the gradient direction in order to compute single edge responses. Due to the separability of the Gaussian functions, the above scheme can be implemented efficiently by first convolving the image with a 1D

Gaussian in each dimension and then computing the derivative in the edge direction only.

Compared to the Laplacian, the latter can be decomposed into second derivative components in two arbitrary orthogonal directions. If we choose as directions the gradient direction and its normal, then we will have a contribution in the gradient direction which is essentially the same as the operator described by Canny, and another contribution which does not contribute to detection and localization but to noise only.

The last stage of the Canny algorithm is to threshold the edges in order to remove the response for false edges by using *hysteresis thresholding*, which is a sort of adaptive thresholding. The algorithm is sensitive to weak edges but the problem is that this also makes it sensitive to spurious or unstable edges [15].

Canny also devised a way to combine the output from multiple scales in what is known as *feature synthesis*. In a similar approach Schunk [160] also performed scale integration by combining ridge information obtained from detected edges across scales.

One recurrent problem in multi-scale approximation is that sometimes there are no indications on how to choose the number and range of scales. Jeong and Kim [74] tried to find the optimal scale for every pixel by minimizing the following energy function on the filter width domain σ:

$$E(\sigma) = \int\int \left[(I * g)^2 + \lambda \left| \nabla \sigma^{-1} \right|^2 \right] \tag{4.23}$$

designed for large apertures in flat areas and small apertures in places of high intensity variation and smoothness in the resulting scale map. It is slow, but its performance could be greatly improved with a preselection of candidate points. A similar adaptive idea by Deng and Cahill [42] uses the following formula for scale selection:

$$\sigma^2(x) = \frac{k\sigma_n^2}{\sigma_f^2(x) + \sigma_n^2} \tag{4.24}$$

where σ_f is the local variance and σ_n is the standard deviation of the image noise, assumed Gaussian.

Lindeberg [105] proposed, within the scale-space framework (see Section 4.4) a method for edge detection based on the maximization of two γ-normalized edge strength measures:

$$\mathscr{G}_{\gamma-norm} L = \sigma^{\gamma} \left(L_x^2 + L_y^2 \right) \tag{4.25}$$

$$\mathscr{T}_{\gamma-norm} L = \sigma^{3\gamma} \left(L_x^3 L_{xxx} + L_y^3 L_{yyy} + 3L_x^2 L_y L_{xxy} + 3L_x L_y^2 L_{xyy} \right) \tag{4.26}$$

where L is the scale-space representation of the image and γ is a parameter that makes the scale selection dependent on the edge diffuseness. Equation 4.25 corresponds to the gradient magnitude equation 4.26 takes into account that the edge is located at a maximum of gradient magnitude, that is, with zero second derivative and negative third derivative.

The problem with this approach is that the user has to provide a set of desired scales in a range and the use of high order derivatives may be problematic and not justified by the results, which are similar to other existing methods [15]. However, the automatic scale selection and multiple scale integration used by Lindeberg are interesting concepts that can be applied directly to most line structure detectors that are based on derivative calculations.

4.3.4.2 Steerable Filters

Canny-like filters use optimal 1D edge detection operators in the gradient direction and smoothing in the orthogonal direction(s). Freeman and Adelson [55] proposed an alternative approach that uses a set of directional filter banks for predefined orientations, what is known as *steerable filters*. In this approach, detectors for arbitrary orientation can be generated by linear combination using these oriented filters as basis functions. They demonstrated that all functions that can be expressed as a Fourier series in angle or as a polynomial multiplying a radially symmetric window function are steerable in orientation. Hence, derivatives of Gaussian of all orders are steerable since they consist of polynomials (here the Hermite polynomials) multiplying a Gaussian which is rotationally symmetric (see section 4.4.2). In order to synthesize filters with arbitrary phase response, they use filters in quadrature (same frequency response but with a phase difference of 90º) which can be found using a Hilbert transform [23], that may be approximated via polynomial fit. Thus, a set of steerable filters is combined with another set whose originating functions (the non-rotated versions) are in quadrature.

One example of such combination of filters is to combine the second derivative of Gaussian $f(x,y) = G_2^{0^\circ} = \left(4x^2 - 2\right)\exp(x^2+y^2)^4$, with rotated versions for 0º, 60º and 120º:

$$G_2^\theta = k_1(\theta)G_2^{0^\circ} + k_2(\theta)G_2^{60^\circ} + k_3(\theta)G_2^{120^\circ} \tag{4.27}$$

where the k_i can be found solving a set of equations for the steering conditions yielding

$$k_i(\theta) = \frac{1}{3}\left[1 + 2\cos\left(2(\theta - \theta_j)\right)\right] \tag{4.28}$$

Then, the Hilbert transform of G_2 can be approximated by a third order polynomial, namely H_2 with four rotated versions that are used as basis functions. Thus the seven basis functions of G_2 and H_2 are sufficient to shift G_2 to the desired phase and orientation. Similar approximations can be found for other orders of derivatives.

Steerable filters can be used, among other things, to estimate local feature orientation and strength. The squared magnitude of the quadrature pair filter can be used to estimate the orientation θ_d with largest strength:

[4] We follow here the notation from Freeman and Adelson with the subscript for the derivative order and the superscript for the angle

$$E_2(\theta_d) = \left[G_2^{\theta_d}\right]^2 + \left[H_2^{\theta_d}\right]^2 \tag{4.29}$$

Using a scheme similar to Canny's but replacing the feature detector with this energy, one obtains single responses to different features, as compared with Canny's method that gives spurious responses to non-edge features, such as double responses for lines. One major drawback is that the process of obtaining the Hilbert transform in order to design quadrature filter pairs is very difficult and tedious. Weiping and Huazhong propose an alternative to the Hilbert transform that uses dyadic B-spline wavelets [186].

Jacob and Unser [72] developed a set of truly 2D feature detectors following Canny-like optimization criteria but obtaining explicit expressions. Moreover, they used the ideas of Freeman and Adelson in order to design optimal 2D detectors which were steerable. The use of this framework is demonstrated by developing specific detectors for edge, ridge and wedge features that outperform Canny's detector without any relevant additional computational cost.

4.4 Image Analysis in Scale-space

4.4.1 Concept of Scale-space

When faced with the problem of image analysis, one important consideration is that an image is a *physical observable* that represents the reality as measured by some apparatus that is able to register some physical measure (typically illumination, but may be any other physical observable phenomenon such as X-ray attenuation, magnetic resonance, etc.) in a regular discrete finite grid and with a certain dynamic range. This implies that there exist a finite scale range at which observations are made [49]. The lower bound of this scale range, often referred to as the *inner scale*, is determined by the sampling characteristics of the device and it refers to the size of the finest possible feature that can be detected. The *upper scale* bound is limited by the scope of the field of view and refers to the coarsest features that can be observed on the image. Moreover, objects, illumination changes, details and other features represented in digital images have different sizes and some of them are only meaningful at a certain range of scale(s). This finite scale range and multi-scale image nature must be taken into account when performing any image analysis task in order to fix the proper scale(s) at which calculations are meaningful.

Sometimes, calculations performed at a single scale may miss some information. No single filter can be optimal simultaneously at all scales and a multi-scale approach is necessary, which deals with every relevant scale separately. This happens for example when trying to detect some objects or entities whose coarse and fine details span a variable range of scales and all the information is relevant. This is the case for example of images of the human vasculature. A complex vascular network is comprised of multiple vessels of varying length and diameter and multi-scale approaches are required in most cases for the detection and extraction of the whole vascular tree.

When faced with the problem of multi-scale analysis of digital images, it is necessary to find a way to convert the images into a multi-scale representation and deal with

each scale separately. This leads to the basic idea of taking local averages at various resolutions, in a sort of smoothing filter, and detecting changes of intensity that occur at each one. To achieve this, it is necessary to:

- Find the optimal smoothing filter in order to obtain image representations at different scales, which is known as a *scale-space image representation*.
- Detect the intensity changes at each scale.
- Integrate the information obtained at different scales.

When designing the optimal smoothing filter two important considerations must be taken into account [122]:

- Filtering should reduce the range of scales over which intensity changes take place. This implies that the frequency spectrum of the filter must be smooth and roughly band-limited with a small variance $\Delta\varpi$.
- Features at each scale should be spatially localized. This implies that the contributions to each point in the filtered image should be obtained from a smoothed average of nearby points, so the filter must be smooth and localized in the spatial domain with a small variance Δx.

The problem is that these two localization requirements, one in the spatial and the other in the frequency domain, are conflicting and related by the uncertainty principle that states that $\Delta\varpi\Delta x \geq \pi/4$ [23]. This means that it is impossible to concentrate a function both in the spatial and frequency domain. The more concentrated it is in the spatial domain, the more spread it is in the frequency domain. The best trade-off is achieved with the use of Gaussian functions.

The structure of images, the properties that a scale-space representation of an image should have and the way to accommodate such a scale-space representation in a mathematical theory was studied in depth by several authors [195, 82, 206, 103, 49]. Their basic idea for a scale-space representation of an image is that it should consist of a one-parameter family of derived signals from fine to coarse scales as the *scale* parameter t increases, where the fine details are suppressed successively at coarser scales. The original signal will be the one with the finest details, that is, the one at the lowest scale. Mathematically, for an N-dimensional signal $f : \mathbb{R}^N \to \mathbb{R}$, its scale-space representation $L : \mathbb{R}^N \times \mathbb{R}_+ \to \mathbb{R}$ is defined as the convolution:

$$L(x;t) = (T_t f)(x) \int_{\vec{\xi} \in \mathbb{R}^N} f(x-\xi)\, g(\xi;t)\, d\xi = g(x;t) * I(x) \tag{4.30}$$

where $g : \mathbb{R}^N \times \mathbb{R}_+ \to \mathbb{R}$ is a family of functions in the scale parameter t. These functions act as *operators* that interact with the data in order to extract relevant information and generate the corresponding representations. The scale parameter t is equivalent to the *aperture* of the physical observation device. Sometimes g is called the *aperture function*.

A key requirement for obtaining this scale-space representation is that structures obtained at coarser scales, should be a simplification of the structures at lower scales, and that no new structures should be generated when going from a fine to a coarse scale. Instead, the fine details should be "flattened" when moving to coarser scales. This idea was formalized by several authors in order to reach similar conclusions, by taking also into consideration some *scale-space axioms* [82]. These axioms take into account some desired properties of the scale-space representation as well as some practical issues and reduce the number of possible scale-space representations to a smaller class. We summarize here some of the most important ones:

- *linearity*

$$T_t(af(x)+bh(x)) = aT_t f(x) + bT_t h(x) \tag{4.31}$$

- *spatial shift invariance,* implies the convolution in 4.30, that is, we scan the aperture over any possible location of the signal (image).

- *non-creation of local extrema* (zero-crossings) in one dimension, meaning that no new information or spurious details should be generated when going from fine to coarse scales.

- *non-enhancement of local extrema* (zero-crossings) with increasing scale in multiple dimensions, meaning that fine details should not be enhanced at larger scales. For spatial maxima and minima respectively:

$$\partial_t L(x;t) \leq 0 \tag{4.32}$$

$$\partial_t L(x;t) \geq 0 \tag{4.33}$$

- *rotational symmetry / isotropy*, meaning that there is no preferred orientation.

- *scale invariance*, meaning that there is no preferred scale.

- *semi-group structure,* meaning that the action of two operators is equivalent to the same action done by a single operator of the same type. That is a concatenation of two rescalings, should be a third rescaling in the form:

$$g(x;t_1) * g(x;t_2) = g(x;t_1+t_2) \tag{4.34}$$

- *cascade smoothing property*, related to the previous:

$$L(x;t_2) = g(x;t_2-t_1) * L(x;t_1) \tag{4.35}$$

It can be demonstrated [12, 82, 195, 206] that the Gaussian kernel[5]

$$g(x;t) = \frac{1}{\left(2\pi t^2\right)^{N/2}} e^{-\Sigma^N x_i^2/(2t)} \tag{4.36}$$

[5]Note the change of variable $t = \sigma^2$ with respect to the standard representation of the Gaussian function. This notation using the scale parameter t is typically used in the scale-space framework.

is the only family of functions that meet all these requirements. From these, the "non-creation / non-enhancement of local extrema" are the crucial axioms which relate scale-space to smoothing, hence the selection of the Gaussian.

Thus, one can obtain a multi-scale representation $L(x;t)$ of the image $f(x)$ by convolving the original image with a Gaussian kernel $g(x;t)$ for different values of the scale parameter t.

Equivalently, this family of functions can be obtained as the solution of the diffusion equation:

$$\partial_t L = \frac{1}{2}\nabla^2 L = \frac{1}{2}\sum_i^N \partial_{ii} L \tag{4.37}$$

with initial condition $L(x;0) = f(x)\ \forall x \in \mathbb{R}^N$ [101].

4.4.2 Scale-space and Derivatives

The scale-space representation provides a consistent way of calculating scaled, smoothed image derivatives. Spatial derivatives of the smoothed intensity function L can be calculated at each level of scale, the so called *Gaussian derivatives*. For example, for 2D images, these partial derivatives would be:

$$L_{x^i y^j}(x,y;t) = \left(\partial_{x^i y^j} L\right)(x,y;t) = \frac{\partial^{i+j} L}{\partial x^i \partial y^j} \tag{4.38}$$

We have already seen how some methods, such as the Marr-Hildreth operator, incorporated implicitly this concept of Gaussian derivatives as a method for scale selection. As Florack states [49] disregarding the intrinsic size of the entities depicted on an image or, in other words, the scaling degree of freedom, is the cause of the failure of naively applying differential methods in image analysis. Hence, equation 4.38 provides a way of appropriately computing scaled, smoothed derivatives that take into account the scale of the different features and that deals at the same time with noise.

Since the derivative operator commutes with the Gaussian operator we have that

$$L_{x^i y^j}(x,y;t) = \partial_{x^i y^j}(g * I) = g * \partial_{x^i y^j} I = \partial_{x^i y^j} g * I \tag{4.39}$$

This means that we can smooth the whole image and then compute its derivatives, or compute derivatives and then smooth the image or even generate a derivative of Gaussian kernel which is convolved with the image [112]. Depending on the situation this may lead to a reduced number of operations. If several derivatives must be computed, it is sometimes easy to convolve the image with a Gaussian kernel first, and then compute the desired derivatives. However, if a single derivative must be calculated, or derivatives are calculated in a few points only, it may be better to use Gaussian derivative kernels.

When computing scaled derivatives, we must take into account that the whole image should be scaled for consistency using the Gaussian kernel, even if in some directions the derivative order is zero. Take for example the case of computing the second

derivative in the x direction of a 2D image. We would precompute a 1D kernel for the second derivative of Gaussian at the desired scale t and then apply it in the x direction. However, this would be inconsistent with filtering the image with a Gaussian and calculating the second derivative in the x direction, since the y direction remains unscaled, and is not affected by the smoothing. Unless we explicitly want an anisotropic behavior, we should also convolve the image in the y direction with a (zero-order) Gaussian kernel with the same aperture.

Another related property is that the derivative of a Gaussian is another Gaussian multiplied by a polynomial of the same order as the derivative. Calculating the derivatives analytically we obtain:

$$g_x = \frac{\partial g}{\delta x} = -\frac{x}{\sigma^2} g, \tag{4.40}$$

$$g_{xx} = \frac{\partial^2 g}{\partial x^2} = \frac{x^2 - \sigma^2}{\sigma^4} g, \tag{4.41}$$

$$g_{xxx} = \frac{\partial^3 g}{\partial x^3} = \frac{-x^3 + 3\sigma^2 x}{\sigma^6} g, \tag{4.42}$$

$$g_{4x} = \frac{\partial^4 g}{\partial x^4} = \frac{x^4 - 6\sigma^2 x^2 + 3\sigma^4}{\sigma^8} g, \tag{4.43}$$

$$g_{5x} = \frac{\partial^5 g}{\partial x^5} = \frac{-x^5 + 10\sigma^2 x^3 - 15\sigma^4 x}{\sigma^{10}} g. \tag{4.44}$$

Thus, the derivatives take the form:

$$g_{nx} = \frac{(-1)^n}{\sigma^{2n}} H_n(x;\sigma)\, g \tag{4.45}$$

where $H_n(x)$ are the *Hermite polynomials*[6] modified by the introduction of the sigma parameter (they are derived from the derivatives of $e^{-x/2\sigma^2}$ instead of $e^{-x/2^2}$) but the properties are the same. These polynomials form an *orthogonal polynomial sequence* which means that the Hermite polynomials are orthogonal in the interval $[-\infty, \infty]$ with respect to the weight function $W(x) = e^{-x^2/2}$. Mathematically:

$$\forall \{m, n \in N \,|\, m \neq n\} \Rightarrow \int_{-\infty}^{\infty} H_m(x) H_n(x)\, e^{-x^2/2} dx = 0 \tag{4.46}$$

Hermite polynomials of any order can be obtained using recursive and explicit formulas. We can easily find a recursive formula for these modified polynomials.

$$\frac{\partial^n g}{\partial x^n} = \frac{\partial}{\partial x}\left(\frac{\partial^{n-1} g}{\partial x}\right) = \frac{\partial}{\partial x}\left(\frac{(-1)^{n-1}}{\sigma^{2(n-1)}} H_{n-1}(x,\sigma) g(x)\right)$$

[6] We use the probabilistic definition of Hermite polynomials. The physics definition is slightly different in the coefficients and derived recursion and explicit formulas.

$$= \frac{(-1)^{n-1}}{\sigma^{2(n-1)}} \left(\frac{\partial}{\partial x} \left(H_{n-1}(x,\sigma) \right) g(x) + H_{n-1}(x,\sigma) \frac{\partial g}{\partial x} \right)$$

It can be proved [8] that :

$$H_n^{'}(x) = \frac{\partial}{\partial x} \left(H_n(x,\sigma) \right) = n H_{n-1}(x,\sigma)$$

and hence we obtain

$$\frac{\partial^n g}{\partial x^n} = \frac{(-1)^{n-1}}{\sigma^{2(n-1)}} \left((n-1) H_{n-2}(x,\sigma) g(x) - \frac{x}{\sigma^2} H_{n-1}(x,\sigma) g(x) \right)$$

$$g_{nx} = \frac{\partial^n g}{\partial x^n} = \frac{(-1)^{n-1}}{\sigma^{2n}} \left((n-1)\, \sigma^2 H_{n-2}(x,\sigma) - x H_{n-1}(x,\sigma) \right) g(x) \tag{4.47}$$

and thus, comparing with equation 4.45 we obtain the recursive relationship:

$$H_n(x,\sigma) = (n-1)\, \sigma^2 H_{n-2}(x,\sigma) - x H_{n-1}(x,\sigma) \tag{4.48}$$

that allows to calculate polynomials up to any order easily. We used this property in [112] to calculate Gaussian derivative kernels as an alternative to finite differences.

4.4.3 Scale-space and Discrete Signals

In order to implement the scale-space representation for discrete signals, one must think of discretizing the Gaussian function and its derivatives. Derivatives are usually discretized using finite difference approximations. However, discretization of the Gaussian function is more complicated since it has theoretically infinite support. A direct way is to compute a *sampled Gaussian kernel*, by sampling the Gaussian function at discrete intervals and truncating it at the ends in order to obtain a filter with finite impulse response. Suppose we obtain a sampled Gaussian kernel with $2M+1$ terms that is convolved with the input signal

$$L(x;t) = \sum_{n=-M}^{M} g(n;t)\, f(x-n) \tag{4.49}$$

For an normalized Gaussian we can find a reasonable value for M on the basis of the unit integral, by adding the generated coefficients up to a desired error:

$$1 - \sum_{n=-M}^{M} g(n;t) < \varepsilon \tag{4.50}$$

However, the sampled Gaussian kernels may lead to implementation problems, in particular for small scales or when calculating higher order derivatives. Moreover, it can be demonstrated that scale-space properties are not preserved [101].

Lindeberg [100] studied how the scale-space framework in the continuous domain should be discretized so the scale-space properties hold also in the discrete domain, developing a scale-space theory for discrete signals. This included the conception of a *discrete Gaussian kernel*, and a way of calculating discrete Gaussian derivative approximations with scale-space properties. The discretization, however, allowed for a continuous scale parameter t, so discrete kernels could be generated for virtually any scale if needed.

Starting from a set of scale-space axioms, the scale-space representation of a discrete image is obtained as a convolution with a family of kernels T on the continuous scale parameter t. For a one-dimensional signal f:

$$L(x;t) = \sum_{n=-\infty}^{\infty} T(n;t)\, f(x-n) \tag{4.51}$$

Such kernels take the form

$$T(n;t) = e^{-\alpha t} I_n(\alpha t)$$

where I_n are the modified Bessel functions of integer order [2]

$$I_n(x) = \sum_{m=0}^{\infty} \frac{1}{m!\,\Gamma(m+n+1)} \left(\frac{x}{2}\right)^{2m+n} \tag{4.52}$$

and the scaling parameter α is usually set to 1. The kernel $T(n;t)$ is called the discrete analogue of the Gaussian kernel or simply the *discrete Gaussian kernel*. We can see that we can obtain a kernel for every desired value of the continuous scale parameter t. In practice, the kernel may be truncated on the basis of the unit integral error as with the sampled Gaussian kernel.

An implementation of such a kernel for N-dimensional images can be found in [205] and extended for Gaussian derivatives in [112]. We used these implementations for all scaled derivative calculations performed in the experiments of this thesis.

4.5 Ridge Detection

The study of ridges is closely related to line-like structures. Line structures may present a visible ridge or, if not present, it may be obtained by some means of mathematical operation, such as scaled Gaussian smoothing, or as a result of applying a medialness function, that is, a function that obtains, for every point, the likelihood of being part of the the centerline of medial axis.

4.5.1 Ridge Definition

Ridges are closely related to line structures. Most of the times, line-like structures in medical images present intensity ridges with maxima in their medial axes or centerlines. If the centerlines do not present an intensity maximum at the centerlines, such

as with MR Time-of-Flight (TOF) images [65], image processing methods, such as Gaussian filtering, could be applied in order to create an intensity ridge so as to create a maximum in the central part of the tubular section [11]. Specially interesting is the case where a *medialness* filter [86] is applied to the vascular image for vessel detection and/or enhancement. The response of such a filter is designed to be maximum in the medial axis of the vascular structures or very close to it and thus, it creates an intensity ridge in the line structure whose extraction will provide the approximate centerline.

From the analysis in Section 4.3 we can now state that finding the maximum of gradient magnitude in the gradient direction, as in the method of Canny, is equivalent to finding the ridges of gradient magnitude, since this corresponds to the definition of a ridge. As Eberly states [46], the method of edge detection consists of following ridges of edgeness. Hence, though not exclusively, *both edge detection and line structure detection can be both approached as a problem of ridge detection using differential calculus*, applied to the gradient magnitude in the first case and to the source intensity image in the second case (probably with some pre-processing). Ridges are also related to the notion of a medial axis of an object [158] and thus may provide local information complementary to edge information.

Ridges could be considered as a generalization of a function maximum. Intuitively if a maximum is the highest value of a function in a local neighborhood in all N space directions, assuming the function is locally smooth, a ridge is a *maximum in N-1 principal directions*. Conversely, the notion of *valley* can be considered as a generalization of the minimum of the function and we indistinctly will talk of ridges when referring to both ridges and valleys[7]. Note that the ridge is defined in terms of the principal directions or image (surface) curvatures, which corresponds to the eigenvectors of the local Hessian matrix.

We will now provide a formal definition of *height ridges* from Eberly[8] [46].

Definition 1. Let $f : \mathbb{R}^n \to \mathbb{R}$ be a $\mathscr{C}^2$smooth function. Let $\lambda_i \quad 1 \leq i \leq n$ be the eigenvalues of the Hessian matrix $\mathscr{H}$ of f with $\lambda_1 \leq \ldots \leq \lambda_n$. Let $v_i \quad 1 \leq i \leq n$ be the corresponding eigenvectors. Let V be a $(n-d) \times (n-d)$ matrix, whose columns are the $n-d$ first eigenvectors, corresponding to the negative eigenvalues. A point x_0 is a d-dimensional ridge point if

$$V^T \nabla f(x_0) = 0 \tag{4.53}$$

and

$$\lambda_{n-d}(x_0) < 0 \tag{4.54}$$

The first condition is a set of $n-d$ equations in the form $v_i \cdot \nabla f(x_0) = 0$ which means that the directional derivatives in the direction of those eigenvectors must be zero and, hence, the point is a local extreme in that direction.

[7] Sometimes these are collectively referred to as *crease points*.

[8] The *height definition* of ridges is more useful for image analysis but some other definitions exist.

The second condition implies that there are $n-d$ negative eigenvalues (since these are ordered in the definition). These eigenvalues represent the curvature in the direction of the corresponding eigenvectors. Negative eigenvalues imply that the local extrema defined by the first condition are maxima, and not minima, of local curvature. This second condition is obtained from a more general condition that $V^T \mathscr{H} V$ must be negative definite and this corresponds to a diagonal matrix whose non-zero values are the eigenvectors. For finding local minima and valleys we just have to change the sign of the second condition.

When $d = 0$ we have a *local maximum* and $\mathscr{H}$ is a negative definite matrix. We are mostly interested in one-dimensional ridges, corresponding to curves, so in our case $d = 1$. This means that the function is a local maximum, except in one direction, of the set of linearly independent directions defined by the eigenvectors. In other words, a ridge point is a maximum in the subspace defined by the $n-d$ eigenvectors corresponding to negative eigenvalues.

If this concept is applied to the detection and extraction of vascular structures in medical images, this intensity ridge will approximately correspond to the centerline or medial axis of the vessel[9], assuming that the image of the vessel presents such a peak along its path.

Jacob and Unser [72] developed a set of specific ridge detectors in the form of steerable filters following Canny-like optimization criteria that have better orientation selectivity without no extra computational cost as compared with the eigenanalysis of the Hessian matrix.

4.6 Second-order Local Structure and the Hessian Matrix

4.6.1 Hessian Matrix for Local Structure Estimation

The Hessian matrix is an important tool for line structure detection based on differential operators. For a three dimensional image $I : \mathbb{R}^3 \to \mathbb{R}$ the scale-space Hessian matrix $\mathscr{H}(x;\sigma)$ is defined as the matrix of scaled second order derivatives of the image

$$\mathscr{H}(x;\sigma) = \begin{bmatrix} L_{xx} & L_{xy} & L_{xz} \\ L_{xy} & L_{yy} & L_{yz} \\ L_{xz} & L_{yz} & L_{zz} \end{bmatrix} \tag{4.55}$$

which describes the second order local image structure, that is, local image curvatures. The parameter σ is the scaling parameter and corresponds to the Gaussian smoothing, assuming that the derivatives are calculated in scale-space (see section 4.4.2).

The three ordered eigenvalues λ_i, $\lambda_3 \leq \lambda_2 \leq \lambda_1$ of this Hessian matrix describe the principal image curvatures which best describe the local image second-order variations.

[9] We say approximately because the medial axis is defined in terms of the real object boundaries, which are usually unknown, and not in terms of the intensity peaks in the sections. However, in practice, in most vascular images, the loci of medial axis and the ridges are close to each other.

The corresponding eigenvectors v_i describe the directions in which the principal curvatures occur. Note that, since, they are calculated from a scale-space Hessian matrix, these eigenvalues and vectors are defined also in scale-space.

The local structure of images can be intuitively described as the apparent shape taken by their local intensity distribution. The Hessian Matrix, was introduced previously (see 4.3.3) as a tool that could be used to obtain different second-order differential features of images, such as ridges (section 4.5).

The eigenvalues and eigenvectors of the Hessian matrix at an image point can be used as local shape descriptors describing the local structure of images. The eigenvalues correspond to the principal image curvatures and the eigenvectors correspond to the direction of those curvatures. These principal curvatures correspond to the second-order derivatives of the image in the directions of the reference system described by the eigenvectors, which are called the principal directions. Thus the eigenvalue analysis of the Hessian matrix provides two types of information at every point of the image:

- It describes the local distribution of intensities in the image in terms of three curvatures (for 3D images) corresponding to three main orthogonal directions. These are the eigenvalues.

- It describes the reference system that best fits the local structure of the image, in which the principal curvatures are measured. In other words, it describes the orientation of the local shape. This local reference system, defined by the eigenvectors, constitute the principal directions of curvature. Somehow, obtaining the eigenvectors, we find the orthogonal directions that are more suitable for describing the local shape.

As stated previously (see Section 4.4.1), discrete derivative calculations always imply obtaining scaled calculations and therefore the corresponding Hessian matrix and eigenvalue analysis must be performed at each point at the appropriate scale, which depends on the size of the structures of interest to be analyzed in the image.

Frangi *et al*. [53] classified the local structure of a 3D image in several basic shapes, according to the values of the eigenvalues (in magnitude and sign) of the local Hessian matrix, ordered by magnitude ($|\lambda_1| < |\lambda_2| < |\lambda_3|$) as follows:

- *Line structures*: also called tubular structures, they present low curvature in one of the principal directions and high curvature in the other two directions. The low curvature corresponds to the axial direction of the local tube-like shape, since the intensity hardly varies in this directions. In the other directions, the curvature is high, since they correspond to the radial directions of the tube, where the intensity varies rapidly from the center to the external part of a tube-like shape. In medical images, they may correspond to local shapes of vessels or other line-like structures.

- *Plate structures*: also called sheet structures or flat structures, their intensity varies wildly in a single direction and hardly varies in the other two directions. Here, the structure is locally flat, as if forming a plane. This is typical of some organs appearing in medical images, that are not vessels or tubes.

2D		3D			local shape
λ_1	λ_2	λ_1	λ_2	λ_3	
N	N	N	N	N	noisy (blob-like)
		L	L	H-	plate-like (bright)
		L	L	H+	plate-like (dark)
L	H-	L	H-	H-	tubular (bright)
L	H+	L	H+	H+	tubular (dark)
H-	H-	H-	H-	H-	blob-like (bright)
H+	H+	H+	H+	H+	blob-like (dark)

Table 4.1: Basic local structure shapes in terms of eigenvalues of the Hessian matrix according to [53]. H=high, L=low, N=noisy, usually small, +/- indicate sign.

- *Blob structures*: they represent symmetrical spherical-like structures, with no preferred direction, where the intensity varies considerably from its center. Noisy structures are also typically blob-like, since they eigenvalues are usually of similar magnitude.

The classification criterion into the different shape types according to the relative value of eigenvalues is shown in Table 4.1. They also provided a geometric interpretation of the eigenvalues in terms of an ellipsoid whose axes represent the principal image curvatures corresponding to the eigenvalues. Danielsson *et al.* [36] extended this analysis to other types of shapes.

As we can see, by measuring the eigenvalues at points of interest of the images, we can obtain a local shape description at those points and distinguish between tubular, plate and blob structures at a local level. This is the basis of some of eigenvalue filters commonly used in vessel detection, such as those from Sato *et al.* [155] or Frangi *et al.* [53]. These methods try to discriminate points that are locally line-like from the rest of points in the images by building a *vesselness* function, based on these eigenvalues, that is maximum for line structures and yields low values for other types of structures.

4.7 Other Image Features

Other interesting image features may be of interest depending on the application, such as blobs, corners or junctions, for which specific detectors exist in the literature. As we have seen in Section 4.6, for the purpose of 3D vascular structure detection, it is important to distinguish line structures from other types of structures such as plate or blob structures. These structures may represent adjacent organs to vessels. Sometimes, the local shape of a vessel may differ from that of a line structure. For example bifurcation points in vessel branches resemble more a blob-like structure than a line-like structure and an aneurysm can be considered in most cases a blob structure. In this case, it is necessary to develop specific operators or strategies for these structures. In Chapter we have developed such an strategy for the segmentation of the thrombus in AAA after EVAR. Other examples of interesting vascular features which cannot be treated as line structures can be found at [97, 13].

Chapter 5

Vascular Detection

In this chapter, we introduce the problem of vascular detection and provide a review of some of the most popular *vesselness* functions for vascular detection. The emphasis is on the subset of *medialness* methods for vessel centerline detection and, more specifically, those that are based on calculations requiring an estimate of the vessel section, since they will be used for vascular tracking in Chapter 6.

Next, we proceed to identify and study the scaling parameters of these methods, testing their individual influence and their relationship against synthetic datasets with different noise levels. This will allow us to establish some scale selection criteria for multi-scale analysis of vessels in angiographic image modalities. The conclusions may also be applied to the study of other line-like structures in medical images, such as airway trees or biliary ducts.

The structure of the chapter is as follows: Section 5.1 provides an introduction explaining the main difficulties found in vascular detection. Relevant medialness features are grouped into *central medialness* features, reviewed in section 5.2 and *offset medialness* features, reviewed in section 5.3. Section 5.4 discusses some scale considerations that are taken into account in the experiments described in section 5.5 that allow us to set the scale selection criteria. Finally, conclusions are drawn in section 5.6.

5.1 Introduction

Curvilinear structures, also called line or tubular structures[1], are of particular interest for medical image analysis where they appear in different forms, both in anatomical structures, such as blood vessels, bronchi, nerves, biliary ducts, etc. as well as in artificial structures, such as catheters, electrodes, stents, etc. that may be of clinical interest.

The detection of vascular structures in medical imaging is particularly challenging. Some of the difficulties that the detection methods must cope with include:

[1]We will use indistinctly both terms for referring to elongated structures of small width represented in medical images both in 2D and 3D. The term line structure or line filtering is more used in the literature in the context of detection and the term tubular structure is more used in volumetric image analysis.

- *Complexity*: vascular structures may be highly ramified structures creating complex networks of connected branches. In general, these branches are curved and sometimes very tortuous.

- *Multi-scale structures*: a high variation in diameters may be observed from the root to the visible endpoints of a vascular network which makes necessary to define detectors operating at multiple scales in order to detect vessels of all expected sizes. Moreover, different sizes may require different approaches due to considerations such as accuracy or computation time. Some methods are best suited for the smallest scales, even close to the inner scale of the data. Others are specific for the largest of vessels such as the aorta.

- *Presence of bifurcations or anomalies such as stenoses and aneurysms*: even if most of the times vessels resemble linear structures, sometimes, along their paths, the local shape may differ from a linear structure. For example, an aneurysm, which is a local dilation of the vessel wall, may resemble a blob structure rather than a line structure..

- *Volume of information*: the volumetric nature of 3D angiographic images, which may consist of hundreds of slices in the case of CTA, implies a very large search space in which vascular structures have to be detected, even if the structures themselves do not occupy a high percentage of this volume. The evergrowing size of the datasets demands the development of strategies for large-scale computing, which include GPU processing, parallelization of algorithms and grid or cloud computing.

- *Non-uniformity of image contrast*: many angiographic modalities make use of a contrast agent injected in the blood stream in order to enhance the visualization of vascular structures. Failure to adequately inject the contrast agent at the time of the scan may result in non-uniform contrast agent distribution and, hence, of the image intensities along the vessel paths. Even if the contrast was correctly injected, distances are sometimes too large for the contrast bolus to reach all the vascular structures of interest.

A line or tubular structure has the basic geometrical property that its length exceeds by far its diameter [109] and thus, it can be considered as a 1D manifold in the embedding space, which is typically 2D or 3D. At every point of the line structure (with the exception of the end and bifurcation or branching points) we can associate a direction, corresponding to direction of the centerline or central axis of the tubular structure, and a section line (2D) or plane (3D), that is normal to the axis direction.

The typical intensity profile of a line structure shows an elevation across the longitudinal direction. The shape of this elevation may vary but typically can be modeled as a Gaussian, boxcar (also known as rectangular or bar-like) or roof cross-section, both in their 2D and 3D modalities. On the other hand, the intensity profile along the tube direction varies slowly, if we assume that there is no blockage preventing the diffusion of the contrast media. These hyperintensity properties are exploited by many detection methods.

The main goal of the vascular detection process is to detect curvilinear structures in medical images of, within some limits, arbitrary shape, size (in diameter and length) and section profile (bar, roof, Gaussian-like...) together with the following information[2]:

- *Geometric Information*: such as an estimation of the diameters, lengths or curvatures.
- *Topological Information*: such as the number of total branches and the number of bifurcations at a branch point.
- *Luminance Information*: it may be used in posterior image analysis processes or as low-level information for the detection of blockages, time and extension of contrast arrival etc.

The same requirements of detection and localization expressed in the previous chapter are also applicable here: we would like to detect all vessels, discard noisy branches or other spurious structures and locate the vessel position with the maximum precision. However, as we have seen in Chapter 4, high detection rates and accurate localization are conflicting requirements..

The accuracy of the analysis of vascular structures is determined greatly by the accuracy of the vessel detection or enhancement technique used. If the method is not accurate enough or presents limitations, for example at branching points or in the presence of some features such as stenoses and aneurysms, it may result in incorrect vessel extraction results. If the algorithm fails, user interaction may be required but, depending on the application, this process can be very cumbersome or practically impossible if the target vascular network is very dense and its vessels small or tortuous. In this sense, manual vascular extraction is, in general, a more tedious process than manual segmentation of organs.

Many vessel detection methods are generally based on the calculation, either locally or globally, of a vascular measure or feature which is usually known as '*vesselness*'. By *vesselness* measure, we refer to a function that assigns to each voxel a value, usually a floating point scalar, that is proportional to the likelihood of a voxel belonging to a blood vessel in the original image. If the vesselness measure is specially designed to detect the vessel centerlines, we call it *medialness* as it refers to the medial line or medial axis of the curvilinear structure [201]. This thesis focuses on medialness features since we are mostly interested in detecting the centerline of vessels. In Chapter 6 this will allow us to detect and track the vessel centerline along the vessel path.

Pizer *et al*. [145] classify medialness measures in:

- *central* vs *offset* medialness: central medialness attempts to localize object boundaries by averaging spatial information over some region whose average radius is proportional to the scale[3], which is in practice performed using local scaled derivatives at the point location. On the other hand, offset medialness attempts

[2] We refer here only to basic low-level information, and not higher level information that may be inferred from this, such as the presence of an aneurysm or stenoses.

[3] Note that in Krissian *et al*. [87] this description is used incorrectly for offset medialness.

to localize boundaries by accumulating information of a relatively small scale at neighbors which are at a distance proportional to the scale from the test point, which in practice means that boundary information is integrated at offset locations from the current point. Central medialness is adequate only when the objects of interest contain uncorrelated, small-scale noise or do not contain other objects inside.

- *linear* vs *adaptive* medialness: linear medialness uses radially symmetric operators whereas adaptive medialness is not symmetric and depends on the image content.

5.2 Central Medialness Features

In general, central medialness features use differential approaches, in which the scale of the derivatives is chosen in such a way that the kernel support covers the vessel section region and extends through the boundaries, obtaining a response by the difference of contrast between the regions outside and inside the vessel. This allows to detect the transition between the vessel lumen and its surroundings.

5.2.1 Basic Differential Approaches

A line structure corresponding to a vessel can be considered as a generalized double-sided edge. Building optimal detectors following Canny-like criteria (see Chapter 4), usually requires assumption on the line intensity profiles (see Appendix A). As an alternative, the second-order Gaussian derivative of the image is a good approximation for the optimal filter for different types of profiles, such as bar or roof-like [109]. This derivative is depicted in Figure 5.1 (a). When convolved with a line profile, it acts as a probe filter measuring the contrast between the regions inside and outside the range $[-\sigma,\sigma]$ [54] and therefore, gives a high response at the center of the profile. Hence, the value of this convolution, when measured in the direction normal to the line, can be considered as a *central medialness* measure obtaining the likelihood of a point to be part of the center of the profile. Moreover, an appropiate normalization of the filter and selection of the correct scale may provide an estimate of the height and width of the line structure.

However, linear filters are sensitive to step edges and provide multiple responses to a line due to side lobes which difficult simple scale integration schemes as stated by Koller *et al*. [85]. They proposed a non-linear integration scheme of two shifted first-order Gaussian derivatives, where the shift depends on the width of the line. The response is obtained by combining both shifted derivatives, one of them inverted, and taking the minimum value of both when they are both positive and zero outside this interval (see Figure 5.1 (b)). This simple scheme provides a single response for line-like structures, no response to step edges and works for most types of line profiles. Moreover, integration across scale-space provides one maximum at a scale proportional to the vessel width.

In practice, applying this concept to 2D and 3D profiles requires first to determine whether the current point is part of a line structure or not, and second to estimate

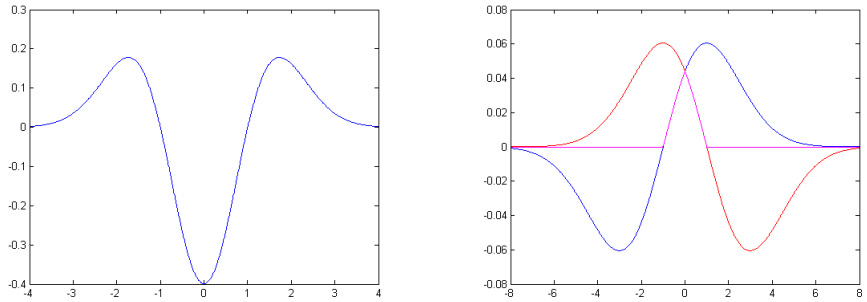

(a) (b)

Figure 5.1: (a) Second-order Gaussian derivative for $\sigma = 1.0$ (b) Shifted first-order Gaussian derivatives (red and blue) and response of Koller line filter (magenta).

the direction of the line. This can be done, for example, by using directional filter banks measuring the response in several directions [72]. However, applying non-linear combinations of finite difference operators in a set of orientations is computationally expensive, specially when we are dealing with 3D detection of line-like (tube-like) structures.

5.2.1.1 The Hessian Matrix for Vessel Detection

As an alternative to directional filter banks, the Hessian matrix was first used by Koller *et al.* [84] to estimate the local direction of the vessel, as an extension of their non-linear detector for 2D and 3D. They used the Hessian matrix to directly find the optimal orientation in which to apply their non-linear filtering scheme, corresponding to the eigenvector associated to the smallest eigenvalue.

The eigenvalue analysis of the Hessian matrix for vessel detection and direction estimation was first introduced in [109]. When the point x is close to the centerline or medial axis of a vessel and an appropriate scaling parameter is chosen, the local structure of the image is that of a bright (or dark) tubular structure, and the eigenvalues exhibit the following properties [54, 156]:

$$\lambda_2 \approx \lambda_3 \tag{5.1}$$

$$\lambda_2, \lambda_3 \ll 0 \tag{5.2}$$

$$\lambda_1 \approx 0 \tag{5.3}$$

This assumes that the local curvature of the vessel is not too high and that the section shows radial symmetry. If these conditions are not met, the eigenvalues differ from this ideal situation.

When the above conditions are met, the eigenvectors will align with the line (tube) direction. The eigenvector v_1 corresponds to the direction of the local vessel/tube axis

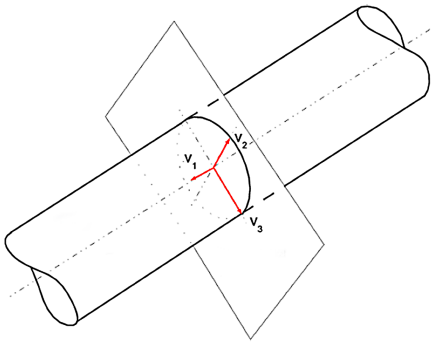

Figure 5.2: Ideal 3D line structure and corresponding eigenvectors defining the section plane.

where the curvature barely varies, hence λ_1 is almost zero. The other two principal curvatures, λ_2 and λ_3, occur in directions that go from the center of the tube to the external part of the vessel, where the curvature varies highly. Hence these eigenvalues are negative and of high absolute value (positive for a dark vessel in a bright background). The associated eigenvectors v_2, v_3 are estimators of the local vessel section plane, since they are aligned with the directions of maximum curvature. Thus, they constitute what we define as a *section estimator*, which computes an estimate of the normal plane to the line structure (see Figure 5.2).

The Hessian matrix can be thought of as an extension to N-dimensions of the second derivative. The main curvature, corresponding to the most negative eigenvalue λ_3, would represent the maximum image curvature in the estimated vessel cross-section, assuming that the current point is on the vessel centerline. For 3D images, the ratio of the two most negative eigenvalues represent the anisotropy of the profile. For ideal circular vessel cross-sections the ratio λ_2/λ_3 of these eigenvalues should be exactly one.

To sum up, in the context of line detection, the eigenvalue analysis of the scale-space Hessian matrix, allows us, to:

- Estimate whether a point has locally the structure of a line at the chosen scale.
- Obtain a measure of vesselness through the eigenvalues.
- Estimate the plane of the vessel cross-section and its symmetry.

5.2.1.2 Ridge Detection

An alternative to this approach is to consider the centerlines of the vessel structures as intensity ridges at the appropiate scale. Aylward *et al.* [11] obtain the centerlines of vessels by traversal of intensity ridges. For a point to be part of a ridge at a given scale they test the following conditions :

- N-1 eigenvalues must be negative. For 3D images

$$\lambda_3 \leq \lambda_2 < 0 \tag{5.4}$$

- The point must be on a (N-1) dimensional extreme, and thus, the projection of the gradient onto to the N-1 directions must be zero. For 3D images:

$$\begin{array}{l} v_2 \cdot \nabla L(x;t) \simeq 0 \\ v_3 \cdot \nabla L(x;t) \simeq 0 \end{array} \tag{5.5}$$

- In order to ensure that the tubular structure has nearly cross-section the ratio of the two most negative eigenvalues must be one within some tolerance:

$$\lambda_2/\lambda_3 \geq 1 - \in \tag{5.6}$$

where the eigenvalues of the Hessian matrix are ordered according to[4] $\lambda_3 \leq \lambda_2 \leq \lambda_1$ and v_i are the corresponding eigenvectors.

5.2.2 Features based on Hessian Matrix Eigenvalues

Several detectors or filters may be designed using these second-order local structure properties of the Hessian matrix. One approach is to take non-linear combination of the eigenvalues, trying to distinguish tube-like local structures from other shapes, such as plate-like or blob-like structures, which exhibit different relationships between the eigenvalues (see Chapter 4). For example, for plate-like structures two eigenvalues are similar to zero, and blob-like structures show three eigenvalues of the same relatively large value [54]. The filters are designed to enhance even the smallest vessels and remove the effects of non-linear structures and noise.

Lorenz *et al*. proposed a filter based on a simple combination of eigenvalues, ordered as $|\lambda_3| \leq |\lambda_2| \leq |\lambda_1|$, corresponding to the equation[5]:

$$\mu = \frac{|\lambda_2| + |\lambda_3|}{2\,|\lambda_1|} \tag{5.7}$$

The problem is that this filter could also give high responses to plate-like structures where $|\lambda_3| \gg 0$ and $|\lambda_2| \simeq 0$. Sato *et al*. [155] proposed a filter based on a non-linear combination of eigenvalues, ordered as $\lambda_3 \leq \lambda_2 \leq \lambda_1$, which consists of two terms:

$$\lambda_{23} = \begin{cases} |\lambda_3| \left(\frac{\lambda_2}{\lambda_3}\right)^{\gamma_{23}} & \lambda_2 < 0 \quad \text{and} \quad \lambda_3 < 0 \\ 0 & \text{otherwise} \end{cases} \tag{5.8}$$

[4]Note that, in some of the methods exposed in this chapter the eigenvalues are ordered by their value and in others by their absolute and sometimes in the literature the roles of λ_1 and λ_3 are inverted. We always refer to λ_3 as the most negative eigenvalue and to λ_1 to the eigenvalue in the direction of the line structure.

[5]For consistency with other filters we use λ_1 for the eigenvalue in the vessel direction. Moreover we remove the scale-space normalization, assuming that derivatives are normalized when the eigenvalues are calculated.

$$\lambda_{12} = \begin{cases} \left(1 + \frac{\lambda_1}{|\lambda_2|}\right)^{\gamma_{12}} & \lambda_1 \leq 0 \\ \left(1 - \alpha \frac{\lambda_1}{|\lambda_2|}\right) & \frac{|\lambda_2|}{\alpha} > \lambda_1 > 0 \\ 0 & \text{otherwise} \end{cases} \tag{5.9}$$

The term λ_{23} corresponds to the conditions 5.1 and 5.2 enhancing structures with two large negative eigenvalues of similar magnitude. This distinguishes line-like from sheet-like structures, since for the later $\lambda_3 \ll 0$ but $\lambda_2 \approx 0$. The parameter γ_{23} controls the cross-section anisotropy. Note that due to the ordering of eigenvalues $\lambda_2/\lambda_3 < 0$. If strong sheet-like structures are expected $\gamma_{23} = 1$ is a good choice. More assymetrical values are more tolerated when γ_{23} is closer to zero, for example γ_{23} =0.5 allows some degree of anisotropy. $\gamma_{23} = 0$ is a limit case where sheet-like structures would also be enhanced.

The term λ_{12} is introduced in order to accomplish the condition 5.3 and the condition $\lambda_2 \ll 0$ in 5.2. This distinguishes line-like from blob-like structures with the parameter γ_{12}.

Combining both conditions, the following single-scale filter response is obtained:

$$\lambda_{123} = \begin{cases} |\lambda_3| \left(\frac{\lambda_2}{\lambda_3}\right)^{\gamma_{23}} \left(1 + \frac{\lambda_1}{|\lambda_2|}\right)^{\gamma_{12}} & \lambda_1 \leq 0,\ \lambda_2 < 0,\ \lambda_3 < 0 \\ |\lambda_3| \left(\frac{\lambda_2}{\lambda_3}\right)^{\gamma_{23}} \left(1 - \alpha \frac{\lambda_1}{|\lambda_2|}\right)^{\gamma_{12}} & \frac{|\lambda_2|}{\alpha} > \lambda_1 > 0,\ \lambda_2 < 0,\ \lambda_3 < 0,\ 0 \leq \alpha \leq 1 \\ 0 & \text{otherwise} \end{cases} \tag{5.10}$$

Experiments performed on ideal curved tubes show that this filter gives high response at lower slopes of the profiles in the opposite side of the center of curvature with the curvature κ increasing. The introduction of the α provides an asymmetrical response depending on the sign of λ_1 which helps to mitigate this effect. However, selecting $\alpha = 0$ results in some lines broken, so $\alpha = 0.25$ is shown to be a good compromise. On the other hand, in experiments with branch models, the authors show that, at bifurcation or branch points, there is a trade-off between obtaining spurious branches in the response (reduce γ_{12} and increase α) and fragmentation of the line, due to a different eigenvalue becoming dominant at the edge of the line. Moreover, spurious holes may appear on the branch point. Finally, single-scale filter responses are combined in order to obtain a multi-scale filter response.

Almost simultaneously, Frangi *et al.* [53] proposed a similar non-linear filter. They ordered the eigenvalues according to their magnitude $|\lambda_3| \leq |\lambda_2| \leq |\lambda_1|$ and interpreted geometrically as describing a second-order ellipsoid. They proposed the following single-scale vesselness measure:

$$\mathcal{V}_0(s) = \begin{cases} 0 & \text{if } \lambda_2 > 0 \text{ or } \lambda_3 > 0 \\ \left(1 - e^{\left(-\frac{R_A^2}{2\alpha^2}\right)}\right) e^{\left(-\frac{R_B^2}{2\beta^2}\right)} \left(1 - e^{\left(-\frac{S^2}{2c^2}\right)}\right) & \text{otherwise} \end{cases} \tag{5.11}$$

with

$$R_A = \frac{|\lambda_2|}{|\lambda_3|} \quad R_B = \frac{|\lambda_1|}{\sqrt{|\lambda_2 \lambda_3|}} \quad S = \|H\|_F = \sqrt{\sum_{j \leq D} \lambda_j^2} \tag{5.12}$$

Here R_A is interpreted as the largest cross-section area of the ellipsoid (normal to v_1) and similarly to λ_{23} in the approach of *Sato el al*. distinguishes between tube-like and sheet-like structures. On the other hand R_B represents the volume divided by the largest cross-section area of the ellipsoid and accounts for the deviation from a blob-like structure as in λ_{12} in the approach of Sato *et al*. Moreover, the Frobenius norm S of the Hessian matrix is incorporated, in order to distinguish real tubular structures from background noise. The parameters α, β, c control the sensitivity of each term. The authors use $\alpha = \beta = 0.5$ in their experiments, whereas c is used as a threshold that depends on the gray-scale range of the image. A multi-scale line measure is obtained by computing the maximum value over a range of discrete user-selected scales, assuming derivatives are normalized across-scale.

Another similar vesselness feature is the one proposed by Erdt *et al*. [47]. They devised a filter based on a linear combination of the Hessian matrix components in the form:

$$\mathscr{V}(x) = \sum_{i=1}^{3} \sum_{j=1}^{i} \alpha_{ij} h_{ij} \tag{5.13}$$

By optimization via Lagrange multipliers of the convolution of a filter in this form, with an ideal model with Gaussian cross-section they conclude that the best response is obtained for a filter with the form:

$$\mathscr{V}(x) = c \left(\frac{2}{3} h_{xx} - h_{yy} - h_{zz} \right) \tag{5.14}$$

where

$$c = \sqrt{\frac{3\sigma_0}{5\pi^{3/2}}} \tag{5.15}$$

and σ_0 is the standard deviation of the Gaussian section of the tube. Generalizing to an arbitrary vascular direction by using the Hessian eigenvalues they obtain:

$$\mathscr{V}(x) = c\kappa \left(\frac{2}{3} \lambda_1 - \lambda_2 - \lambda_3 \right) \tag{5.16}$$

with $\lambda_1 \geq \lambda_2 \geq \lambda_3$. The factor κ is incorporated in order to distinguish tube-like from sheet-like structures by penalizing anisotropy in the smallest (most negative) eigenvalues:

$$\kappa = 1 - \frac{||\lambda_2| - |\lambda_3||}{|\lambda_2| + |\lambda_3|} \quad \in [0,1] \tag{5.17}$$

This factor takes a maximum value of 1 when $\lambda_2 = \lambda_3$. However, note that this factor also would give a value of 1 for $\lambda_2 = -\lambda_3$ and hence we propose the modified factor:

$$\kappa_{mod} = 1 - \frac{|\lambda_2 - \lambda_3|}{|\lambda_2| + |\lambda_3|} \quad \in [0,1] \tag{5.18}$$

Note that this method is parameter-less, as compared with the previous ones.

Krissian *et al*. [87] demonstrated that eigenvalues are sensitive to the vessel curvature and elliptical cross-sections. The sensitivity to vessel curvature is corroborated by our own study on the toroid and helix ideal models in Appendix A. However, the estimation of the cross-section plane by means of the eigenvalues is more stable. In Appendix A we can see that, under constant curvature (toroid model), the eigenvectors remain the same as in the ideal cylinder. In the helix model, however, the estimation of two of the eigenvectors is affected by curvature and torsion.

Another problem found with this family of central medialness detectors is that the support of the derivative kernels at the best detection scales (usually similar to the vessel size) extends beyond the limits of the vessel structures, thus averaging information that may be affected by external spurious structures as it is demonstrated in [91].

5.3 Offset Medialness Features

Offset medialness features are based mostly on integral approaches where information is accumulated along the vessel boundaries. Usually this information is obtained from the image gradient vector field. We include in this group flux-based features, since they are derived from the image gradient vector field on the boundaries. In general, these approaches uses small scales for the gradient [91]. The reason is that, in this case, the scale of the derivatives for the gradient calculations should be chosen according to the expected vessel boundary width. This boundary width is smaller than the total vessel width, usually with a transition due to partial volumen effects, as modeled in the convolved-bar section profile (see Appendix A).

5.3.1 Krissian Offset Medialness

The *offset medialness* of Krissian *et al*.[6] [87] is an integral measure defined in the section plane as:

$$\mathscr{M}_\sigma^+(x;r) = \frac{1}{2\pi}\int_{\alpha=0}^{2\pi} -\nabla I_\sigma\left(x + r v_{\alpha_i}\right)\cdot v_{\alpha_i} d\alpha \tag{5.19}$$

where v_α is a rotating vector, or phasor given by:

[6] From now on we will refer to this feature when talking about offset medialness.

$$v_\alpha = v_3 \cos\alpha + v_2 \sin\alpha \tag{5.20}$$

Equation 5.19 is the integral of the projection of the negate of the gradient vector in the radial direction of a circle of radius r around the considered point. This circle is located in the estimated section plane formed by the eigenvectors v_2 and v_3 of the local Hessian matrix $\mathscr{H}(x;\sigma)$. In fact, any other section estimator could be used. As we can see, by tuning r we have an estimate of the local vessel radius.

The corresponding discrete implementation samples the circle points in which the gradient is calculated and corresponds to:

$$\mathscr{M}_\sigma(x;r) = \frac{1}{N}\sum_{i=0}^{N-1} -\nabla I_\sigma\left(x + r v_{\alpha_i}\right)\cdot v_{\alpha_i}, \qquad \alpha = 2\pi i/N \tag{5.21}$$

Figure 5.3 depicts the calculation of Krissian offset medialness. An optimal situation is shown in Figure 5.3 (a) where the current point x is on the centerline. If the scale is adequate for detecting the tube (here the tube and circle radius coincide) the gradient will be high, since the offset points will be at the tube boundaries and the gradient will be aligned with the local normal of the offset point. It results in an optimal value of medialness. Figure 5.3 (b) shows a situation where the point x is not on the centerline. In this case, the section estimation is not good, sometimes does not even make sense since we may not be close to a vessel, and most of the points are not on the tube boundaries yielding small values for the offset gradients. Moreover, the gradients and corresponding circle normals will not be aligned. The result is a low value of medialness. Such points can be prefiltered, for example by eigenvalue analysis of the Hessian matrix using a relaxed form of the conditions 5.1 to 5.3.

Pock *et al*. [146, 176] modified this medialness measure by introducing some variations for better centerline detection and increased robustness. They follow the notation in [201] which defines the *boundariness* space as[7]

$$B(x) = \nabla I_\sigma(x) = I(x) * \nabla G(x;\sigma) \tag{5.22}$$

with

$$b(x) = \|B(x)\| \tag{5.23}$$

and

$$n(x) = \frac{B(x)}{\|B(x)\|} \tag{5.24}$$

the magnitude and direction of the boundariness space respectively. Their initial offset medialness measure is defined as:

[7] In the following, we omit the scale-spaca derivative normalization factors σ^γ

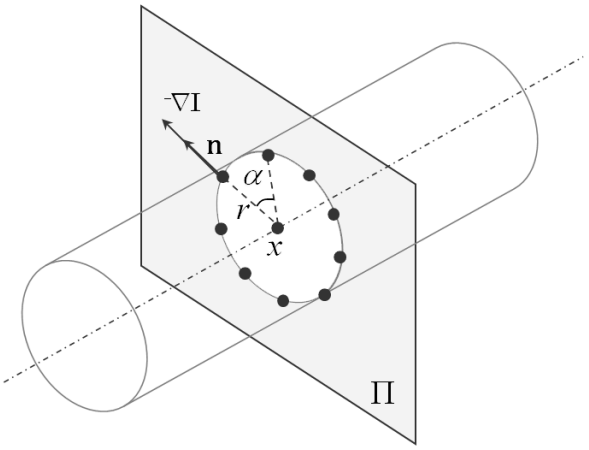

(a)

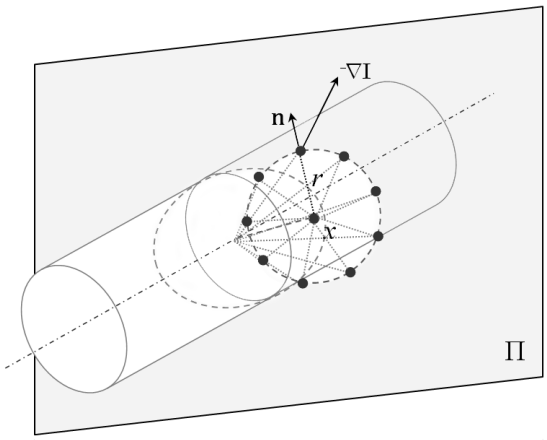

(b)

Figure 5.3: Discrete Krissian medialness calculation. (a) Point x on centerline with correct section and scale. (b) Point x not on centerline with incorrect section estimation. Here the estimated section is misaligned with respect to the vessel.

$$\mathscr{M}_{\sigma 0}(x;r) = \frac{1}{N}\sum_{i=0}^{N-1} b\left(x + r v_{\alpha_i}\right) \cdot c_i^n \qquad \alpha = 2\pi i/N \tag{5.25}$$

where

$$c_i = \begin{cases} -n\left(x + r v_{\alpha_i}\right) \cdot v_{\alpha_i} & if \ -n\left(x + r v_{\alpha_i}\right) \cdot v_{\alpha_i} > 0 \\ 0 & otherwise \end{cases} \tag{5.26}$$

The constant n is called circularity parameter which they set to $n = 2$.

In [176] Pock *et al.* introduce the following symmetry coefficient:

$$\omega(b_i) = \exp\left[-\frac{1}{2\xi^2}\left(1 - \frac{b_i}{\mathscr{M}^+_{\sigma 0}}\right)^2\right], \quad \xi \in (0,1] \subset \mathbb{R} \tag{5.27}$$

where:

$$b_i = -\nabla I_\sigma\left(x + r v_{\alpha_i}\right) \cdot v_{\alpha_i} \tag{5.28}$$

is the contribution of each radial point. The resulting adaptive medialness function is:

$$\mathscr{M}_\sigma(x;r) = \frac{1}{N}\sum_{i=0}^{N-1} \omega(b_i)\, b_i \tag{5.29}$$

The symmetry coefficient ξ penalizes asymmetry in the radial distribution of gradient values. When $\xi = 1$ no penalization is performed. The lower the value the more the asymmetry is penalized. There is a trade-off between the asymmetry of the section and the detection rate. If very asymmetrical sections are expected, the value should be one or close to one. Otherwise, $\xi = 0.5$ gives good results in most situations. We also divide the resulting medialness by one plus the gradient magnitude at the center point, since it should be low in a centerline point. This last step was also used by Pock *et al.* in [176] but they subtracted this value instead of dividing it.

Another variation of the symmetry concept was described by the same authors in [146][8]. Here, the variance of the boundariness samples is defined as:

$$s^2(x;r) = \frac{1}{N}\sum_{i=0}^{N-1}\left(b_i - \bar{b}\right)^2 \tag{5.30}$$

where $\bar{b}$ is the mean boundariness of all radial samples. A symmetry coefficient is thus obtained as:

$$S(x;r) = 1 - \frac{s^2(x;r)}{\bar{b}^2} \tag{5.31}$$

[8] We found no additional information about which of these two symmetry coefficients is more adequate.

which quantifies the homogeneity of the boundariness along the circle. The weighted response is then:

$$\mathscr{M}_{\sigma}(x;r) = \mathscr{M}_{\sigma 0}(x;r) \cdot S(x;r) \tag{5.32}$$

The original implementation of Krissian *et al*. makes the radius r dependent on the scale in the form $r = \tau\sigma$. In practice, it is not necessary to change r linearly with the scale. Additionally, with large diameters, we would need large scales with increased computational costs. A better approach is to choose a single or a few scales valid enough for the range of diameters to be considered and then adjust r to obtain a maximum response.

5.3.2 Optimally Oriented Flux

A major criticism for features based on second derivatives, such as those described in 5.2.2, is that it computes the difference between the intensities outside and inside the object. In a kernel-based implementation, this means the kernel support extends beyond the limits of the structures. Furthermore, a criticism for standard flux-based features is that they do not take into account directionality. In order to overcome this problem, the concept of Optimally Oriented Flux (OOF) is presented in [91].

The OOF first calculates the flux of projected gradient that enters or leaves a sphere surface around the current point. The gradient is projected along a specific direction becoming an oriented flux. The OOF tries to find the optimal projection direction that minimizes this oriented flux. If the current point is in the center of a vessel, this direction will correspond to the vessel axis direction. The radius of the sphere acts as an scale parameter, which allows adapting the detector to different vessel sizes in a multi-scale fashion.

Given a sphere S_r with radius r and a projection direction v the oriented flux can be calculated as the sum:

$$\mathscr{F}(x;r,v) = \int_{\partial S_r} (\nabla I(x+rn) \cdot v)\, v \cdot n \, dA \tag{5.33}$$

where n is the normal to the surface on the infinitesimal surface area dA. The authors show that this expression can be converted into a quadratic form as follows:

$$\mathscr{F}(x;r,v) = \int_{\partial S_r} \left\{ \sum_{k=1}^{3} \sum_{l=1}^{3} (\nabla I_k(x+rn) \cdot v_k \cdot v_l \cdot n_l) \right\} dA = v^T Q_{r,x} v \tag{5.34}$$

where the component (i, j) of the matrix $Q_{r,x}$ is calculated as the integral

$$q_{r,x}^{i,j} = \int \nabla I_i(x+rn) \cdot n_j dA \tag{5.35}$$

which does not depend on the projection direction v but solely on the gradient image values and the sphere geometry. We will call the matrix $Q_{r,x}$ the *oriented flux matrix*, since it allows us to calculate the oriented flux along a given projection direction v.

Figure 5.4 depicts the oriented flux calculation. A sphere is created centered at the point P whose medialness value is calculated. For every point M with normal n on the sphere surface, the image gradient is calculated and projected along the direction v and then, the flux of this projected vector across the surface is obtained. The total flux is obtained as the sum (integral) for all sphere surface points. The flux is minimized if v corresponds to the vessel axis direction and P is on the vessel centerline. Figure 5.4 (a) shows the calculation when P is not on the centerline. The image gradient point towards the center of the tube and is not aligned with the sphere normal. The projection of the gradient on v is then projected on n to calculate the flux and is not close to zero. In Figure 5.4 (b) P is on the centerline and the gradient is almost aligned with n and normal to v. This results on a flux across the sphere surface that is almost zero and thus, it is optimally oriented.

Obtaining the direction v which minimizes eq. 5.33 can be considered as a generalized eigenvalue problem on the matrix Q. The analysis obtains a set of ordered eigenvalues $\lambda_i(x;r)$, $\lambda_3 \leq \lambda_2 \leq \lambda_1$ [9] with their corresponding eigenvectors $v_{\lambda(i)}$.

A parallelism is found with the Hessian matrix features in 5.2.2. For a point x in the interior of a tubular structure brighter than the background the eigenvalues follow the relations described in eqs. 5.1 to 5.3. The eigenvectors $v_{\lambda_2}, v_{\lambda_3}$ corresponding to the most negative eigenvalues estimate the cross-section plane of the tube and the eigenvector v_{λ_1} estimates the optimal orientation that minimizes flux, which corresponds to the tube axis.

Once the eigenvalues and eigenvectors are estimated, several vesselness metrics may be devised, following again a parallelism with the features based on the Hessian matrix. The authors use the geometric mean of the two most negative eigenvalues:

$$\mathscr{M}(x;r) = \begin{cases} \sqrt{\lambda_2 \cdot \lambda_3} & \lambda_3 \leq \lambda_2 < 0 \\ 0 & \text{otherwise} \end{cases} \tag{5.36}$$

However, any other features based on eigenvalues, described in 5.2.2, could be used, with their calculation based on the oriented flux matrix instead of the Hessian matrix. Moreover, the estimation of the section plane and normal of the tube, allows to use any other feature that may be computed on the plane, such as the Krissian medialness in 5.3.1. In this case, we are replacing the estimation of the section plane, by another estimation based on oriented flux.

[9] Note that, to be consistent with previous analysis, we named the eigenvalues differently from [91]

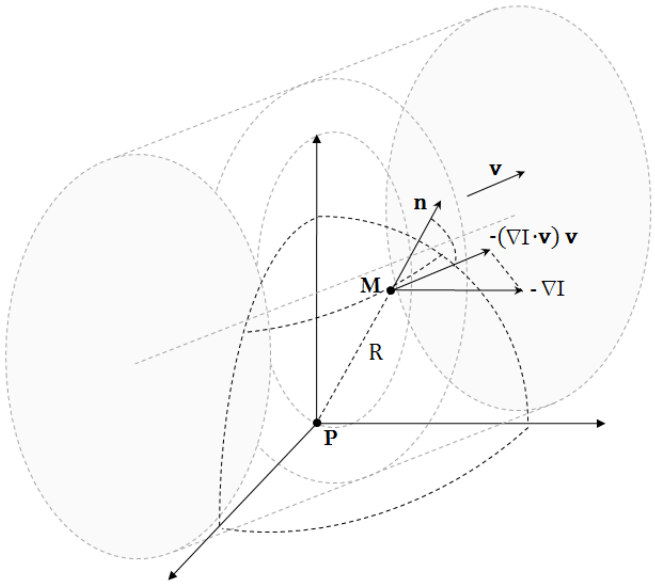

(a)

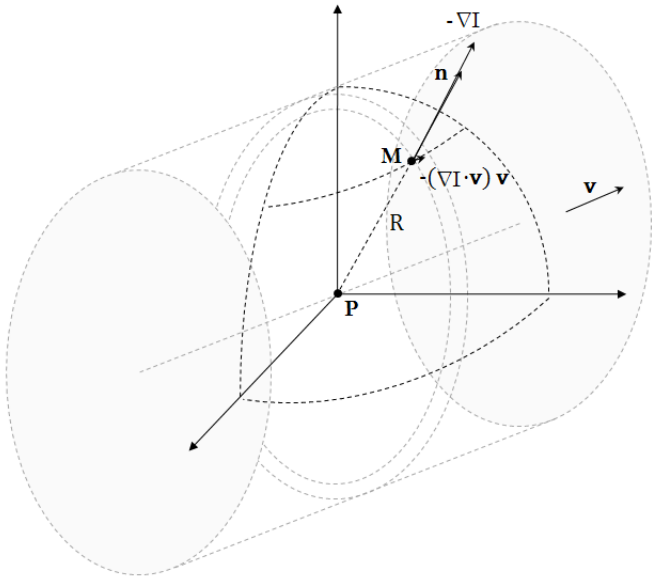

(b)

Figure 5.4: Details of oriented flux calculation with sphere not centered (a) and centered (b) on vessel centerline.

5.3.3 M-Flux

Flux-based approaches are based on the computation of the flux of an image-derived vector field, usually the gradient vector field, through the surface of the extracted object. This gradient flux is maximized when the surface is aligned with the gradient vector field. It has been demonstrated [183] to be well adapted for the extraction of thin, low-contrasted vessels.

Lesage *et al*. [96] propose computing this flux in circular cross-sections considered as surface patches. For vessels with slowly varying radius, the radial directions from the cross-section centers are a good approximation to the vessel surface normal. By local discretization of the circular cross-section into N points x_{ri}, for a center point x the *Flux* is measured as:

$$\Phi(x,r) = \sum_{i=1}^{N} \nabla I(x_{ri}) \cdot u_i \tag{5.37}$$

where

$$u_i = \frac{x - x_{ri}}{|x - x_{ri}|}$$

are the unit vectors in the radial directions from the center point.

Similarly to Krissian medialness, this flux yields high values when x is part of the centerline of the vessel and for an appropriate values of the radius scaling parameter r.

However, this flux may obtain high responses for step edges by asymmetric contributions along the cross-section contour. Following the idea on [85] the authors introduce a symmetry constraint. They pair opposite points (x_{ri}, x_{ri}^{π}) of the contour (assuming N is even) and take the minimum contribution per pair in order to obtain a new measure called *M-Flux*:

$$\Phi_M(x,r) = \frac{2}{N} \sum_{i=1}^{N/2} \min\left(\nabla I(x_{ri}) \cdot u_i, \nabla I(x^{\pi}{}_{ri}) \cdot u^{\pi}{}_i\right) \tag{5.38}$$

The authors use scale-independent regularization for the gradient vector as in the Optimally Oriented Flux (see section 5.3.2), where a Gaussian smoothing with small aperture is used for the gradient calculations. This is consistent with small scales used for boundary detection in offset medialness detectors.

Flux and *M-Flux* are increasingly discriminative relative to the vessel size, as compared with Frangi vesselness [54] whose behaviour is scale-independent. Compared with central medialness, the response is almost symmetric around the optimal vessel size, dropping faster for larger vessels. Values are higher at the centerlines, with better responses for small vessels and branching points. As compared with the Optimally Oriented Flux, it requires testing for different orientations or a prior estimate of the vessel direction, being faster for tracking approaches but is not well adapted for analyzing complete volumes [96].

5.4 Scale Considerations

5.4.1 Scaling Parameters for Single-scale Responses

One problem we have found with some popular medialness functions is that some of their parameters represent scales for different entities and sometimes are chosen depending on a single geometrical property, usually the radius. However, certain scaling parameters should be chosen according to other magnitudes, for example the vessel boundary width. For example, in the original Krissian medialness function (see section 5.3.1), the scale for the Hessian, the radius r and the gradient calculations are dependent on a single scale σ which is selected according to the vessel diameter.

However, in our opinion, the gradient should be chosen according to the expected vessel boundary, which is smaller, since in this case it is the observable feature to be detected. In the case of the vesselness measures derived from the Optimally Oriented Flux (see section 5.3.2) the authors mention this fact implicitly by selecting a fixed small scale for the sphere boundary flux calculations. The same idea is used in M-Flux for computing gradients at small scales.

Comparing central and medialness functions, central medialness functions follow principles of Gaussian linear scale-space theory and use detection scales proportional to the expected vessel radius. This induces a trade-off between detection and accuracy. For medium or large vessels this means that:

- Vessels that differ from the ideal circular cross-section may be detected.
- Vessels at a broader range of scales may be detected, usually obtaining an asymetric response with slower response decays for vessel sizes larger than the optimal. The scale becomes a poor estimate of the vessel size[10].
- Since the scale is proportional to the vessel size, larger kernels are required for convolutions which is computationally expensive.
- High noise levels are tolerated.

On the other hand, offset medialness functions tend to use fixed small aperture values for regularization of the gradient field. This involves:

- More accuracy and discriminative power for the target vessel size, which implies symmetric responses that decay faster for larger vessel radius values [96].
- Faster calculations since kernels are smaller.
- Lower detection rate, specially for medium or large vessel sizes that may require a large number of discrete scales.
- Less robustness to noise and less tolerance to non-circular cross-sections.

[10] Assuming the filter is scale-normalized with respect to the vessel size.

In our work, we classify the different scales according to the geometrical feature they represent and try to establish a relationship between the scales so as to reduce the number of scale-spaces involved. With respect to regularization of the gradient boundary calculations, we tend to use smaller scales for boundary detection in offset medialness, but, for medium or larger vessels, we allow for moderate increments in the scale in order to increase the detection rate while mantaining a considerable degree of accuracy. This is supported from the experimental evidence developed in section 5.5 where we derive relationship between the different scale-spaces involved in some of the most popular medialness filters.

5.4.2 Scale Integration of Filter Responses

Multi-scale analysis is essential in vascular image processing, since vascular trees consist of branches of varying size. Even along the same branch, the vessel diameter may vary. In order to obtain a multi-scale response from the vesselness functions it is necessary to:

1. Select the range of scales for the application.
2. Normalize the single-scale responses for consistent integration.
3. Select a criterion for scale integration.

5.4.2.1 Selection of Range of Scales

Even if the scale parameter is continuous in nature, in practice it is impossible to obtain a response for all possible scales and a discrete range of scales must be selected. Decissions on the number, range and separation of scales must be made and a compromise must be found here. On one hand, the larger the number of scales the more computational resources will be required. On the other hand, if scales are too separated, the response obtained for vessels whose size lies in-between computed scales may be low, negatively influencing the overall result. Sato *et al*. [156] implement some criteria for their vesselness measure following this criteria.

5.4.2.2 Single-scale Response Normalization

Normalization of single-scale responses is necessary to integrate the information from multiple scales in a consistent and meaningful way. If no vessel size is preferred, then the maximum response of the vesselness filter accross scales obtained for different vessel diameters should be the same.

5.4.2.3 Criterion for Scale Integration

The most common criterion for scale integration is to select the scale that gives maximum vesselness response at a given point [106]. If the single-scale response of a given vesselness function is $R(x;\sigma_i)$ then the multi-scale response computed for N discrete scales is found as:

$$R(x) = \max_{\sigma} R(x;\sigma_i) \qquad i = 1 \ldots N \tag{5.39}$$

Most of the approaches use this simple criterion for scale integration. Figures 5.5(a)-(d) show the single-scale responses. The corresponding multi-scale response shown in Figure 5.5 (e) is obtained by computing the Krissian medialness for an MRI image of a pre-segmented liver parenchyma at four discrete scales following this criterion. Note how the larger vessel appear only at the larger scales, whereas the thinner vessels are dimmed or not shown at these scales. The multi-scale response is able to depict most vessels of different sizes.

Recently Dreschler *et al*. proposed an alternative to the maximum response criterion called *weighted additive response*. Instead of selecting the maximum across discrete scales, they propose sum the contribution of all discrete scales with a weighting factor:

$$R(x) = \sum_{i=1}^{N} \omega_{\sigma} R(x;\sigma_i) \tag{5.40}$$

The authors chose $\omega_{\sigma} = \sigma^{-\lambda}$ $(\lambda > 0)$[11] to give preference to small scales. For vesselness functions based on scale-space differential approaches, this weighting acts inversely as the γ-normalization of derivatives [106]. In fact, if $\lambda = \gamma$ no normalization at all would be performed. They demonstrate that this has the effect of enhancing small vessels and reducing the diffusion of nearby vessels that are often identified as a single vessel of larger size. On the other hand, larger vessels appear thinner in comparison with the maximum response approach but this is not a problem if the objective is to obtain a maximum response in the centerline.

5.5 Scale Selection Criteria

In the following, we isolate the individual scaling parameters of some popular vesselness filter described, and test their relationship and influence in the final response by a set of experiments on synthetic datasets. The objective is to determine useful scale selection criteria for these filters, in terms of number and separation of discrete scales, so as to detect the expected range of vessel sizes in a given practical application.

5.5.1 Features Based on Hessian Matrix Eigenvalues

The scale selection mechanism for the methods described above consists of choosing the maxima over scales of a combination of the discrete, second-order, Gaussian derivatives used in the Hessian matrix [106], where the scale is changed by varying the aperture of the Gaussian in the derivative calculations.

[11] This is the original notation used by the authors. It should not be confused with the eigenvalues of the Hessian matrix.

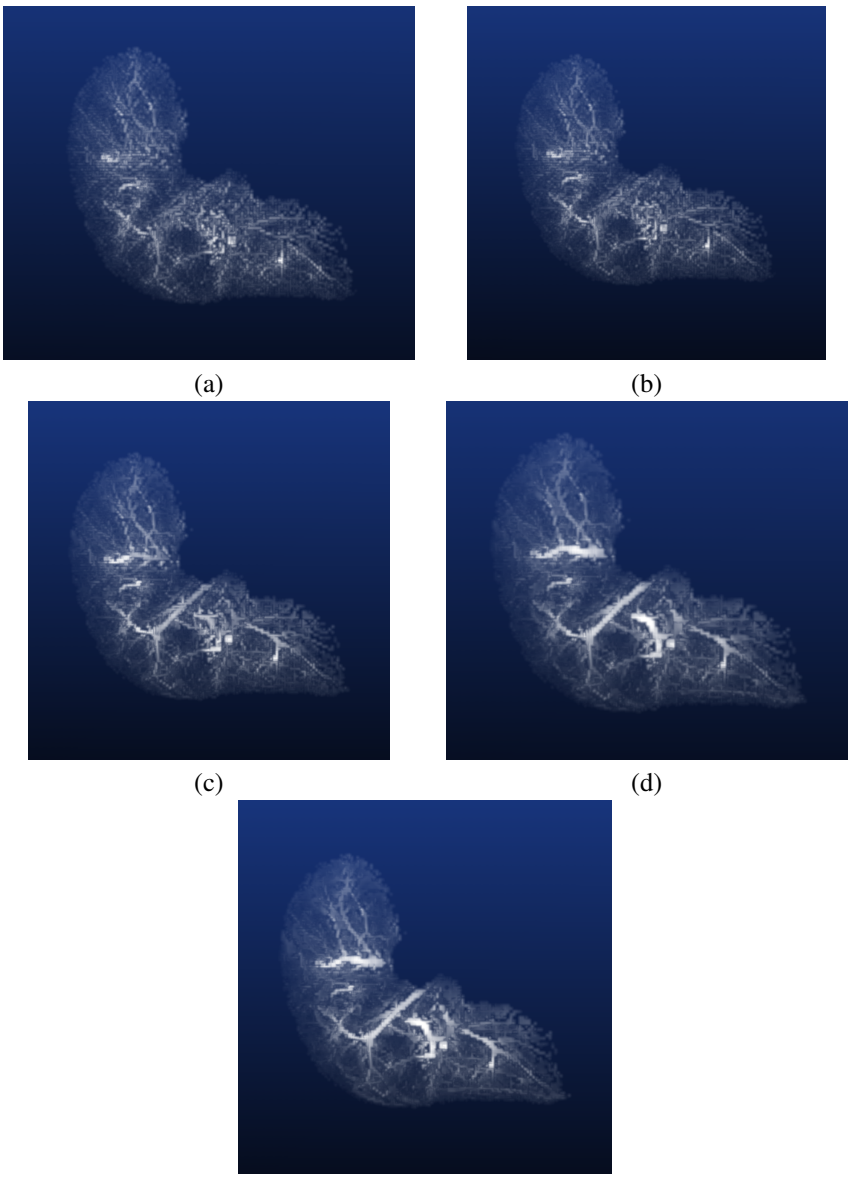

(a) (b) (c) (d) (e)

Figure 5.5: Multi-scale Krissian medialness response obtained for a MRI image of a pre-segmented liver parenchyma. (a)-(d) Single scale responses for σ =1,25, 1.75, 2.50, 4.0 (e) Multi-scale response with the maximum criterion.

One idea would be to test the methods separately against ideal tubes in order to see how they perform with different tube sizes and detection scales, but this is a very cumbersome analysis. However, scale selection criteria may be established on the basis of the interpretation of the eigenvalues of the Hessian matrix for the detection of tubular structures corresponding to conditions 5.1 to 5.3. These eigenvalues represent the principal curvatures which are second derivatives oriented in the local spatial orientation that best describes the shape. If we restrict our analysis to ideal circular tubes with radial symmetry, these curvatures will be oriented with the tube axis and the conditions described will hold almost exactly. Since in this case $\lambda_1 \simeq 0$ and $\lambda_2 \simeq \lambda_3 \ll 0$ it is sufficient to analyze the behavior of λ_3 to obtain criteria for scale selection. Moreover, if the ideal tube images are aligned with the z-axis, this eigenvalue will coincide with the second derivatives on the x or y-axis, which does not even require the calculation of the Hessian matrix for this analysis. However, in the following experiments we will calculate the eigenvalues in order to test the described ideal conditions.

Based on this idea, we performed experiments on radially symmetric ideal cylinders of different sizes whose axis is aligned with the image z-axis. We created two sets of cylinders (see Appendix A for corresponding shape models and cross-section profiles), one set with Gaussian cross-sections and another set with bar (flat) sections convolved with a Gaussian with a small value of aperture (we used $\sigma = 1.0$). The radii were chosen as:

$$R_i = s^i R_0 \quad i = 1 \ldots N_R \tag{5.41}$$

where $R_0$is the initial radius and s the scale factor and N_r is the number of cylinders. We chose $R_0 = 0.75$, $s = 1.225$ and $N_R = 10$.

For each cylinder, we calculated the Hessian matrix and corresponding eigenvalues in a discrete set of scales and observed the behaviour of the most negative eigenvalue λ_3. The set of discrete scales for the Gaussian derivatives of the Hessian matrix where chosen as:

$$\sigma_{hj} = s_h^j \sigma_{h0} \quad j = 1 \ldots N_h \tag{5.42}$$

where we used $\sigma_{h0} = 0.5$, $s_h = 1.025$, $N_h = 110$ for both types of cross-sections.

As expected, we observed a perfect match in the values of λ_2 and λ_3 whereas λ_1 was zero or practically zero (in the order of between -1.0×10^{-12} and -1.0×10^{-16}). Figure 5.6 (left) shows the plots of the values obtained for λ_3 for different scales for both tube profiles. A visible minimum is found for all tube sizes, where the peak tends to flatten for larger scales and is more prominent for small scales, specially for the tubes with Gaussian section. The minimum value for Gaussian tubes is almost equal (Figure 5.6 top row), since derivatives where normalized accross-scale. For smaller scales the minimum is larger in magnitude, possibly due to discretization effects since scales are close to the image resolution. In tubes with bar-convolved section profile (Figure 5.6 center row), we can see that the minimum is not normalized accross-scale, since derivatives where normalized for Gaussian tubes. This could be achieved by modifying the normalization factor γ of the derivatives (see Appendix A). In this case

(Figure 5.6 bottom row) the position of the minimum barely varies (see equations 5.5.1 and 5.5.1).

Figure 5.6 (right) shows the relationship between the maxima across scales for each tube size with respect to the tube size itself. An almost linear relationship is found between the scale and the radius ($R^2 = 0.998$ and $R^2 = 0.995$ for Gaussian and bar-convolved tubes respectively). For tubes with Gaussian section this relationship is:

$$\sigma_{hmax} = 0.973R + 0.117 \tag{5.43}$$

And for tubes with bar-convolved section (non-normalized and normalized respectively):

$$\sigma_{hmax} = 0.662R + 0.578 \tag{5.44}$$

$$\sigma_{hmax} = 0.671R + 0.545 \tag{5.45}$$

Compared to the ideal line $\sigma_h = R$ we can observe that for Gaussian tubes the best scale is slightly over the radius value. For bar-convolved tubes, however, the scale should be smaller than the radius for small scales and larger for large scales. From the formulas of the straight lines, the cross-point is found at $\sigma_h = R = 1.71$. For practical applications and in the context of vascular analysis, this may help us to select a correct range of scales knowing the possible range of vessel sizes present in our images.

The experiment also shows that scale-space normalization is not a trivial issue. In accordance with Lindeberg [106] we see that adequate normalization depends both on the combination of derivatives used and assumptions on the intensity profile of the structure to detect. Nevertheless, we were able to derive useful relationship between the scale and the radius of the tube to detect for Gaussian and bar-convolved tubes, and, in the second case, results where very similar before and after normalization.

5.5.2 Krissian Medialness

The calculation of the Krissian medialness measure requires the definition of at least three scales:

- The *Hessian scale* σ_h corresponds to the scale for the second order Gaussian derivatives of the Hessian matrix. It is used to estimate the section normal as the eigenvector corresponding to the lowest eigenvalue (close to zero) of the Hessian which, for points on the centerline, coincides with the tube axis. In Chapter 6 we analyze this estimation in detail in the context of vascular extraction using centerline tracking. The ideal scale for the Hessian should be proportional to the radius tube and usually a bit larger.
- The *radius scale* σ_r is the radius of the section circle where offset gradients are estimated. It is the most critical scale and should be approximately equal to the tube radius. Failing to choose the appropriate radius scale will result in a poor estimation or even missing the tube at all.

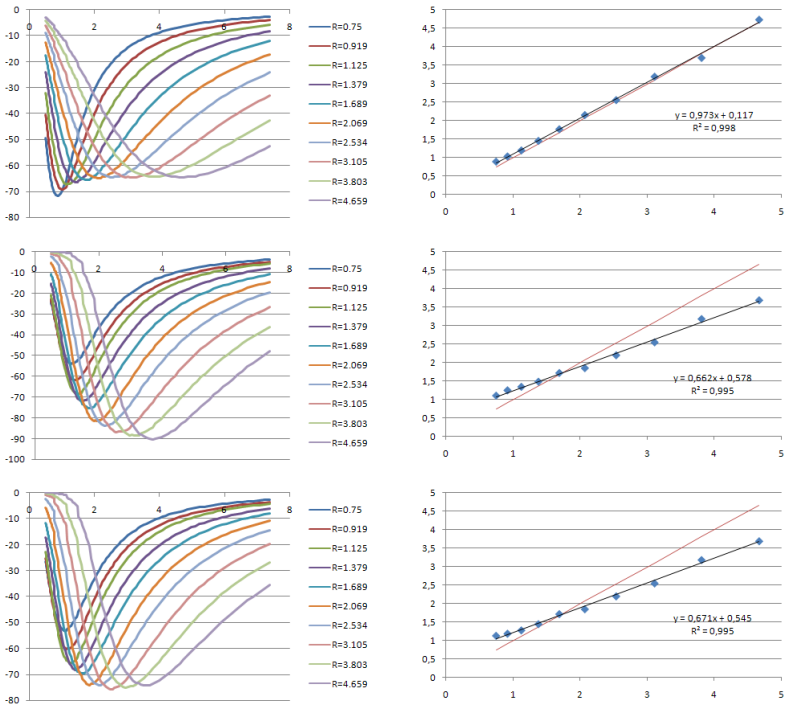

Figure 5.6: Values of the most negative eigenvalue λ_3 obtained in the center of the tube for different tube sizes for different Hessian scales σ_h and for tubes with Gaussian (top row) and bar-convolved (center row: non-normalized; bottom row: normalized) section profile. Left column shows all values obtained varying σ_h. Right column shows the relationship between the tube radius (x-axis) and radius scale for the maximum values obtained for each radius. Here, the black line shows the obtained linear trend line and the red line represents the line $\sigma_h = R$.

- The *gradient scale* σ_g is the scale at which offset gradients, also called *boundariness* [201], are calculated. It should be chosen according to the expected tube boundary width and thus should be smaller than σ_r. In general, for small and medium tube sizes, a small scale should be chosen, close to the inner scale of the image (resolution). However, for larger scales, increasing the gradient scale could improve the detection rate at the cost of a worse localization. This is specially important in multi-scale approaches when a small set of scales is used for detection.

In Krissian *et al*. the relationships $\sigma_g = \sigma_h$ and $\sigma_r = \tau\sigma_h$ where used, where the constant τ was calculated so as to maximize the response for a cylindrical model with Gaussian cross-section. In Pock *et al*. [146] an attempt was made of separating the Hessian and gradient scale spaces for the Krissian medialness detector. They used $\sigma_r = \sigma_h$ and established a more flexibe relationship:

$$\sigma_g = \sigma_h^{\eta} \tag{5.46}$$

where $\eta \in [0,1]$ depended on the image noise level. In contrast, we initially consider these scaling parameters independent, so as to establish a dependency only from experimental evidence.

In order to establish some criteria for scale selection, we performed some experiments on the same set of ideal cylinders described in section 5.5.1. Testing the influence of the three types of scales in all tube sizes involves a very large parameter space in which maxima of medialness have to be found. However, as expected, we noticed that results were independent of the Hessian scale value and hence it will remain fixed in the following. The reason is that this scale is only used for the estimation of the section in which offset gradient values are calculated and, for ideal noiseless tubes, the result is always the tube axis but for very small or very large scales.

The first set of experiments used a fixed Hessian and gradient scale values of $\sigma_h = 2.25$ and $\sigma_g = 1.0$ with σ_r varying according to:

$$\sigma_{rj} = s_r^j \sigma_{r0} \quad j = 1 \ldots N_r \tag{5.47}$$

where we used $\sigma_{r0} = 0.5$, $s_r = 1.005$, $N_r = 550$. The idea is to set a criteria for the selection of the radius scale using fixed small gradient scale values.

Figure 5.7 (left) shows the medialness values obtained for this experiment for both tubes with Gaussian and bar-convolved section profile. In all cases, there is a visible maximum for each tube size. This maximum is more prominent for small scales in the case of Gaussian tubes, but the plots tend to flatten for higher scales. The absolute values also reach a maximum for medium scales and tend to decrease. For bar-convolved tubes, the prominence of the peak is similar in all scales and the maximum seems to increase and stabilize for larger scales, obtaining in general a better localization. This is expected, since, in the Gaussian tubes, the tube boundaries are more diffuse. Moreover, an increase in the signal seems to reflect that there is less uncertainty in the radius location when the scale increases, as long as the correct scales are chosen (a wrong scale

selection may imply a lower detection rate). With small scales, the small smoothing of the boundary may be significant enough as compared to the tube radius to induce some uncertainty. Moreover, the peak seems to flatten with respect to the Gaussian tubes.

Figure 5.7 (right) shows the values of the gradient scale that resulted in maxima of medialness with respect to the tube size of that maxima. As we can see in the linear trend lines depicted in black, there is almost a perfect linear relationship ($R^2 = 0.993$ and $R^2 = 0.988$ for Gaussian and bar-convolved tubes respectively) between the gradient scale and the tube radius. For Gaussian tubes the relationship is approximately:

$$\sigma_{rmax} = 0.926R + 0.471 \tag{5.48}$$

and for bar-convolved tubes:

$$\sigma_{rmax} = 0.946R + 0.506 \tag{5.49}$$

We can see that the best values are obtained approximately for scales about 92-95% the tube radius plus 0.5 mm, which is a bit more than the expected 100% of the tube radius. From the plots we can also see that, even if the right scale is not chosen, there is still some margin for radius scale selection that provides reasonable medialness values. Tables 5.1 and 5.2 represent the range of radius scales between which the response decays less than 10% and 25%, for Gaussian and bar-convolved tubes respectively.

Table 5.3 shows corresponding averages and minimum values. We can see that there is some margin for error in the scale selection that still gives reasonable responses. The margin is narrower for bar-convolved tubes but these may represent better real vessels, specially for larger widths. Still, average errors of 37 and 45% are obtained. Note that these results are approximate, since they are calculated for the discrete set of tube sizes and scales used in our experiments. However, the radius scale discretization had enough resolution to give significant results for the chosen tube sizes. Similar analysis can be performed to set a criteria for discrete scale selection for a given application similar to that in [156].

Keeping the gradient scale fixed as in the previous experiment does not necessarily yield the best results. In order to test the influence of both, the radius and gradient scales, we computed the Krissian medialness value at the center of each cylinder i for a set of discrete scales, chosen as:

$$\begin{array}{ll} \sigma_{rj} = s_r^j \sigma_{r0} & j = 1 \ldots N_r \\ \sigma_{gj} = s_g^i \sigma_{g0} & j = 1 \ldots N_g \end{array} \tag{5.50}$$

A first set of experiments combining these scales used $\sigma_h = 2.25$, $\sigma_{r0} = 0.8R_i$, $s_r = 1.5$, $N_r = 11$, $\sigma_{g0} = 0.5$, $s_g = 1.25$, $N_g = 30$. Note that here, for every tube size, the first radius scale σ_{r0} depends on the tube size. For the gradients scale, the initial scale is fixed.

Figure 5.8 shows the Krissian medialness values obtained in the center of the Gaussian and bar-convolved tubes depending on the gradient scale values σ_g. Since the Hessian scale is not relevant, we fixed $\sigma_h = 2.25$. For each tube radius, we selected the radius scale σ_r that gave the best medialness value. The plots obtained are asymmetrical with respect to the peak values, meaning that is worse underestimating than

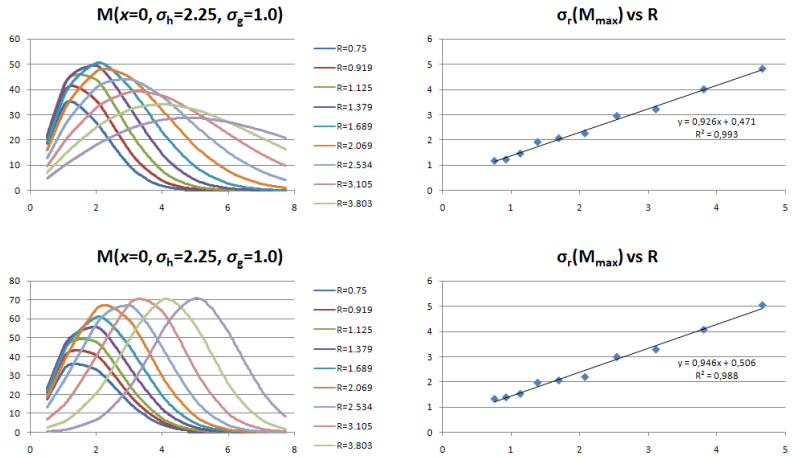

Figure 5.7: Krissian medialness values obtained in the center of the tube for different tube sizes with $\sigma_h = 2.25$ and $\sigma_g = 1.0$ and varying σ_r (x-axis), for tubes with Gaussian (top row) and bar-convolved (bottom row) section profile. Left column shows all values obtained varying σ_r. Right column shows the relationship between the tube radius (x-axis) and radius scale for the maximum values obtained for each radius.

$\mathscr{M}_{max}$		$\triangle\mathscr{M} = 10\%$				$\triangle\mathscr{M} = 25\%$			
R	σ_r	σ_{rmin}	σ_{rmax}	$\Delta\sigma_{rmin}$	$\Delta\sigma_{rmax}$	σ_{rmin}	σ_{rmax}	$\Delta\sigma_{rmin}$	$\Delta\sigma_{rmax}$
0.75	1.1791	0.9373	1.6063	20.50%	36.24%	0.7564	2.0105	35.85%	70.52%
0.919	1.2332	0.9610	1.8379	22.07%	49.03%	0.7794	2.2436	36.80%	81.94%
1.125	1.4684	1.0001	2.1667	31.89%	47.55%	0.8152	2.5038	44.49%	70.52%
1.379	1.9222	1.1500	2.3939	40.17%	24.54%	0.9007	2.7803	53.14%	44.64%
1.689	2.0716	1.4684	2.6451	29.12%	27.68%	1.0305	3.1653	50.25%	52.80%
2.069	2.2661	1.6801	3.1495	25.86%	38.98%	1.2149	3.6945	46.39%	63.03%
2.534	2.9518	1.9127	3.6945	35.20%	25.16%	1.4538	4.3555	50.75%	47.55%
3.105	3.2130	2.2889	4.3992	28.76%	36.92%	1.7311	5.1862	46.12%	61.41%
3.803	4.0015	2.7803	5.2907	30.52%	32.22%	2.0613	6.2063	48.49%	55.10%
4.659	4.8124	3.3272	6.3948	30.86%	32.88%	2.5038	7.5389	47.97%	56.66%

Table 5.1: Deviation in radius scale for Krissian medialness response decays of 10% and 25% for tubes with Gaussian cross-section. σ_{rmax} and σ_{rmin} represent respectively the minimum and maximum radius scales for the corresponding decay percentage.

$\mathscr{M}_{max}$		$\triangle\mathscr{M} = 10\%$				$\triangle\mathscr{M} = 25\%$			
R	σ_r	σ_{rmin}	σ_{rmax}	$\Delta\sigma_{rmin}$	$\Delta\sigma_{rmax}$	σ_{rmin}	σ_{rmax}	$\Delta\sigma_{rmin}$	$\Delta\sigma_{rmax}$
0.75	1.3290	0.9804	2.0408	26.23%	53.56%	0.7991	2.3702	39.87%	78.35%
0.919	1.3900	0.9902	2.1028	28.76%	51.28%	0.8111	2.4300	41.65%	74.82%
1.125	1.5282	1.0203	2.1993	33.23%	43.92%	0.8357	2.5164	45.31%	64.67%
1.379	1.9708	1.2028	2.3584	38.97%	19.67%	0.9234	2.6984	53.14%	36.92%
1.689	2.0613	1.5435	2.5416	25.12%	23.30%	1.1106	2.9666	46.12%	43.92%
2.069	2.1993	1.7926	2.9080	18.49%	32.22%	1.4180	3.3272	35.53%	51.28%
2.534	2.9963	2.1345	3.4112	28.76%	13.85%	1.7660	3.7878	41.06%	26.42%
3.105	3.2941	2.8082	4.0015	14.75%	21.47%	2.4179	4.3773	26.60%	32.88%
3.803	4.0821	3.5856	4.6939	12.16%	14.99%	3.1339	5.1092	23.23%	25.16%
4.659	5.0585	4.4433	5.5613	12.16%	9.94%	3.9815	5.9635	21.29%	17.89%

Table 5.2: Deviation in radius scale for Krissian medialness response decays of 10% and 25% for tubes with bar-convolved cross-section.

	$\Delta\sigma_{rmin}$		$\Delta\sigma_{rmax}$	
	Avg.	Min.	Avg.	Min.
$\triangle\mathscr{M} = 10\%$				
Gaussian	$29.50 \pm 5.52\%$	20.50%	$35.12 \pm 8.48\%$	24.54%
Flat-conv.	$23.86 \pm 8.70\%$	12.16%	$28.42 \pm 15.97\%$	9.94%
$\triangle\mathscr{M} = 25\%$				
Gaussian	$46.03 \pm 5.70\%$	35.85%	$60.42 \pm 11.50\%$	44.64%
Flat-conv.	$37.38 \pm 10.57\%$	21.29%	$45.23 \pm 21.38\%$	17.89%

Table 5.3: Averages obtained for values in Tables 5.1 and 5.2.

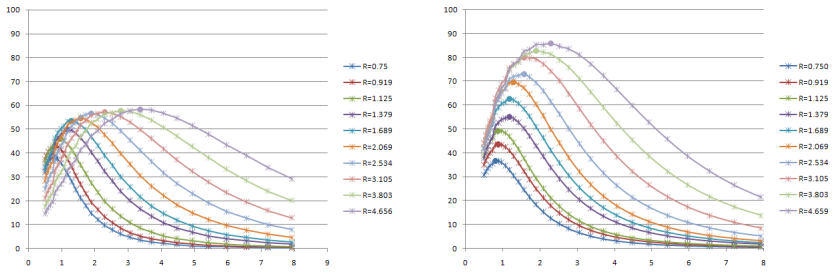

Figure 5.8: Krissian medialness values obtained in the center of the tube for different tube sizes and gradient scales σ_g, with $\sigma_h = 2.25$ and the best radius scale σ_r obtained for each tube. Left: tubes with Gaussian section profile. Right: tubes with bar-convolved section profile.

overestimating the scale. These peak values in the bar-convolved tubes are stronger, since the tubes are less smooth, and the best values for σ_g are smaller than for Gaussian tubes. The selectivity of the response is also higher for the bar-convolved tubes since the peaks are more prominent. With respect to the tube radius, responses are more selective for smaller radii whereas, for large radii, peaks tend to flatten, specially in the Gaussian tubes due to their smoothness.

In order to refine the results we performed a new set of experiments with a better scale resolution centered around the best values obtained in the previous experiment. For the Gaussian tubes we used $\sigma_{r0} = R_i/(s_r^{N_r/4})$, $s_r = 1.04$, $N_r = 40$, $\sigma_{g0} = 0.56\sigma_r/(s_g^{N_g/6})$, $s_g = 1.04$ and $N_g = 40$. For the bar-convolved tubes we used $\sigma_{r0} = R_i/(s_r^{N_r/4})$, $s_r = 1.04$, $N_r = 40$, $\sigma_{g0} = 0.424\sigma_r/(s_g^{N_g/4})$, $s_g = 1.04$ and $N_g = 60$. The factors 0.56 and 0.454 were obtained as an approximate linear relationship between σ_r and σ_g for the maximum values obtained for each tube radius in the previous experiment.

Figure 5.9 shows the maximum values obtained for the Krissian medialness at the tube centers depending on the radius scale. For each radius scale, the maximum was chosen by varying the gradient scale. We can see that for Gaussian tubes the curves of maxima are more abrupt for small tube sizes, being more selective, and then to flatten for large tube sizes, increasing the detection rate but with less selectivity. For the bar-convolved tubes we obtain a more uniform response for all tube sizes. With respect to the gradient scale corresponding to these maxima, they seem to be approximately piece-wise constant, giving the same value for a range of radius scales, except for high scales where some linearity is shown. The results for Gaussian tubes seem to be more stable. This means that results are not so dependent on the gradient scale for some reasonable values of the gradient scale.

Figure 5.10 represents the radius σ_{rmax} and gradient σ_{gmax} scales that yield the maximum value of medialness for each tube size. These corresponds to the maxima of each series in Figure 5.9. Note that for both section types, the relationship is almost linear as shown by the linear trend lines.

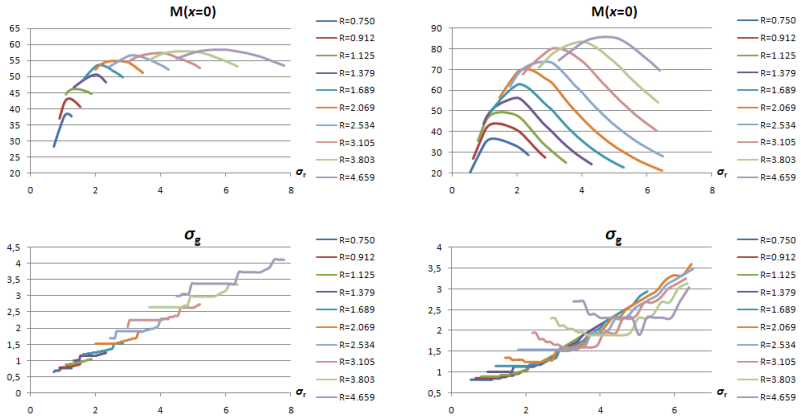

Figure 5.9: Maximum values of Krissian medialness obtained for each tube size and radius scale. Top row: medialness values obtained at the center of the tubes for each radius. Bottom row: corresponding gradient scales that give this maximum values. Left: tubes with Gaussian section. Right: tubes with bar-convolved section.

From these plots we can infer some criteria for scale selection as a result of our analysis. For tubes with Gaussian section the linear relationship between the radius and gradient scales for the maxima is approximately:

$$\sigma_{gmax} = 0.540\sigma_{rmax} + 0.150 \tag{5.51}$$

For tubes with bar-convolved section, the linear relationship is approximately:

$$\sigma_{gmax} = 0.411\sigma_{rmax} + 0.316 \tag{5.52}$$

Then, in order to select the right scales, we just need to search for the maxima of medialness across radius scales and select the gradient scales according to these linear relationships depending on the expected tube profile.

5.5.3 Optimally Oriented Flux

The calculation of an OOF-based measure requires the definition of at least two scales: the radius of the sphere in whose surface the flux is calculated, and the scale of the projected gradients whose flux is computed. The authors mention:

- The *radius scale* σ_r, as in the Krissian medialness case (section 5.5.2) it is the most critical scale and should be approximately equal to the tube radius. Failing to choose the appropiate radius scale will result in a poor estimation or even missing the tube at all. The idea is that the sphere surface should touch the vessel boundary in order to obtain enough signal for the flux-based calculations.

- The *gradient scale* σ_g, again, as in section 5.5.2, it should be chosen according to the expected tube boundary width and thus should be smaller than σ_r. The

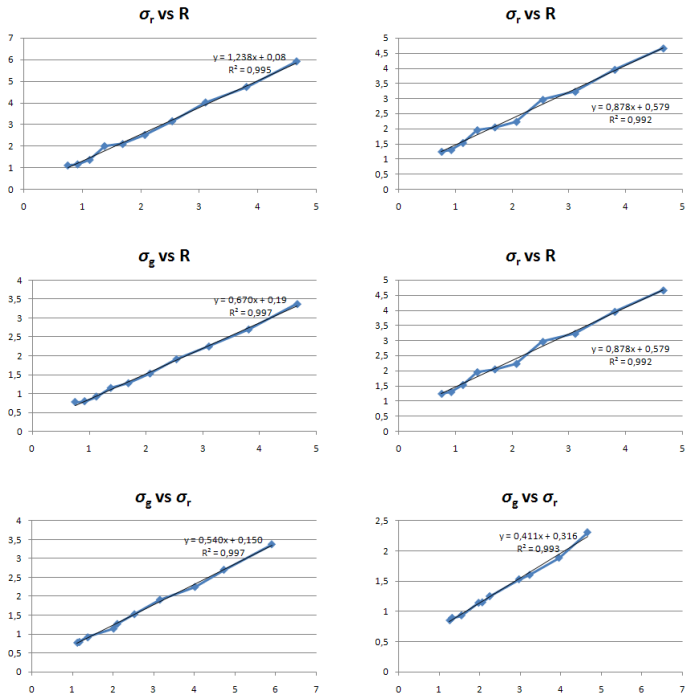

Figure 5.10: Radius and gradient scales that yield the maximum of Krissian medialness for each tube size with corresponding linear trend lines (in black). Left column: tubes with Gaussian section. Right column: tubes with bar-convolved section.

authors in [91] propose using a fixed small scale factor (they use $\sigma_g = 1.0$) for all sphere radii. However, in our experiments we have seen that this is not always the best option since, for large scales, such a small scale for the gradients may result in a good localization but poor detection rate, with the risk of missing the vessel boundaries when a small discrete set of scales is chosen.

Again, to establish some criteria for scale selection, we performed some experiments on ideal cylinders of different sizes. The set of cylinders used is the same as in section 5.5.1. The first set of experiments used a fixed gradient scale $\sigma_g = 1.0$ and σ_r varying according to

$$\sigma_{rj} = s_r^j \sigma_{r0} \quad j = 1 \ldots N_r \tag{5.53}$$

where we used $\sigma_{r0} = 0.5$, $s_r = 1.005$, $N_r = 600$. The idea is to set a criteria for the selection of the radius scale using fixed small gradient scale values as in [91].

Figure 5.11 (left) shows the medialness values obtained for both tubes with Gaussian and bar-convolved section profile. Results are similar with respect to the equivalent experiment in section 5.5.2 with respect to the shape of the plots both types of tubes. However, the peaks seems to be less prominent and tend to flatten. Some irregularities may be observed for the smallest tube sizes, probably due to discretization effects, since the apparent tube radius is at the scale of the image resolution (here, we used a spacing of 1.0 mm. for all tubes).

Figure 5.11 (right) shows the relationship obtained for the maximum radius scales versus the corresponding tube radii. Here, still a good linear relationship may be observed ($R^2 = 0.988$ and $R^2 = 0.969$ for Gaussian and bar-convolved tubes respectively). For Gaussian tubes the relationship is approximately:

$$\sigma_{rmax} = 1.094R + 0.482 \tag{5.54}$$

and for bar-convolved tubes:

$$\sigma_{rmax} = 0.947R + 0.887 \tag{5.55}$$

However, a better relationship may be obtained for the bar-convolved tubes, since the scale values for small radii are very close to $\sigma_r = 2.0$. Therefore, we provide an estimation using a linear piece-wise function:

$$\sigma_{rmax} = \begin{cases} 2.0 & R \leq 1.4 \\ 1.079R + 0.44 & R > 1.4 \end{cases} \tag{5.56}$$

As can be seen in 5.11 (right bottom) this gives a match of $R^2 = 0.990$ for the second linear stretch. Here, the best scales are obtained for values even larger than in the case of the Krissian medialness, approximately 110% plus 0.5 mm.

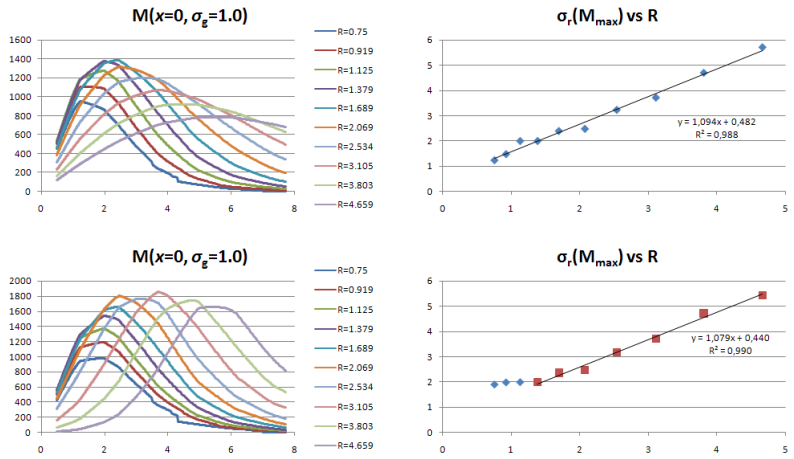

Figure 5.11: OOF medialness values obtained in the center of the tube for different tube sizes with $\sigma_g = 1.0$ and varying σ_r (x-axis), for tubes with Gaussian (top row) and bar-convolved (bottom row) section profile. Left column shows all values obtained varying σ_r. Right column shows the relationship between the tube radius (x-axis) and radius scale for the maximum values obtained for each radius.

$\mathscr{M}_{max}$		$\triangle\mathscr{M} = 10\%$				$\triangle\mathscr{M} = 25\%$			
R	σ_r	σ_{rmin}	σ_{rmax}	$\Delta\sigma_{rmin}$	$\Delta\sigma_{rmax}$	σ_{rmin}	σ_{rmax}	$\Delta\sigma_{rmin}$	$\Delta\sigma_{rmax}$
0.75	1.23935	1.0305	2.01049	16.85%	62.22%	0.831588	2.39394	32.90%	93.16%
0.919	1.4831	1.05652	2.26614	28.76%	52.80%	0.852587	2.65828	42.51%	79.24%
1.125	2.00048	1.17319	2.479	41.35%	23.92%	0.932669	2.87911	53.38%	43.92%
1.379	2.00048	1.44658	2.68493	27.69%	34.21%	1.04604	3.213	47.71%	60.61%
1.689	2.39394	1.68845	3.04148	29.47%	27.05%	1.18495	3.69454	50.50%	54.33%
2.069	2.479	1.89369	3.63967	23.61%	46.82%	1.41095	4.29084	43.08%	73.09%
2.534	3.22907	2.15589	4.2695	33.23%	32.22%	1.64687	5.05851	49.00%	56.66%
3.105	3.71302	2.65828	5.0083	28.41%	34.88%	1.96097	5.99334	47.19%	61.41%
3.803	4.69388	3.11828	6.1754	33.57%	31.56%	2.3118	7.24401	50.75%	54.33%
4.659	5.70175	3.73158	7.38998	34.55%	29.61%	2.83635	8.75567	50.25%	53.56%

Table 5.4: Deviation in radius scale for OOF medialness response decays of 10% and 25% for tubes with Gaussian cross-section.

$\mathscr{M}_{max}$		$\triangle\mathscr{M} = 10\%$				$\triangle\mathscr{M} = 25\%$			
R	σ_r	σ_{rmin}	σ_{rmax}	$\Delta\sigma_{rmin}$	$\Delta\sigma_{rmax}$	σ_{rmin}	σ_{rmax}	$\Delta\sigma_{rmin}$	$\Delta\sigma_{rmax}$
0.75	1.90316	1.12169	2.38203	41.06%	25.16%	0.896188	2.75273	52.91%	44.64%
0.919	1.99053	1.15576	2.41794	41.94%	21.47%	0.923412	2.79422	53.61%	40.38%
1.125	2.00048	1.22094	2.49139	38.97%	24.54%	0.965807	2.86478	51.72%	43.20%
1.379	2.00048	1.49052	2.64505	25.49%	32.22%	1.07245	3.10276	46.39%	55.10%
1.689	2.35839	1.73974	2.8935	26.23%	22.69%	1.25803	3.42823	46.66%	45.36%
2.069	2.479	1.99053	3.26144	19.70%	31.56%	1.59832	3.82581	35.53%	54.33%
2.534	3.16529	2.34665	3.94203	25.86%	24.54%	1.93185	4.37731	38.97%	38.29%
3.105	3.71302	3.213	4.3123	13.47%	16.14%	2.71185	4.93392	26.96%	32.88%
3.803	4.71735	3.84494	5.29075	18.49%	12.16%	3.3942	5.81664	28.05%	23.30%
4.659	5.42435	4.69388	6.29984	13.47%	16.14%	4.3123	6.75545	20.50%	24.54%

Table 5.5: Deviation in radius scale for OOF medialness response decays of 10% and 25% for tubes with bar-convolved cross-section.

	$\Delta\sigma_{rmin}$		$\Delta\sigma_{rmax}$	
	Avg.	Min.	Avg.	Min.
$\triangle\mathscr{M} = 10\%$				
Gaussian	$29.75 \pm 6.29\%$	16.85%	$37.53 \pm 12.33\%$	23.92%
Flat-conv.	$26.47 \pm 10.28\%$	13.47%	$22.66 \pm 6.50\%$	12.16%
$\triangle\mathscr{M} = 25\%$				
Gaussian	$40.13 \pm 11.96\%$	32.90%	$40.20 \pm 10.88\%$	43.92%
Flat-conv.	$37.38 \pm 10.57\%$	20.50%	$45.23 \pm 21.38\%$	23.30%

Table 5.6: Averages obtained for values in Tables 5.4 and 5.5.

Tables 5.1 and 5.2 represent the range of radius scales between which the response decays less than 10% and 25%, for Gaussian and bar-convolved tubes respectively.

Then, we tried to evaluate the joint influence of the radius and gradient scales. For this, we computed the OOF medialness value corresponding to equation 5.36 value at the center of each cylinder i for a set of discrete scales, chosen as:

$$\begin{array}{ll} \sigma_{rj} = s_r^j \sigma_{r0} & j = 1 \ldots N_r \\ \sigma_{gj} = s_g^i \sigma_{g0} & j = 1 \ldots N_g \end{array} \tag{5.57}$$

Our experiments used $\sigma_{r0} = 0.5$, $s_r = 1.05$, $N_r = 60$, $\sigma_{g0} = 0.7R_i$, $s_g = 1.05$, $N_g = 30$ for Gaussian tubes and $\sigma_{r0} = 0.5$, $s_r = 1.05$, $N_r = 50$, $\sigma_{g0} = 0.7R_i$, $s_g = 1.05$, $N_g = 30$ for bar-convolved tubes.

Figure 5.12 shows the maximum values obtained for the OOF medialness at the tube centers depending on the radius scale. For each radius scale, the maximum was chosen by varying the gradient scale. We can see that for Gaussian tubes the curves of maxima are more abrupt for small tube sizes, being more selective, and then to flatten for large tube sizes, increasing the detection rate but with less selectivity. For the bar-convolved tubes, lower responses and less abrupt are observed for small tube sizes. With respect to the gradient scale corresponding to these maxima, there is an approximate piece-wise constant behavior for both tube types. For Gaussian tubes, the gradient scale remains fixed with respect to the radius scale until the maximum of medialness is reached for that tube size. Then, an approximate linear relationship holds as the medialness value decreases. For bar-convolved tubes, there is an additional ascending ramp at the beginning of the plots at the lowest radius scales.

Figure 5.13 represents the radius σ_{rmax} and gradient σ_{gmax} scales that yield the maximum value of OOF medialness for each tube size. These correspond to the maxima of each series in Figure 5.12. Again, for both section types, the relationship is almost linear as shown by the linear trend lines.

From these plots we can infer some criteria for scale selection as a result of our analysis. For tubes with Gaussian section the linear relationship between the radius and gradient scales for the maxima is approximately:

$$\sigma_{gmax} = 0.530\sigma_{rmax} + 0.040 \tag{5.58}$$

For tubes with bar-convolved section, the linear relationship is approximately:

$$\sigma_{gmax} = 0.439\sigma_{rmax} + 0.115 \tag{5.59}$$

Then, in order to select the right scales, we just need to search for the maxima of medialness across radius scales and select the gradient scales according to the these linear relationships depending on the expected tube profile.

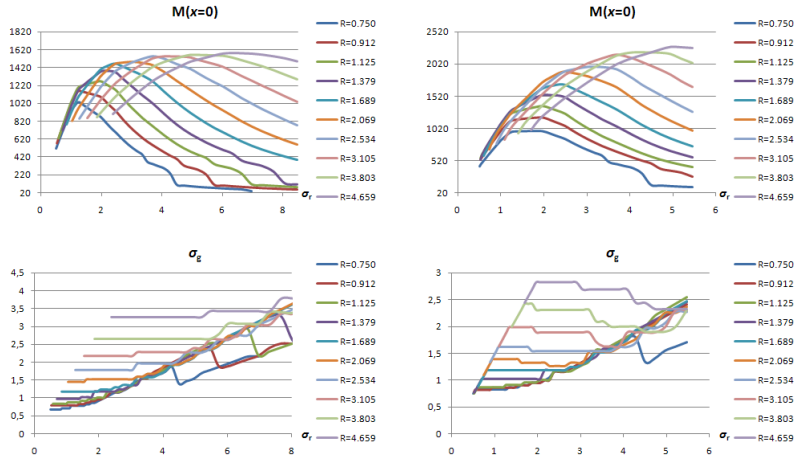

Figure 5.12: Maximum values of *OOF medialness* obtained for each tube size and radius scale. Top row: medialness values obtained at the center of the tubes for each radius. Bottom row: corresponding gradient scales that give this maximum values. Left: tubes with Gaussian section. Right: tubes with bar-convolved section.

5.6 Conclusions

We have provided a review of some of the most popular vesselness functions in the literature describing their properties and parameters, with particular emphasis in those features that provide an estimation of the vessel section plane, as they will be used for vascular tracking in Chapter 6.

The main contribution of this chapter is the identification of the different scaling parameters for the Hessian-based, Krissian medialness and OOF filters, where other authors used a single value for all the parameters involved. We have analyzed the properties of the identified scaling parameters, their relationship and the influence in the final response by means of a set of experiments using synthetic tubes of known geometry and intensity profile.

From the experimental results, we determine the most critical parameters for the filters, quantitative criteria for scale selection based on response decay, and, in some cases, a set of mathematical relationships between scaling parameters and tube sizes for optimal filter responses. These scale selection criteria allows us to determine an appropiate number and separation of discrete scales so as to detect the expected range of vessel sizes in a given practical application.

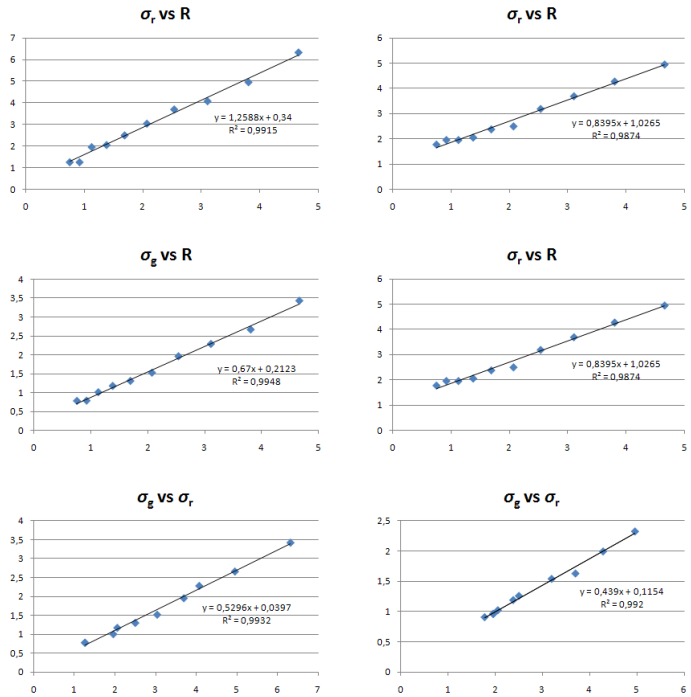

Figure 5.13: Radius and gradient scales that yield the maximum of *OOF medialness* for each tube size with corresponding linear trend lines (in black). Left column: tubes with Gaussian section. Right column: tubes with bar-convolved section.

Chapter 6

Vascular Extraction

The focus of this chapter is on *vascular tracking* methods which are a subset of *direct centerline extraction* methods [11]. These methods are more robust in many circumstances, specially for small vessels, and may be more appropriate for quantification or navigation purposes, since a full segmentation of the vessels is not required. We propose a canonical system framework for vascular tracking, called *Generalized Vascular Tracking (GVT) Framework*, that models the vascular tracking process by dividing it into individual system components and stages, allows exploring the influence of these individual system components and provide a means of combining existing methods in innovative ways. We show how this approach can be used for a systematic approach to vascular tracking, by incorporating components in increasing complexity. This is demonstrated by experiments providing qualitative and quantitative results on centerline tracking accuracy on synthetic and real datasets. We also propose an evolutionary strategy method for vascular section estimation, where the fitness function is constructed by adapting a medialness vascular detector and which is validated with experiments on real datasets. For a family of medialness functions the procedure can be performed at small fixed scales which is computationally efficient for local kernel-based estimators. We also demonstrate how this novel method is easily accommodated within the proposed GVT framework.

Section 6.1 describes the GVT Framework. Section 6.2 provides results of vascular tracking experiments with synthetic and real datasets at increasing degrees of complexity. Section 6.3 proposes the evolutionary strategy optimization method for vascular section estimation during tracking procedures. Finally, conclusions are drawn in Section 6.4.

6.1 Generalized Vascular Tracking (GVT) Framework

6.1.1 Motivation

The literature on vascular structure detection and extraction from medical images is very extensive [98][150]. Focus of the works varies, including, among other contri-

butions, measures of vesselness for detection, innovative extraction approaches, and different combinations of system components independently influencing the final extraction result. There is an increasing need of taking into account the influence of the individual components, clarifying their inter-dependencies, and designing interchangeable components for the different stages and abstraction levels of the extraction [98].

In other words, there is a need for tools to design software pipelines for vascular extraction consisting of connected and interchangeable components, allowing to compare existing methods, assess the effect of the different components and their relationship, with the aim of performing systematic studies and rapid prototyping of complex vessel extraction schemes. This is the motivation for the *Generalized Vascular Tracking (GVT) Framework* which is described next.

6.1.2 Description

The GVT Framework provides a model of vascular tracking processes identifying different *components* and *stages*. The tracking procedure is an iterative process with different sequential *stages*. The different interchangeable models, metrics and algorithms [98] invoked in these stages are called *components*.

6.1.2.1 Vascular Tracking Components

We define the following common components for vascular tracking:

- *Section Estimator*: locally obtains for every point an estimate of the section normal and possibly of the local radius based on image content, previous estimations and section models. The Hessian Matrix and the Oriented Flux Matrix (OFM) are examples of section estimators from the eigenvalue analysis of these matrices.

- *Vesselness Metric*: is a measure of point likelihood of being part of a vessel. If the measure refers to the likelihood of being part of the centerline we call it *medialness*. The metric may be used in several parts of the extraction process, for example to estimate the correct scale maximizing this metric, or to search for the centerline point.

- *Centerline Model*: defines which output extraction information is stored. It may be a set of centerline points, including an underlying mathematical model, i.e. an interpolating B-spline curve, and/or a section model for each centerline point, such as an estimate of the section radius.

- *End Condition*: gives the stopping criterion for the algorithm. It may be as simple as maximum number of iterations, or a threshold minimum vesselness value. Adaptive methods with variable step size may incorporate the step size as a stopping criterion.

- *Scale Estimator* (optional): used in multi-scale approaches. It estimates the optimal scale for performing calculations on the current point. In general, the scale

is proportional to the relative size of the vascular structures to detect but its interpretation depends on the algorithm used. For example, in Hessian-based calculations, it determines the aperture of the Gaussian kernel used for scaled derivatives; in oriented flux calculations, it determines the radius of the sphere used to calculate the flux. The estimation of the scale is usually based on a (vesselness) metric.

- *Bifurcation Detector* (optional): used for detecting bifurcation points. It may be based on the vesselness measures. The detector may additionally provide estimates of the number and orientation of the bifurcations.

- *Optimizer* (optional): refers to an optimization of a cost function the most simple form of optimization is to take the maximum (minimum) value between a set of sampled points in parameter space (exhaustive search), more complex optimization procedures used, are gradient descent, simplex, Levenberg-Marquardt or evolutionary algorithms.

Most of these components, are used in every iteration but some may only be used once during the tracking procedure, for example at initialization. Some components are regarded as optional, depending on whether the tracking performs some kind of action, for example an optimization procedure.

6.1.2.2 Vascular Tracking Stages

A process diagram describing the GVT process is shown in Figure 6.1. Most of the stages are performed at every iteration. Other, such as the *Initialize* and *Post-process* stages are performed only once. We proceed to describe the different stages shown:

- *Initialize*: initializes the tracking procedure. The simplest initialization consists of providing a seed point in the vessel centerline. More advanced initialization involves finding the closest centerline point from the seed point, assuming this point is not on the centerline.

- *Turn*: finds the correct orientation and section of the vessel when a new (centerline) point is obtained, after advancing one step (*Step stage*) or after searching for the correct centerline point (*Search stage*). The process involves using a *Section Estimator* and possibly, in multi-scale approaches, a *Scale Estimator* and a *Vesselness Function*.

- *Search*: This stage aims to correct the trajectory in the vicinity of the new vessel candidate point. For example, it might be the maximum value of the vesselness (medialness) in the previously estimated plane or the closest ridge point of a medialness function. A *Turn stage* estimates the orientation and section of the new centerline point. This may be done once or in an iterative loop as shown in Figure 6.1. Note that the *Turn* and *Search* stages only involve calculations for the current point and do not involve estimating the new step direction (*Step* stage).

- *Measure*: once a new vessel (centerline) point is found, local or cumulative quantitative measurements may be performed. This may involve for example a detailed section shape or profiles, curvatures or cumulative lengths.

- *Step*: this stage estimates the new direction of advance and performs a step following the current direction. The simplest direction estimation is the current section's normal direction. More advanced strategies include filtering (i.e. averaging) the trajectory, extrapolation, etc. The process also involves setting the size of the current step. This may be fixed or adaptive, i.e. decreasing the step depending on curvature.

- *Check Branch* (optional): this stage uses a *Branch Detector* in order to verify if the current point is a branch point. If a bifurcation is found, the current branch extraction is finished and new extraction processes are spawned for each branch. The process can be seen on the diagram as an *Initialization stage* for each new branch.

- *Check End*: this stage checks if we have reached the end of the vessel. This may be as simple as checking a maximum number of iterations, or, more practically, checking the value of a *Vesselness Metric* or the step size for some adaptive approaches.

- *Post-process*: this stage performs any post-processing operation in the extracted branch or tree, such as quantification processes, filtering of centerlines and sections, etc.

6.2 A Systematic Approach to Vascular Tracking Using GVT

We perform vessel extraction experiments in synthetic and real datasets of increasing complexity to assess the effect of each GVT component. Experiments range from single-scale to multi-scale approaches; from methods with no search stage to exhaustive or optimized search based methods, etc.

As the number of combinations of components is very large, we provide some representative designs in increasing complexity. For each, we provide a list of components used and the corresponding stage.

6.2.1 Fixed-scale Extraction

Fixed-scale extraction performs extraction using component operators at a single, user-defined, scale. It is assumed that the size (diameter) of the target vessels is in the range of sizes that can be detected at the selected scale. Moreover, for simplicity, we do not provide initially any *Search* stage to correct the trajectory.

Experiments on ideal tubes test the accuracy of the section estimation and the influence of several parameters, such as the tube radius, detection scale, and noise level. We

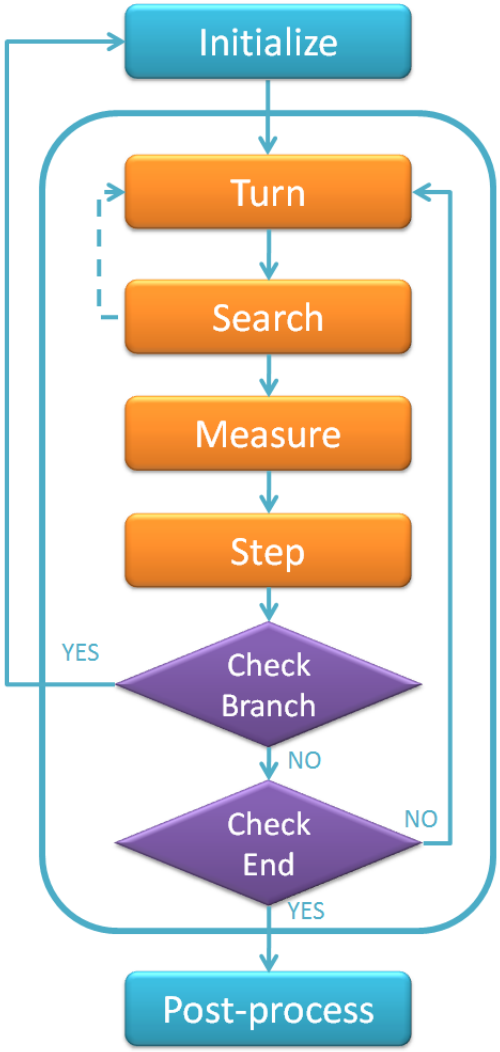

Figure 6.1: Process diagram of the GVT showing the different stages.

used the eigenvectors of the Hessian matrix and Oriented Flux (OF) Matrix in order to compare the accuracy and robustness of both *Section Estimators*.

Experimental data consists of a set of six ideal cylinders (see Appendix A) with maximum intensity of 255 and radius values according to:

$$R = s R_0 \tag{6.1}$$

where R_0 is the initial radius and s the scale factor. We chose $R_0 = 1.0$ and $s = 1.5$. Experimental data includes noisy versions with additive Gaussian noise of 10%, 25%, 50% and 75% with respect to the signal. We use two models of tubes: one with Gaussian cross-section and another with flat section convolved with a Gaussian (aka bar-convolved) with a small value of aperture (we used $\sigma = 1.0$) (see Appendix A for models of cross-section profiles). The second model better represents real vessels and partial volume effects [87], but the first model makes the tube boundary more diffuse.

Similarly, we selected a set of six discrete scales for calculations as in:

$$\sigma = s\,\sigma_0 \tag{6.2}$$

We chose $\sigma_0 = 0.7698$ and $s = 1.5$. According to [87], for Gaussian tubes, the scale that gives best response for their offset medialness function is $\sigma = \sqrt{3}R$. thus $\sigma_2 = s^2\sigma_0 = 1.732 \backsimeq \sqrt{3}$. In general, the best detection scale is a bit larger than the tube radius.

The extraction algorithm starts from a seed point on the centerline of the tube, but not in the end points in order to avoid boundary effects. The algorithm uses a fixed step size of 1.0 advancing in the estimated direction for a fixed number of 40 iterations.

We analyze two different quantitative measures in these experiments, obtained for different radius of the tubes and noise levels:

- *Mean (in section) centerline error* : corresponds to the mean of calculating the distance to the true centerline for the 40 sections (one for every iteration). We do not take into account here the error in the z direction, which accumulates with the deviation in the angle estimation, because we are more interested in the precision of the centerline estimation. Thus, for every section, to estimate the error, we compute the distance to the centerline and project it into the section.

- *Mean angle error* : corresponds to the mean of the angle between the estimated and ground truth section normals, taking the z-axis as ground truth, as:

$$\theta = \arccos(v \cdot u_z) = \arccos(v_1 u_{z1} + v_2 u_{z2} + v_3 u_{z3}) = \arccos(v_3) \tag{6.3}$$

  where v is the estimated unit vector, u_z is the z-axis unit vector, and $v \cdot u_z$ is the cosine of the angle formed by both unit vectors, which corresponds to the z component of the v vector. This also takes into account the sign of the vector giving values from 0 to 180º (in the opposite direction) which allows to check that the tracking does not turn back pointing to the wrong direction.

However, these quantitative measures do not provide information about the quality of the tracking, that is, whether the tracking was succesful or not or whether difficulties were found. We consider here five different situations:

- *Accurate tracking*: errors are minimal and the tracking proceeds without difficulties (Figure 6.2(a)).
- *Oscillating tracking*: centerline tracking is achieved, but tracking tends to oscillate around the true centerline position. It is typical of a situation where the scale is overestimated (Figure 6.2(b)).
- *Difficult tracking*: difficulties arise. Tracking is not totally lost but many centerline and angle estimates are incorrect, resulting in a non-smooth centerline and poor local section angle estimations (Figure 6.2(c)).
- *Lost tracking*: tracking is correct at the beginning but centerline is lost at some point. Some cases of lost tracking may end up in a partial recovery. When using small scales with large tubes, this may happen when the tracking progresses close to the external contour, as it partially finds some of the vessel boundary obtaining a fairly high response from the estimator (Figure 6.2(d)).
- *No tracking*: tracking is not achieved at all (Figure 6.2(e)).

Tables 6.1 to 6.4 show the values of the mean centerline and angle error for different tube radii, detector scales, and noise levels. Values are color coded according to tracking quality . We do not distinguish between correct and oscillating tracking, since sometimes this classification is not clear. Instead we classify the experiments as good when no difficulties are found and we also mark the best values with a different color (see Table 6.1).

From the tables we can see that scale selection is important to achieve a good or optimal tracking. The scales that yield best values are in most cases larger than the radius. In Table 6.5 we provide approximate values obtained for the qualitative types of tracking described above. A rough interpretation of this table attending the mean centerline error is that values under $0.15-0.2$ correspond to an *accurate tracking*; values between $0.15-0.2$ and $0.4-0.5$ to correct tracking with some local accuracy loss, such as *oscillating tracking*; values between $0.4-0.5$ and 1.0 represent tracking with difficulties; finally values above 2.0 mean that there is no tracking at all.

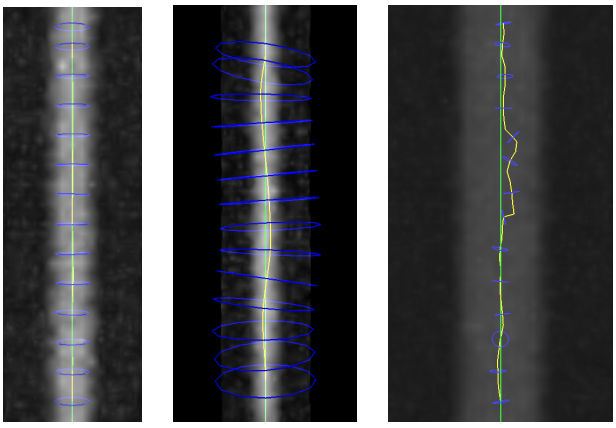

Figure 6.2: Different characteristic vessel tracking situations obtained in experiments with synthetic ideal cylinders with additive Gaussian noise. Examples use Hessian section estimator. (a) *Accurate tracking* (Gaussian section, $R = 1.5$, 10% noise $\sigma = 1.73$), (b) *Oscillating tracking* (Gaussian section, $R = 1.0$, 10% noise $\sigma = 5.84$), (c) *Difficult tracking* (Gaussian section, $R = 3.37$, 10% noise $\sigma = 0.76$), (d) *Lost tracking with recovery* (Flat-convolved section, $R = 2.25$, 25% noise, $\sigma = 0.76$), (e) *No tracking* (Flat-convolved section, $R = 7.59$, 50% noise, $\sigma = 1.73$). Figures shows cylinders as volume render with adjusted contrast levels for better visualization. Yellow line shows estimated trajectory; green line shows ground truth centerline; blue circles represent scale used and estimated orientation.

Radius	1	1	1	1	1	1	Radius	1	1	1	1	1	1
Scale	0,7698	1,1547	1,73205	2,59808	3,8971	5,8457	Scale	0,7698	1,1547	1,73205	2,59808	3,8971	5,8457
Mean 0%	0,000	0,000	0,000	0,000	0,000	0,000	Mean° 0%	0,000	0,000	0,000	0,000	0,000	0,000
Mean 10%	0,052	0,040	0,039	0,063	0,208	0,570	Mean° 10%	2,110	1,332	1,055	1,175	3,092	6,978
Mean 25%	0,171	0,094	0,069	0,108	0,820	5,368	Mean° 25%	5,839	3,237	2,256	2,718	7,679	80,396
Mean 50%	4,554	0,167	0,176	0,335	3,732	6,010	Mean° 50%	86,306	6,528	4,525	6,632	61,928	87,682
Mean 75%	5,319	0,529	0,447	0,681	5,537	5,836	Mean° 75%	87,051	15,345	7,354	10,876	77,000	88,053
Radius	1,5	1,5	1,5	1,5	1,5	1,5	Radius	1,5	1,5	1,5	1,5	1,5	1,5
Scale	0,7698	1,1547	1,73205	2,59808	3,8971	5,8457	Scale	0,7698	1,1547	1,73205	2,59808	3,8971	5,8457
Mean 0%	0,000	0,000	0,000	0,000	0,000	0,000	Mean° 0%	0,000	0,000	0,000	0,000	0,000	0,000
Mean 10%	0,075	0,051	0,045	0,059	0,083	0,214	Mean° 10%	3,879	1,983	1,150	0,811	0,956	2,466
Mean 25%	0,714	0,149	0,112	0,092	0,179	0,935	Mean° 25%	30,344	4,810	2,370	1,520	1,429	6,909
Mean 50%	4,032	0,318	0,182	0,209	0,551	3,794	Mean° 50%	91,763	9,807	4,330	2,825	3,569	40,699
Mean 75%	5,928	2,130	0,357	0,454	1,013	3,950	Mean° 75%	80,348	49,105	6,436	6,041	9,954	51,718
Radius	2,25	2,25	2,25	2,25	2,25	2,25	Radius	2,25	2,25	2,25	2,25	2,25	2,25
Scale	0,7698	1,1547	1,73205	2,59808	3,8971	5,8457	Scale	0,7698	1,1547	1,73205	2,59808	3,8971	5,8457
Mean 0%	0,000	0,000	0,000	0,000	0,000	0,000	Mean° 0%	0,000	0,000	0,000	0,000	0,000	0,000
Mean 10%	0,248	0,092	0,045	0,037	0,042	0,027	Mean° 10%	10,623	3,628	1,208	0,514	0,416	0,285
Mean 25%	7,957	0,261	0,104	0,078	0,091	0,161	Mean° 25%	84,657	6,915	2,154	1,364	1,012	0,675
Mean 50%	6,718	0,526	0,209	0,197	0,215	0,138	Mean° 50%	102,892	22,266	6,207	2,584	2,090	1,405
Mean 75%	9,127	1,090	0,380	0,294	0,329	0,206	Mean° 75%	89,733	35,103	9,953	3,940	3,134	2,078
Radius	3,375	3,375	3,375	3,375	3,375	3,375	Radius	3,375	3,375	3,375	3,375	3,375	3,375
Scale	0,7698	1,1547	1,73205	2,59808	3,8971	5,8457	Scale	0,7698	1,1547	1,73205	2,59808	3,8971	5,8457
Mean 0%	0,000	0,000	0,000	0,000	0,000	0,000	Mean° 0%	0,000	0,000	0,000	0,000	0,000	0,000
Mean 10%	0,645	0,247	0,105	0,061	0,039	0,025	Mean° 10%	23,044	5,235	1,411	0,495	0,328	0,182
Mean 25%	5,809	0,504	0,122	0,071	0,103	0,131	Mean° 25%	68,370	15,038	3,596	1,419	0,863	0,799
Mean 50%	3,249	1,643	0,452	0,287	0,218	0,163	Mean° 50%	91,975	77,716	7,296	2,399	1,254	0,896
Mean 75%	10,301	2,976	0,412	0,201	0,319	0,419	Mean° 75%	94,345	87,391	10,895	4,238	2,582	2,502
Radius	5,0625	5,0625	5,0625	5,0625	5,0625	5,0625	Radius	5,0625	5,0625	5,0625	5,0625	5,0625	5,0625
Scale	0,7698	1,1547	1,73205	2,59808	3,8971	5,8457	Scale	0,7698	1,1547	1,73205	2,59808	3,8971	5,8457
Mean 0%	0,000	0,000	0,000	0,000	0,000	0,000	Mean° 0%	0,000	0,000	0,000	0,000	0,000	0,000
Mean 10%	8,110	0,667	0,140	0,048	0,026	0,012	Mean° 10%	81,317	8,828	2,743	0,941	0,353	0,183
Mean 25%	7,909	1,568	0,336	0,120	0,064	0,031	Mean° 25%	92,220	21,652	6,370	2,281	0,877	0,459
Mean 50%	6,240	2,588	0,967	0,287	0,232	0,167	Mean° 50%	104,006	89,613	16,698	2,744	1,532	0,761
Mean 75%	4,158	2,734	1,116	0,416	0,238	0,123	Mean° 75%	66,272	85,535	26,246	7,118	2,306	0,576
Radius	7,59375	7,59375	7,59375	7,59375	7,59375	7,59375	Radius	7,59375	7,59375	7,59375	7,59375	7,59375	7,59375
Scale	0,7698	1,1547	1,73205	2,59808	3,8971	5,8457	Scale	0,7698	1,1547	1,73205	2,59808	3,8971	5,8457
Mean 0%	0,000	0,000	0,000	0,000	0,000	0,000	Mean° 0%	0,000	0,000	0,000	0,000	0,000	0,000
Mean 10%	6,575	3,419	0,262	0,099	0,047	0,019	Mean° 10%	85,147	29,390	4,665	1,264	0,430	0,162
Mean 25%	4,123	6,456	0,807	0,281	0,122	0,048	Mean° 25%	84,606	76,378	16,234	3,199	1,088	0,407
Mean 50%	7,513	4,032	2,115	0,699	0,464	0,282	Mean° 50%	100,376	89,285	39,238	9,693	2,993	1,407
Mean 75%	6,036	7,759	2,366	0,907	0,351	0,157	Mean° 75%	85,618	73,679	48,581	11,620	5,044	1,801

Table 6.1: Mean values for in-section center point estimation error for different detector scale values (x axis) along tubes of $R = 1.0$ and $R = 1.5$ as calculated for the Hessian (H) section estimator for tubes with Gaussian (G) cross-section. Results are shown for different levels of noise with respect to the signal (0, 10, 25, 50 and 75%). Color codes provide qualitative information (bright green: best values, green: good or fair estimates, yellow: obvious difficulties in tracking, orange: centerline is lost during tracking, red: unable to track the vessel).

Radius	1	1	1	1	1	1	Radius	1	1	1	1	1	1
Scale	0,7698	1,1547	1,73205	2,59808	3,8971	5,8457	Scale	0,7698	1,1547	1,73205	2,59808	3,8971	5,8457
Mean 0%	0,000	0,000	0,000	0,000	0,000	0,000	Mean° 0%	0,000	0,000	0,000	0,000	0,000	0,000
Mean 10%	0,101	0,059	0,054	0,066	0,106	1,525	Mean° 10%	3,026	2,408	1,990	1,810	2,740	11,073
Mean 25%	0,148	0,115	0,128	0,212	0,622	2,319	Mean° 25%	5,345	4,118	3,206	2,631	6,010	27,788
Mean 50%	0,364	0,326	0,315	0,308	0,474	9,198	Mean° 50%	12,698	10,823	9,315	10,040	14,862	45,219
Mean 75%	2,533	0,741	0,358	2,905	3,276	2,816	Mean° 75%	36,267	21,550	11,309	68,951	36,891	87,678
Radius	1,5	1,5	1,5	1,5	1,5	1,5	Radius	1,5	1,5	1,5	1,5	1,5	1,5
Scale	0,7698	1,1547	1,73205	2,59808	3,8971	5,8457	Scale	0,7698	1,1547	1,73205	2,59808	3,8971	5,8457
Mean 0%	0,000	0,000	0,000	0,000	0,000	0,000	Mean° 0%	0,000	0,000	0,000	0,000	0,000	0,000
Mean 10%	0,116	0,066	0,065	0,060	0,098	0,303	Mean° 10%	2,762	2,141	1,720	1,228	1,479	6,713
Mean 25%	0,245	0,197	0,142	0,178	0,107	0,702	Mean° 25%	5,454	4,629	3,393	2,568	3,207	12,983
Mean 50%	0,431	0,400	0,327	0,221	0,439	2,003	Mean° 50%	14,243	11,724	8,577	5,648	8,824	112,484
Mean 75%	0,858	0,949	0,510	0,398	1,162	8,176	Mean° 75%	23,952	23,578	13,567	9,096	15,159	49,978
Radius	2,25	2,25	2,25	2,25	2,25	2,25	Radius	2,25	2,25	2,25	2,25	2,25	2,25
Scale	0,7698	1,1547	1,73205	2,59808	3,8971	5,8457	Scale	0,7698	1,1547	1,73205	2,59808	3,8971	5,8457
Mean 0%	0,000	0,000	0,000	0,000	0,000	0,000	Mean° 0%	0,000	0,000	0,000	0,000	0,000	0,000
Mean 10%	0,121	0,058	0,050	0,035	0,031	0,187	Mean° 10%	3,599	2,369	1,485	0,833	0,790	3,091
Mean 25%	0,218	0,163	0,123	0,086	0,117	0,484	Mean° 25%	7,939	6,122	3,445	2,093	1,818	5,853
Mean 50%	0,605	0,371	0,239	0,176	0,232	1,956	Mean° 50%	16,367	10,766	6,636	3,924	3,664	13,666
Mean 75%	0,581	0,470	0,300	0,193	0,188	1,218	Mean° 75%	29,711	19,112	12,851	6,744	5,070	20,688
Radius	3,375	3,375	3,375	3,375	3,375	3,375	Radius	3,375	3,375	3,375	3,375	3,375	3,375
Scale	0,7698	1,1547	1,73205	2,59808	3,8971	5,8457	Scale	0,7698	1,1547	1,73205	2,59808	3,8971	5,8457
Mean 0%	0,000	0,000	0,000	0,000	0,000	0,000	Mean° 0%	0,000	0,000	0,000	0,000	0,000	0,000
Mean 10%	0,786	0,219	0,117	0,064	0,035	0,089	Mean° 10%	9,430	7,475	3,872	1,599	0,765	1,266
Mean 25%	1,359	1,237	0,286	0,190	0,058	0,286	Mean° 25%	20,693	19,239	10,334	4,902	1,768	3,360
Mean 50%	1,788	1,738	2,232	0,469	0,113	1,040	Mean° 50%	26,674	45,332	156,974	9,262	3,585	6,118
Mean 75%	1,831	1,485	1,215	0,491	0,299	0,712	Mean° 75%	114,443	31,598	24,813	9,921	6,022	8,230
Radius	5,0625	5,0625	5,0625	5,0625	5,0625	5,0625	Radius	5,0625	5,0625	5,0625	5,0625	5,0625	5,0625
Scale	0,7698	1,1547	1,73205	2,59808	3,8971	5,8457	Scale	0,7698	1,1547	1,73205	2,59808	3,8971	5,8457
Mean 0%	0,000	0,000	0,000	0,000	0,000	0,000	Mean° 0%	0,000	0,000	0,000	0,000	0,000	0,000
Mean 10%	2,218	1,872	1,443	0,429	0,060	0,046	Mean° 10%	70,825	68,808	19,133	9,776	1,938	0,647
Mean 25%	3,313	3,045	1,580	1,030	0,266	0,080	Mean° 25%	141,619	89,912	26,874	13,322	4,995	1,864
Mean 50%	3,320	3,217	3,357	1,239	0,709	0,299	Mean° 50%	146,202	137,494	141,748	19,674	7,882	3,142
Mean 75%	4,325	2,573	3,693	1,894	0,858	0,287	Mean° 75%	142,352	91,161	139,657	24,983	12,173	5,686
Radius	7,59375	7,59375	7,59375	7,59375	7,59375	7,59375	Radius	7,59375	7,59375	7,59375	7,59375	7,59375	7,59375
Scale	0,7698	1,1547	1,73205	2,59808	3,8971	5,8457	Scale	0,7698	1,1547	1,73205	2,59808	3,8971	5,8457
Mean 0%	0,000	0,000	0,000	0,000	0,000	0,000	Mean° 0%	0,000	0,000	0,000	0,000	0,000	0,000
Mean 10%	3,608	4,077	4,957	2,558	1,672	0,232	Mean° 10%	53,982	83,861	147,481	29,482	24,779	3,945
Mean 25%	4,790	4,263	4,239	4,141	2,659	1,107	Mean° 25%	97,816	66,737	73,718	148,320	46,369	8,557
Mean 50%	4,291	4,714	5,768	3,588	2,608	1,661	Mean° 50%	52,002	57,354	92,208	96,559	68,692	13,388
Mean 75%	3,794	7,084	5,601	3,823	2,646	2,201	Mean° 75%	94,505	77,146	81,212	34,245	41,264	15,235

Table 6.2: Same as Table 6.1 for Gaussian tubes with Optimally Oriented Flux section estimator.

Radius	1	1	1	1	1	1	Radius	1	1	1	1	1	1
Scale	0,7698	1,1547	1,73205	2,59808	3,8971	5,8457	Scale	0,7698	1,1547	1,73205	2,59808	3,8971	5,8457
Mean 0%	0,000	0,000	0,000	0,000	0,000	0,000	Mean° 0%	0,000	0,000	0,000	0,000	0,000	0,000
Mean 10%	0,109	0,062	0,049	0,066	0,237	0,942	Mean° 10%	3,702	1,989	1,411	1,520	2,422	6,542
Mean 25%	0,349	0,111	0,158	0,307	0,764	6,841	Mean° 25%	8,624	3,127	2,017	2,376	7,655	90,158
Mean 50%	5,103	0,279	0,231	0,501	3,124	4,293	Mean° 50%	86,770	10,047	6,742	9,116	53,647	56,034
Mean 75%	4,998	5,111	0,354	0,521	3,236	3,559	Mean° 75%	82,969	80,625	8,848	9,003	56,190	62,403
Radius	1,5	1,5	1,5	1,5	1,5	1,5	Radius	1,5	1,5	1,5	1,5	1,5	1,5
Scale	0,7698	1,1547	1,73205	2,59808	3,8971	5,8457	Scale	0,7698	1,1547	1,73205	2,59808	3,8971	5,8457
Mean 0%	0,000	0,000	0,000	0,000	0,000	0,000	Mean° 0%	0,000	0,000	0,000	0,000	0,000	0,000
Mean 10%	0,162	0,073	0,050	0,068	0,094	0,200	Mean° 10%	4,645	1,889	0,898	0,690	0,686	1,487
Mean 25%	0,715	0,209	0,117	0,095	0,157	0,382	Mean° 25%	30,207	4,006	2,127	1,756	1,670	3,212
Mean 50%	4,914	0,686	0,244	0,224	0,411	2,984	Mean° 50%	69,263	13,359	4,948	4,011	4,070	40,670
Mean 75%	6,100	3,050	0,299	0,288	0,747	6,667	Mean° 75%	74,101	55,734	7,434	6,085	6,242	72,624
Radius	2,25	2,25	2,25	2,25	2,25	2,25	Radius	2,25	2,25	2,25	2,25	2,25	2,25
Scale	0,7698	1,1547	1,73205	2,59808	3,8971	5,8457	Scale	0,7698	1,1547	1,73205	2,59808	3,8971	5,8457
Mean 0%	0,000	0,000	0,000	0,000	0,000	0,000	Mean° 0%	0,000	0,000	0,000	0,000	0,000	0,000
Mean 10%	0,577	0,075	0,027	0,027	0,043	0,059	Mean° 10%	12,192	2,308	0,655	0,507	0,664	0,575
Mean 25%	1,879	0,174	0,083	0,073	0,081	0,096	Mean° 25%	48,608	5,901	1,743	1,034	1,072	0,741
Mean 50%	3,947	0,406	0,163	0,142	0,162	0,198	Mean° 50%	70,307	14,048	3,470	2,029	2,135	1,500
Mean 75%	6,998	1,130	0,168	0,178	0,304	0,467	Mean° 75%	74,422	24,451	6,155	2,389	2,524	2,854
Radius	3,375	3,375	3,375	3,375	3,375	3,375	Radius	3,375	3,375	3,375	3,375	3,375	3,375
Scale	0,7698	1,1547	1,73205	2,59808	3,8971	5,8457	Scale	0,7698	1,1547	1,73205	2,59808	3,8971	5,8457
Mean 0%	0,000	0,000	0,000	0,000	0,000	0,000	Mean° 0%	0,000	0,000	0,000	0,000	0,000	0,000
Mean 10%	2,055	0,207	0,045	0,027	0,019	0,021	Mean° 10%	91,201	7,138	1,120	0,430	0,229	0,201
Mean 25%	4,563	1,196	0,113	0,049	0,040	0,062	Mean° 25%	78,409	123,139	3,478	1,036	0,609	0,675
Mean 50%	6,367	2,165	0,232	0,095	0,080	0,123	Mean° 50%	83,897	122,998	7,429	2,099	1,228	1,345
Mean 75%	6,299	1,385	0,441	0,194	0,164	0,212	Mean° 75%	68,116	38,931	9,362	3,523	1,932	1,799
Radius	5,0625	5,0625	5,0625	5,0625	5,0625	5,0625	Radius	5,0625	5,0625	5,0625	5,0625	5,0625	5,0625
Scale	0,7698	1,1547	1,73205	2,59808	3,8971	5,8457	Scale	0,7698	1,1547	1,73205	2,59808	3,8971	5,8457
Mean 0%	0,000	0,000	0,000	0,000	0,000	0,000	Mean° 0%	0,000	0,000	0,000	0,000	0,000	0,000
Mean 10%	3,001	1,948	0,246	0,035	0,014	0,012	Mean° 10%	100,449	26,726	6,220	0,585	0,191	0,138
Mean 25%	3,471	2,835	0,659	0,087	0,068	0,073	Mean° 25%	112,345	122,760	9,969	1,317	0,555	0,340
Mean 50%	2,686	2,191	0,738	0,176	0,067	0,064	Mean° 50%	113,321	113,381	18,422	2,838	0,952	0,698
Mean 75%	6,887	6,882	1,830	0,241	0,197	0,210	Mean° 75%	95,839	97,540	17,590	4,007	1,673	0,995
Radius	7,59375	7,59375	7,59375	7,59375	7,59375	7,59375	Radius	7,59375	7,59375	7,59375	7,59375	7,59375	7,59375
Scale	0,7698	1,1547	1,73205	2,59808	3,8971	5,8457	Scale	0,7698	1,1547	1,73205	2,59808	3,8971	5,8457
Mean 0%	1,424	0,000	0,000	0,000	0,000	0,000	Mean° 0%	18,368	0,000	0,000	0,000	0,000	0,000
Mean 10%	5,321	2,988	2,647	0,282	0,050	0,035	Mean° 10%	62,361	58,202	28,178	5,081	0,429	0,161
Mean 25%	4,873	3,765	3,568	0,726	0,086	0,036	Mean° 25%	74,698	83,559	37,430	7,900	0,810	0,295
Mean 50%	6,622	2,408	2,646	1,200	0,234	0,175	Mean° 50%	84,621	64,481	109,410	18,689	2,083	0,796
Mean 75%	7,452	2,667	3,726	1,500	0,348	0,261	Mean° 75%	81,679	84,755	67,088	27,993	3,136	1,186

Table 6.3: Same as Table 6.1 for bar-convolved tubes with Hessian section estimator.

Radius	1	1	1	1	1	1	Radius	1	1	1	1	1	1
Scale	0,7698	1,1547	1,73205	2,59808	3,8971	5,8457	Scale	0,7698	1,1547	1,73205	2,59808	3,8971	5,8457
Mean 0%	0,000	0,000	0,000	0,000	0,000	0,000	Mean° 0%	0,000	0,000	0,000	0,000	0,000	0,000
Mean 10%	0,022	0,016	0,015	0,020	0,013	0,134	Mean° 10%	0,410	0,327	0,291	0,284	0,347	2,765
Mean 25%	0,033	0,024	0,018	0,022	0,045	0,477	Mean° 25%	0,959	0,758	0,577	0,616	0,896	5,728
Mean 50%	0,099	0,082	0,061	0,097	0,141	0,660	Mean° 50%	2,343	2,054	1,715	1,824	2,262	11,574
Mean 75%	0,200	0,129	0,133	0,104	0,117	0,945	Mean° 75%	2,840	2,404	1,941	1,722	2,596	14,757
Radius	1,5	1,5	1,5	1,5	1,5	1,5	Radius	1,5	1,5	1,5	1,5	1,5	1,5
Scale	0,7698	1,1547	1,73205	2,59808	3,8971	5,8457	Scale	0,7698	1,1547	1,73205	2,59808	3,8971	5,8457
Mean 0%	0,000	0,000	0,000	0,000	0,000	0,000	Mean° 0%	0,000	0,000	0,000	0,000	0,000	0,000
Mean 10%	0,013	0,008	0,007	0,008	0,011	0,072	Mean° 10%	0,469	0,338	0,269	0,211	0,223	1,519
Mean 25%	0,026	0,022	0,022	0,016	0,027	0,180	Mean° 25%	1,416	1,029	0,809	0,594	0,511	2,706
Mean 50%	0,054	0,042	0,054	0,032	0,055	0,376	Mean° 50%	2,791	2,082	1,725	1,183	1,023	5,066
Mean 75%	0,101	0,067	0,081	0,062	0,090	0,946	Mean° 75%	4,198	3,097	2,312	1,529	1,834	6,896
Radius	2,25	2,25	2,25	2,25	2,25	2,25	Radius	2,25	2,25	2,25	2,25	2,25	2,25
Scale	0,7698	1,1547	1,73205	2,59808	3,8971	5,8457	Scale	0,7698	1,1547	1,73205	2,59808	3,8971	5,8457
Mean 0%	0,000	0,000	0,000	0,000	0,000	0,000	Mean° 0%	0,000	0,000	0,000	0,000	0,000	0,000
Mean 10%	0,021	0,018	0,015	0,010	0,003	0,022	Mean° 10%	0,552	0,366	0,269	0,162	0,112	0,388
Mean 25%	0,106	0,051	0,042	0,027	0,015	0,086	Mean° 25%	1,752	1,304	0,951	0,556	0,312	1,255
Mean 50%	0,192	0,141	0,123	0,053	0,030	0,160	Mean° 50%	3,393	3,021	1,904	1,112	0,629	2,412
Mean 75%	0,177	0,119	0,110	0,081	0,026	0,153	Mean° 75%	4,114	3,183	1,995	1,224	0,833	2,705
Radius	3,375	3,375	3,375	3,375	3,375	3,375	Radius	3,375	3,375	3,375	3,375	3,375	3,375
Scale	0,7698	1,1547	1,73205	2,59808	3,8971	5,8457	Scale	0,7698	1,1547	1,73205	2,59808	3,8971	5,8457
Mean 0%	0,000	0,000	0,000	0,000	0,000	0,000	Mean° 0%	0,000	0,000	0,000	0,000	0,000	0,000
Mean 10%	0,098	0,053	0,040	0,019	0,006	0,016	Mean° 10%	2,671	1,681	0,960	0,343	0,119	0,215
Mean 25%	0,340	0,233	0,123	0,039	0,018	0,057	Mean° 25%	5,173	3,682	1,863	0,765	0,303	0,608
Mean 50%	0,797	0,227	0,225	0,079	0,025	0,051	Mean° 50%	10,593	8,067	3,741	1,611	0,574	1,043
Mean 75%	1,243	0,752	0,300	0,114	0,053	0,168	Mean° 75%	12,351	9,536	5,312	2,275	0,906	1,875
Radius	5,0625	5,0625	5,0625	5,0625	5,0625	5,0625	Radius	5,0625	5,0625	5,0625	5,0625	5,0625	5,0625
Scale	0,7698	1,1547	1,73205	2,59808	3,8971	5,8457	Scale	0,7698	1,1547	1,73205	2,59808	3,8971	5,8457
Mean 0%	0,000	0,000	0,000	0,000	0,000	0,000	Mean° 0%	0,000	0,000	0,000	0,000	0,000	0,000
Mean 10%	0,958	0,934	0,484	0,088	0,017	0,007	Mean° 10%	23,271	15,936	9,547	2,779	0,372	0,123
Mean 25%	2,013	1,871	1,075	0,301	0,053	0,016	Mean° 25%	25,181	20,810	15,216	6,042	1,155	0,291
Mean 50%	2,880	2,489	1,850	0,559	0,115	0,026	Mean° 50%	147,633	145,145	77,879	8,895	1,853	0,604
Mean 75%	2,460	2,719	2,085	0,773	0,116	0,066	Mean° 75%	31,177	30,287	23,641	13,655	3,006	0,891
Radius	7,59375	7,59375	7,59375	7,59375	7,59375	7,59375	Radius	7,59375	7,59375	7,59375	7,59375	7,59375	7,59375
Scale	0,7698	1,1547	1,73205	2,59808	3,8971	5,8457	Scale	0,7698	1,1547	1,73205	2,59808	3,8971	5,8457
Mean 0%	0,000	0,000	0,000	0,000	0,000	0,000	Mean° 0%	0,000	0,000	0,000	0,000	0,000	0,000
Mean 10%	3,404	3,449	2,797	2,321	0,780	0,029	Mean° 10%	34,711	28,510	113,732	20,681	7,663	0,652
Mean 25%	3,752	3,606	4,113	2,641	1,158	0,081	Mean° 25%	45,371	39,791	138,681	36,544	17,193	1,625
Mean 50%	3,355	4,259	4,477	3,095	3,018	0,282	Mean° 50%	80,002	143,234	149,401	33,800	141,633	3,831
Mean 75%	4,672	4,588	2,711	3,861	2,294	0,187	Mean° 75%	117,694	46,195	48,416	134,737	17,705	5,001

Table 6.4: Same as Table 6.1 for bar-convolved tubes with Optimally Oriented Flux section estimator.

Type	Centerline Error		Angle Error	
	Min	Max	Min	Max
Accurate	0.0	0.15-0.2	0.0	2.0-3.0
Not accurate/ Oscillating	0.15-0.2	0.4-0.5	2.0-3.0	5.0-7.5
Difficult	0.4-0.5	1.0	5.0-7.5	20.0-25.0
Lost / No tracking	1.0-2.0	∞	20.0-25.0	180.0

Table 6.5: Range of performance values obtained for each qualitative tracking type

Here we can make some disctintions according to the tube size:

- For small radii ($R = 1.0$ and $R = 1.5$) the best values are found for scales around $\sqrt{3}R$ in agreement with the theory of Gaussian tubes [87]. Good tracking is achieved in most cases, except for the larger scale values due to poor localization. There are sometimes problems with high levels of noise (50 and 75%) and the lowest scales, specially for the Hessian estimator, since the smoothing of the kernel is too small for the noise levels and scales are close to the inner scale of the data (sampling). The OF estimator is more robust in these situations.

- For medium radii ($R = 2.25$ and $R = 3.375$) best values are mostly found for scales around $1.2R$. For small scales, the tracking start to fail since they are too small with respect to the size of the tube and, for the case of the Gaussian, the smoothing is not so strong, which is robust against noise. Again, the behavior of the OF estimator is better for small scales.

- For larger radii ($R = 5.0625$ and $R = 7.59385$) best scales are likely beyond the ones we used in our experiments and better results are obtained in general for the Hessian estimator. This is due to the large amount of smoothing with large Gaussian derivative kernels, which are very robust against noise and give good responses for a number of scales. On the other hand, the OF estimator has a very good localization, since it uses gradient values at small scales in the sphere surface, but this makes the detection rate much worse at large scales. One solution to this problem is increasing the scale for the gradient calculations in the sphere, but keeping into account that it should not be according to the radius but to the width of the boundary of the tube. Regarding computation times, the Hessian is much slower due to the large kernels involved whereas, in the case of the OF estimator, computation times are the same[1].

Figures 6.3 to 6.5 show the plots for the mean centerline error for different values of tube radius and noise levels. For the datasets without noise, there is no error in all situations except one of the worst (largest radius, smallest scale and highest noise level). For the noisy datasets we can distinguish three situations:

- For small radius values ($R = 1.0$ and $R = 1.5$) the OF estimator shows more precision, with an excellent behavior for bar-convolved (BC) tubes. This is normal since the OF estimator adapts very well to this section profile in which there is a narrow transition for the boundary. The behavior of the OF estimator with the Gaussian tubes is similar to the Hessian estimator but a bit better. Larger scales give the worse results and also small scales with high levels of noise in the case of the Hessian estimator.

- For medium radius values ($R = 2.25$ and $R = 3.375$) we can see a transition in behaviour. At $R = 2.25$ results are still very good for the OF estimator, specially with BC tubes. However the Hessian estimator starts to behave quite well except for the smallest scales. Its behaviour is quite similar at $R = 3.375$ but here the

[1] Unless the sampling of the sphere where flux is calculated is increased with the radius.

OF estimator starts to give poor results for the Gaussian where there is no sharp edge involved. At this radius, results are good for the Hessian estimator except for the smallest scales which are starting to be inadequate.

- For larger radius values ($R = 5.0625$ and $R = 7.59385$) we can confirm that the Hessian estimator gives more precise and consistent responses for a larger range of scales, and the error increases abruptly for some small scale values, which leaves them out of the plots. The behaviour of the OF estimator is specially poor for the BC tubes when the scale chosen is too small. In these cases, the sphere used to calculate the flux lies completely inside the tube and since it is flat in most of its section, no boundary is detected and the section estimation is poor or completely fails. In the case of the Hessian estimator, the aperture of the derivative kernels extends beyond the expected boundaries and thus results are slightly better. Results are worse in this case for the BC tubes, since their boundary is less diffuse. The increased smoothness due to large Gaussian kernels also works against very noisy data. The OF estimator definitely behaves poorly with Gaussian tubes. We can also see that the OF estimator only gives good values for a few large scales, for the reasons mentioned above, and thus is more selective but may miss the tube if the right scale is not chosen. In all cases, the scale needed for optimal detection at $R = 7.59385$ seems to be larger than the ones used.

Figures 6.6 and 6.7 contain the plots of the mean angle error along the 40 calculated cross-sections obtained by the Hessian and OF section estimators for different scale values and noise levels. Again we compare results for Gaussian versus bar-convolved (BC) tubes and distinguish three situations:

- For small radius values ($R = 1.0$ and $R = 1.5$) we can see that the angle estimation is poor for high levels of noise due to the small sizes of the tubes to be detected with respect to the inner scale of the data (resolution). Best results are found again for BC tubes with OF estimation. Here, the effect of noise in the angle estimated by the Hessian is more evident than in the center position. For larger scales, in the cases where the tube is still tracked successfully, the centerline oscillates in a zig-zag pattern, since no correction of the trajectory is involved, yielding higher angular errors.

- For medium radius values ($R = 2.25$ and $R = 3.375$) the behaviour is very similar for both detectors, except for the OF estimator with BC tubes which shows very accurate results at all scales and noise levels. In most cases, at small scales either the tracking is lost or important difficulties are found, which some sections very poorly estimated.

- For larger radius values ($R = 5.0625$ and $R = 7.59385$) the behaviour is also similar to the mean centerline error. Many values out of the plots represent unsuccessful tracking attempts. The OF estimator is lost in most circumstances or shows lost of difficulties and for an appropriate behaviour of this estimator, larger scales should be selected and probably in larger number due to the selec-

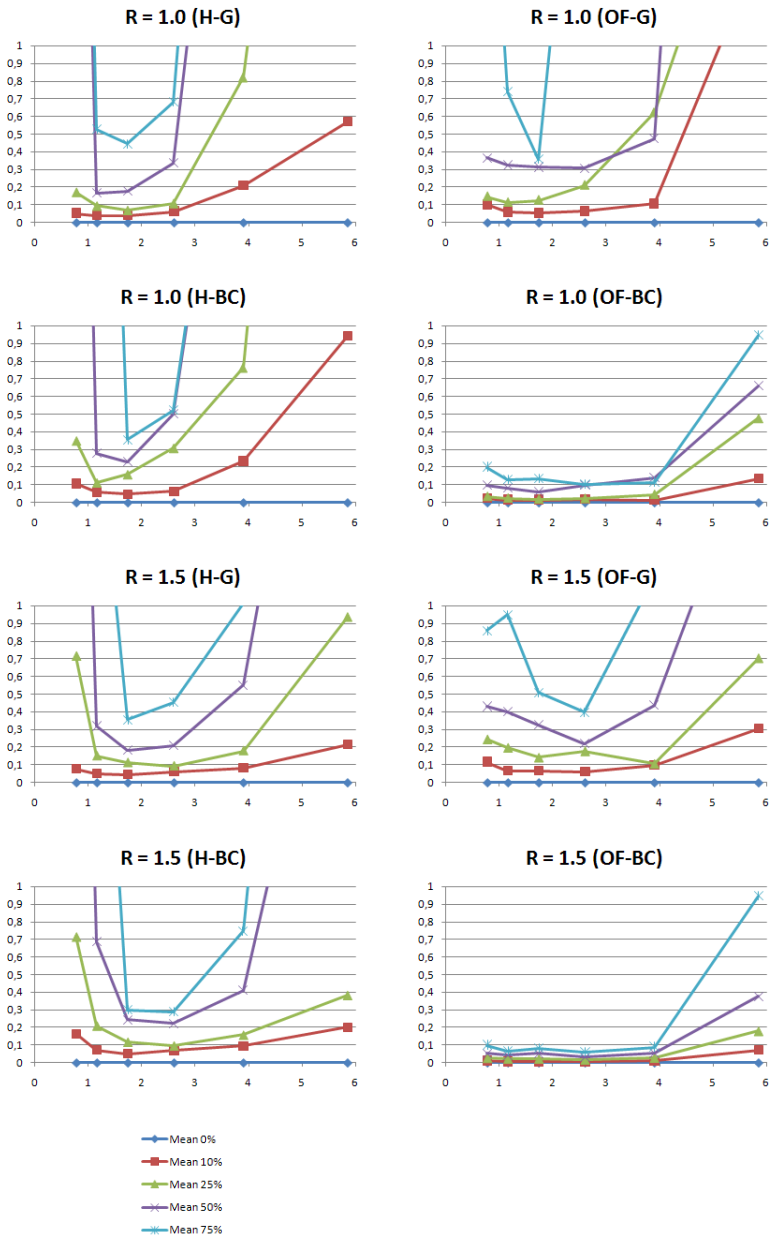

Figure 6.3: Mean values for in-section center point estimation error for different detector scale values (x axis) along tubes of $R = 1.0$ and $R = 1.5$ as calculated for the Hessian (H) and Oriented Flux (OF) section estimators and for tubes with Gaussian (G) and bar-convolved (BC) cross-section. Series show results for different levels of noise with respect to the signal (0, 10, 25, 50 and 75%).

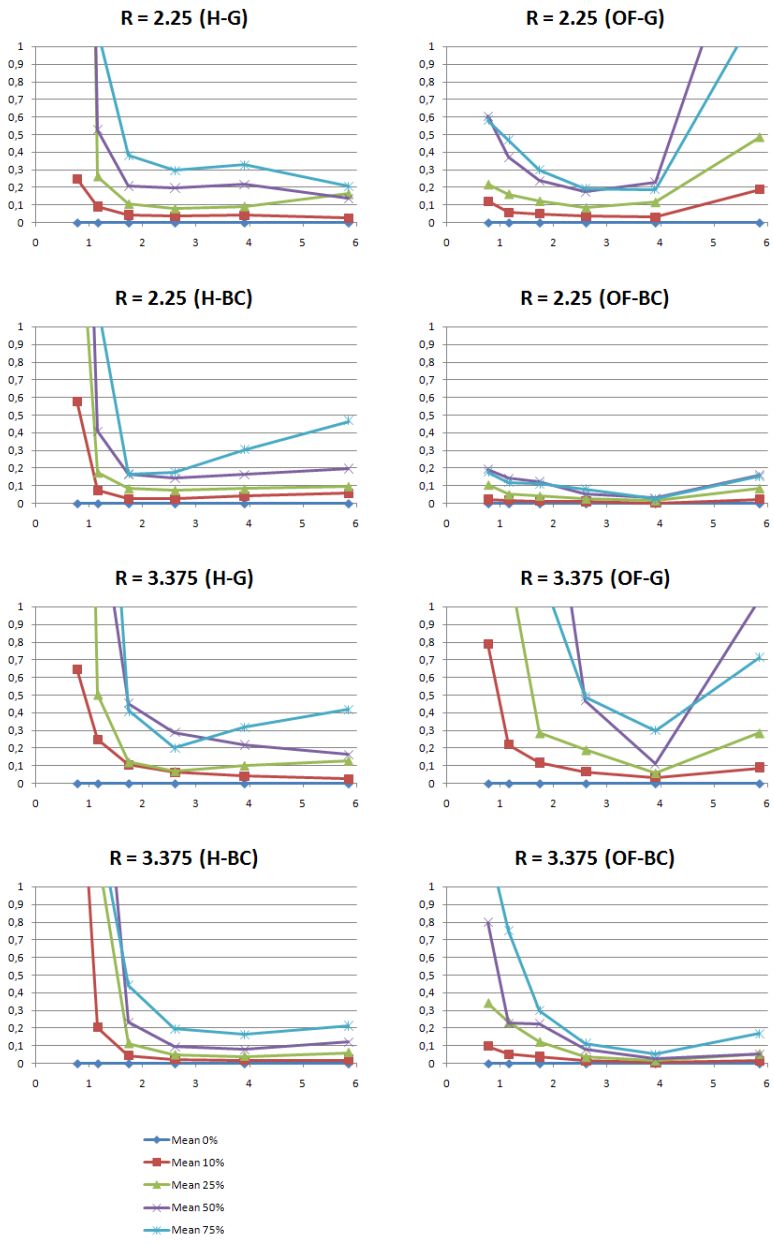

Figure 6.4: Same as Fig. 6.3 for $R = 2.25$ and $R = 3.375$.

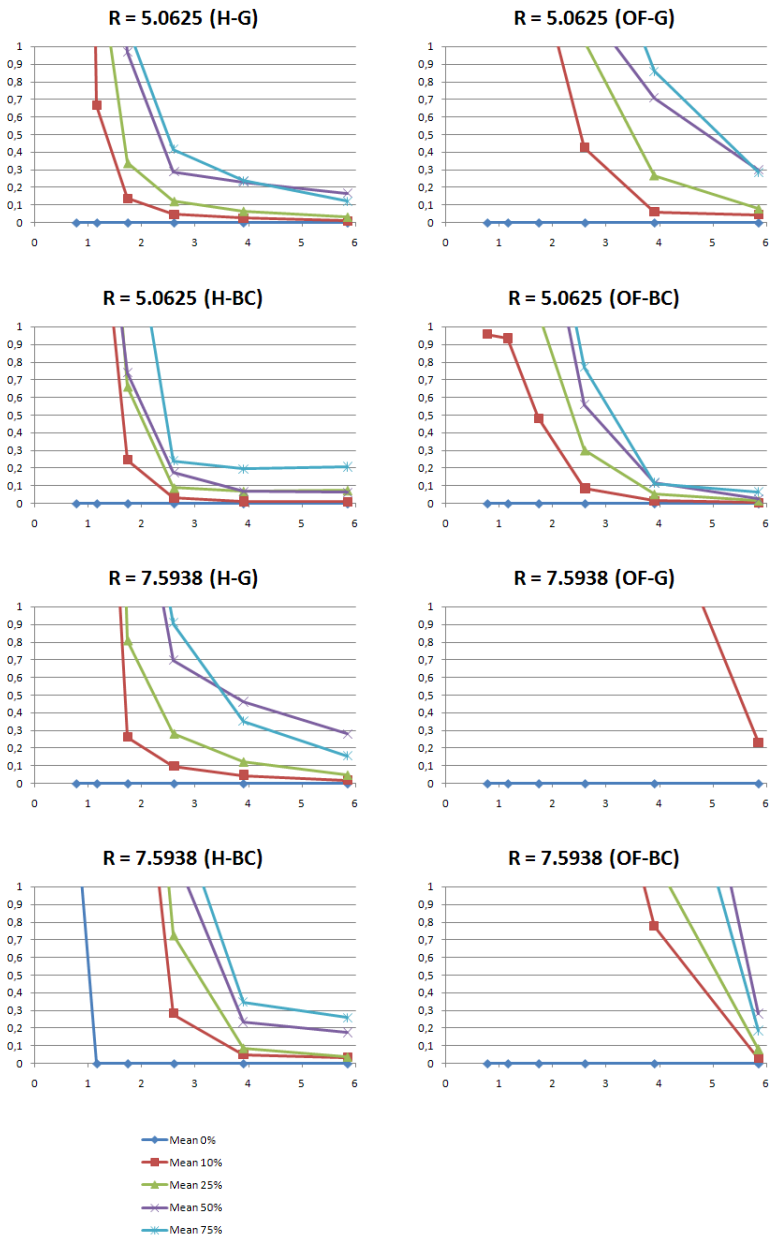

Figure 6.5: Same as Fig. 6.3 for $R = 5.0625$ and $R = 7.5938$.

tivity of the estimator. The Hessian estimation is better at large scales yielding acceptable angular errors.

As we have seen, the BC tube requires more precision in the scale selection, specially for large scales. One advantage of the OF estimator with respect to the Hessian estimator, is that it requires smaller apertures and thus, calculations are faster. This allows to test a wider range of scales to mitigate the problem of missing the tube border due to the selectivity of the filter. There is a compromise between detection and accuracy. The Hessian estimator seems to be less sensitive to the scale selection but also is less selective. In order to improve the detection rate of the OF for large scales, one may choose to increase the scale of the gradient calculations involved (which was fixed in our experiments to $\sigma = 1.0$ as were used in [91]) but according to the expected transition width of the tube boundary, and not according to the whole tube radius.

The OF estimator is more selective in the scale selection, but at the cost of failing to detect the tube with a wrong scale choice. On the other hand, the Hessian results to be very robust against noise, specially with larger radius values and is able to detect the tubes at a wider range of scales. This is due to the large support of the Gaussian kernel at wide apertures, which increases the smoothing and the detection rate at the cost of poorer localization and slower calculations. Moreover, the support of the Gaussian derivative kernels at large scales tend to extend far beyond the tubes to be detected, resulting in an influence by external spurious structures which may hamper the detection. This was one of the main reasons for proposing the OF algorithm in [91].

Figure 6.9 shows the result of the fixed scale tracking on a volumetric toroid sector (which by definition has constant curvature, see Appendix A) with Gaussian cross-section using the Hessian matrix as section estimator. Starting from the real centerline of the toroid, we can see that there is a constant drift in the centerline estimation. The reason is that the centerline is apparently correctly estimated, but the step size makes the location estimation of the centerline for the next step incorrect. Hence the errors accumulate without any centerline correction after the *Step* stage. Hence, the need for a *Search* stage in real situations becomes evident.

6.2.2 Multi-scale Extraction

In order to cope with varying vessel sizes, tracking must be performed at multiple scales. The component that must operate at multiple scales is the *section estimator*. As mentioned in Chapter 5, for doing so, first we need to select the set of discrete scales to be used; then, we need to devise a means of selecting, for every point of the image, the scale or scales that will contribute to the multi-scale response; finally we need to integrate these scales into a single multi-scale response.

In order to determine, for every point, the best scale(s) for the section estimator we need to obtain a function that depends on both, the current center of the section and its orientation. For this we propose to use a medialness function that depends on the estimation of the cross-section.

In our experiments, we used the *Krissian* medialness [87] as vesselness function for the section estimator , because this function explicitly computes the medialness in a cross-section plane. Moreover, this function may be used with both section estimators

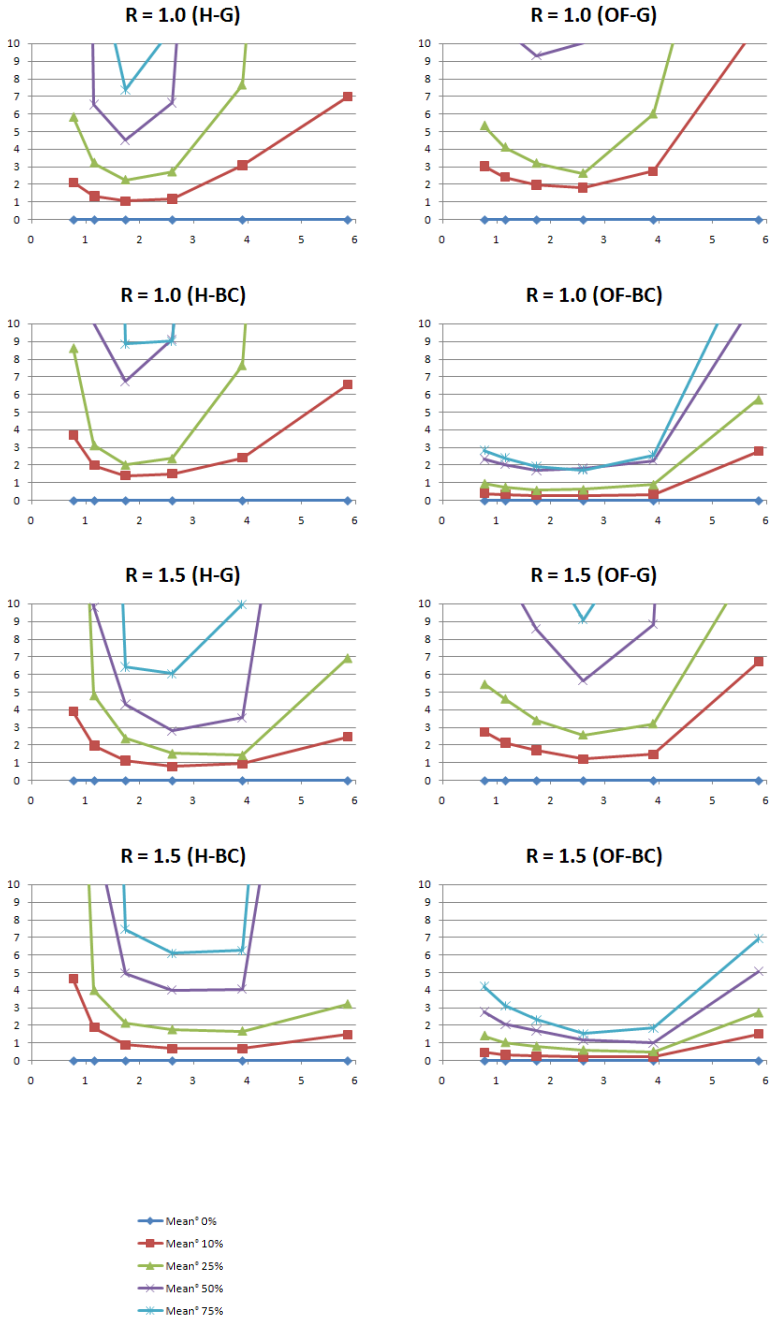

Figure 6.6: Mean values for section angle estimation error (with respect to the z-axis) for different detector scale values (x axis) along tubes of $R = 1.0$ and $R = 1.5$ as calculated for the Hessian (H) and Oriented Flux (OF) section estimators and for tubes with Gaussian (G) and bar-convolved (BC) cross-section. Series show results for different levels of noise with respect to the signal (0, 10, 25, 50 and 75%).

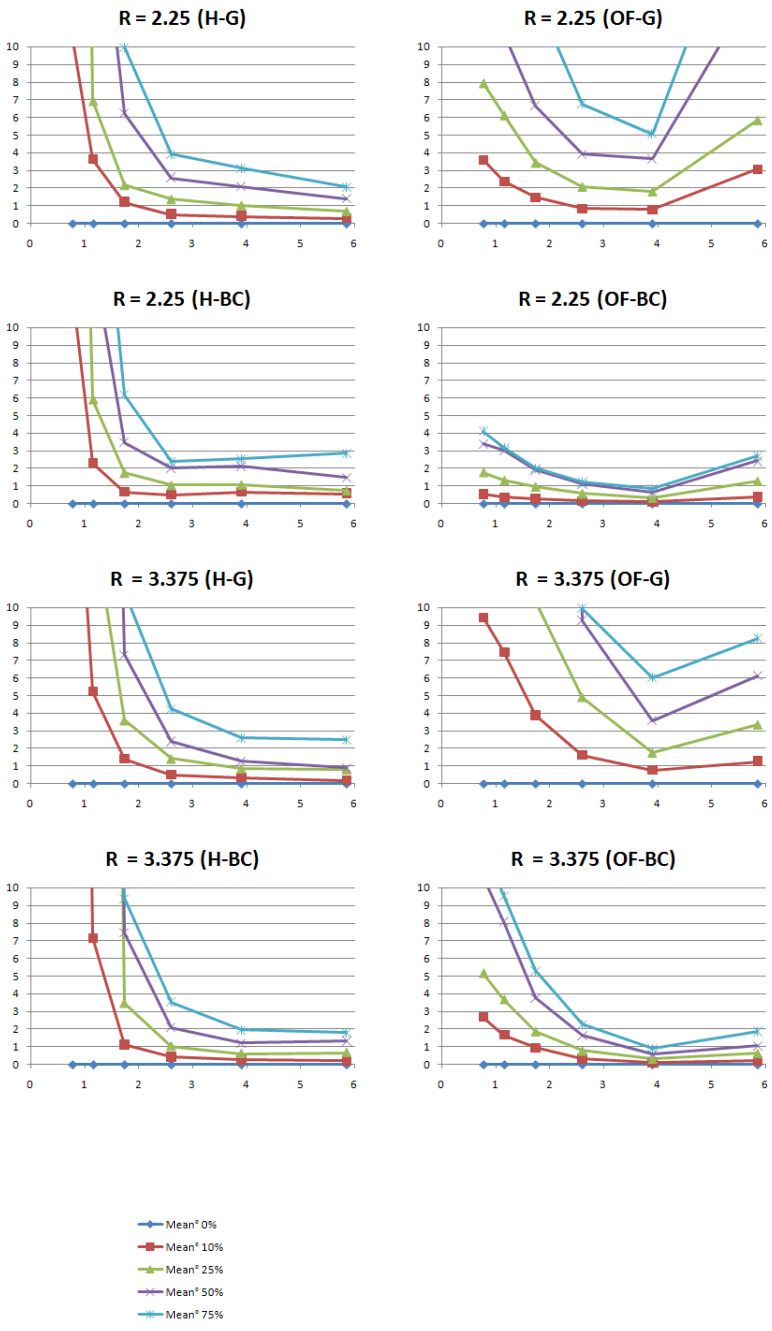

Figure 6.7: Same as Fig. 6.6 for $R = 2.25$ and $R = 3.375$.

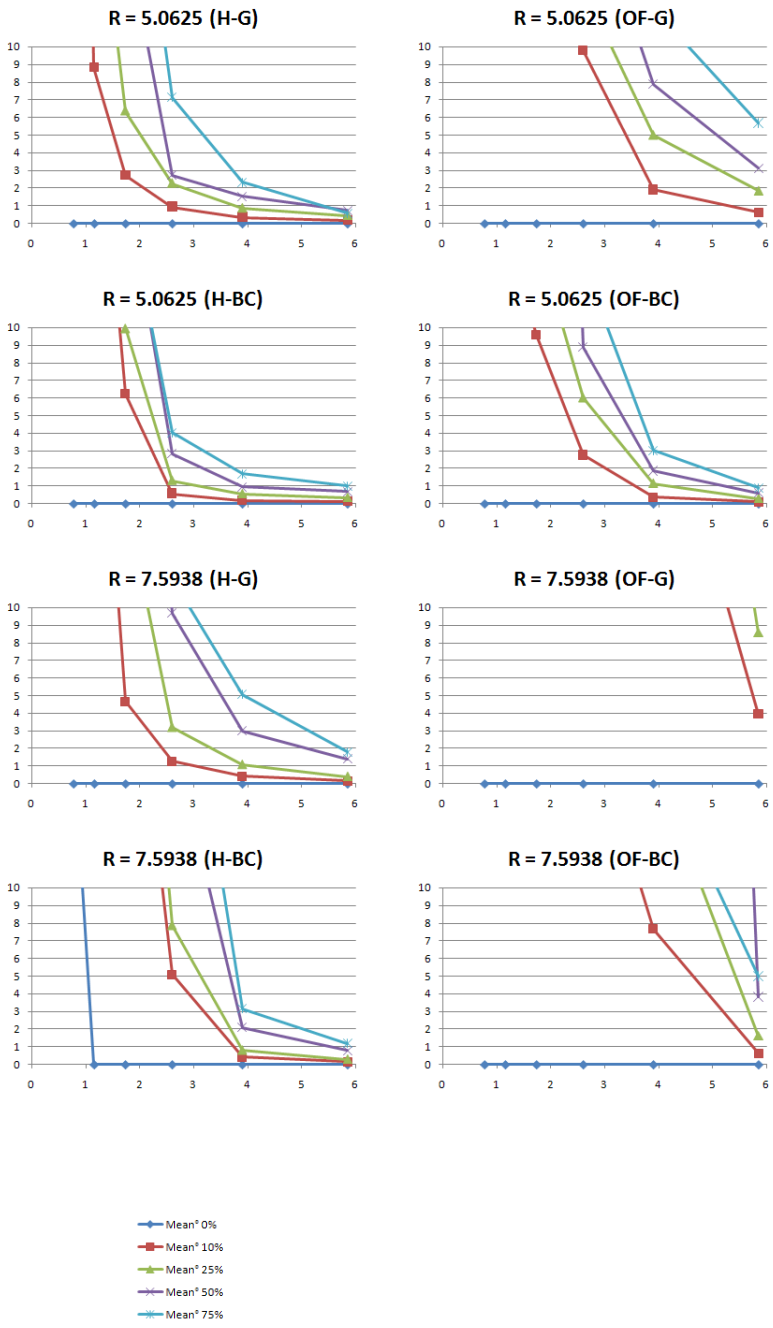

Figure 6.8: Same as Fig. 6.6 for $R = 5.0625$ and $R = 7.5938$.

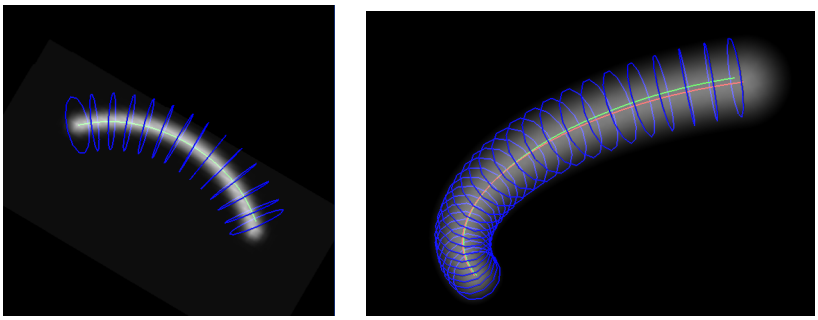

(a) (b)

Figure 6.9: Vascular tracking at fixed scale for synthetic volumetric toroids with Gaussian cross-section. Figure shows Maximum Intensity Projection (MIP) renderings of the volumetric toroids. The extracted centerline is shown in green. The circles show the estimated cross-sections with their radius obtained through the eigenvectors of the Hessian matrix. (a) Toroid with internal radius $\sigma_0 = 1.0$ and radius of curvature $R = 25$; Hessian scale $\sigma = 3.0$ (b) Toroid with $\sigma_0 = 3.0$, $R = 50$; Hessian scale $\sigma = 3.0$. Here, the ground truth centerline may also be seen in red.

used in our experiments: the Hessian section estimator and the OOF estimator. The original implementation of Krissian *et al*. uses the Hessian for estimation of the cross-section, but nothing prevents us from using any other type of estimator, such as the OOF and computing the Krissian medialness on the estimated cross-section.

The GVF framework allows to replace component functions at each stage. Here we used the Krissian medialness but GVF allows exchanging a function without replacing the rest of components, as long as the function depends on an estimate of the section.

Figure 6.10 shows the results of two qualitative experiments performed in the same CTA dataset. A single branch is extracted with both, the Hessian estimator (a) and the OOF estimator (b) at multiple scales using the Krissian medialness for scale selection. Results show accurate estimation for most of the vessel trajectory. Tracking errors produced in the OOF estimation are due to the drift under curvature, which is considered in the next section.

6.2.3 Multi-scale Extraction with Search Stage

In order to mitigate the drift effects happening due to tube curvature, it is necessary to perform a *Search* stage after the section estimation, correcting the position of the center point of the section or even re-estimating the section itself.

Let us initially assume that a section has been estimated at the correct scale. for which a medialness measure was obtained for the current center point of the section x_C. We propose to estimate a new section center $x_C^{'}$ by searching for a medialness ridge on the current section π. Since we are dealing with a single cross-section, this will correspond to a local maximum of the medialness function used for scale selection. After this new maximum is found, we re-estimate the section plane so as to obtain a

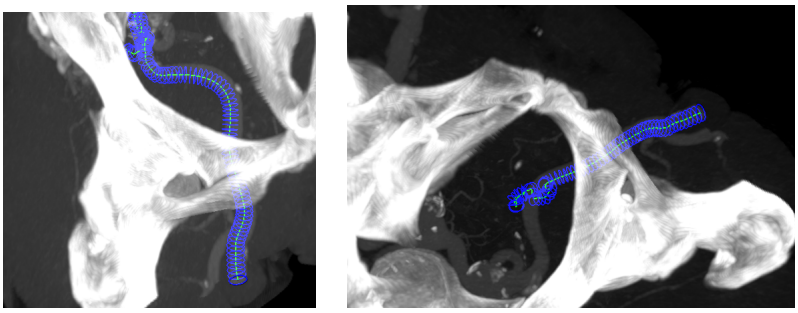

(a) (b)

Figure 6.10: Vascular tracking at multiple-scales in CTA datasets of the abdomen. (a) Result with Hessian estimator and Krissian medialness as strength measure. (b) Result with OOF estimator and Krissian medialness as strength measures.

new section π' at $x_C^{'}$. This is shown in Figure 6.11.

Any maximization algorithm may be used restricting the search to the current section plane. In practice, we create a discrete uniform polar grid around the center point, discretizing both in the angular and radial directions and establishing a maximum search radius. The medialness is measured in all the grid points at the current scale, checking first the values at radial locations closer to the center point. If no point with larger value is found, then our center point is considered the maximum. Otherwise we can proceed to the next radius and so on.

We followed this approach in the qualitative experiments shown in Figure 6.12 which show 3D MIP views of the extraction of the iliac arteries (Figures 6.12 (a)-(b)) and a major heart vessel in Figure 6.12 (d). Depicted centerlines shows continuous correction of the centerline, that can be easily refined by online or posterior smoothing as in [11]. The accuracy of the section and radius estimation is also demonstrated. Note that the radius estimation is obtained directly from the scale of the medialness operator as computed on the centerline. Further refinements could be obtained by applying some specialized boundary detector on the estimated centerline.

Figure 6.13 illustrate some problems that arise in multi-scale tracking. Figure 6.13 (a) shows an attempt of extraction of the aorta and its iliac arteries bifurcation in a CTA dataset where two difficulties are shown. First, due to an excessive actual vessel diameter with respect to the expected range of scales, the centerline of the aorta is not correctly extracted. However, the medialness detector gives an estimation inside the vessel boundary (this could be avoided by using some symmetry factor) and is able to track the vessel across the bifurcation. Since no bifurcation detector is used, tracking follows the closest iliac artery. Here an aneurysm, which resembles a blob structure, prevents the medialness function from obtaining good values and the tracking fails. This problem with very large vessels, such as the aorta, and aneurysms is treated specifically in Chapter 7 for the segmentation of the aorta and abdominal aortic aneurysms.

Figure 6.13 (b) shows a vessel image instance with bifurcations. In this case the

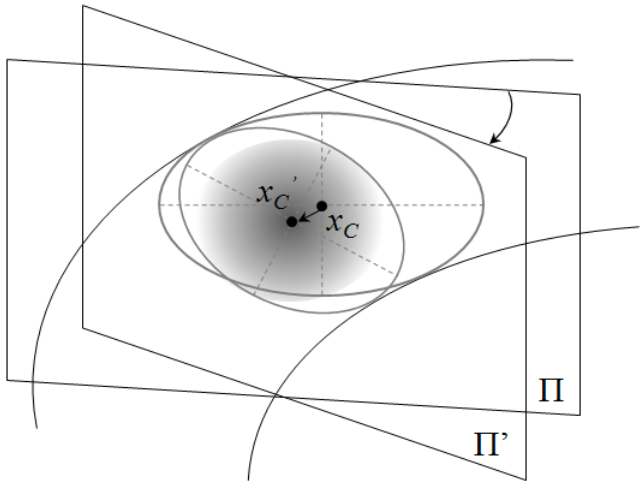

Figure 6.11: Section estimation with search stage. Higher medialness values are shown as darker gray tones.

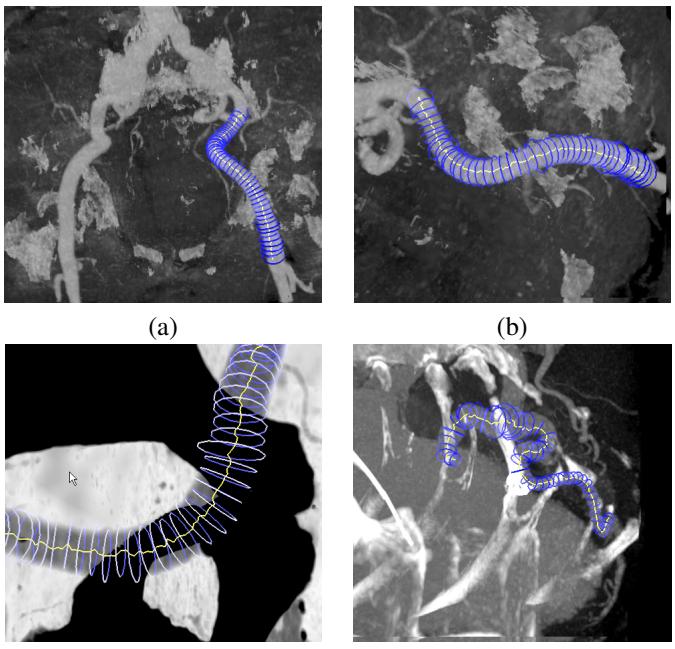

Figure 6.12: Qualitative experiments on real CTA datasets. (a)(b)(c) Iliac arteries. (d) Major heart vessel.

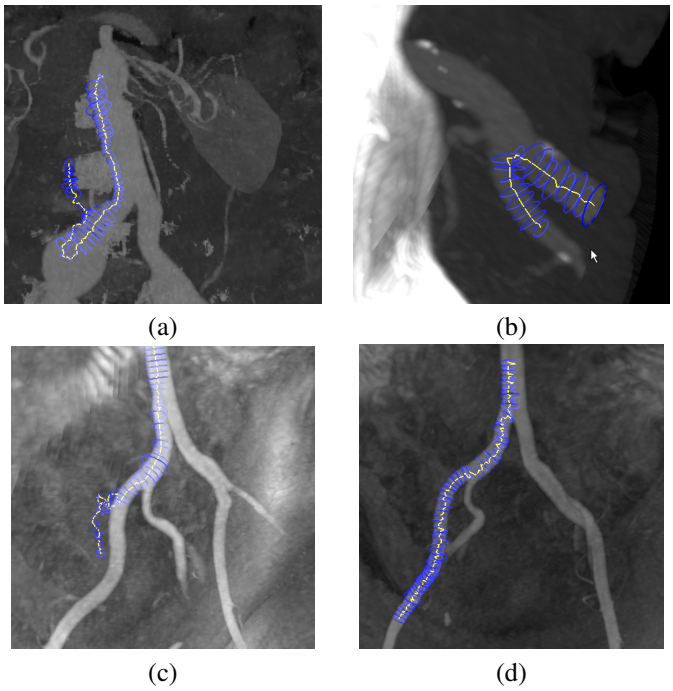

Figure 6.13: Common problem found during multi-scale extraction. (a) Wrong-scale selection / blob-like structure on aorta and iliac aneurysms on a CTA dataset. (b) Non -filtering of trajectory. (c) Excessive search radius on a MRA dataset. (d) Search radius limited in the same dataset.

vessel was traversed in the opposite direction. If the direction is not filtered tracking may follow the wrong bifurcation. Figure 6.13 (c) illustrates the *Search* stage failing on a bifurcation in a MRA dataset due to a too large search radius or too large scale range. Both bifurcated vessels are detected as a single one at a larger scale and the tracking gets lost. The effect of limiting the search radius is shown in Figure 6.13 (d) where tracking successfully follows one of the branches. In order to follow both branches, a bifurcation detector must be used, so when the bifurcation is found, two tracking procedures are started, one for each branch.

6.3 Optimal Vessel Section Estimation

6.3.1 Introduction

In order to improve the accuracy and robustness of the section normal and radius estimation, we propose to combine the direct solution from the *Section Estimator* with an evolutionary optimization procedure. The approach described in this chapter uses a 1+1 evolutionary strategy (ES) algorithm [174] for optimization and a cost function based on classical *Section Estimator* approaches such as the ones described before, in

order to detect the local optimal orientation and size (radius) of the vascular structure. The optimization may also be useful to find the optimal parameters for the estimators.

6.3.2 Evolutionary Optimization Scheme for Section Estimation

The evolutionary optimization vascular feature detection optimizes a vesselness measure assumed as the fitness function of the individuals. Individuals are instances of the value assignments to a set of parameters. Currently, we use the optimization in order to obtain an optimal section estimator. For this purpose, the vesselness measure needs to be a medialness measure, with the largest values on the vessel axis. In our experiments, we have used the Krissian medialness [87] described in Chapter 5. The optimization procedure tries to find the optimal unit section normal n and radius r of the medialness at each section center point x_c (assuming that it is the real vessel section center). The problem can be expressed mathematically as:

$$\arg\max_{u\in\Omega} R_\sigma(x_c,u), \quad \Omega=\left\{u=(n,r)\in\mathbb{R}^4\right\} \quad \text{s.t. } \|n\|=1 \tag{6.4}$$

We could incorporate the unit normal constraint into the optimization by using Lagrange multipliers:

$$\arg\max_{u\in\Omega,\lambda\in\mathbb{R}} \Lambda(x_c u,\lambda)=R_\sigma(x_c,u)-\lambda\left(1-\|n\|^2\right) \tag{6.5}$$

This would involve a 4D parameter search space . We can reduce the dimensionality of the parameter space and avoid the use of the Lagrange multipliers. For the first purpose, we observe that the components of the unit section normal, which are the director cosines, are related to each other by the expression:

$$\|n\|=\sqrt{n_x^2+n_y^2+n_z^2}=1 \tag{6.6}$$

Then, the optimization procedure can be expressed as:

$$\arg\max_{u\in\Omega} R_\sigma(x_c,u), \quad \Omega=\left\{u=(n_x,n_y,r)\in\mathbb{R}^3\right\} \quad \text{s.t. } \left\{|n_x|<1,\left|n_y\right|<1\right\} \tag{6.7}$$

This means that we have a 3D search space with two unit normal coordinates and the radius of the detector since the last coordinate is functionally dependent on the other according to the above formula.

On the other hand, the new constraints for the n_x and n_y coordinates can be implemented very easily by returning a zero value for the cost function when the constraints are not met. This is a fast and simple alternative to other more complex approaches such as using Lagrange multipliers.

Note that here the section center is assumed to be previously calculated, but it could be incorporated into the procedure. The scale σ of the derivative calculations could also be included into the optimization parameter set. However, discrete Gaussian scale-space derivatives [102] are calculated locally using an implementation with

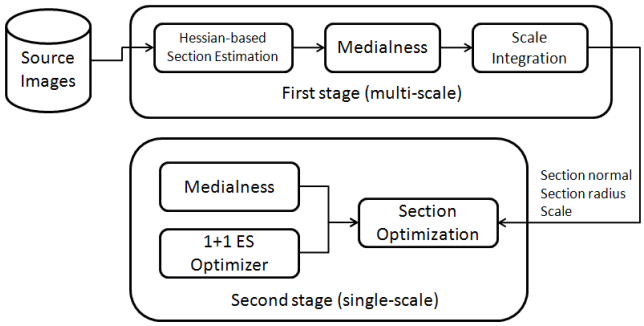

Figure 6.14: Two-stage vessel estimation scheme used in our experiments.

discrete kernels [113] and this would require the calculation of a large kernel at each optimization step for each value of the scale parameter.

The procedure for obtaining the section normal then becomes a two stage method (see Figure 6.14), assuming that we are located on a vessel center point:

1. Estimate the local section using a conventional estimator. This gives a single solution for the section normal, given the scale, radius and center point. The initial parameters are chosen from the neighbor point if previously calculated. A multiscale approach tests a discrete range of scales and selects the scale that yields the maximum medialness value.

2. Compute the best parameters for the optimization problem in eq. 6.7 using a (1+1)-ES evolutionary optimizer. Take as starting point the parameters and value of the section normal and radius calculated on the first stage.

6.3.3 Embedding into the GVT Framework

In the following experiments, we seamlessly incorporated the described scheme into our implementation of the GVT Framework as a specific realization of the *Search Stage* (see 6.1.2.2) that uses an *Optimizer* component (see section 6.1.2.1). In turn, the *Optimizer* uses a *Vesselness Metric* component adapted as a cost function. For the following experiments, we used a single algorithm both for the *Optimizer* and *Vesselness Metric*, but the software realization framework implemented in the IVAN library (see Appendix B) allows changing these individual components in order to test their influence separately. This demonstrates the validity and versatility of the framework for different experimental setups.

6.3.4 Experiments

We test our optimization methods with real 3D datasets, one Contrast-enhanced Magnetic Resonance Image (MRI) of the liver, one Magnetic Resonance Angiography

(MRA) of the abdomen and one Computerized Tomography Angiography (CTA) of the abdomen. The resolution of the data is variable, with the liver MRI $1.56 \times 1.56 \times 3.0$ mm. spatial resolution, the CTA with $0.72 \times 0.72 \times 1.5$ mm. and the MRA $1.0 \times 1.0 \times 1.5$ mm.

For each dataset, we manually delineate the approximate centerline of one or two long vessels: one major liver vein in the MRI dataset, the aorta in the MRA dataset, and iliac arteries in the other two CTA datasets. The points were interpolated by a B-Spline curve which is then sampled in order to increase the number of centerline points.

First, we estimated the sections by the direct method of calculating the eigenvectors of the Hessian matrix. In order to select the scale, for each centerline point, we computed the Krissian medialness in the estimated section plane and chose the parameters for the best value (scale, section normal and radius). We used a discrete range of scales ranging from 1.0 to 7.0 using a step size of 1.0. The radius used was the scale times a factor of $\sqrt{3}$ which is a good radius estimate for Gaussian tubes [87]. For all our experiments we used $\xi = 0.5$ for the medialness asymmetry parameter.

Second, we computed the sections with our optimization scheme. In order to keep the two normal components in the range $[-1,1]$, we simply returned zero as the medialness value outside this interval. The radius was also constrained in the range $[0, R_{max}]$ where R_{max} was chosen above the maximum expected radius value on the images. The scale was fixed in all our experiments to $\sigma = 1.0$, since we found out that the detection was more sensitive to the radius.

The optimization scheme uses a (1+1)-Evolution Strategy (ES) [174] as implemented in [204], which belongs to the family of Evolutionary Algorithms [162]. As initial parameters, we chose the normal and the radius from the first step. The medialness was calculated each time on the estimated section. The stop condition was either 5000 iterations or a minimal search radius of 0.25 (Frobenius norm of the covariance matrix). Most of the times the procedure was finished after about 2000 iterations. Note, that our focus here was to test the validity of the approach and not the performance of the optimizer. The latter has quite a lot of margin for improvements, for example, by trying to reduce the search space or by tuning the parameters for optimal performance.

6.3.5 Results

Results of the described method for both stages are shown in Fig. 6.15. The 3D render shows the estimated sections and radius depicted as circles at each centerline point (actually a subset of all centerline points was drawn). Note that the standard estimator works quite well at estimating the sections, since most of the vessels were clearly visible. However, there was a high variation in the scale and radius estimation along the vessels. The optimized procedure shows very precise results at estimating the section and radius, except maybe at bifurcations, where the first stage also fails. Note specially that the accuracy in the radius estimation is really high, which would be difficult to estimate by manually setting the parameter on the first stage.

It is important to note that our method can be applied to virtually any vesselness function. In this sense, the method can be thought of as both a shape and parameter estimator, thus decreasing the number of parameters of the original estimator. In our experiments, we have initialized the parameters for each section independently of the

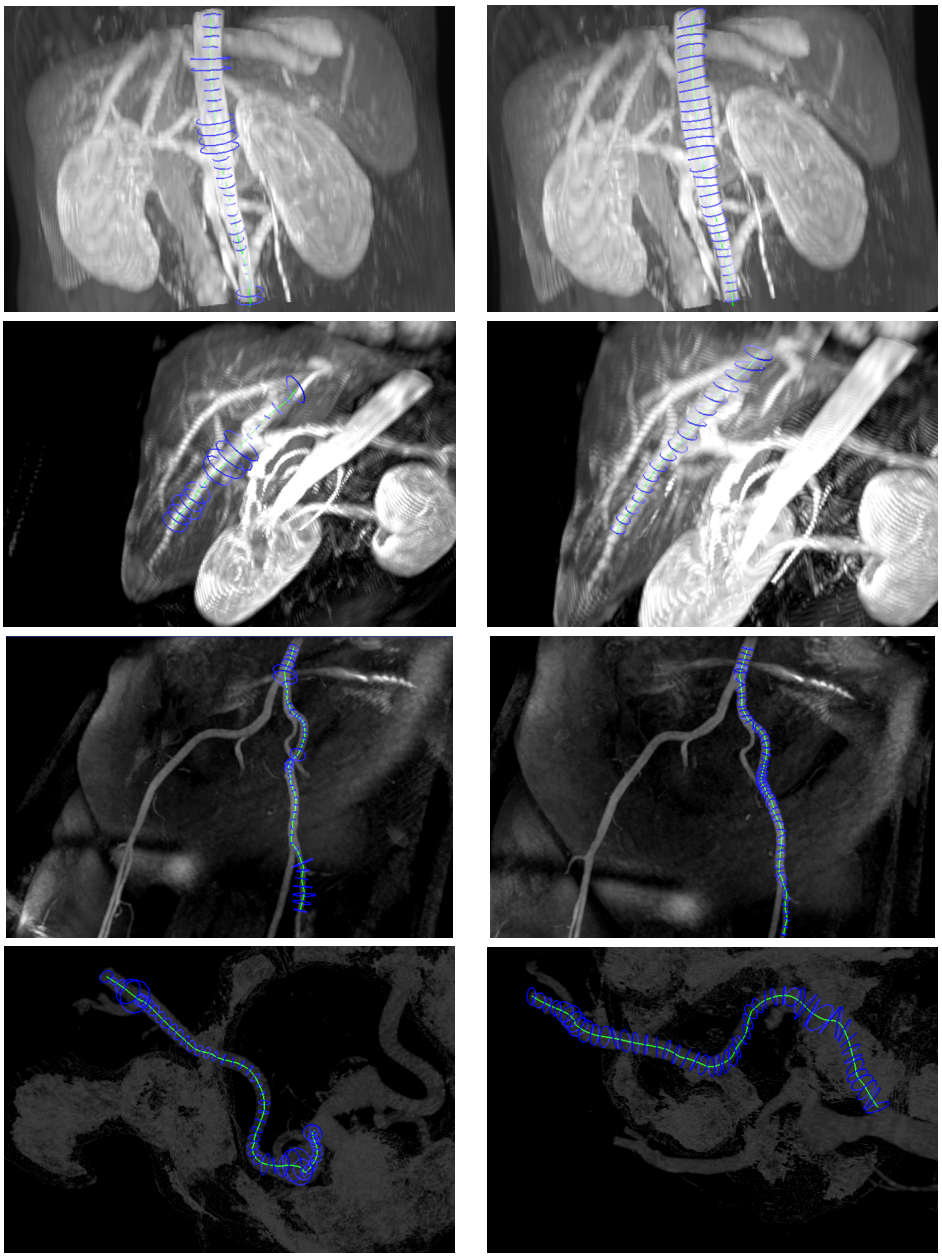

Figure 6.15: Volume rendering of real datasets with rendering of estimated vessel sections. Delineated centerlines are shown in green and estimated sections in blue. For each row, from top to bottom, results for an aorta in a MRI, one major liver vessel in the same MRI, and iliac arteries for a MRA (third row) and CTA (fourth row) study. Left column depicts the results of the first, direction estimation stage. Right column shows the results after the evolutionary optimization procedure.

results of the previous optimization. However, the optimizer can be initialized with an initial position corresponding to the previously calculated point. In this way, the optimization procedure would be less time consuming.

The optimization stage is slower than the previous step (in the order of minutes, rather than in the order of seconds). In practice, it should only be used when we require accurate values of radius and section normal or when the value of the direct section estimator is likely to be incorrect. During a tracking procedure, this can be detected as an outlier, for example, when the normal exceeds an angle with respect the previous normal along the vessel path (assuming that the step size is small enough). It may also be used as a parameter estimator for the standard procedure obtaining parameter values to be used in a given application.

6.4 Conclusions

We have proposed a process architecture for vascular tracking procedures called *Generalized Vascular Tracking (GVT) Framework*. By sucessive incorporation of different components and certain optional stages into the system with increasing complexity we show that the system can be used as a systematic approach to vessel tracking, which allows analyzing the influence of the different components into the final result. We also show how to combine different components, such as the section estimators or vesselness functions, in innovative ways, providing a means of combining the most interesting parts of different existing methods so as to obtain new powerful hybrid extraction schemes. This is demonstrated with experiments with synthetic and real datasets for the Krissian medialness and OOF medialness features.

We have also proposed, within the GVF framework, a means of estimating optimized vessel sections during tracking procedures, by adapting medialness functions as cost functions to be optimized with respect to the parameters describing the section (mainly its orientation). The validity of the approach is demonstrated with experiments with real datasets, which show improved accuracy with respect to direct section estimation.

An implementation of the GVF framework is provided in the IVAN library (see Appendix B) and was used in all our experiments.

Chapter 7

Analysis of Abdominal Aortic Aneurysms

Abdominal Aortic Aneurysms (AAAs) are one of the major complications in great blood vessels. Endovascular aneurysm repair (EVAR) is the preferred technique for its intervention and its success is measured on the basis of the bulge retraction in Computed Tomography Angiography (CTA) volumes. Thus, CTA image segmentation for AAA quantification is a relevant task for primary diagnosis and follow-up after intervention and requires a specific approach due to the size of the aorta and shape of the aneurysm. This chapter describes and evaluates a refined version of a fast and accurate method for the segmentation of the thrombus of AAAs after EVAR based on a radial model approach for the aneurysm and a prior aortic lumen segmentation. Thrombus segmentation results are presented in real clinical CTA images used for EVAR follow-up which demonstrate the high speed and accuracy of the method.

Another important contribution is the proposal of a method for the automatic detection and quantification of endoleaks in AAA thrombus as depicted in CTA images. To the best of our knowledge, there were no previous works in the literature dealing with this specific task.

The structure of the chapter is organized as follows. Section 7.1 gives an introduction to the medical problem and development of the chapter. Section 7.2 provides the state of the art in thrombus segmentation. Section 7.3 describes the initial approach to aortic lumen and AAA thrombus segmentation, reporting some experimental results. Section 7.4 presents the improved thrombus segmentation process with some experimental results. Section 7.5 gives conclusions on the AAA thrombus processes. Section 7.6 presents the endoleak detection process reporting experimental results. Finally, Section 7.7 gives our conclusions on the endoleak detection process.

7.1 Introduction

Abdominal Aortic Aneurysm (AAA) is a condition where the weakening of the aortic wall leads to its widening and generation of a thrombus in the abdominal region of

the aorta. AAAs are one of the most recurrent conditions in cardiovascular surgery, if untreated, AAA usually tends to wear and rupture with high risk of mortality [179]. To prevent a possible rupture of the aortic wall, AAA can be treated minimally-invasively by means of the Endovascular Aneurysm Repair technique (EVAR), consisting of placing a stent-graft inside the aorta by a catheter to exclude the aneurysm sac from the blood circulation. A cloth graft with a stent exoskeleton is placed within the lumen of the AAA, extending distally into the iliac arteries. This serves as a bypass and decreases the pressure exerted on the aortic wall, leading to a reduction in AAA size over time and a decrease the risk of aortic rupture. An Intraluminal Thrombus (ILT) is formed in the majority of AAA. Correctly excluded aneurysms progressively shrink after EVAR surgery.

The pre-operative planning and prognosis are done on the basis of CTA imaging [14]. Close follow-up is required after EVAR the routine consists of performing CTA examinations 1, 6 and 12 months after the intervention and annually thereafter. The aneurysm volume change is to date the best indicator to determine whether the surgery has been successful [187], which requires a segmentation of the thrombus. In a successful case it is expected to shrink completely until the aortic wall sticks to the stent graft. However, in many cases, due to the lack of fast and robust methods, a complete aneurysm segmentation is not available in order to obtain volumetric measurements, and the largest aneurysm diameter is used, despite not being an accurate indicator of evolution [1].

A major complication is the presence of liquid blood turbulences, known as *endoleaks*, in the thrombus formed within the space between the aortic wall and the stent-graft, due to incorrect positioning, displacement or torsion of the graft. Although endoleaks are more likely to occur soon after the intervention, lifelong surveillance is required [88]. Endoleaks can be classified in several types depending on the cause [190, 191]. The most common ones are Type II endoleaks, which arise from persistent retrograde flow in collateral vessel branches. They typically appear in the periphery of the aneurysm sac without touching the stent [173]. Some of them thrombose spontaneously but others do not, causing an increase in aneurysm size and risk of rupture. In these cases intervention is required, usually consisting in an embolization of collateral branches. Endoleaks are shown in a CTA images as brighter material inside the excluded aneurysm sac [173, 177] (see Figure 7.1 right). The actual image intensity value of the endoleak varies and depends on the size of the leak and the distribution of contrast material at the moment the image was acquired. They can be confused with calcifications which appear in the outer aortic wall and are brighter, whereas Type II endoleaks appear typically close to the wall perfusing into the sac and showing an amorphous shape (see Figure 7.1). We believe that an automatic detection and quantification system for Type II endoleaks is possible, and would be very helpful, specially in cases where endoleaks are not clearly visible but may become evident from the analysis of subtle changes in the image content.

7.1.1 Chapter Contributions

This chapter addresses two related image analysis problems.

1. AAA thrombus segmentation. We propose a procedure working on a radial representation of the thrombus contours, enhanced with *a priori* knowledge and modeling of spatial coherence. As seen in the right hand of figure 7.1, thrombus may be touching with other structures of similar intensity, so their boundaries are quite difficult to find, even for a trained radiologist.

2. Semi-automatic detection of endoleaks in CTA images after thrombus volume segmentation.

   (a) Thrombus Connected Components (TCCs) obtained from segmentation of the thrombus image area using a Morphological Grayscale Watershed Transform [32]. Image content-based characteristics are obtained for each TCC.

   (b) Multilayer Perceptron (MLP) [63] classifier is built for the automatic detection of (Type II) endoleaks applied on the segmented lumen and thrombus of the AAA. Classification features are geometric and image content-based characteristics of the TCCs. Ground truth for training the MLP are provided by the human experts that classify a large sample of TCCs into two classes "endoleak" and "non-endoleak".

Experimental results over a collection of abdominal CTA images show good performance of MLP since it is able to characterize and correctly classify image regions inside the aneurysm corresponding to endoleaks after training over the provided labeled sample. Endoleaks are not frequent, therefore imaging data featuring them is scarce. For this reason our system has to be validated at the level of 2D slices, however a 3D extension is straightforward and will be performed when more data is available for training and validation.

The improved thrombus segmentation method is very fast and needs little human interaction for initialization or parameter tuning. Due to its nature, it can be easily incorporated into a user interface in order to provide visual feedback and correction to provide suitable results if, for any reason, the algorithm failed. It may also be adapted for the segmentation of AAAs in non-enhanced CT images. Our approach also considers the presence of the ramification of the iliac arteries in the thrombus region.

7.2 State of the Art

The lumen of the aorta usually presents high contrast in CTA. However, aneurysm thrombus segmentation is not a trivial task due to low-contrast in the ILT region compared to adjacent structures (see Figure 7.1). Manual segmentation by trained radiologists is a time-consuming task and suffers from intra- and inter-observer variability. With the advent of last generation CT scanners, the number of slices per examination has increased and the manual delineation of tenths to hundreds of slices becomes impossible during clinical routine. Hence, the development of automatic or semi-automatic methods for AAAs segmentation is required. Furthermore, quantitative assessment of evolution of aneurysms after EVAR is usually performed by taking the largest diameter or cross-sectional area on a single slice, but volume measurement

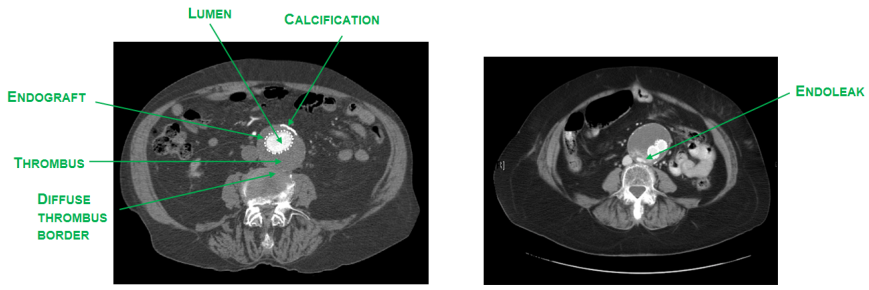

Figure 7.1: Slice showing Abdominal Aortic Aneurysm with different parts (left). A Type II endoleak appears as bright tissue in the thrombus area.

has been demonstrated to show the smallest intra-observer variability [188]. Thus, a (semi)automatic segmentation method would allow patient follow-up using volumetric measurements of aneurysm size.

Automatic or semi-automatic aneurysm segmentation in CTA images is hindered by noise and similarity of Hounsfield Unit (HU) values for neighboring (touching) tissues. Thrombus segmentation strategies proposed in the literature include, among others, deformable models [175, 135, 41], level-set methods [210, 209, 37] or Active Shape Models (ASM) [38]. Some of these methods give reasonable good results but either they are to complex to setup or control by a non-expert or depend on the availability of a good set of training data. Moreover, they are time consuming and require some degree of user interaction, sometimes difficult to implement in an interface for clinical routine.

Previous work presented in [175, 38, 39] need manual delineations to initialize their models. The method of De Bruijne *et al.* needs posterior user intervention in case of thrombus boundary overflow. Olabarriaga *et al.* [135] employs a binary thresholding to obtain the lumen which is used as an initialization for a deformable model to segment the thrombus. Simple thresholding takes into account other tissues not connected to the lumen, so further processing is usually needed to avoid those structures. Furthermore, the use of deformable models needs fine parameter tuning to obtain acceptable results. In this regard, Subasic *et al.*[175] uses a level set approach and Bruijne *et al.* [39] applies an Active Shape Model (ASM). Zhuge *et al.* [209] also presents an algorithm based on a *level-set* approach whose main advantage is the automatization and parameter insensitivity. Nevertheless, the required computing time (about several minutes) is a main drawback. Borghi *et al.* [20] uses region growing segmentation techniques in order to obtain the lumen boundary and then uses manual delineation of the aneurysm wall to obtain a 3D model of Thoracic Aortic Aneurysm (TAA). A computational study of the drag forces that can produce stent displacement is given in [57] for TAA. The work of Lee *et al*. [93] performs an initial estimation of the lumen based on region growing after anisotropic smoothing. Then both the lumen and the thrombotic surfaces are built up using a 3D graph search with cost functions specially designed for the lumen and the thrombus surfaces. Parameter values are empirically set, and the algorithm requires interactive guidance of the thrombus segmentation. Dehmeshky *et*

al. [40] proposed a grayscale and geometric appearance model. Similarly, we use prior knowledge on the appeareance of the aneurysm, but their method requires masking of several adjacent structures.

Regarding endoleak detection, we have not found any work in the literature that addresses the problem of automatic detection and quantification of endoleaks in CTA images.

7.2.1 AAA Segmentation Process

We briefly present the complete AAA segmentation process, consisting of five stages:

1. *Lumen Segmentation*: an initial lumen segmentation is obtained using a region growing algorithm based on confidence measures from a pair or more seed points as implemented in [204]. A robust segmentation of the lumen and thrombus of the AAA is required as input for the automatic endoleak detection system in order to isolate the lumen and thrombus area.

2. *Lumen Centerline Extraction*: performed on a slice by slice basis using 2D image moments on the connected components (CCs). CCs not corresponding to the lumen are discarded by calculating distances of centroids to adjacent slices.

3. *Polar Reformatting*: a slice-based polar reformatting is generated in order to obtain a linear representation of the radial model which is faster to be processed. For each slice, the reformatted is restricted to a certain distance, slightly larger than the expected maximum thrombus diameter. Strictly, this does not constitute a reformatting on cylindrical coordinates but rather, a generalized cylinder. This allows to adapt the shape of the centerline, taking into account its curvature. The presence of a dominant vertical direction makes the method still valid.

4. *Initial Thrombus Segmentation*: based on the analysis of connected components (CCs) described both radially and at slice level. The result is a set of radial contours describing the thrombus outer boundary starting from the inner boundary. It requires a pre-processing step consisting on median filtering in order to remove noise, and a raw thresholding which removes the hyperintense structures corresponding to the stent and other spurious structures. Note that in contrast with other methods, we do not remove any structure outside the thrombus region. The results is a good approximation of the external thrombus contour, with the exception of some areas where the thrombus region invades adjacent structures.

5. *Thrombus Contour Correction*: based on the analysis of discontinuities in the initial contours and statistical information, outlier sectors in radial contours are identified and replaced by interpolation between valid contour segments.

6. *3D Reconstruction and Smoothing*: introduces some volumetric coherence by removing remaining spurious edges.

We first describe the initial approach developed in [114], which is the basis for an improved correction algorithm developed later.

7.3 Lumen and Thrombus Segmentation

In this section we fully describe the lumen segmentation, centerline extraction and thrombus segmentation. Our thrombus segmentation approach is based on a radial description of the thrombus contours.

7.3.1 Region Growing-based Lumen Segmentation

Segmentation of the lumen is based on a 3D region growing algorithm [70] computed on the CTA volume. First, a Volume of Interest (VOI) is defined in order to reduce the data volume and afterwards it is preprocessed to reduce noise. A manually given seed point on the lumen is at least required for the region growing algorithm. The algorithm includes voxels whose intensity values lie in a confidence interval defined in the current segmented region over an iterative process. At each iteration, all neighborhood voxels are visited and the confidence criterion is evaluated. Then, statistics are recomputed and the next iteration begins. The resulting identified region is smoothed by morphological closing so as to fill possible small holes.

7.3.2 Centerline Extraction

The centerline computed as the approximate centroid of the lumen region at each slice is a good approximation of the morphological skeleton of the whole aorta. It serves as the starting point for the thrombus segmentation. A single point on the centerline is obtained for every slice using 2D image moments, since the aorta is almost normal to axial slices. Image moments provide information on the spatial distribution of a given image region corresponding to a structure. The moments of a 2D image are defined as

$$M_{p,q} = \sum_{y=0}^{Y-1} \sum_{x=0}^{X-1} x^p y^q I(x,y), \tag{7.1}$$

where $I(x,y)$ is a discrete image. The centroid is defined as the pair $\left[\frac{M_{10}}{M_{00}}, \frac{M_{01}}{M_{00}}\right]$.

At each slice, we compute the centroid of each connected component of the lumen segmentation mask. The centroid which is the nearest to the centerline point detected in the previous slice is kept as the next centerline point. The algorithm 7.1, yields a series of points that conform the centerline of the segmented lumen.

7.3.3 Thrombus Segmentation

We model the internal and external radius of the thrombus of the aneurysm as radial distance functions in cylindrical coordinates. We can express the volume of interest around the lumen centerline as

$$\Psi = \Psi(r, \theta, z). \tag{7.2}$$

At every z value, corresponding to a slice of the CTA volume, we choose the origin of these functions to be the centerline point at the corresponding slice. The external

Algorithm 7.1 Centerline extraction from 3D lumen region

```
Initialization of region: center line in first processed slice
for all slices in 3D image do
    Identify lumen connected components from the 3D lumen region
    for each lumen component in slice do
        Compute centroid
        Compute Euclidean distance to centerline point in previous slice
    end for
    Keep nearest centroid as the centerline point
end for
```

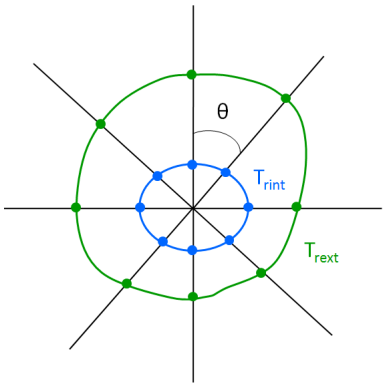

Figure 7.2: Radial model for the thrombus segmentation

and internal radii of the thrombus and the aneurysm can be defined as two contours given by functions of the angle in polar coordinates:

$$\begin{aligned} T_{rint} &= \Psi_{rint}(\theta, z), \\ T_{rext} &= \Psi_{rext}(\theta, z). \end{aligned} \tag{7.3}$$

This idea is depicted in Figure 7.2. The segmentation procedure consists of calculating the values of the internal and external radii T_{rint} and T_{rext} at every angle, which define the closed boundaries enclosing the region corresponding to the thrombus.

Conversion from Cartesian to polar coordinates requires resampling the input VOI. For every slice, a new image is obtained, where X coordinate represents the radius, starting from the centerline point at the left, and Y coordinate represents the angle θ, covering 360 degrees with the origin at the top. This polar representation is visualized in Figure 7.3(b). The original CTA slice is shown in 7.3(a).

Polar representation presents several advantages. Firstly, the VOI is converted to a quasi cylindrical VOI (it is not exactly cylindrical because the centerline is not a vertical line), instead of the typical rectangular prism, and it is treated as a standard volume with a regular grid. Secondly, computation speed is increased, since resampling is only performed once and the polar slices are processed as conventional 2D images.

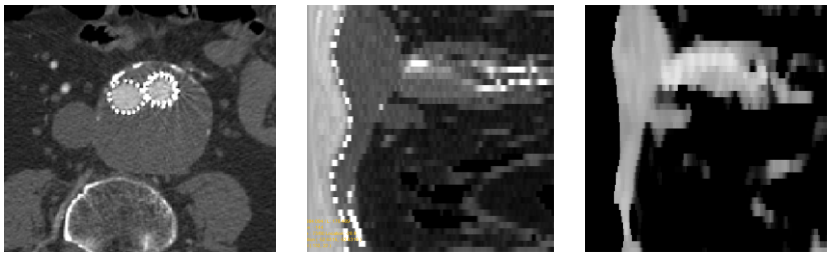

(a) (b) (c)

Figure 7.3: (a) AAA after EVAR viewed on axial slice, (b) polar representation, and (c) median filtered version with lumen and stent thresholded and removed. The origin for the polar coordinate representation of (b) is taken as the centerline in (a).

Following, polar slices are smoothed using a median filter to remove speckle and additive noise coming both for the original and resampled image needed for the polar transformation visualization. In order to remove the lumen and the stent from the images without affecting the thrombus voxels, every slice is thresholded in such a way that those image values higher than a threshold Th_{lmn} are converted into a value I_{bgr}, which approximates the background value of the tissue around the thrombus. In our experiments we chose Th_{lmn}=150 HU[1] and I_{bgr}= -100 HU. The result of this operation is shown in 7.3(c). After noise filtering and lumen/stent thresholding, the thrombus appears as the brightest structure closest to the centerline and we can use this *a priori* information for the segmentation.

The internal thrombus radius T_{rint}, which corresponds to the lumen external contour when no endoprosthesis is present, can be found moving away from the centerline (which corresponds to moving along a row in the polar slice image) as a boundary where values different from I_{bgr} appear. The median filter removes the small regions with lower image values that may exist in between.

Localization of the external radius of the thrombus on each slice in polar coordinates is achieved by a local analysis based on two concepts: *radial connected components* (RCC) and *slice connected components* (SCC). We define an RCC as a connected segment over a row of a polar slice and a SCC as a 2D connected component on a polar slice. First, a row-by-row analysis is performed in all slices to create an image of RCCs of each slice. An RCC is created for consecutive pixels of a row that follow a given membership criterion. We use the absolute difference from the mean of the currently detected RCC with a threshold value Th_{RCC} (we use $Th_{RCC} = 20$HU in our experiments). Obtaining T_{rint} and RCC at each row can be done simultaneously. Algorithm 7.2 illustrates the process for creating the RCCs.

Following, we proceed to filter the RCCs. First, RCCs whose average values are not in the intensity range of $Th_{tlow} - Th_{thigh}$ are removed. In our experiments we used $Th_{tlow} = 0$ HU and $Th_{thigh} = 200$ HU which are conservative values to characterize the thrombus image intensity that apply to most AAA CTA datasets. Second, RCCs that do not start from a distance d_{max} from the external lumen radius are removed. This

[1] HU = Hounsfield Units, a normalized CT image intensity value representing X-ray absorption.

Algorithm 7.2 Creating the Radial Connected Components (RCC)

```
1: Move to the origin of the first polar slice (upper left corner)
2: for all polar slices do
3:     for all rows in the current polar slice do
4:         create a new RCC and insert first pixel on the current row
5:         for all pixels in the current row do
6:             if ( intensity(pixel) ∈ intensity confidence interval of the currentRCC)
   then
7:                 insert pixel in the current RCC
8:             else
9:                 calculate and store row internal thrombus radius
10:        end for
11:    end for
12: end for
```

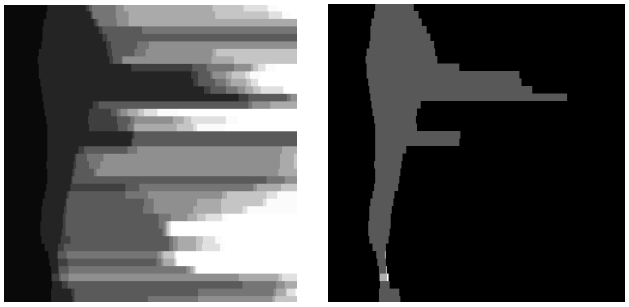

(a) (b)

Figure 7.4: (a) RCCs computed from figure 7.3(c). Different RCCs found along each row are represented in different color (from darker to brighter). (b) filtered RCCs

criterium is based on the fact that if a thrombus exists, this must be almost close to the previously thresholded area of the lumen and endoprosthesis. In our experiments we choose in a very conservative manner $d_{max} = 5$mm. Results of the RCC computation procedure are shown in Figure 7.4. It can be seen that the thrombus has been almost completely isolated, but some RCCs that are not part of the thrombus still remain (see Figure 7.4(b)).

SCCs are computed using 2D connectivity and the same intensity criteria used for RCCs. Each SCC keeps a list of RCCs which are included in it. SCCs are used to filter RCCs by using spatial coherency information on each slice. First, SCCs (and its corresponding RCCs) that contain less than N_{min} voxels (we use $N_{min} = 10$) are discarded since they are not significant at slice level. Next, SCCs are filtered by the position of the centroid, having into account that most of the RCC candidates at this moment are part of the thrombus. For each slice, the position of the centroid for all RCCs and the corresponding centroids median values are calculated. Median value is a good indicator for the real position of the thrombus. Then we compute the distance from the

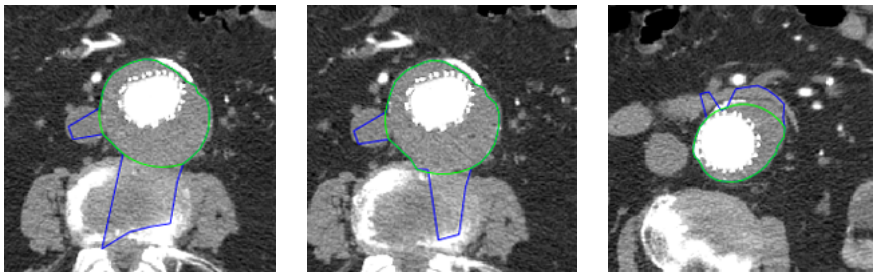

(a) (b) (c)

Figure 7.5: Thrombus segmentation results. Correction (green line) of the initial external thrombus radius (blue line). Examples of appropriate correction (a) and (b) and underestimation (c).

centroid of every SCC on that slice to the median centroid value and if the distance is greater than a threshold like $d_{centroid} = 20mm$, the SCC is completely removed.

Initial values for the thrombus contours T_{rint} and T_{rext} are obtained by taking, for every row on all slices, the first index of the first RCC and the last index of the last RCC on that row (it is assumed that the RCCs remaining after filtering are part of the thrombus). This results in a good approximation to the real external thrombus contour, with the exception of some areas where the thrombus region invades adjacent structures which represent a discontinuity in T_{rext} (see figure 7.5 blue contours). In order to solve this problem and regularize the contours, a continuity constraint is imposed over T_{rext} and the contour points whose radii are part of a discontinuity are interpolated. Discontinuities are identified as significant radius changes from line to line in the polar image. Then, the radii in these areas are linearly interpolated in order to obtain the final result (green contours in figure 7.5).

7.3.4 Initialization Issues

The segmentation of the thrombus may start from a prior lumen segmentation or by automatic detection of the lumen boundaries, as in the experiments performed in this paper. In routine EVAR follow-up CTA images two problems arise at the initialization difficulting the thrombus segmentation: the presence of the stent and the iliac arteries bifurcation.

In our segmentation method, we do not deal with the problem of an accurate stent segmentation. However, the segmentation based on CC analysis is less problematic if we first detect the stent and consider the region outside its boundaries. We simply detect the stent as CCs of high intensity in the close vecinity of the lumen. After removal, it is assumed that the thrombus region corresponds to the adjacent area extending radially.

One major problem found during our initial experiments, was the presence of double iliac arteries in the thrombus region as can be seen in Figure 7.6 (a) and (c). Most of the methods assume that the thrombus is only present in the aortic area, where there is a single branch where the lumen may be found. However, the bulge may be present in the area where the iliac arteries start, even when the aneurysm itself was not present

in this area before the intervention. In this case, the stent forces the two branches of the iliac arteries to be close to each other and there exist two centerline branches.

One solution consists of first segmenting the lumens of both iliac arteries and then extend this segmentation in order to create a convex contour by filling the concave areas between both branches at each slice, as shown on Figure 7.7. This allows us to apply the rest of the segmentation algorithm for the thrombus without further modification. The convex contour may be obtained easily using open and close morphological operations. The radius for the kernel used in such operations may be set manually or may be determined as the apparent radius obtained for each iliac artery. In practice, one has two consider also the presence of the stent so the radius is usually a bit larger and complete convexity is not always needed for the algorithm to work (see Figure 7.6 (c) where the mask is overlaid).

7.3.5 Experimental Results for Thrombus Detection

Our radial-based thrombus segmentation method has been tested on real human CTA datasets with endoleaks detected by radiologists. These images are obtained from a LightSpeed16 CT scanner (GE Medical Systems, Fairfield, CT, USA) with $512 \times 512 \times 354$ voxel resolution and $0.725 \times 0.725 \times 0.8$ mm spatial resolution. Two points inside the lumen, defining the limits of the thrombus region in axial direction, were manually selected as seed points for the 3D region growing segmentation of the lumen. The lumen centerline was then extracted to be used as the origin for the polar representation in an area of radius 10 mm. around the centerline at each slice. Finally, the described radial function-based model was used to segment the thrombus. Some results of the thrombus segmentation method have been presented in Figure 7.5 where the initial estimation (blue) and the corrected external thrombus contours (green) are shown.

7.4 Improved Thrombus Contour Correction

The external thrombus contour correction is based on a continuity constraint imposed over the external contour T_{ext}. We assume that the thrombus is radially smooth, which allows small discontinuities to be first identified as significant radial changes from point to point by using a discontinuity parameter δ.

In order to remove bias in the radius function, we first recompute the centroid and update the angles, which yields a new radial function T'_{rext} for the external contour in which discontinuities are easier to identify. This can be seen in Figure 7.8where the bias due to the offset of the centerline with respect to the thrombus contour was considerably removed. Note that the real center is still unknown and the estimated centroid position can be influenced by the incorrect radial estimates.

After the identification of discontinuities, the contour is divided in radial sectors $S_i(\theta_i, \theta_{i+1})$ defined as:

$$S_i(\theta_i, \theta_{i+1}) = \left\{ T'_{rext}(\theta) : \theta \in [\theta_i, \theta_{i+1}) \right\} : \left| T'_{rext}(\theta_i) - T'_{rext}(\theta_{i-1}) \right| > \delta, \quad \left| T'_{rext}(\theta_{i+1}) - T'_{rext}(\theta_i) \right| > \delta \quad (7.4)$$

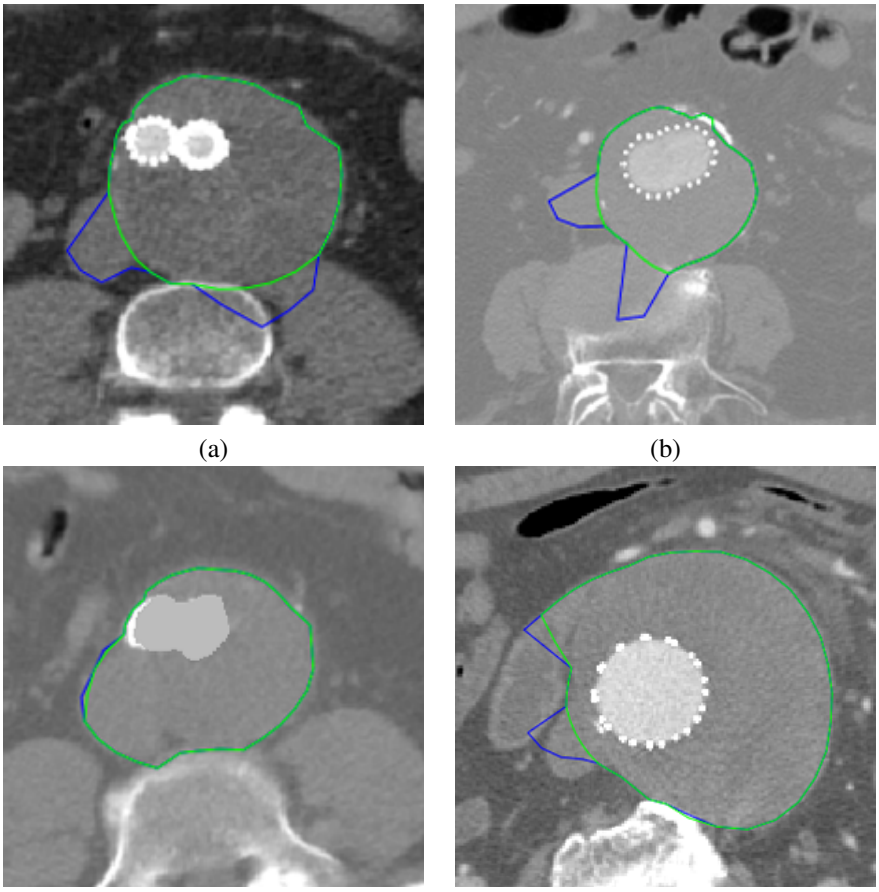

(a) (b)

(c) (d)

Figure 7.6: Segmented slices by our approach showing the initial (blue) and the corrected (green) contours. Note the accuracy in difficult areas. Figure (d) shows some problems found.

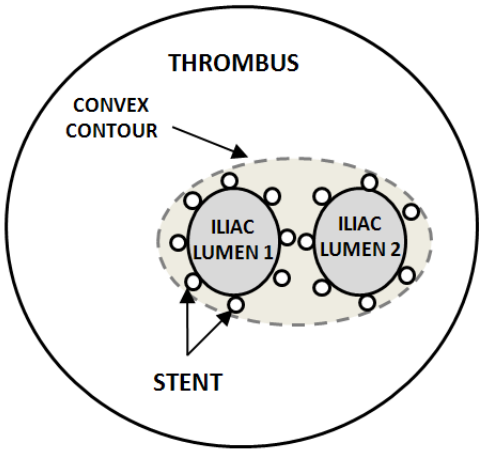

Figure 7.7: Proposed scheme for the lumen segmentation in presence of the iliac arteries in the thrombus region.

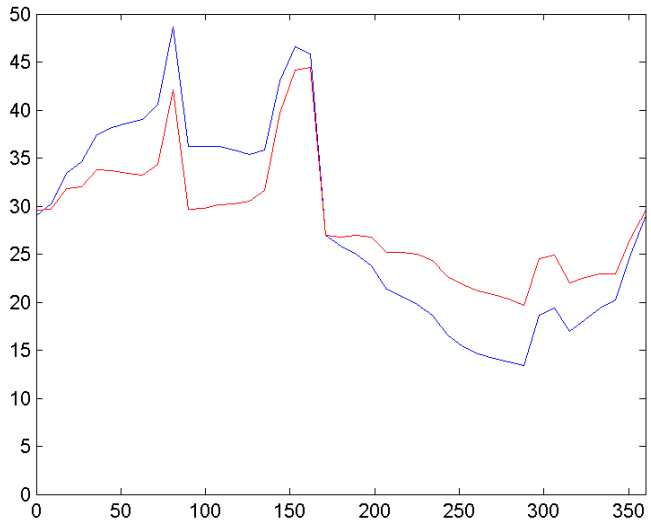

Figure 7.8: Partial removal of bias in radial function of external contour due to recentering. The initial contour is shown in blue and the recentered contour in red. The horizontal axis corresponds to the angle in degrees.

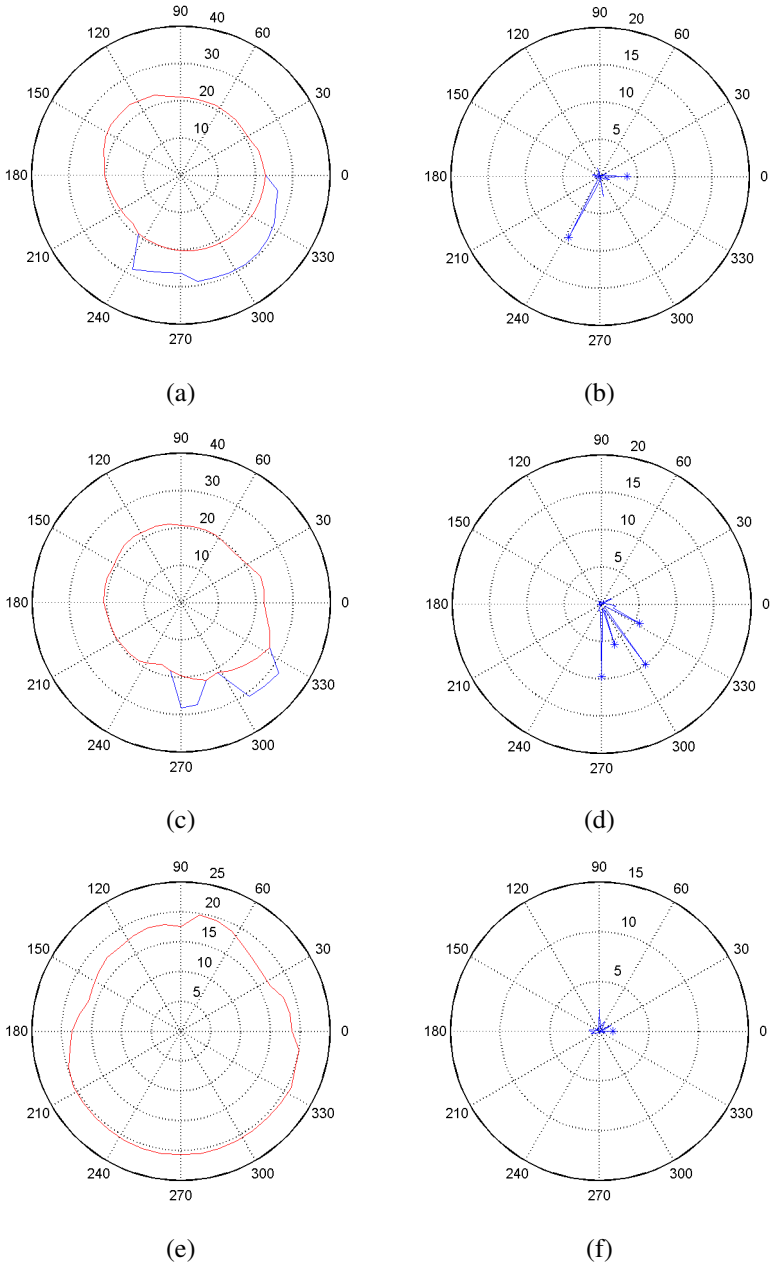

Figure 7.9: Contour correction procedure. Each row corresponds to a different slice. Left column shows the initial contour (blue) and the corrected contour (red) in a polar plot. Right column shows derivative of initial contour and identified discontinuities.

Next we identify the spurious radial sectors. We calculate their average values comparing them with the standard deviation from the median of all radial values. For this purpose, we mark a sector S_i as spurious if:

$$\mu(S_i) > \kappa\sigma_{median}(T'_{rext}) \tag{7.5}$$

where κ is a scaling factor and $\sigma_{median}(T'_{rext})$ is the standard deviation taking the median of the radius values. The use of the median here, instead of the mean, avoids spurious values to influence the calculations by contributing with high radial values to the mean. Confirmed contiguous radial sectors are joined to obtain new sectors. Finally, discarded radial sector values are replaced by linear interpolation between the boundary values of adjacent valid sectors. The procedure is depicted in Figure 7.9 where several initial and corrected contours are depicted. Note how the correction removes the spurious sectors and how some small discontinuities are preserved, that appear naturally in the thrombus due to the presence of adjacent structures pushing it. If necessary, this can be adjusted with the discontinuity parameter δ.

7.4.1 Experimental Results of Improved Thrombus Segmentation

Our method has been initially tested on 5 CTA datasets from real patients under follow-up after EVAR, obtained from a LightSpeed16 CT scanner (GE Medical Systems, Fairfield, CT, USA) with an average $0.725 \times 0.725 \times 0.8$ mm. spatial resolution. These datasets were manually segmented and delineated by experts for comparison. A volume of interest was defined to reduce memory requirements and two seed points inside the lumen were selected for the segmentation of the lumen. Polar representation of the lumen is obtained in an area of 10 mm around the centerline. The described radial approach is used to segment the thrombus contours and finally a mask is obtained by rasterization of the contour on the image grid. In all our experiments, we used 40 angular and 250 radial samples respectively (0.4 mm. radial resolution) for the polar reformatting.

The parameters for the initial thrombus segmentation *were not changed* in our experiments. For the correction step we used values of δ in the range $1.5 - 3.5$. The scaling factor κ was fixed to 1.5 except in one dataset which was 2.5. This allowed us to verify that the parameter sensitivity is low, which is good for routine applications. The results were accurate except in some slices with smooth spurious structures that showed no visible boundaries with respect to the thrombus. Furthermore, the processing time was considerably fast, thrombus segmentation of a single dataset of about 20 slices consumed less than 1 s.in all cases.

In order to assess the accuracy of the thrombus segmentation we performed an initial validation against manual segmentations carefully delineated by experimented raters. For this segmentation, the average overlapping ratio of the automated A and manual B segmentations was calculated as shown in Table 7.1. The first dataset is a typical case of a thrombus segmentation that our method solves with high accuracy (overlapping ratios of 93.52% and 86.76%). The four other datasets are from the follow-up of a single patient and can be considered as a worst-case scenario. The thrombus has a region with double lumen in the iliac arteries and the lumen is very

Dataset	(a)	(b)	(c)	(d)
1	93.52±2.51	86.76±5.17	-	-
2	89.86±7.28	83.55±7.07	95.43±2.67	89.79±3.35
3	93.95±8.86	83.88±10.47	96.07±2.32	89.07±3.54
4	89.91±9.28	81.85±10.33	94.98±2.38	88.73±3.04
5	92.10±6.69	79.65±9.63	93.95±5.72	86.72±4.27

Table 7.1: Overlapping areas in % between proposed method segmentations and ground-truth manual segmentations. (a) = B/A$\bigcup$B, (b) = A$\bigcap$B/A$\bigcup$B. (c)=(a) and (d)=(b) both after removing incorrect contours. Table shows average values for all slices in each datasets.

eccentric. Still, good values are obtained. We also present some filtered values where we removed the slices were the contour was leaking in a few contour points in order to test the accuracy in the remaining slices. Note that these could be easily corrected changing the parameter values for those slices or by manual correction of the contour. Finally, we present a 3D reconstruction of the contours, depicted in Figure 7.10.

7.5 Conclusions on AAA Thrombus Segmentation

The method developed for thrombus segmentation obtains good results in defining the external contour as shown in Figure 7.5, where thrombus density is very similar to adjacent structures, and thus, very prone to segmentation error in areas close to them. The obtained contour is very accurate due to the assumption of a radial model. The method needs the settings of several thresholds to work. However, our experience is that the sensibility of the method to these parameters is low as they were chosen very conservatively. One of the main advantages of the method is its computational speed. It took less than 20s to process 80 slices on a Pentium Core 2 Quad at 2.4 GHz. However, the method requires further improvements since we have observed an underestimation of the radius in some places which were identified as leaks (see Figure 7.5 (c)). Results of this segmentation are comparable to the state of the art found in the literature [93] with less human intervention. Our algorithm does not depend on any user-defined contour or initial manual segmentation. User interaction is minimal: it only requires two seed points contained in the lumen and the range of slices of interest. Accurate segmentations are obtained in areas where it is difficult to distinguish the thrombus from adjacent structures. In addition to this, the speed of the whole process makes it suitable for routine clinical use.

One of the main advantages of the improved method is its efficiency, as it can process a large number of slices in a few seconds with high accuracy (Figure 7.6). Parameter setting is minimal and most of our experiments have used the same set of parameters. The value of δ may be changed in order to allow some tolerance to discontinuities. Increasing the value of κ allows more deviation from the median radius value when the thrombus is very eccentric with respect to the centerline. This makes the method suitable for clinical applications for preoperative planning and follow-up

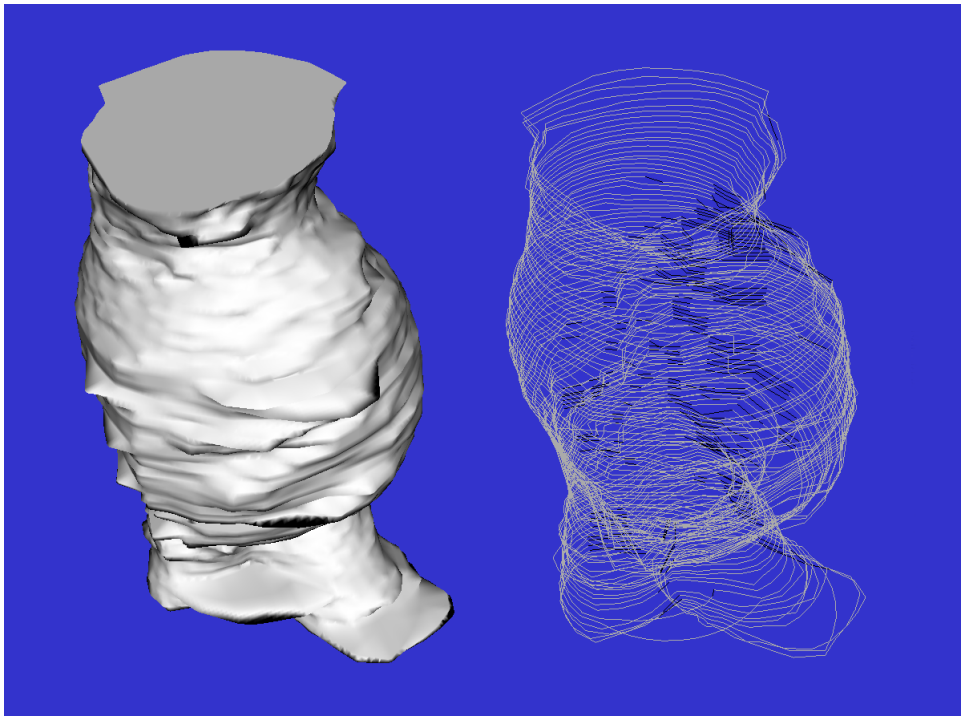

Figure 7.10: 3D polygonal reconstruction (left) and 3D contours (right) for dataset 1.

of EVAR interventions.

We emphasize that the improved method is well suited for the segmentation of AAAs by non image processing experts. The nature of the method, that makes use of a radial approach, can be integrated in a friendly user interface for fast segmentation of CTAs. The user simply would have to invalidate possible incorrect regions of the contour and mark only a few radial points at each erroneous section, either manually or by providing the radius value. Parameter setting is relatively simple and the speed of the method allows for quick visual feedback. . This has been a major consideration in the design of the method, since we expect our algorithm to be part of a software for preoperative planning and follow-up of EVAR interventions. Most of the algorithms fail for one reason or other and we believe that it is important to provide alternatives to fix these errors easily, without fine tuning of complex parameters or complicated contour drawing.

The segmentation algorithm works on a slice-by-slice basis in order to take into account the symmetry with respect to the centerline and to reduce the influence of possible large leaks at volumetric level, where some coherence is introduced by the 3D polygonal smoothing. The polar representation is also advantageous, since it presents the data in the form of a generalized cylinder VOI around the centerline, which implicitly takes into account the radial symmetry, and allows fast calculations based on CCs and run-length encoding.

The method provides accurate results where other methods would fail due to absence of visible thrombus boundaries (Figure 7.6). It improves accuracy with respect to some methods based on smooth curves or deformable models which involve complex calculations. Future work will be oriented to further improve the robustness of the method and perform a more exhaustive clinical validation.

7.6 Endoleak detection

An overview of the processes involved in the automatic endoleak classification system can be seen in Figure 7.11. First the aneurysm lumen and thrombus are segmented using the proposed segmentation method described above. We start from a segmentation of the lumen, based on a 3D region growing algorithm, followed by the calculation of the aorta centerline. The thrombus contour is modeled as a function of the radial distance to the computed centerline. The volume of interest is resampled into polar coordinates centered in the aorta centerline.

The thrombus content is further segmented into Thrombus Connected Components (TCC) (section 7.6.1). Using this polar coordinate reference system, the watershed segmentation obtains the TCCs in the thrombus region at both radial and slice level using heuristics based on *a priori* knowledge and spatial coherence. The radial distance functions that describe the thrombus contour are obtained from the resulting connected components and define the target segmented region. The main advantages of this method are its robustness and speed, compared with the state of the art approaches described previously. It neither employs sophisticated numerical methods, nor needs fine parameter tuning. The TCC features are extracted to be used for classification (section 7.6.2). Once all the features for the TCCs are obtained, these are manually

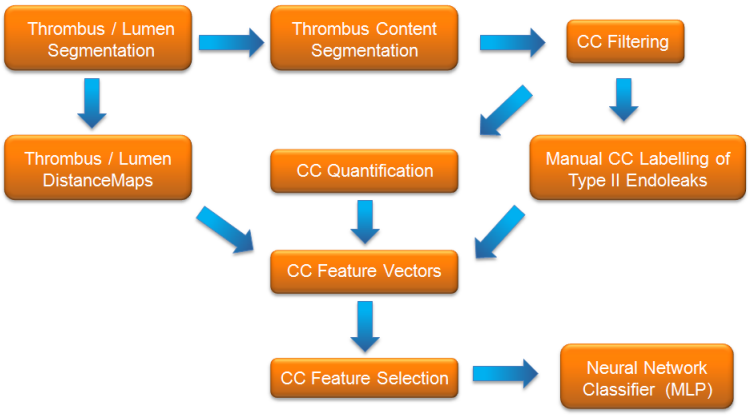

Figure 7.11: Processes of the Automatic Endoleak Classification System

labeled by the experts as endoleaks or non-endoleaks. A feature selection is performed (section 7.6.3) to remove redundant or confusing features. This data is used as input for the training and validation of the MLP neural network classifier. Our approach to endoleak detection is based on *a priori* knowledge of the possible location and appearance of endoleaks in CTA images according to what it is described in medical articles, the indications given by expert interventional radiologists, and their manual labeling of relevant TCCs corresponding to endoleaks.

7.6.1 Thrombus Connected Component Extraction

After the initial thrombus and lumen segmentation, the thrombus is further segmented in Thrombus Connected Components (TCCs) which will be later classified as being endoleaks or not. This segmentation is based on a Topological Grayscale Watershed Transform [32] applied on a slice by slice basis in the area of the segmented thrombus on each slice (see Figure 7.12). First, the image is smoothed using an edge-preserving smoothing filter based on a level-set modified curvature diffusion equation (MCDE) [189]. Two parameters are required for the filter: the conductance parameter, which controls the strength of the edges to preserve and the number of smoothing iterations, which controls the degree of smoothing. After filtering, in order to define the watersheds basins, we then calculate the image gradient magnitude.

The Topological Grayscale Watershed Transform is an algorithm for calculating the well-known Watershed Transform [16] in which the image is segmented based on its topology. The gradient magnitude is interpreted as an elevation map and the image relief is flooded dividing it into catchment basins. The pixels of each basin share a local minima and the basin boundaries corresponds to the image edges. The Watershed transform calculation is controlled by a single parameter, the Water Level, that controls the height of the flooding, merging adjacent regions as the 'water' ascends to reduce the effect of oversegmentation.

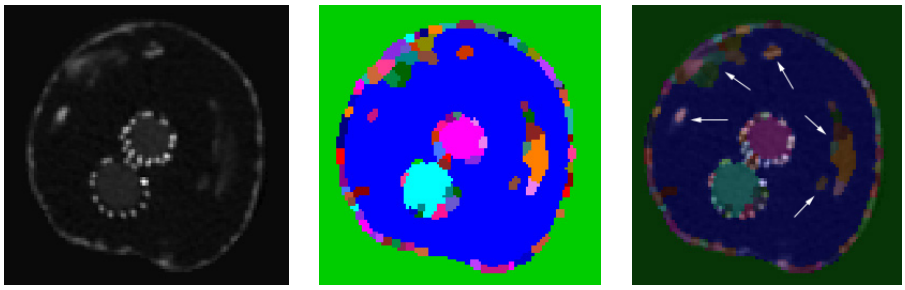

(a) (b) (c)

Figure 7.12: Extraction of Thrombus CCs. (a) Source slice with visible endoleaks, (b) result of Watersheds segmentation, and (c) blended result. Endoleaks are indicated by arrows in (c). Each endoleak corresponds to more than one colored region (oversegmentation).

The parameters for all filters involved in this segmentation are chosen in order to distinguish the endoleaks from the background region corresponding to the thrombus, or other adjacent structures. Endoleaks can correspond to a single or several TCCs (oversegmentation) if the water level is low. If it is high, we would have TCC corresponding to both endoleak and other tissues (undersegmentation). Classifying oversegmented endoleaks is not a problem, but solving the undersegmentation problem is not easy. Therefore the Water Level parameter is set to avoid undersegmentation.

7.6.2 Feature Extraction from TCC

We calculated the following geometric features for each labeled TCC that will be used by the MLP-based classification system to determine if the TCC is part of an endoleak region:

- *Area*: number of pixels of the TCC.
- *Area-region Ratio*: ratio of the TCC's bounding box and the area.
- *Binary Principal Moments*: TCC's principal moments of inertia (two features).
- *Equivalent Radius*: radius of a circle of the same area as the TCC and the following image content-based statistical features computed from the image intensity of the CTA image region corresponding to the TCC: *Mean*, *Sigma*, *Median*, *Kurtosis*, *Skewness* and *Elongation* (ratio of the largest to smallest principal image moments).

Besides these features, we need to incorporate another feature that describes the relative position of the TCC with respect to the lumen and thrombus boundaries. We can profit from the observation that Type II endoleaks typically appear close to the thrombus boundary and perfusing inwards. We need this feature to be normalized, since the radius and shape of the thrombus and lumen, and the eccentricity of the lumen with

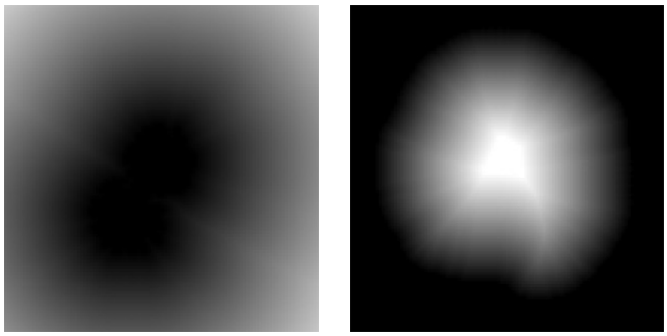

(a) (b)

Figure 7.13: Visualization of the distance maps used to calculate the NTD feature. (a) distance to the lumen δ_{lm} and (b) distance to the thrombus δ_{th}.

respect to the thrombus is not uniform. Moreover, the lumen can show two branches when the aorta splits in two, forming the iliac arteries (see Figure 7.12(a)), so we cannot take the distance to the lumen centroid. Taking all these considerations into account, we propose a feature called Normalized Thrombus Distance (NTD). Two distance maps are first calculated from the thrombus boundary inwards (δ_{lm}), and from the lumen thrombus boundary outwards (δ_{th}), using Danielsson's algorithm [35] (see distance visualization in figure 7.13). In the rest of image regions the NTD value is zero. Then, we calculate the NTD as:

$$NTD = \begin{cases} \frac{\delta_{lm}}{\delta_{th}} & \text{if} \quad \delta_{lm} \leq \delta_{th} \\ \frac{\delta_{th}}{\delta_{lm}} & \text{if} \quad \delta_{th} \leq \delta_{lm} \end{cases} \tag{7.6}$$

The NTD takes its maximum value of one at thrombus points that are equidistant to the lumen and thrombus boundaries. NTD minimum value is zero and it is taken at the thrombus boundary and outside the thrombus, and at the lumen boundary and inside the lumen. NTD takes values in $[0,1]$ inside the thrombus. For the thrombus and lumen boundaries used as input for the NTD, we can use the segmentation described in 7.3 or a manual segmentation.

7.6.3 Reduced Feature Vector for MLP

Let us call the dependent indicative variable *IsLeak*. Its value is 0 for negative TCC and 1 for TCC inside endoleaks. In order to reduce the classifier system's complexity and increase the speed of the calculations, a subset of features is selected as input for the network based on the absolute value of the *Pearson* correlation coefficients between the dependent variable *IsLeak* and the rest of variables (features) defined as:

$$r = \frac{\sigma_{XY}}{\sigma_X \sigma_Y} \tag{7.7}$$

In Figure 7.14 we can see the results of calculating the absolute value of the *Pearson Coefficients* for the CCs of all the slices in the aneurysm region for a given dataset. As

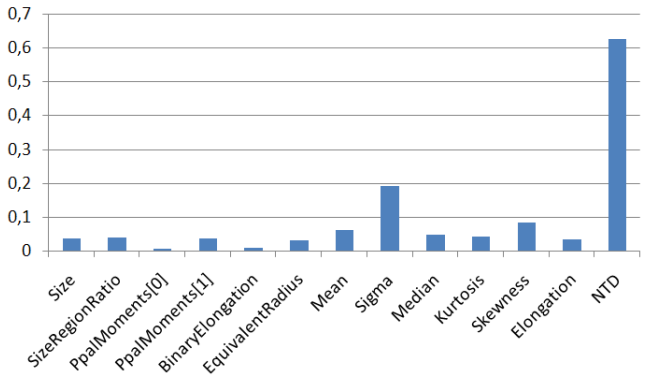

Figure 7.14: Absolute value of Pearson's Correlation Coefficients of each feature with the indicative variable *IsLeak*.

expected, we can see that the NTD feature is highly correlated with the dependent variable, since the feature was designed to incorporate the *a priori* knowledge of the spatial distribution of the endoleaks. As it can be seen, the standard deviation value plays an important role in the characterization of endoleaks, as it was expected. The experimental results show that the reduced feature vector obtain by this straightforward approach give comparable classification results.

7.6.4 Endoleak Detection Experimental Results

The classification scheme was tested independently on each single CTA volume from patients with Type II endoleak after EVAR treatment. The whole volumes consisted of 383 slices in a 512×512 matrix, with an in-plane spatial resolution of 0.703 mm. and a slice thickness of 0.8 mm. Due to the scarce availability of volumes from patients affected with endoleaks, we tested our approach independently on each volume, working on a 2D slice-by-slice basis. In each case, we took as input for the MLP training the results of a segmentation of the lumen and thrombus regions validated by expert radiologists. The Watershed-based segmentation was performed on the slices corresponding to the aneurysm region in each dataset using the implementation provided by the *Insight Toolkit* [70] for the Topological Grayscale Watershed Transform. We used the following parameters for the different filters involved in the watershed segmentation: smoothing conductance = 50.0, smoothing number of iterations = 10, Watersheds water level[2] = 9.0. The *NTD* distance-map feature was calculated from the input thrombus and lumen segmentations. The TCCs were manually labeled as being part of an endoleak. From the group of negative TCCs, we proceeded to select randomly an equal number of samples in order to obtain a balanced training/testing set.

Classification experiments were performed using the MLP implementation provided in [197]. The MLP neural network consisted feature described in section 7.6.2,

[2] As a percentage of current image dynamic intensity range

DataSet	Accuracy	Sensitivity	Specificity
1	92.39	93.43	91.36
2	93.68	93.66	93.69
3	93.09	93.66	92.52
4	93.21	94.13	92.29
5	92.16	93.43	90.89
Av.	92.90	93.66	92.15

Table 7.2: Classification results for the training/test data build from full feature vectors, 10-fold cross-validation. The table shows the total accuracy, sensitivity and specificity for each dataset. Last row shows the average across datasets. All calculations were performed with 3 hidden nodes, learning rate = 0.3 and training time = 550 epochs.

DataSet	Accuracy	Sensitivity	Specificity
1	93.79	94.84	92.76
2	94.73	94.37	95.09
3	93.68	94.60	92.76
4	93.33	94.13	92.52
5	92.74	93.90	91.59
Av.	93.65	94.37	92.94

Table 7.3: Classification results for the training/test data build from reduced feature vector, 10-fold cross-validation. The table shows the total accuracy, sensitivity and specificity for each dataset. Last row shows the average across datasets. All calculations were performed with 3 hidden nodes, learning rate = 0.3 and training time = 550 epochs.

a hidden layer with three neurons and two binary outputs, with sigmoid functions. Network training and validation was performed using 10-fold cross-validation in all computational experiments. Initially, we used the full training/test set consisting of the full feature vectors described in section 7.6.2. The results are shown in table 7.2. Results are above 90% accuracy, with a high sensitivity which is very interesting because the cost of false negatives is much higher than that of false positives.

Next, we tested the improvement in the classification results by testing reduced sets of features selected according to the correlation results found in section 7.6.3 (Figure7.14). The best results were obtained by selecting the following features: *Area*, *Mean*, *Sigma* and *NTD*. We can see in Table 7.3 that the classification rate improves, reaching 93.65% accuracy with a sensitivity of 94.37% and a specificity of 92.94%. The best results give a success rate of 94.73% with a sensitivity of 94.37% and a specificity of 95.09% for the second dataset.

Figure 7.15 shows the influence of several parameters of the MLP in the classification performance measures. The best results are obtained when setting the training time to 550 epochs, the learning rate to 0.3 and hiding 3 nodes. These sensitivity experiments were performed on the training/test dataset that gave best results on the reduced feature vector (dataset 2).

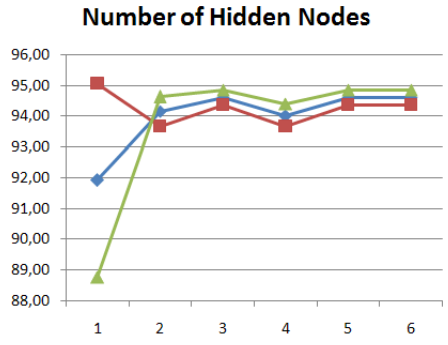

(a)

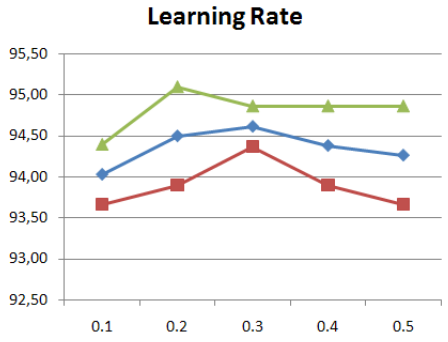

(b)

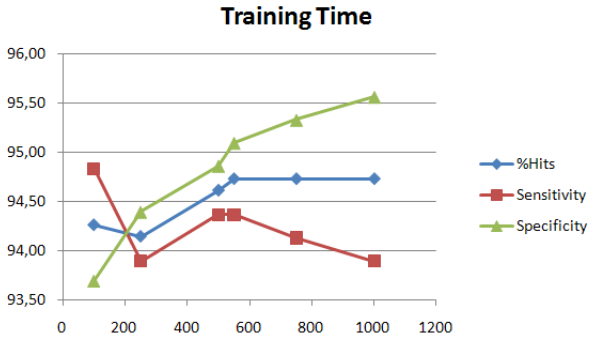

(c)

Figure 7.15: Influence of Neural Network Parameters. Accuracy, sensitivity and specificity are calculated. Parameters tested are number of hidden nodes (a), learning rate (b) and training time measured in number of epochs (c).

7.7 Conclusions on Endoleak Detection

We have demonstrated an automatic system for the detection of (Type II) endoleaks in CTA images of Abdominal Aortic Aneurysms. The classification results show that the system is able to detect endoleaks with high accuracy based on the analysis of extracted TCCs. The use of neural networks is specially adequate for this case, since we do not need to explicitly incorporate the clinical *a priori* knowledge in terms of precise parameters and thresholds for image intensities, distances, etc. This is a common characteristic in many classification problems in medical imaging, in which the specialist is able to discriminate at first sight the object of interest, but is not able to explicitly indicate the rules that guide their mental discourse while diagnosing, which is usually the product of accumulated experience and observations.

Classification results over several real datasets in Tables 7.2 and 7.3 show that the system obtains accuracy results above 90% with high sensitivity, which is specially important given the high cost of not recognizing endoleaks present in the image. We have also demonstrated that a careful selection of features decreases the complexity of the problem and improves the results. There is no similar work in the literature, therefore the results can be assumed as a initial reference for future works.

Regarding the parameters used for the MLP model, in the case of using five features, the results are very similar when the number of hidden nodes are two or more. Using five, six or more nodes does not improve the results and so the best balance is found with three nodes. It can be seen that the influence of the learning rate is limited when the number of epochs is high enough (around 500). With respect to the training time, best results are obtained with 550 epochs and global classification results do not improve by increasing this number. However, the plots show that the sensitivity decreases as the specificity increases, keeping a constant rate of total hits. This is undesirable since we want the sensitivity to be high, and thus the optimum is found at 550 epochs.

In the near future, we expect to extend the system to 3D analysis of TCCs and to the detection of endoleaks obtained from several datasets. Since the diagnosis of endoleaks is not totally certain, we also expect to incorporate a fuzzy or probabilistic description in order to determine which TCCs are endoleaks. Another possible improvement to the system is the classification of other types of endoleaks (I, III, IV and V) since currently the system was trained only to identify Type II endoleaks. This would probably need the incorporation of other types of features for the analysis. Finally, the system would need deeper clinical validation in order to integrate it in clinical environments for diagnosis support of the evolution of AAAs treated with EVAR.

Appendix A

Ideal Shape Models for Vascular Analysis

A.1 Ideal Cylinder

A.1.1 Definition

Definition 2. The equation of a such a volumetric cylinder model with Gaussian cross-section, in cartesian coordinates is:

$$I_{cyl}(x,y,z) = K \exp\left(-\frac{x^2+y^2}{2\sigma_0^2}\right), \tag{A.1}$$

where σ_0 is the standard deviation of the Gaussian section which defines the apparent radius of the cylinder, and constant K is the intensity at the center of the cylinder[1].

If $K = 1/2\pi\sigma_0^2$ we obtain the unit area integral for the 2D Gaussian section, but in general we will assume $K = 1$in most of the following calculations unless told otherwise. This will allow us to compare values for different choices of radius.

A.1.2 Derivatives of the Ideal Cylinder

The first order derivatives are computed as follows:

$$\frac{\partial I_{cyl}}{\partial x} = -\frac{x}{\sigma_0^2} I_{cyl} \tag{A.2}$$

$$\frac{\partial I_{cyl}}{\partial y} = -\frac{y}{\sigma_0^2} I_{cyl} \tag{A.3}$$

[1]Do not confuse this standard deviation with the scale corresponding to the standard deviation σ of the Gaussians used for derivative calculations. Here, $\sigma_0$is the real diameter of the tube, which is usually unknown at the detection stage in real datasets.

$$\frac{\partial I_{cyl}}{\partial z} = 0 \tag{A.4}$$

which are zero at the center of the tube. The second order derivatives are computed as follows:

$$\frac{\partial^2 I_{cyl}}{\partial x^2} = -\frac{1}{\sigma_0^2} I_{cyl} + \left(-\frac{x}{\sigma_0^2}\right)\left(-\frac{x}{\sigma_0^2}\right) I_{cyl} = \frac{x^2-\sigma_0^2}{\sigma_0^4} I_{cyl} \tag{A.5}$$

Similarly we can calculate the rest of derivatives. The resulting Hessian matrix is:

$$H = \frac{1}{\sigma_0^4} I_{cyl} H' \tag{A.6}$$

with

$$H' = \begin{bmatrix} x^2-\sigma_0^2 & xy & 0 \\ xy & y^2-\sigma_0^2 & 0 \\ 0 & 0 & 0 \end{bmatrix} \tag{A.7}$$

A.1.3 Eigenvalues and Eigenvectors of the Hessian Matrix

Lemma 3. *The Hessian matrix of an ideal cylinder with Gaussian cross-section has three different eigenvalues. The eigenvalue corresponding to the axial direction is identically zero for all values of the radius $r = \sqrt{x^2+y^2}$. The remaining eigenvalues correspond to derivatives of the Gaussian function of odd order with respect to r multiplied by some constant.*

Proof. The characteristic equation of $H'$is:

$$\left(x^2-\sigma_0^2-\lambda'\right)\left(y^2-\sigma_0^2-\lambda'\right)\left(-\lambda'\right)+x^2y^2\lambda' = 0. \tag{A.8}$$

The first eigenvalue, corresponding to the z direction is:

$$\lambda_3 = 0. \tag{A.9}$$

The other two eigenvalues are the solution to the equation:

$$\left(x^2-\sigma_0^2-\lambda'\right)\left(y^2-\sigma_0^2-\lambda'\right)-x^2y^2 = 0.$$

By multiplying and reordering terms we obtain the second order equation:

$$\lambda'^2+\left(-x^2+2\sigma_0^2-y^2\right)\lambda'+\left[\sigma_0^4-\left(x^2+y^2\right)\sigma_0^2\right] = 0$$

The solution can be obtained analytically:

$$\lambda' = \frac{1}{2}\left(x^2-2\sigma_0^2+y^2\right) \pm \frac{1}{2}\sqrt{\left(-x^2+2\sigma_0^2-y^2\right)^2-4\left[\sigma_0^4-\left(x^2+y^2\right)\sigma_0^2\right]} = 0,$$

$$\lambda' = \frac{1}{2}\left(x^2-2\sigma_0^2+y^2\right) \pm \frac{1}{2}\sqrt{x^4+4\sigma_0^4+y^4-4\left(x^2+y^2\right)\sigma_0^2+2x^2y^2+4\left(x^2+y^2\right)\sigma_0^2-4\sigma_0^4} = 0,$$

$$\lambda' = \frac{1}{2}\left(x^2 - 2\sigma_0^2 + y^2\right) \pm \frac{1}{2}\sqrt{x^4 + 2x^2y^2 + y^4} = 0,$$

$$\lambda' = \frac{1}{2}\left(x^2 - 2\sigma_0^2 + y^2\right) \pm \frac{1}{2}\left(x^2 + y^2\right) = 0,$$

which results in the eigenvalues:

$$\lambda_1 = \frac{x^2 + y^2 - \sigma_0^2}{\sigma_0^4} I_{cyl}. \tag{A.10}$$

$$\lambda_2 = \frac{-1}{\sigma_0^2} I_{cyl}. \tag{A.11}$$

The third eigenvalue is zero for all values of r. The second eigenvalue is the inverted cylinder function, which can be considered a zero order derivative. The third eigenvalue correspond to the second derivative of the Gaussian function with respect to r. □

Lemma 4. *The Hessian matrix of the ideal cylinder with Gaussian cross-section has three different eigenvectors, one in the axial direction and the rest in radial directions perpendicular to each other.*

Proof. For the first eigenvector we have the set of equations:

$$-y^2 v_x + xyv_y = 0$$

$$xyv_x - x^2 v_y = 0$$

$$\left(-x^2 - y^2 + \sigma_0^2\right) v_z = 0$$

The first two equations yield the relationship:

$$v_x = \frac{x}{y} v_y$$

From the last equation we obtain:

$$v_z = 0$$

Since any multiple of an eigenvector is also an eigenvector, we can arbitrarily choose $v_y = y$ obtaining the eigenvector:

$$x_1 = [x, y, 0]^T, \tag{A.12}$$

which is in the radial direction. For the second eigenvector the set of equations is:

$$x^2 v_x + xyv_y = 0,$$

$$xyv_x + y^2 v_y = 0,$$

$$\sigma_0^2 v_z = 0.$$

Then, the second eigenvector is:

$\lambda_1 = \frac{x^2+y^2-\sigma_0^2}{\sigma_0^4} I_{cyl}$	$\lambda_2 = \frac{-1}{\sigma_0^2} I_{cyl}$	$\lambda_3 = 0$
$x_1 = \begin{bmatrix} x & y & 0 \end{bmatrix}$	$x_2 = \begin{bmatrix} -y & x & 0 \end{bmatrix}$	$x_3 = \begin{bmatrix} 0 & 0 & 1 \end{bmatrix}$

Table A.1: Eigenvalues and vectors for the ideal Gaussian cylinder

$$x_2 = [-y, x, 0]^T \tag{A.13}$$

which is also in the radial direction. Finally, for the third eigenvector the set of equation is:

$$\left(x^2 - \sigma_0^2\right) v_x + xy v_y = 0$$
$$xy v_x + \left(y^2 - \sigma_0^2\right) v_y = 0$$
$$0 v_z = 0$$

The first two equations give $v_x = 0$ and $v_y = 0$, whereas v_z can take any value. We arbitrarily choose $v_z = 1$ obtaining:

$$x_3 = [0, 0, 1]^T \tag{A.14}$$

which is in the axial direction. □

Table A.5 summarizes the eigenvalues and vectors for the ideal cylinder. As we can see the eigenvalue λ_3 is ideally zero at any point of the cylinder, not only at the center. The reason is that there is no intensity change in the direction of the cylinder axis. We can see that λ_2 is strictly negative and λ_1 is negative inside the cylinder, that is when the distance to the center $r^2 = x^2 + y^2$ is smaller than the radius, that is $r < \sigma_0$.

A.1.4 Cylindrical Coordinates

The expressions for the ideal cylinder can be simplified by taking cylindrical coordinates as a reference system which, due to its cylindrical symmetry are the most natural way of describing the model. The change from cartesian (x, y, z) to cylindrical (r, θ, z) coordinates is:

$$\begin{aligned} r &= \sqrt{x^2 + y^2} \\ \theta &= atan\left(\tfrac{y}{x}\right) \\ z &= z \end{aligned} \tag{A.15}$$

The inverse coordinate transformation is:

$$\begin{aligned} x &= r\cos\theta \\ y &= r\sin\theta \\ z &= z \end{aligned} \tag{A.16}$$

The change of coordinates results in the following expression for the ideal cylinder:

$$I_{cyl}(r,\theta,z) = K \exp\left(-\frac{r^2}{2\sigma_0^2}\right) \tag{A.17}$$

We can see that this expression only depends on the variable r.

A.1.5 Derivatives in Cylindrical Coordinates

The first-order derivatives of the ideal cylinder are:

$$\frac{\partial I_{cyl}}{\partial r} = -\frac{r}{\sigma_0^2} I_{cyl} \tag{A.18}$$

$$\frac{\partial I_{cyl}}{\partial \theta} = \frac{\partial I_{cyl}}{\partial z} = 0 \tag{A.19}$$

The calculation of the Hessian matrix is also straightforward:

$$H = \frac{1}{\sigma_0^4} I_{cyl} \begin{bmatrix} r^2 - \sigma_0^2 & 0 & 0 \\ 0 & 0 & 0 \\ 0 & 0 & 0 \end{bmatrix} \tag{A.20}$$

Proposition 5. *The Hessian matrix of the ideal cylinder with Gaussian crosss-section expressed in cylindrical coordinates has a single non-zero eigenvalue corresponding to a function of the second-derivative of the Gaussian with respecto to r. This main curvature occurs in the radial direction.*

Proof. From the above matrix we have the characteristic equation:

$$\left(r^2 - \sigma_0^2 - \lambda\right)\lambda^2 = 0 \tag{A.21}$$

The eigenvalues are:

$$\lambda_1 = \frac{r^2 - \sigma_0^2}{\sigma_0^4} I_{cyl} \tag{A.22}$$

$$\lambda_2 = 0 \quad (m = 2) \tag{A.23}$$

The eigenvector corresponding to the eigenvalue in the radial direction is obtained by the equations:

$$\begin{gathered} \left(r^2 - \sigma_0^2 - r^2 + \sigma_0^2\right) r_1 = 0 \\ \left(\sigma_0^2 - r^2\right) \theta_1 = 0 \\ \left(\sigma_0^2 - r^2\right) z_1 = 0 \end{gathered}$$

From the last two expressions $\theta_1 = z_1 = 0$ The first expression is true for any r_1 and we can take arbitrarily $r_1 = 1$. In order to obtain a vector in cartesian coordinates we can replace these values in equation A.16:

$\lambda_1 = \frac{r^2-\sigma_0^2}{\sigma_0^4} I$	$\lambda_2 = 0 \quad (m=2)$
$x_1 = \begin{bmatrix} x & y & 0 \end{bmatrix}$	$x_2 = \begin{bmatrix} 0 & 0 & 1 \end{bmatrix}$

Table A.2: Eigenvalues and eigenvectors for the ideal Gaussian cylinder in polar coordinates

$$x_1 = \begin{bmatrix} 1 \\ 0 \\ 0 \end{bmatrix} \tag{A.24}$$

which points in the direction of x. In fact, the condition that $r = 1$ means that $\sqrt{x^2+y^2} = 1$ so we could take any eigenvector that satisfies the conditions:

$$\begin{aligned} &\sqrt{x^2+y^2} = 1 \\ &z = 0 \end{aligned} \tag{A.25}$$

which is any radial direction. □

Note that the condition that $r = 1$ was taken arbitrarily, so instead a section circle of unit radius, the eigenvector degenerates to the section plane passing by the origin at $z = 0$. Thus, we can rewrite the first eigenvector as[2]:

$$x_1 = \begin{bmatrix} x \\ y \\ 0 \end{bmatrix} \tag{A.26}$$

The second eigenvector corresponds to:

$$\begin{aligned} \left(r^2 - \sigma_0^2\right) r_2 &= 0 \\ 0\,\theta_2 &= 0 \\ 0\,z_2 &= 0 \end{aligned}$$

The first expression yields $r_2 = 0$ and the other two expressions are valid for any θ_2, z_2. By replacing these values in eq. A.16 we obtein the z axis as eigenvector:

$$x_2 = \begin{bmatrix} 0 \\ 0 \\ 1 \end{bmatrix} \tag{A.27}$$

To sum up, we have obtained the following eigenvalues and eigenvectors for the ideal cylinder with Gaussian cross-section:

The eigenvalues and vectors reflect that one the principal curvatures occurs in the z direction (cylinder axis) and the other two curvatures occur in any two orthogonal directions in cross-section plane containing the origin. Hence the double multiplicity

[2]Note that for the unit eigenvector we would need to divide by $r = \sqrt{x^2+y^2}$ but we avoid this for simplicity.

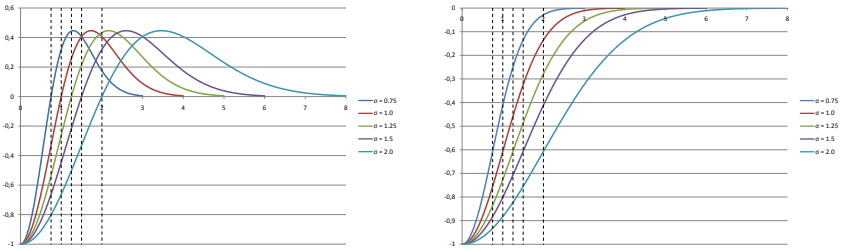

Figure A.1: Analytical values of the scale-normalized eigenvalues λ_1(left) and λ_2(right) as a function of the distance to the center obtained for the ideal cylinder model at different scales.

of the second eigenvalue. Thus, intensity only varies on the radial direction and the surface defined by any r value is an iso-surface with value:

$$I_{cyl}(r = R, \theta, z) = K \exp\left(-\frac{R^2}{2\sigma_0^2}\right) \tag{A.28}$$

Figure A.1shows the values of λ_1 and $\lambda_2$as a function of the distance to the cylinder axis for different cylinder radius, where the apparent radius is the standard deviation of the Gaussian section. In order to be able to compare the absolute values, they have been normalized across-scale by multiplying by σ_0^2.[3]

We can see that both eigenvalues take a value of zero at the center of the cylinder. The first eigenvalue $\lambda_1$is exactly zero at the cylinder radius, and starts increasing until it reaches a maximum value outside the cylinder. Its maximum value can be obtained analytically by the condition:

$$\frac{\partial \lambda_1(r)}{\partial r} = 0$$

for $r \neq 0$. The value of the radius for this maximum is:

$$r(\lambda_{1MAX}) = \sqrt{3}\sigma_0 \tag{A.29}$$

and the corresponding maximum value is:

$$\lambda_{1MAX} = 2\,e^{-1.5} = 0.4463 \tag{A.30}$$

Thus, for any cylinder radius, λ_1 gives a positive response with a peak of 44,63% of the maximum negative response at a distance of approximately $0.732\sigma_0$ from the

[3]Note that the derivatives calculated here are not scaled derivatives but analytical exact derivatives. However, by multiplying by σ_0^2 the values of the derivatives are normalized with respect to the cylinder radius as if we were computing derivatives in scale-space. This way values can be compared in a straightforward manner.

radius outside the cylinder. The signal recays rapidly from the center, and crosses zero exactly at the cylinder radius.

The second eigenvalue λ_2 corresponds exactly to an inverted Gaussian function, which is negative for any value of r and tends to zero at some distance outside the cylinder. It is easy to calculate the decay of this signal. For example, the normalized 97% decay of the signal can be calculated as:

$$0,03 = \exp\left(-\frac{r^2}{2\sigma_0^2}\right)$$

By taking logarithms on both sides we obtain:

$$r(\lambda_2 = 0.03) = 2.2648\sigma_0 \tag{A.31}$$

For the 50% decay, we obtain:

$$r(\lambda_2 = 0.5) = 1.1774\sigma_0 \tag{A.32}$$

That is, the signal of λ_2 is still quite powerful in the close neighborhood of the tube, and decays rapidly until being close two zero at more than twice the radius distance.

From the plots we can also visualize another property of the response of λ_2 that can be demostrated analytically.

Proposition 6. *The second eigenvalue of the Hessian matrix of the ideal cylinder with Gaussian cross-section, has an inflection point exactly at the location of the radius, that is for* $r = \sigma_0$

Proof. The condition for the inflection point is:

$$\lambda_2''(r) = \frac{\partial^2 \lambda_2}{\partial r^2} = 0 \tag{A.33}$$

The second derivative is:

$$\lambda_2''(r) = \frac{\sigma_0^2 - r^2}{\sigma_0^4} exp\left(-\frac{r^2}{2\sigma_0^2}\right) = -\lambda_1 \tag{A.34}$$

resulting in:

$$r\left(\lambda_2'' = 0\right) = \sigma_0$$

The value at this inflection point is:

$$\lambda_2\left(r\left(\lambda_2'' = 0\right)\right). \tag{A.35}$$

□

A.2 Non-tubular Shape Models

A.2.1 Ideal Flat Structure

Definition 7. The ideal flat structure represents a thin, planar structure of infinite extension. The intensity variation occurs only in a principal direction corresponding to the normal to the surface. We can model the intensity profile accross the surface by a Gaussian function. If we make this direction coincide with the z axis, the corresponding equation is:

$$I_{flat}(x,y,z) = K \exp\left(-\frac{z^2}{2\sigma_0^2}\right) \tag{A.36}$$

A.2.2 Ideal Blob Structure

Definition 8. A blob structure is an structure with no preferred direction for the intensity variation and can be modelled as a Gaussian sphere corresponding to the equation:

$$I_{blob}(x,y,z) = K \exp\left(-\frac{x^2+y^2+z^2}{2\sigma_0^2}\right) \tag{A.37}$$

We can take into account the symmetry of the problem an analyze it in spherical coordinates, using the following coordinate transformation:

$$\begin{array}{ll} r = \sqrt{x^2+y^2+z^2} & \\ \theta = a\tan\left(\frac{y}{x}\right) & 0 \leq \theta < 2\pi \\ \varphi = a\cos\left(\frac{z}{r}\right) & 0 \leq \varphi < \pi \end{array} \tag{A.38}$$

The inverse coordinate transformation is:

$$\begin{array}{l} x = r\cos\theta\sin\varphi \\ y = r\cos\theta\sin\varphi \\ z = r\cos\varphi \end{array} \tag{A.39}$$

The resulting equation in spherical coordinates is straightforward:

$$I_{blob}(r,\theta,\varphi) = K \exp\left(-\frac{r^2}{2\sigma_0^2}\right) \tag{A.40}$$

A.3 Toroid

A.3.1 Toroid Centerline

Definition 9. A *toroid* is a volumetric solid generated by the revolution of a circle around a coplanar axis. The resulting shape is that of a doughnut, assuming that the circle do not intersects the axis. If we just take the external surface, the shape is called *torus*. Assume that the circle revolves around the axis at a constant distance R which is

the radius of the toroid, and that the radius of the circle is constant during the revolution. The centerline of such a toroid is a circle whose equation is given by:

$$\begin{aligned} x_C(\theta) &= R\cos\theta \\ y_C(\theta) &= 0 \\ z_C(\theta) &= R\sin\theta \end{aligned} \tag{A.41}$$

where we assume that the centerline lies in the plane $y = 0$, or, in other words, that the axis of revolution coincides with the y-axis. This orientation is more suitable for a comparison with the ideal cylinder model.

A.3.2 Curvilinear Coordinates

Definition 10. The volumetric toroid may be described in terms of a set of *curvilinear coordinates* taking into account the geometry of the solid. The position of a point P in the volumetric toroid is given by the vectorial equation:

$$x_P(x,y,z) = x_C + r\cos\varphi e_1 + r\sin\varphi e_2 \tag{A.42}$$

The position vector x_C of the center of the cross-section in which P lies corresponds to the centerline defined in equation 9. We need to find an expression for e_1 and e_2, the basis vectors for the section that contains points P and C, in terms of the global reference system. Since $e_1$follows the direction of the segment $\overline{OC}$ we have that:

$$e_1 = \cos\theta i + \sin\theta k \tag{A.43}$$

On the other hand, the section normal n is tangent to the centerline circumference and thus:

$$n = -\sin\theta i \ \ + \cos\theta k + \tag{A.44}$$

Finally, from the figure, it is easy to see that

$$e_2 = j \tag{A.45}$$

which can also be derived from the cross-product

$$e_2 = n \times e_1 = \begin{vmatrix} i & j & k \\ -\sin\theta & 0 & \cos\theta \\ \cos\theta & 0 & \sin\theta \end{vmatrix} = \left(\cos^2\theta + \sin^2\theta\right) j = j$$

Replacing in equation 10 we obtain the inverse coordinate transformation from the curvilinear coordinates (r,φ,θ) to the cartesian coordinates:

$$\begin{aligned} x(r,\varphi,\theta) &= R\cos\theta + r\cos\varphi\cos\theta \quad (1) \\ y(r,\varphi,\theta) &= r\sin\varphi \quad (2) \\ z(r,\varphi,\theta) &= R\sin\theta + r\cos\varphi\sin\theta \quad (3) \end{aligned} \tag{A.46}$$

We will proceed to find the direct coordinate transformation that takes the form:

$$\begin{array}{l} r = r(x,y,z) \\ \varphi = \varphi(x,y,z) \\ \theta = \theta(x,y,z) \end{array} \tag{A.47}$$

Combining equations A.3.2 (1) and (3):

$$r\cos\varphi = \frac{x - R\cos\theta}{\cos\theta} = \frac{z - R\sin\theta}{\sin\theta}$$

From here we obtain[4]:

$$\begin{array}{ll} \tan\theta = \frac{z}{x} & (1) \\ \cos\theta = \frac{x}{\sqrt{x^2+z^2}} & (2) \\ \sin\theta = \frac{z}{\sqrt{x^2+z^2}} & (3) \end{array} \tag{A.48}$$

For the curvilinear coordinate r we know that

$$r^2 = (x - x_C)^2 + (y - y_C)^2 + (z - z_C)^2$$

$$r^2 = (x - R\cos\theta)^2 + y^2 + (z - R\sin\theta)^2$$

$$r^2 = x^2 + y^2 + z^2 + R^2 - 2R(x\cos\theta + z\sin\theta)$$

$$r^2 = x^2 + y^2 + z^2 + R^2 - 2R\sqrt{x^2+z^2}$$

Finally we obtain:

$$r = \sqrt{y^2 + \left(\sqrt{x^2+z^2} - R\right)^2} \tag{A.49}$$

From equation A.3.2 (2):

$$\sin\varphi = \frac{y}{r} = \frac{y}{\sqrt{y^2 + \left(\sqrt{x^2+z^2} - R\right)^2}} \tag{A.50}$$

On the other hand:

$$\cos\varphi = \sqrt{1 - \sin^2\varphi} = \sqrt{1 - \frac{y^2}{y^2 + \left(\sqrt{x^2+z^2} - R\right)^2}}$$

[4]Note that P is not necessarily on the centerline so in general $\sqrt{x^2+z^2} \neq R$

$$\cos\varphi = \frac{\sqrt{x^2+z^2}-R}{\sqrt{y^2+\left(\sqrt{x^2+z^2}-R\right)^2}} = \frac{\sqrt{x^2+z^2}-R}{r} = \frac{\sqrt{r^2-y^2}}{r} \tag{A.51}$$

Finally:

$$\tan\varphi = \frac{y}{\sqrt{r^2-y^2}} = \frac{y}{\sqrt{x^2+z^2}-R} \tag{A.52}$$

A possible expression for the direct coordinate transformation is thus:

$$\begin{aligned} r &= \sqrt{y^2+\left(\sqrt{x^2+z^2}-R\right)^2} \quad (1)\\ \theta &= \arctan\left(\tfrac{z}{x}\right) \quad (2)\\ \varphi &= \arctan\left(\frac{y}{\sqrt{x^2+z^2}-R}\right) \quad (3) \end{aligned} \tag{A.53}$$

Alternatively we can use any of the expressions derived above.

A.3.3 Derivatives of Curvilinear Coordinates

Now we will proceed to obtain some derivatives that we will use for our future analyses. By differentiating both sides of equation A.3.2 (1):

$$dr = \frac{1}{2r}2\left(\sqrt{x^2+z^2}-R\right)\frac{2x}{2\sqrt{x^2+z^2}}dx$$

Replacing from equation A.51 and A.3.2 (2):

$$\frac{dr}{dx} = \cos\varphi\cos\theta \tag{A.54}$$

Similarly we obtain:

$$\frac{dr}{dy} = \frac{y}{r} = \sin\varphi \tag{A.55}$$

$$\frac{dr}{dz} = \cos\varphi\sin\theta \tag{A.56}$$

By taking derivatives on both sides of A.3.2 (1):

$$\frac{d\theta}{\cos^2\theta} = -\frac{z}{x^2}dx = -\frac{\tan\theta}{x}dx$$

$$\frac{d\theta}{dx} = -\frac{\cos^2\theta\,\frac{\sin\theta}{\cos\theta}}{\cos\theta\,(R+r\cos\varphi)}$$

$$\frac{d\theta}{dx} = -\frac{\sin\theta}{R + r\cos\varphi} \tag{A.57}$$

Similarly:

$$\frac{d\theta}{\cos^2\theta} = \frac{dz}{x}$$

$$\frac{d\theta}{dz} = \frac{\cos^2\theta}{x} = \frac{\cos^2\theta}{R\cos\theta + r\cos\varphi\cos\theta}$$

$$\frac{d\theta}{dz} = \frac{\cos\theta}{R + r\cos\varphi} \tag{A.58}$$

And since y does not depend on θ and they are both independent variables:

$$\frac{d\theta}{dy} = 0 \tag{A.59}$$

To obtain similar relationships for the coordinate φ we can differentiate both sides of equation A.52 and use the chain rule:

$$\frac{d\varphi}{\cos^2\varphi} = \frac{-y\frac{x}{\sqrt{x^2+z^2}}}{\left(\sqrt{x^2+z^2} - R\right)^2} dx$$

$$\frac{d\varphi}{dx} = -\frac{r\sin\varphi\cos\theta}{r^2\cos^2\varphi}\cos^2\varphi$$

$$\frac{d\varphi}{dx} = -\frac{1}{r}\sin\varphi\cos\theta \tag{A.60}$$

Similarly

$$\frac{d\varphi}{dy} = \frac{1}{r}\cos\varphi \tag{A.61}$$

$$\frac{d\varphi}{dz} = -\frac{1}{r}\sin\varphi\sin\theta \tag{A.62}$$

Now we can proceed to study the derivatives of the toroid model.

A.3.4 Gaussian Toroid Model

At any point on the toroid centerline, we will consider the section to have a constant Gaussian intensity distribution corresponding to:

$$G(x_s, y_s) = K \exp\left(-\frac{x_s^2 + y_s^2}{2\sigma_0^2}\right) \tag{A.63}$$

With our curvilinear coordinate system we have that:

$$r^2 = x_s^2 + y_s^2$$

and thus the equation of the volumetric toroid with Gaussian cross-section, expresed in curvilinear coordinates is:

$$I_{tor}(r, \theta, \varphi) = K \exp\left(-\frac{r^2}{2\sigma_0^2}\right) \tag{A.64}$$

Note that the expression in cylindrical coordinates is the same as the equation for the cylinder. However, the coordinate system chosen is different. We can also express the volumetric toroid in cartesian coordinates by using the direct coordinate transformation of equation A.3.2 resulting in:

$$I_{tor}(x, y, z) = K \exp\left(-\frac{y^2 + \left(\sqrt{x^2 + z^2} - R\right)^2}{2\sigma_0^2}\right)$$

where we have conveniently chosen the centerline of the toroid to lie on the plane $y = 0$.

A.3.5 Gaussian ToroidDerivatives

First, we need to calculate the first-order derivatives. We may use the chain rule for obtaining the *total* (not partial) first-order derivative[5] with respect to x:

$$\frac{dI}{dx} = \frac{\partial I}{\partial r}\frac{\partial r}{\partial x} = -\frac{r}{\sigma_0^2} I \cos\varphi \cos\theta$$

$$\frac{dI}{dx} = -\frac{r}{\sigma_0^2} \cos\varphi \cos\theta I \tag{A.65}$$

where the value of $\partial r / \partial x$ is taken from equation A.102. In a similar fashion we obtain:

[5] When we use here the concept of total derivative of I with respect to x, y or z, we take into account all the indirect dependencies with respect to the variable we are obtaining the derivative for. When we use the partials derivatives, we do not take into account these dependencies. Note that in fact if $I = I(x, y, z)$ and if we didn't not have these intermediate dependencies, we would be talking about partial derivatives only since I depends on several variables, as we do in other parts of this thesis. Here we need a way to establish a difference and so we use the notation for total derivatives.

$$\frac{dI}{dy} = -\frac{r}{\sigma_0^2}\sin\varphi I \tag{A.66}$$

$$\frac{dI}{dz} = -\frac{r}{\sigma_0^2}\cos\varphi\sin\theta I \tag{A.67}$$

Now we can proceed to obtain the second-order partial derivatives. We start with the second derivative with respect to x. By the chain rule[6]:

$$\frac{d^2I}{dx^2} = \frac{\partial}{\partial r}\left(\frac{dI}{dx}\right)\frac{\partial r}{\partial x} + \frac{\partial}{\partial\theta}\left(\frac{dI}{dx}\right)\frac{\partial\theta}{\partial x} + \frac{\partial}{\partial\varphi}\left(\frac{dI}{dx}\right)\frac{\partial\varphi}{\partial x} \tag{A.68}$$

$$\frac{d^2I}{dx^2} = \frac{I}{\sigma_0^2}\left[\frac{r^2-\sigma_0^2}{\sigma_0^2}\cos^2\varphi\cos^2\theta - \frac{\sin^2\theta}{1+\frac{R}{r\cos\varphi}} - \sin^2\varphi\cos^2\theta\right]$$

Similarly we obtain:

$$\frac{d^2I}{dy^2} = \frac{I}{\sigma_0^2}\left[\frac{r^2-\sigma_0^2}{\sigma_0^2}\sin^2\varphi - \cos^2\varphi\right] \tag{A.69}$$

$$\frac{d^2I}{dz^2} = \frac{I}{\sigma_0^2}\left[\frac{r^2-\sigma_0^2}{\sigma_0^2}\cos^2\varphi\sin^2\theta - \frac{\cos^2\theta}{1+\frac{R}{r\cos\varphi}} - \sin^2\varphi\sin^2\theta\right] \tag{A.70}$$

$$\frac{d^2I}{dxdy} = \frac{I}{\sigma_0^2}\left[\frac{r^2}{\sigma_0^2}\cos\theta\sin\varphi\cos\varphi\right] \tag{A.71}$$

$$\frac{d^2I}{dxdz} = \frac{I}{\sigma_0^2}\sin\theta\cos\theta\left[\frac{r^2-\sigma_0^2}{\sigma_0^2}\cos^2\varphi - \frac{1}{1+\frac{R}{r\cos\varphi}} - \sin^2\varphi\right] \tag{A.72}$$

$$\frac{d^2I}{dydz} = \frac{I}{\sigma_0^2}\left[\frac{r^2}{\sigma_0^2}\sin\theta\sin\varphi\cos\varphi\right] \tag{A.73}$$

Due to the symmetry of the problem we can choose the values of the angles to be $\theta = 0$ (origin of the toroid centerline) and $\varphi = 0$ (zero polar angle for the section). This yields the following simplified Hessian matrix:

$$H = \frac{I}{\sigma_0^2}H' \tag{A.74}$$

$$H'(\theta=0,\varphi=0) = \begin{bmatrix} \frac{r^2-\sigma_0^2}{\sigma_0^2} & 0 & 0 \\ 0 & -1 & 0 \\ 0 & 0 & -\frac{1}{1+\frac{R}{r}} \end{bmatrix} \tag{A.75}$$

However, the previous expression is only valid for values of r from the centerline to the external boundary of the toroid ($\varphi = 0^o$). If we choose values of r towards the internal part of the toroid, then $\varphi = 180^o$ and the expression becomes

[6]Note that we must also take into account that $I = I(r)$when calculating derivatives with respect to r.

$\lambda_1 = \frac{r^2-\sigma_0^2}{\sigma_0^4} I_{tor}$	$\lambda_2 = -\frac{1}{\sigma_0^2} I_{tor}$	$\lambda_3 = -\frac{1}{\sigma_0^2}\frac{1}{1+\frac{R}{r}} I_{tor}$
$x_1 = \begin{bmatrix} 1 & 0 & 0 \end{bmatrix}$	$x_2 = \begin{bmatrix} 0 & 1 & 0 \end{bmatrix}$	$x_3 = \begin{bmatrix} 0 & 0 & 1 \end{bmatrix}$

Table A.3: Eigenvalues and vectors for the ideal Gaussian toroid with $\theta = 0$, $\varphi = 0$.

$\lambda_1 = \frac{r^2-\sigma_0^2}{\sigma_0^4} I_{tor}$	$\lambda_2 = -\frac{1}{\sigma_0^2} I_{tor}$	$\lambda_3 = -\frac{1}{\sigma_0^2}\frac{1}{1-\frac{R}{r}} I_{tor}$
$x_1 = \begin{bmatrix} 1 & 0 & 0 \end{bmatrix}$	$x_2 = \begin{bmatrix} 0 & -\tau & \kappa \end{bmatrix}$	$x_3 = \begin{bmatrix} 0 & \kappa & \tau \end{bmatrix}$

Table A.4: Eigenvalues and vectors for the ideal Gaussian toroid with $\theta = 0$, $\varphi = 180$. Note that in these expressions $r > 0$.

$$H'(\theta = 0, \varphi = 180) = \begin{bmatrix} \frac{r^2-\sigma_0^2}{\sigma_0^2} & 0 & 0 \\ 0 & -1 & 0 \\ 0 & 0 & -\frac{1}{1-\frac{R}{r}} \end{bmatrix} \tag{A.76}$$

This is the same as considering that the expression A.75 can take both positive and negative values for r.

A.3.6 Hessian Eigenvalues and Eigenvectors

The eigenvalues and eigenvectors for the regular toroid with Gaussian cross-section at the starting point of the helix ($\theta = 0, \varphi = 0$) correspond to:

The eigenvalues and vectors for ($\theta = 0, \varphi = 180$), that is, for points in the internal part of the toroid with respect to the centerline correspond to:

We can get a single combined expression by considering that r can take both positive and negative values in the expressions of Table A.3. In fact what we change is the value of the angle φ by 180º and not the sign of the radius but the effect is the same.

Lemma 11. *The radius of curvature R of the ideal toroid model with Gaussian cross-section has only influence in the principal curvature corresponding to a direction perpendicular to the local toroid section.*

Proof. We can see that, for $\theta = 0$ and $\varphi = 0$, the first and second principal curvatures λ_1 and λ_2 for $\theta = 0$ and $\varphi = 0$ coincide with the first two principal curvatures of the ideal cylinder in cartesian coordinates (see equations A.10 and A.11) and are not influenced by the radius of curvature R of the toroid. However, we can see that, compared with the cylinder model, the third eigenvalue, corresponding to the z direction at the origin is not zero anymore and depends on the distance r to the centerline and the radius of curvature R of the toroid. Due to the symmetry of the problem, the same holds for other angles other than $\theta = 0$ and $\varphi = 0$. □

A.3.7 Effect of Curvature

Lemma 12. *Let $\overline{OC}$ be a line that connects the center of the toroid O with any point C on the centerline of the toroid with $d\left(\overline{OC}\right) \equiv R$. Let $P_1$and P_2 be symmetrical points on that line with respect to C at a distance r with P_1 the closest to O. Then, $|\lambda_3(P_1)| \geq |\lambda_3(P_2)| \forall r$.*

Proof. From the simplified expression of λ_3

$$\lambda_3 = -\frac{1}{\sigma_0^2}\frac{1}{1+\frac{R}{r}}I$$

where r can take positive or negative values depending if we are in the external ($\varphi = 0$) or internal ($\varphi = 180$) part of the cylinder we can see that, for the same absolute value of r we obtain two points P_1, P_2 in the line with respective values

$$\lambda_3^- = \lambda_3(P_1) = -\frac{1}{\sigma_0^2}\frac{1}{1-\frac{R}{|r|}}I \tag{A.77}$$

$$\lambda_3^+ = \lambda_3(P_2) = -\frac{1}{\sigma_0^2}\frac{1}{1+\frac{R}{|r|}}I \tag{A.78}$$

Comparing the quotient in the middle we can distinguish three cases for r. If $\frac{R}{|r|} < 1$ then the denominator in eq. A.77 is always positive and the total value negative. If $\frac{R}{|r|} < 1$ the denominator in eq. A.77 is always negative and the total value positive. If $\frac{R}{|r|} < 1$ then the denominator is zero in the same equation and the total value infinite. In all three cases the denominator in eq. A.77 is smaller in absolute value than in A.78 and thus $|\lambda_3(P_1)| \geq |\lambda_3(P_2)| \forall r$.

□

Thus, in the presence of curvature, the internal part of the toroid presents larger absolute values of λ_3 obtaining an assymetrical response. We can see that there is also asymmetry in the sign in the most typical case where $|r| < R$[7] , since in the internal part of the toroid (P_1), the value of $\lambda_3$becomes positive whereas in the external part is always negative.

A.4 Helix

A.4.1 Helix Centerline

The volumetric helix is a very interesting shape model, because it allows us to study both the effect of curvature and torsion in the derivative-based detection of curvilinear structures.

[7] If $|r| < R$ either we are in places of very little influence or R is very small and the internal radius σ_0 of similar size which barely occurs in practice.

Definition 13. A helix is a smooth curve in three-dimensional space. Its main characteristic is that the tangent line at any point makes a constant angle with the helix axis. The helix revolves around the axis as it ascends (or descends). Helices can be left-handed or right handed, depending on the direction of ascension. The ratio of ascension per angle unit is usually a constant H for regular helices. We will call this constant here helix *unit pitch*. Usually the *pitch* is defined as $2\pi H$, that is, the amount the helix ascends (in the axial direction) in a complete 360º turn. The parametric equation of the centerline of an helix with constant radius and pitch is given by[8]:

$$\begin{aligned} x(\theta) &= R\cos\theta \\ y(\theta) &= R\sin\theta \\ z(\theta) &= H\,\theta \end{aligned} \tag{A.79}$$

where the parameter θ is the angle depicted in Figure . Note that this is not the unit arc length parametrization. Such an helix with a constant radius R and constant unit pitch H is called a *circular helix* [71].

At every point of the helix, we can easily calculate the local coordinate system defined by the *Frenet-Serret frame*, consisting of three orthonormal vectors:

- T is the unit tangent vector to the curve at every point, in the ascending direction.
- N is the unit normal vector. It is normal to the tangent vector and in the direction of its derivative with respect to the arc-length parameter.
- B is the binormal vector, which is the cross-product of T and N.

The unit tangent vector T has the direction of the derivative with respect to the arc length:

$$\alpha'(\theta) = \frac{\partial\alpha}{\partial\theta} = -R\sin\theta i + R\cos\theta j + Hk \tag{A.80}$$

and thus, the expresion of the unit tangent vector of the helix centerline is:

$$T = \frac{\alpha'(\theta)}{|\alpha'(\theta)|} = \frac{1}{\sqrt{R^2+H^2}}\left(-R\sin\theta i + R\cos\theta j + Hk\right) \tag{A.81}$$

The unit arc-length parametrization of the helix can be obtained by dividing the vectorial expression in A.79 by the modulus of the tangent vector $\sqrt{R^2+H^2}$.

Proposition 14. Let $\widetilde{\gamma}: I \longrightarrow \mathbb{R}^3$ be a circular helix. Then, the curvature and torsion of the helix centerline is constant.

Proof. First, we will try to find the value of the normal vector and the curvature. The value of these derivatives is independent of the chosen parametrization and thus, we

[8]The standard notation for a parametric curve typically uses t for the curve parameter. However, we will use here θas the name of the parameter, since we want to emphasize that the parameter is an angle. Moreover, it can be confused with the t parameter in the scale-space representations.

can calculate the derivatives with respect to the angle parameter θ. For the tangent vector we have:

$$\frac{\partial T}{\partial \theta} = \frac{R}{\sqrt{R^2+H^2}}(-\cos\theta i - \sin\theta j) \tag{A.82}$$

$$N = \frac{\frac{\partial T}{\partial \theta}}{\left|\frac{\partial T}{\partial \theta}\right|} = -\cos\theta i - \sin\theta j \tag{A.83}$$

and thus the curvature is

$$\kappa = \left|\frac{\partial T}{\partial \theta}\right| = \frac{R}{\sqrt{R^2+H^2}} \tag{A.84}$$

which is a constant when both R and H are constants. Now we can obtain the binormal vector as:

$$B = T \times N = \frac{1}{\sqrt{R^2+H^2}} \begin{vmatrix} i & j & k \\ -R\sin\theta & R\cos\theta & H \\ -\cos\theta & -\sin\theta & 0 \end{vmatrix} \tag{A.85}$$

$$B = \frac{1}{\sqrt{R^2+H^2}}(H\sin\theta i - H\cos\theta j + Rk) \tag{A.86}$$

and its derivative with respect to the arc-length:

$$\frac{\partial B}{\partial \theta} = \frac{H}{\sqrt{R^2+H^2}}(\cos\theta i + \sin\theta j) \tag{A.87}$$

and thus the the torsion is

$$\tau = \left|\frac{\partial B}{\partial \theta}\right| = \frac{H}{\sqrt{R^2+H^2}} \tag{A.88}$$

which is a constant when both R and H are constants. □

A.4.2 Curvilinear Coordinates

The parametric equation described in equation A.79 represents a 1D helix whose points are at a distance R from the helix axis. However, we are interested in a volumetric helix, that is, an helix that has a section with a given intensity distribution an radius. As in the previous models, we will use a 2D Gaussian function as the intensity distribution for our volumetric helix section, which is more representative for small vessels.

In order to obtain the equation of the volumetric helix with Gaussian cross-section we will use a curvilinear coordinate system with three coordinates (see Figure):

- r = distance to the closest point on the helix centerline as defined by the equation .
- φ= angle formed by the line of shortest distance to the centerline with the cross-section horizontal axis. This line is where r is measured.
- θ= angle formed by the closest point of the centerline with the origin of the centerline as measured in a plane normal to the axis.

Note that the helix cross-section does not contain the helix axis as it happened with the torus model. In we can see that the cross-section is defined by the tangent plane to the helix at every point, and the normal and binormal planes are the base vectors in this section plane.

The position of a point $\overrightarrow{x} \in \mathbb{R}^3$ in a volumeteric helix can be defined in terms of the center $\overrightarrow{x_C} \in \mathbb{R}^3$ of the section where the point is defined and the normal and binormal vectors. The basis vectors of the section are:

$$\begin{aligned} e_1 &= -N \\ e_2 &= B \end{aligned}$$

and thus we have the vectorial equation:

$$x = x_C - r\cos\varphi N + r\sin\varphi B \tag{A.89}$$

where r is the distance to the closest point on the helix centerline. Thus, by combining eq. A.79and A.89and replacing the expressions of the normal and binormal vectors, we obtain a relationship between the curvilinear coordinates we have chosen for the helix and cartesian coordinates:

$$\begin{aligned} x(r,\varphi,\theta) &= R\cos\theta + r\cos\varphi\cos\theta + \tau r\sin\varphi\sin\theta \quad (1) \\ y(r,\varphi,\theta) &= R\sin\theta + r\cos\varphi\sin\theta - \tau r\sin\varphi\cos\theta \quad (2) \\ z(r,\varphi,\theta) &= H\theta + \kappa r\sin\varphi \quad (3) \end{aligned} \tag{A.90}$$

Equation A.90 represents a direct transformation from curvilinear to cartesian coordinates. Ideally, from these equations we could obtain an inverse transformation in the form of equation A.47. However, obtaining such a transformation is not always possible or practical.

In the case of the helix, instead of an explicit expression for the inverse transformation, we obtain a set of implicit equations that involve both, the curvilinear and cartesian coordinates and that will be useful for our derivative calculations. By combining eq. (1) and (2) from the vectorial eq. A.90 we have:

$$r\cos\varphi = \frac{x - R\cos\theta - r\tau\sin\varphi\sin\theta}{\cos\theta} = \frac{x - R\sin\theta - r\tau\sin\varphi\cos\theta}{\sin\theta}$$

$$x\sin\theta - y\cos\theta = \tau r\sin\varphi$$

and replacing the value of $r\sin\varphi$in eq. A.90 (3) we obtain the implicit relationship:

$$z - H\theta = \frac{\kappa}{\tau}(x\sin\theta - y\cos\theta) \tag{A.91}$$

or equivalently

$$z - H\theta = \frac{R}{H}(x\sin\theta - y\cos\theta) \tag{A.92}$$

which corresponds to an explicit expression of the type $f(\theta,x,y,z) = 0$ which is also useful.

Combining equations A.90(1) and (3):

$$r\cos\varphi\cos\theta = x - R\cos\theta - \frac{\tau}{\kappa}\sin\theta\,(z - H\theta)$$

$$r\cos\varphi = \frac{1}{\cos\theta}\left[x - R\cos\theta - \sin\theta\,(x\sin\theta - y\cos\theta)\right] \tag{A.93}$$

Similarly:

$$r\cos\varphi\sin\theta = y - R\sin\theta + \frac{\tau}{\kappa}\cos\theta\,(z - H\theta)$$

$$r\cos\varphi = \frac{1}{\sin\theta}\left[y - R\sin\theta + \cos\theta\,(x\sin\theta - y\cos\theta)\right] \tag{A.94}$$

Finally we obtain two expressions for φ:

$$\tan\varphi = \frac{r\sin\varphi}{r\cos\varphi} = \frac{1}{\tau}\frac{\cos\theta\,(x\sin\theta - y\cos\theta)}{x - R\cos\theta - \sin\theta\,(x\sin\theta - y\cos\theta)} \tag{A.95}$$

$$\tan\varphi = \frac{r\sin\varphi}{r\cos\varphi} = \frac{1}{\tau}\frac{\sin\theta\,(x\sin\theta - y\cos\theta)}{y - R\sin\theta + \cos\theta\,(x\sin\theta - y\cos\theta)} \tag{A.96}$$

which is an expression in the form $\varphi = \varphi(\theta) = \varphi\left[\theta(x,y,z)\right]$

An expression for r can be obtained if we take into account that r is the distance from the current point to the closest centerline point, whose coordinates are given by the helix centerline equation A.79. Thus, this distance is:

$$r^2 = (x - R\cos\theta)^2 + (y - R\sin\theta)^2 + (z - H\theta)^2 \tag{A.97}$$

which is an expression in the form $r = r(x,y,z,\theta) = r\left[x,y,z,\theta(x,y,z)\right]$

A.4.3 Derivatives of Curvilinear Coordinates

By differentiating the expressions above, we can obtain some derivatives of the curvilinear coordinates with respect to the cartesian coordinates that are useful for future calculations. From the expression A.91 by differentiation with respect to θ and x we obtain:

$$-Hd\theta = \frac{\kappa}{\tau}\left(\sin\theta dx + x\cos\theta d\theta + y\sin\theta d\theta\right)$$

$$\frac{d\theta}{dx} = \frac{-\sin\theta}{\frac{\tau}{\kappa}H + x\cos\theta + y\sin\theta} \tag{A.98}$$

Similarly we obtain:

$$\frac{d\theta}{dy} = \frac{\cos\theta}{\frac{\tau}{\kappa}H + x\cos\theta + y\sin\theta} \tag{A.99}$$

$$\frac{d\theta}{dy} = \frac{\tau/\kappa}{\frac{\tau}{\kappa}H + x\cos\theta + y\sin\theta} \tag{A.100}$$

For the r curvilinear coordinate we can differentiate equation A.97 with respect to r and x. However, in this expression, the curvilinear coordinate θalso appears. By the chain rule we know that:

$$dr = \frac{\partial r}{\partial x}dx + \frac{\partial r}{\partial \theta}\frac{\partial \theta}{\partial x}dx \tag{A.101}$$

but $\partial r/\partial\theta = 0$ since they are independent variables. This can be easily seen by differentiating equation A.97 with respect to r and θ:

$$2rdr = 2(x - R\cos\theta)R\sin\theta d\theta - 2(y - R\sin\theta)R\cos\theta - 2H(z - H\theta)$$

Combining with equation A.92:

$$\frac{dr}{d\theta} = (x - R\cos\theta)R\sin\theta - 2(y - R\sin\theta)R\cos\theta - 2R(x\sin\theta - y\cos\theta) = 0$$

Then, from equation A.97 we have:

$$2rdr = 2(x - R\cos\theta)dx$$

$$\frac{dr}{dx} = \frac{1}{r}(x - R\cos\theta) \tag{A.102}$$

Similarly we obtain:

$$\frac{dr}{dy} = \frac{1}{r}(y - R\sin\theta) \tag{A.103}$$

$$\frac{dr}{dz} = \frac{1}{r}(z - H\theta) \tag{A.104}$$

A.4.4 Gaussian Helix Model

Definition 15. After obtaining this relationship between coordinate systems, we can proceed to obtain the expression of the volumetric helix with Gaussian cross-section and its derivatives. The expression of the volumetric is very if we express it in our curvilinear coordinate system for the helix:

$$I_{helix}(r, \varphi, \theta) = K \exp\left(-\frac{r^2}{2\sigma_0^2}\right) \tag{A.105}$$

Note that, again, this is exactly the expression we had for the cylinder in cylindrical coordinates. The curvilinear coordinate system chosen here is also different and does not correspond to the cylindrical coordinates. Our objective in this case is to calculate how both, the curvature and torsion, affects the value of the second order derivatives as compared with the ideal cylinder model.

A.4.5 Gaussian Helix Derivatives

We may use the chain rule for obtaining the *total* (not partial) first-order derivative with respect to x:

$$\frac{dI}{dx} = \frac{\partial I}{\partial r}\frac{\partial r}{\partial x} = -\frac{r}{\sigma_0^2} I \frac{1}{r}(x - R\cos\theta)$$

$$\frac{dI}{dx} = -\frac{I}{\sigma_0^2}(x - R\cos\theta) \tag{A.106}$$

where the value of $\partial r/\partial x$ is taken from equation A.102. In a similar fashion we obtain:

$$\frac{dI}{dy} = -\frac{I}{\sigma_0^2}(y - R\sin\theta) \tag{A.107}$$

$$\frac{dI}{dz} = -\frac{I}{\sigma_0^2}(z - H\theta) = -\frac{I}{\sigma_0^2}\frac{\kappa}{\tau}(x\sin\theta - y\cos\theta) \tag{A.108}$$

Obtaining the second-order partial derivatives is more complicated, since now we have to take into account the derivative with respect to θ. We start with the second derivative with respect to x. By the chain rule:

$$\frac{d^2I}{dx^2} = \frac{\partial^2 I}{\partial x^2} + \frac{\partial}{\partial r}\left(\frac{dI}{dx}\right)\frac{\partial r}{\partial x} + \frac{\partial}{\partial \theta}\left(\frac{dI}{dx}\right)\frac{\partial \theta}{\partial x} \tag{A.109}$$

$$\frac{d^2I}{dx^2} = -\frac{I}{\sigma_0^2} + \frac{r}{\sigma_0^2}\frac{I}{\sigma_0^2}(x - R\cos\theta)\frac{\partial r}{\partial x} + \left(-\frac{I}{\sigma_0^2}\right)R\sin\theta\frac{\partial \theta}{\partial x} \tag{A.110}$$

By replacing the values of the derivatives calculated in section A.4.2 we obtain:

$$\frac{d^2I}{dx^2} = \frac{I}{\sigma_0^2}\left(-1 + \frac{1}{\sigma_0^2}(x - R\cos\theta)^2 + \frac{R\sin^2\theta}{\frac{\tau}{\kappa}H + x\cos\theta + y\sin\theta}\right) \tag{A.111}$$

We can obtain the values of the remaining derivatives in a similar way obtaining:

$$\frac{d^2I}{dy^2} = \frac{I}{\sigma_0^2}\left(-1 + \frac{1}{\sigma_0^2}(y - R\sin\theta)^2 + \frac{R\cos^2\theta}{\frac{\tau}{\kappa}H + x\cos\theta + y\sin\theta}\right) \tag{A.112}$$

$$\frac{d^2I}{dz^2} = \frac{I}{\sigma_0^2}\left(-1 + \frac{1}{\sigma_0^2}(z - H\theta)^2 + \frac{\frac{\tau}{\kappa}H}{\frac{\tau}{\kappa}H + x\cos\theta + y\sin\theta}\right) \tag{A.113}$$

$$\frac{d^2I}{dxdy} = \frac{I}{\sigma_0^2}\left(\frac{1}{\sigma_0^2}(x - R\cos\theta)(y - R\sin\theta) - \frac{R\sin\theta\cos\theta}{\frac{\tau}{\kappa}H + x\cos\theta + y\sin\theta}\right) \tag{A.114}$$

$$\frac{d^2I}{dxdz} = \frac{I}{\sigma_0^2}\left(\frac{1}{\sigma_0^2}(x - R\cos\theta)(z - H\theta) - \frac{\frac{\tau}{\kappa}R\sin\theta}{\frac{\tau}{\kappa}H + x\cos\theta + y\sin\theta}\right) \tag{A.115}$$

$$\frac{d^2I}{dydz} = \frac{I}{\sigma^2}\left(\frac{1}{\sigma^2}(y - R\sin\theta)(z - H\theta) + \frac{\frac{\tau}{\kappa}R\cos\theta}{\frac{\tau}{\kappa}H + x\cos\theta + y\sin\theta}\right) \tag{A.116}$$

Due to the symmetry of the problem and, without loss of generality, we can choose the values of the angles to be $\theta = 0$ (origin of the helix) and $\varphi = 0$ (zero polar angle for the section). This yields the following simplified Hessian matrix:

$$H = \frac{I}{\sigma_0^2}H' \tag{A.117}$$

$$H' = \begin{bmatrix} -1 + \frac{1}{\sigma_0^2}(x-R)^2 & \frac{1}{\sigma_0^2}(x-R)y & \frac{1}{\sigma_0^2}(x-R)z \\ \frac{1}{\sigma_0^2}(x-R)y & -1 + \frac{y^2}{\sigma_0^2} + \frac{R}{\frac{\tau}{\kappa}H+x} & \frac{1}{\sigma_0^2}yz + \frac{\frac{\tau}{\kappa}R}{\frac{\tau}{\kappa}H+x} \\ \frac{1}{\sigma_0^2}(x-R)z & \frac{1}{\sigma_0^2}yz + \frac{\frac{\tau}{\kappa}R}{\frac{\tau}{\kappa}H+x} & -1 + \frac{z^2}{\sigma_0^2} + \frac{\frac{\tau}{\kappa}H}{\frac{\tau}{\kappa}H+x} \end{bmatrix} \tag{A.118}$$

The values of x, y, z in equations A.90 for $\varphi = 0$ and $\theta = 0$:

$$\begin{array}{ll} x(r, \theta = 0, \varphi = 0) = R + r & (1) \\ y(r, \theta = 0, \varphi = 0) = 0 & (2) \\ z(r, \theta = 0, \varphi = 0) = 0 & (3) \end{array} \tag{A.119}$$

and replacing them in the expression of H' we obtain a matrix that depends only on the curvilinear coordinate r:

$$H'(\theta = 0, \varphi = 0) = \begin{bmatrix} \frac{r^2-\sigma_0^2}{\sigma_0^2} & 0 & 0 \\ 0 & -1 + \frac{R}{\frac{\tau}{\kappa}H+R+r} & \frac{\frac{\tau}{\kappa}R}{\frac{\tau}{\kappa}H+R+r} \\ 0 & \frac{\frac{\tau}{\kappa}R}{\frac{\tau}{\kappa}H+R+r} & -1 + \frac{\frac{\tau}{\kappa}H}{\frac{\tau}{\kappa}H+R+r} \end{bmatrix} =$$
$$\begin{bmatrix} \frac{r^2-\sigma_0^2}{\sigma_0^2} & 0 & 0 \\ 0 & -\frac{\frac{\tau}{\kappa}H+r}{\frac{\tau}{\kappa}H+R+r} & \frac{\frac{\tau}{\kappa}R}{\frac{\tau}{\kappa}H+R+r} \\ 0 & \frac{\frac{\tau}{\kappa}R}{\frac{\tau}{\kappa}H+R+r} & -\frac{R+r}{\frac{\tau}{\kappa}H+R+r} \end{bmatrix}$$

Moreover, we have that $\tau/\kappa = H/R$ so we obtain:

$$H'(\theta = 0, \varphi = 0) = \begin{bmatrix} \frac{r^2-\sigma_0^2}{\sigma_0^2} & 0 & 0 \\ 0 & -\frac{\frac{\tau^2}{\kappa^2}+\frac{r}{R}}{\frac{\tau^2}{\kappa^2}+\frac{r}{R}+1} & \frac{\frac{\tau}{\kappa}}{\frac{\tau^2}{\kappa^2}+\frac{r}{R}+1} \\ 0 & \frac{\frac{\tau}{\kappa}}{\frac{\tau^2}{\kappa^2}+\frac{r}{R}+1} & -\frac{\frac{r}{R}+1}{\frac{\tau^2}{\kappa^2}+\frac{r}{R}+1} \end{bmatrix} \tag{A.120}$$

However, the previous expression is only valid for values of r from the centerline to the external boundary of the toroid ($\varphi = 0^o$). If we choose values of r towards the internal part of the toroid, then $\varphi = 180^o$ and the expression becomes

$\lambda_1 = \frac{r^2-\sigma_0^2}{\sigma_0^4} I$	$\lambda_2 = -\frac{1}{\sigma_0^2} I$	$\lambda_3 = -\frac{1}{\sigma_0^2} \frac{\frac{r}{R}}{\frac{\tau^2}{\kappa^2}+\frac{r}{R}+1} I$
$x_1 = \begin{bmatrix} 1 & 0 & 0 \end{bmatrix}$	$x_2 = \begin{bmatrix} 0 & -\tau & \kappa \end{bmatrix}$	$x_3 = \begin{bmatrix} 0 & \kappa & \tau \end{bmatrix}$

Table A.5: Eigenvalues and vectors for the ideal Gaussian helix with $\theta = 0$, $\varphi = 0$.

$\lambda_1 = \frac{r^2-\sigma_0^2}{\sigma_0^4} I$	$\lambda_2 = -\frac{1}{\sigma_0^2} I$	$\lambda_3 = \frac{1}{\sigma_0^2} \frac{\frac{r}{R}}{\frac{\tau^2}{\kappa^2}-\frac{r}{R}+1} I$
$x_1 = \begin{bmatrix} 1 & 0 & 0 \end{bmatrix}$	$x_2 = \begin{bmatrix} 0 & -\tau & \kappa \end{bmatrix}$	$x_3 = \begin{bmatrix} 0 & \kappa & \tau \end{bmatrix}$

Table A.6: Eigenvalues and vectors for the ideal Gaussian helix with $\theta = 0$, $\varphi = 180$. Note that in these expressions $r > 0$.

$$H'(\theta = 0, \varphi = 180) = \begin{bmatrix} \frac{r^2-\sigma_0^2}{\sigma_0^2} & 0 & 0 \\ 0 & -\frac{\frac{\tau^2}{\kappa^2}-\frac{r}{R}}{\frac{\tau^2}{\kappa^2}-\frac{r}{R}+1} & \frac{\frac{\tau}{\kappa}}{\frac{\tau^2}{\kappa^2}-\frac{r}{R}+1} \\ 0 & \frac{\frac{\tau}{\kappa}}{\frac{\tau^2}{\kappa^2}-\frac{r}{R}+1} & -\frac{-\frac{r}{R}+1}{\frac{\tau^2}{\kappa^2}-\frac{r}{R}+1} \end{bmatrix} \tag{A.121}$$

This is the same as considering that the expression A.120 can take both positive and negative values for r.

A.4.6 Hessian Eigenvalues and Eigenvectors

To sum up, we have obtained the following eigenvalues and corresponding eigenvectors for the regular helix with Gaussian cross-section at the starting point of the helix ($\theta = 0, \varphi = 0$):
where I is defined in eq. A.105.

Using a similar procedure, we can obtain the eigenvalues and vectors for ($\theta = 0, \varphi = 180$), that is, for points in the internal part of the helix with respect to the centerline. The resulting eigenvalues and vectors are:

We can get a single combined expression by considering that r can take both positive and negative values in the expressions of Table A.5.

As we can see, the first and second eigenvalues coincide with the ideal Gaussian cylinder (see Table A.1) and with the ideal Gaussian toroid (see Table A.3). This is due to the rotational symmetry of the helix and the choice of coordinate system. The helix with circular cross-section can be considered an special case of cylinder where the centerline has been twisted by adding constant curvature and torsion.

A.4.7 Effect of Curvature and Torsion

A.4.7.1 Theoretical Model

We can already draw some conclusions on the combined effect of curvature and torsion as compared with a straight ideal cylinder from the simplified expressions of the

eigenvalue λ_3:

Lemma 16. *Let I_{helix} be a circular Gaussian helix with internal radius σ_0, external radius R and unit pitch H. Let $\overline{OC}$ be a line that connects the center O of the helix with any point C on the centerline of the helix with $d\left(\overline{OC}\right) \equiv \sqrt{R^2+H^2\theta^2}$. Let P_1 and P_2 be symmetrical points on that line with respect to C at a distance r with P_1 the closest to O. Then, $|\lambda_3(P_1)| \geq |\lambda_3(P_2)| \forall r$.*

Proof. From the simplified expression of λ_3

$$\lambda_3 = -\frac{1}{\sigma_0^2}\frac{\frac{r}{R}}{\frac{\tau^2}{\kappa^2}+\frac{r}{R}+1}I$$

where r can take positive or negative values depending if we are in the external ($\varphi = 0$) or internal ($\varphi = 180$) part of the cylinder we can see that, for the same absolute value of r we obtain two points P_1, P_2 in the line with respective values

$$\lambda_3(P_1) = -\frac{1}{\sigma_0^2}\frac{-\frac{|r|}{R}}{\frac{\tau^2}{\kappa^2}-\frac{|r|}{R}+1}I \tag{A.122}$$

$$\lambda_3(P_2) = -\frac{1}{\sigma_0^2}\frac{\frac{|r|}{R}}{\frac{\tau^2}{\kappa^2}+\frac{|r|}{R}+1}I \tag{A.123}$$

Comparing the quotient in the middle we can distinguish three cases for r. If $\frac{\tau^2}{\kappa^2}+1 > \frac{|r|}{R}$ then the denominator in eq. A.122 is always positive and so is the total value. If $\frac{\tau^2}{\kappa^2}+1 < \frac{|r|}{R}$the denominator in eq. A.122 is always negative and so is the total value. If $\frac{\tau^2}{\kappa^2}+1 = \frac{|r|}{R}$then the denominator is zero in the same equation and the total value infinite. In all three cases the denominator in eq. A.122 is smaller in absolute value than in eq. A.123 and thus $|\lambda_3(P_1)| \geq |\lambda_3(P_2)| \forall r$.

□

Lemma 17. *Let I_1 be a circular Gaussian helix with internal radius σ_{01}, unit pitch H_1 and external radius $R_1 = \rho H_1$. Let I_2 be another circular Gaussian helix with same internal radius σ_{01}, same unit pitch H_1 and different external radius R_2 such that $R_2 = \frac{1}{\rho}H_1$. Then $\lambda_3(I_1(x)) = \lambda_3(I_2(x)) \, \forall x \in \mathbb{R}^3$.*

Proof. For the first helix

$$\lambda_3\left(I_1\right) = -\frac{1}{\sigma_0^2}\frac{\frac{r}{\rho H_1}}{\frac{H_1^2}{\rho^2 H_1^2}+\frac{r}{\rho H_1}+1}\exp\left(-\frac{r^2}{2\sigma_0^2}\right) = -\frac{1}{\sigma_0^2}\frac{r\rho}{H_1+r\rho+\rho^2 H_1}\exp\left(-\frac{r^2}{2\sigma_0^2}\right)$$

and for the second helix

$$\lambda_3(I_2) = -\frac{1}{\sigma_0^2}\frac{\frac{\rho r}{H_1}}{\frac{\rho^2 H_1^2}{H_1^2}+\frac{\rho r}{H_1}+1}\exp\left(-\frac{r^2}{2\sigma_0^2}\right) = -\frac{1}{\sigma_0^2}\frac{r\rho}{\rho^2 H_1 + r\rho + H_1}\exp\left(-\frac{r^2}{2\sigma_0^2}\right)$$

which are identical. □

Corollary 18. *If* $\rho = 1$ *then* $I_1 = I_2$ *and* $\lambda_3(I_1) = \lambda_3(I_2)$ is maximum $\forall r$.

Proof. The maximum for $\lambda_3(I_1) = \lambda_3(I_2)$ can be found by setting

$$\frac{d\lambda_3(I_1)}{d\rho} = \frac{d\lambda_3(I_2)}{d\rho} = 0$$

$$\frac{r\left(H_1 + r\rho + \rho^2 H_1\right) - r\rho\left(r + 2\rho H_1\right)}{\left(H_1 + r\rho + \rho^2 H_1\right)^2} = 0 \tag{A.124}$$

$$H_1 + r\rho + \rho^2 H_1 - \rho r - 2\rho^2 H_1 = 0$$

$$\rho^2 = 1$$

$$\rho = \pm 1 \tag{A.125}$$

Where the negative solution is an helix going downward. By derivating again we can check that this is indeed a maximum by calculating the second derivative.

$$\frac{d^2\lambda_3(I_1)}{d\rho^2} = \frac{d^2\lambda_3(I_2)}{d\rho^2} = \frac{-2r\rho H_1\left(H_1^2 + r^2\rho^2 + \rho^4 H_1^2 + 2r\rho H_1 + 2r\rho^3 H_1 + 2\rho^2 H_1^2\right)}{\left(H_1 + r\rho + \rho^2 H_1\right)^4}$$

$$-\frac{\left(rH_1 - r\rho^2 H_1\right)2\left(H_1 + r\rho + \rho^2 H_1\right)\left(r + 2\rho H_1\right)}{\left(H_1 + r\rho + \rho^2 H_1\right)^4}$$

The denominator is always positive. The second part of the numerator is zero for $\rho = 1$ due to the first term. Replacing $\rho = 1$ in the numerator for the rest of terms, multiplying and removing the common positive factors gives the following simplified numerator

$$-8H_1^2 - 8r^2 H_1^2 - 2r^2 < 0 \quad \forall (r, H_1)$$

which denotes a relative maximum.

□

Thus, in the presence of curvature, the internal part of the helix presents larger absolute values of λ_3 obtaining an assymetrical response. We can see that there is also asymmetry in the sign when $\frac{\tau^2}{\kappa^2} + 1 > \frac{|r|}{R}$, since in the internal part of the helix (P_1), the value of $\lambda_3$becomes positive whereas in the external part is always negative.

A.5 Section Profiles

A.5.1 Gaussian Section Profiles

The Gaussian section profile corresponds to (in 1D):

$$g_{\sigma_0}(x;\sigma_0) = \frac{1}{\sqrt{2\pi}\sigma_0} e^{-\frac{x^2}{2\sigma_0^2}} \tag{A.126}$$

where the aperture σ_0 can be regarded as the apparent radius of the profile.

The γ-normalized second-order Gaussian derivative is:

$$r_g^{''}(x;\sigma_0,\sigma)_{\gamma-norm} = \frac{\sigma^{2\gamma}}{\sqrt{2\pi}} \left(\frac{x^2-\sigma_1^2}{\sigma_1^5} \right) e^{-\frac{x^2}{2\sigma_1^2}} \tag{A.127}$$

where we used the cascade smoothed property for calculating the convolution of a Gaussian with another Gaussian, that yields a Gaussian of aperture $\sigma_1 = \sqrt{\sigma^2+\sigma_0^2}$.

Lemma 19. *Given a Gaussian profile $g_{\sigma_0}(x;\sigma_0)$, its second-order γ-normalized Gaussian derivative $r_b^{''}(x;\sigma_0,\sigma)_{\gamma-norm} = \sigma^{2\gamma} r_b^{''}(x;\sigma_0,\sigma)$ has a minimum in scale-space at $x=0$ for $\sigma=\sigma_0$ when $\gamma = 3/4$.*

Proof. The value of the derivative at $x=0$ is

$$r_g^{''}(x=0;\sigma_0,\sigma)_{\gamma-norm} = -\frac{1}{\sqrt{2\pi}} \frac{\sigma^{2\gamma}}{\sigma_1^3} \tag{A.128}$$

A critical point with respect to the scale parameter is found by calculating and equaling to zero the derivative:

$$\frac{\partial r_g^{''}(x=0;\sigma_0,\sigma)_{\gamma-norm}}{\partial\sigma} = -\frac{1}{\sqrt{2\pi}} \left(\frac{2\gamma\sigma^{2\gamma-1}\sigma_1^3 - 3\sigma^{2\gamma+1}\sigma_1}{\sigma_1^6} \right) = 0 \tag{A.129}$$

The above is expression has a critical point for:

$$\sigma = \sqrt{\frac{2\gamma}{3-2\gamma}}\sigma_0 \tag{A.130}$$

which results in $\sigma=\sigma_0$ when $\gamma = 3/4$, which can be demonstrated to be a minimum.

□

A.5.2 Bar Section Profiles

The bar cross-section profile is studied for the scale-space analysis of curvilinear structures in [171]. It can be modelled as a pulse with height h and width 2ω, which corresponds to the equation:

$$f_b(x;h,\omega) = \begin{cases} h & |x| \leq \omega \\ 0 & |x| > \omega \end{cases} \tag{A.131}$$

It can also be expressed as the sum of two scaled and translated Heaviside functions:

$$f_b(x;h,\omega) = h\,[H(x+\omega) - H(x-\omega)] \tag{A.132}$$

with H being the Heaviside or step function

$$H(x) = \begin{cases} 1 & x \geq 0 \\ 0 & x < 0 \end{cases} \tag{A.133}$$

Here we will reproduce some of the analysis in [171] in order to provide additional proofs and concepts that may be useful for the convolved bar profile, which is used extensively in our experiements in chapters .

We are mostly interested in the behaviour of the second Gaussian derivative in the central point of the profile ($x = 0$). For the profile to be detected, the second derivative should show a clear minimum at this location for a given scale σ. Due to the symmetry of the problem, the analysis can be performed in 1D.

For the scale-space analysis, we need to convolve the bar profile f_b with a Gaussian function. This convolution can be calculated analytically as:

$$r_b(x;h,\omega,\sigma) = f_b(x) \star g_\sigma(x) = \int_{-\infty}^{\infty} f_b(x-\tau)\, g_\sigma(\tau)\, d\tau$$

which can be split as the sum of two integrals

$$r_b(x;h,\omega,\sigma) = h \int_{-\infty}^{\infty} H(x+\omega-\tau)\, g_\sigma(\tau)\, d\tau + h \int_{-\infty}^{\infty} H(x-\omega-\tau)\, g_\sigma(\tau)\, d\tau \tag{A.134}$$

resulting in[9]

$$r_b(x;h,\omega,\sigma) = \frac{h}{\sqrt{2\pi}\sigma} \left(\phi_\sigma(x+\omega) - \phi_\sigma(x-\omega)\right) \tag{A.135}$$

where $\phi_\sigma(x)$ is the Gaussian integral function

[9] Note that here we do not omit the normalization factor of the Gaussian as in [171].

$$\phi_\sigma(x) = \int_{-\infty}^{x} e^{-\frac{x^2}{2\sigma^2}} dx \tag{A.136}$$

Since the derivative of the Gaussian integral is simply the Gaussian function, it is very easy to obtain the first and second order Gaussian derivatives of the bar profile with respect to the spatial variable x which results in:

$$r_b^{'}(x;h,\omega,\sigma) = h\left[g_\sigma(x+\omega) - g_\sigma(x-\omega)\right] \tag{A.137}$$

$$r_b^{''}(x;h,\omega,\sigma) = h\left[g_\sigma^{'}(x+\omega) - g_\sigma^{'}(x-\omega)\right] \tag{A.138}$$

where the first derivative of Gaussian is

$$g_\sigma^{'}(x) = -\frac{x}{\sigma^2}\, g_\sigma(x) \tag{A.139}$$

Now, we can proceed to analyze the behaviour of this second order derivative.

Lemma 20. *Given a bar profile $f_b(x;h,\omega)$, its second-order Gaussian derivative $r_b^{''}(x;h,\omega,\sigma)$ has a critical point at $x=0$ for all positive values of the parameters h,ω and scale σ.*

Proof. The third derivative of the bar profile is:

$$r_b^{'''}(x;h,\omega,\sigma) = h\left[g_\sigma^{''}(x+\omega) - g_\sigma^{''}(x-\omega)\right] \tag{A.140}$$

$$r_b^{'''}(x;h,\omega,\sigma) = \frac{h}{\sqrt{2\pi}\sigma^5}\left\{\left[(x+\omega)^2-\sigma^2\right]e^{-\frac{(x+\omega)^2}{2\sigma^2}} + \left[\sigma^2-(x-\omega)^2\right]e^{-\frac{(x-\omega)^2}{2\sigma^2}}\right\} \tag{A.141}$$

which is zero at $x=0\;\forall\,(h,\omega,\sigma)\in\mathbb{R}: h>0,\omega>0,\sigma>0$.

□

For a given bar profile with parameters (h,ω) the selection of the scale parameter σ will determine if this point will be a maximum, a minimum or an inflection point with respect to x. The following two lemmas are already formulated in [171].

Lemma 21. *Given a bar profile $f_b(x;h,\omega)$, its second-order Gaussian derivative $r_b^{''}(x;h,\omega,\sigma)$ has a minimum with respect to the spatial variable x at $x=0$ if and only if $\sigma \geq \omega/\sqrt{3}$.*

Proof. The derivative of $r_b^{''}(x;h,\omega,\sigma)$ is

$$r_b^{''}(x;h,\omega,\sigma) = \frac{h}{\sqrt{2\pi}\sigma}\left[-\frac{x+\omega}{\sigma^2}e^{-\frac{(x+\omega)^2}{2\sigma^2}} + \frac{x-\omega}{\sigma^2}e^{-\frac{(x-\omega)^2}{2\sigma^2}}\right] \tag{A.142}$$

The conditions for a minimum point at $x=0$ with respect to the spatial variable x are

$$r_b'''(x=0;h,\omega,\sigma)=0 \tag{A.143}$$

$$\frac{\partial^4 r_b}{\partial x^4}(x=0;h,\omega,\sigma)>0 \tag{A.144}$$

The condition in A.143 is demonstrated in Lemma 20. The fourth order derivative is:

$$\frac{\partial^4 r_b}{\partial x^4}(x;h,\omega,\sigma)=\frac{h}{\sqrt{2\pi}\sigma^7}\left\{\left[3(x+\omega)\sigma^2-(x+\omega)^3\right]e^{-\frac{(x+\omega)^2}{2\sigma^2}}-\left[3(x-\omega)\sigma^2-(x-\omega)^3\right]e^{-\frac{(x-\omega)^2}{2\sigma^2}}\right\} \tag{A.145}$$

The value at $x=0$ is

$$\frac{\partial^4 r_b}{\partial x^4}(x=0;h,\omega,\sigma)=\frac{h}{\sqrt{2\pi}\sigma^7}\left(6\omega\sigma^2-2\omega^3\right)e^{-\frac{\omega^2}{2\sigma^2}} \tag{A.146}$$

which is positive for positive values of the parameters if and only if $\sigma\geq\omega/\sqrt{3}$.

□

Lemma 22. *Given a bar profile $f_b(x;h,\omega)$, its second-order Gaussian derivative $r_b''(x;h,\omega,\sigma)$ has a minimum in scale-space at $x=0$ for $\sigma=\omega/\sqrt{3}$.*

Proof. The derivative of $r_b''(x;h,\omega,\sigma)$ at $x=0$ is

$$r_b''(x=0;h,\omega,\sigma)=-\frac{2\omega h}{\sqrt{2\pi}}\frac{1}{\sigma^3}e^{-\frac{\omega^2}{2\sigma^2}} \tag{A.147}$$

The derivative with respect to the scale parameter is

$$\frac{\partial r_b''(x=0;h,\omega,\sigma)}{\partial\sigma}=-\frac{2\omega h}{\sqrt{2\pi}}\left(\frac{\omega^2-3\sigma^2}{\sigma^6}\right)e^{-\frac{\omega^2}{2\sigma^2}} \tag{A.148}$$

which has a critical point at $\sigma=\omega/\sqrt{3}$. This will be a minimum if and only if

$$\frac{\partial^2 r_b'''}{\partial\sigma^2}(x=0;h\omega,\sigma=\omega/\sqrt{3})>0 \tag{A.149}$$

Calculating the derivative

$$\frac{\partial^2 r_b'''}{\partial\sigma^2}(x=0;h,\omega,\sigma)=-\frac{2\omega h}{\sqrt{2\pi}}\left(\frac{12\sigma^4-9\omega^2\sigma^2+\omega^4}{\sigma^9}\right)e^{-\frac{\omega^2}{2\sigma^2}} \tag{A.150}$$

The expression in the parenthesis is negative for $\sigma=\omega/\sqrt{3}$ which makes all the expression positive $\forall(\sigma>0,\omega>0)$. □

The above proofs provide a means of selecting the correct scale for detecting the tube using the second derivative at the center location as a measure of strength. However, one problem found in [171] is that no normalization of derivatives is performed as described in [104] which allows finding a maximum (minimum) across scales that is best suited for the entity we want to detect.

Lemma 23. *Given a bar profile $f_b(x;h,\omega)$, its second-order γ-normalized Gaussian derivative $r''_b(x;h,\omega,\sigma)_{\gamma-norm} = \sigma^{2\gamma} r''_b(x;h,\omega,\sigma)$ has a minimum in scale-space at $x=0$ for $\sigma=\omega$ when $\gamma=1$.*

Proof. The γ-normalized strength measure at the center location would be:

$$r''_b(x=0;h,\omega,\sigma)_{\gamma-norm} = -\frac{2\omega h}{\sqrt{2\pi}}\sigma^{2\gamma-3}e^{-\frac{\omega^2}{2\sigma^2}} \tag{A.151}$$

Calculating the derivative with respect to the scale:

$$\frac{\partial r''_b(x=0;h,\omega,\sigma)_{\gamma-norm}}{\partial\sigma} = -\frac{2\omega h}{\sqrt{2\pi}}\sigma^{2\gamma-4}\left[(2\gamma-3)\,\sigma^2+\omega^2\right]e^{-\frac{\omega^2}{2\sigma^2}} \tag{A.152}$$

which has a critical point for $\sigma=\omega$ when $\gamma=1$ which, as in Lemma 22 corresponds to a minimum.

□

By an appropiate selection of the normalization parameter γ we have obtained a normalized measure of strength, such that, the scale selected estimates the section half-width or radius.

A.5.3 Convolved-Bar Section Profiles

The convolved-bar section profile is obtained as a bar profile that is convolved with a Gaussian function with small aperture. It is a more realistic profile than the Gaussian for most vessel sizes [86]:

- For small vessels it resembles a Gaussian-like profile, since the aperture of the Gaussian is in the scale of the vessel width. It simulates the partial volume effect decreasing the intensity of the vessel.
- For medium and large vessels it shows a plateau in the area around the vessel axis, which is typical for most images of contrasted vessels. The small Gaussian represents the partial volume effect in the vessel boundaries.

As we have seen in the previous section the convolved bar profile corresponds to equation:

$$f_{bc}(x;h,\omega,\sigma_0) = \frac{h}{\sqrt{2\pi}\sigma_0}\left(\phi_{\sigma_0}(x+\omega)-\phi_{\sigma_0}(x-\omega)\right) \tag{A.153}$$

The difference with eq. A.135 is that σ_0 here refers to the aperture used to create the original profile by convolving with an ideal bar profile, and not to the scale selection used for derivative calculations.

Scale selection implies convolving this profile with another Gaussian, which, by the Gaussian cascade property results in:

$$r_{bc}(x;h,\omega,\sigma_0,\sigma) = \frac{h}{\sqrt{2\pi}\sigma_1}\left(\phi_{\sigma_1}(x+\omega) - \phi_{\sigma_1}(x-\omega)\right) \tag{A.154}$$

where $\sigma_1 = \sqrt{\sigma^2+\sigma_0^2}$

Calculating the Gaussian derivatives results in modified versions of eq. A.155 and A.156:

$$r_{bc}^{'}(x;h,\omega,\sigma_0,\sigma) = h\left[g_{\sigma_1}(x+\omega) - g_{\sigma_1}(x-\omega)\right] \tag{A.155}$$

$$r_{bc}^{''}(x;h,\omega,\sigma_0,\sigma) = h\left[g_{\sigma_1}^{'}(x+\omega) - g_{\sigma_1}^{'}(x-\omega)\right] \tag{A.156}$$

The γ-normalized second order Gaussian derivative is (by expanding eq. A.156 and normalizing)[10]:

$$r_{bc}^{''}(x;h,\omega,\sigma_0,\sigma)_{\gamma-norm} = \frac{h\sigma^{2\gamma}}{\sqrt{2\pi}\sigma_1}\left[-\frac{x+\omega}{\sigma_1^2}e^{-\frac{(x+\omega)^2}{2\sigma_1^2}} + \frac{x-\omega}{\sigma_1^2}e^{-\frac{(x-\omega)^2}{2\sigma_1^2}}\right] \tag{A.157}$$

Lemma 24. *Given a convolved-bar profile $f_{bc}(x;h,\omega,\sigma_0)$, its second-order γ-normalized Gaussian derivative $r_{bc}^{''}(x;h,\omega,\sigma_0,\sigma)_{\gamma-norm} = \sigma^{2\gamma}r_b^{''}(x;h,\omega,\sigma_0,\sigma)$ has a minimum in scale-space at $x=0$ for $\sigma=\omega$ when $\gamma=1$ and the value of this minimum does not depend on ω when $\sigma_0 \ll \omega$.*

Proof. The value of this derivative at the center point is:

$$r_{bc}^{''}(x=0;h,\omega,\sigma_0,\sigma)_{\gamma-norm} = -\frac{2\omega h}{\sqrt{2\pi}}\frac{\sigma^{2\gamma}}{\sigma_1^3}e^{-\frac{\omega^2}{2\sigma_1^2}} \tag{A.158}$$

A critical point for this expression with respect to the scale is found by:

$$\frac{\partial r_{bc}^{''}(x=0;h,\omega,\sigma_0,\sigma)_{\gamma-norm}}{\partial\sigma} = 0 \tag{A.159}$$

$$\frac{\partial r_{bc}^{''}(x=0;h,\omega,\sigma_0,\sigma)_{\gamma-norm}}{\partial\sigma} = -\frac{2\omega h\sigma^{2\gamma-1}}{\sqrt{2\pi}\sigma_1^7}\left(2\gamma\sigma_1^4 - 3\sigma^2\sigma_1^2 + \omega^2\sigma^2\right)e^{-\frac{\omega^2}{2\sigma_1^2}} = 0 \tag{A.160}$$

The resulting scales correspond to the solution of the equation:

[10] Note that the normalization is with respect to the scale parameter σ only

$$(3-2\gamma)\,\sigma^4 + \left[(3-4\gamma)\,\sigma_0^2 - \omega^2\right]\sigma^2 - 2\gamma\sigma_0^4 = 0 \tag{A.161}$$

Taking $\gamma = 1$ the solution would be:

$$\sigma = \sqrt{\frac{1}{2}\left(\sigma_0^2 + \omega^2\right) \pm \sqrt{9\sigma_0^4 + 2\sigma_0^2\omega^2 + \omega^4}} \tag{A.162}$$

which in this case depends on both, the width ω of the original bar and the aperture σ_0 used for creating the convolved bar. For small values of σ_0 this expression results in $\sigma \simeq \omega$. If the aperture σ_0 is small with respect to ω then $\sigma_1 = \sqrt{\sigma^2 + \sigma_0^2} \simeq \omega$ and eq. A.158 results in

$$r''_{bc}(x = 0; h, \omega, \sigma_0 \ll \omega, \sigma)_{\gamma-norm} = -\sqrt{\frac{2}{\pi}}\,h\,e^{-1/2} \tag{A.163}$$

which does not depend any more on the width of the bar ω. This can be easily demonstrated to be a minimum as in Lemma 22.

□

Appendix B

Image-based Vascular Analysis Library (IVAN)

B.1 Introduction

The *Image-based Vascular Analysis Library* (IVAN) is a set of cross-platform C++ software libraries for 2D/3D vascular analysis in medical imaging developed using concepts of generic programming. It implements many of the vascular detection, extraction and modelling methods described in this thesis.

The main motivation behind the development of IVAN was the lack of dedicated libraries for image-based analysis of vascular structures.

Some of the existing open-source medical image analysis libraries, such as the *Insight Toolkit* (ITK) [204], implement a few popular vascular detection methods. IVAN may be considered an extension of ITK dedicated specifically to vessel analysis, since it reuses and extends many of the concepts and classes of this library. The *Vascular Modeling Toolkit* (VMTK) [142] is an open-source library dedicated to vascular analysis but is oriented to computational geometry of vessels, generating detailed patient-specific models that can be used for structural or computational fluid dynamics studies. It provides a set of vascular segmentation methods, mainly based on level-set approaches, but it lacks algorithms for image-based analysis of blood vessels, specially for small vessels.

The great number of existing approaches to vascular analysis, its increasing complexity and the absence of a unified framework makes difficult to compare the performance of the different methods in a meaningful and consistent way. Moreover, the implementation of such methods in an object-oriented design allows reusability of its constituent building-blocks, provides a better understanding of its algorithmic mechanisms, reveals important implementation details and improves reproducibility of experiments.

Regarding the scope of the library, it currently provides the following features:

- A repository of vascular detection and extraction algorithms under a unified framework: currently most of the methods are focused on centerline-based detec-

tion and extraction approaches, with focus on medialness functions and vascular tracking algorithms.

- An implementation of the Vessel Knowledge Representation model: it allows the representation of vascular structures in a way that can be easily used to store the results of the vascular extraction algorithms so this information can be readily used by the clinical applications (see Chapter 3).
- An implementation of the Generalized Vascular Tracking (GVT) Framework: it models vascular tracking procedures in a set of different individual stages and components in which existing methods can be accommodated in a flexible manner. Its object-oriented architecture allows testing the influence of the individual components. Moreover, complex extraction schemes can be generated by creating new components or extending existing ones, and by combining different parts of existing methods in innovative ways.
- A means of generating synthetic models of ideal shapes as volumetric images, such as the cylinder, toroid or helix models described in Appendix A, with different cross-sections, shape and image parameters and noise levels.
- A means of reproducing the experiments of this thesis, since they are incorporated as unit tests and examples with configurable parameters.

B.2 Design Criteria

The design of the IVAN library was based on a set of requirements that influenced the design. We can distinguish between functional and non-functional requirements.

B.2.1 Functional Requirements

The library was initially conceived to have, at least, support for:

- *Multi-modality and multi-dimensional images*: the target angiographic images may be 2D or 3D. Support for different modalities implies different pixel types for image representation, which may include support for 16-bit integers (for example for CT or MR) or floating point pixel types.
- *Vascular Networks*: a graph-based structure is required in the VKR model to store the information of the vascular structures, which are ramified by nature. Support for storing associated topological, structural and diagnostic information is also required as described in Chapter 3.
- *Centerline-based Vascular Analysis*: this requires support for medialness functions for vascular detection and tracking and structures for storing vessel centerlines and corresponding section information as described in the VKR information model. These methods may be more accurate for small vessels or are better suited for certain vascular analysis tasks that do not require a full segmentation. Centerline-based analysis also determines that methods are not usually going to

be applied to the whole volume, but sparsely in a set of candidate vessel points, for example during tracking.

- *Segmentation-based Vascular Analysis*: currently the focus is on centerline-based approaches. However, the library may support segmentation-based approaches. The information obtained from a segmentation may be referred to a centerline by using a skeletonization algorithm, which allows the result to be stored in the VKR information model as described in Chapter 4.

- *Multi-scale Analysis*: mechanisms are required for implementing multi-scale detectors in a simple way, with enough flexibility for selecting the number and range of scales.

B.2.2 Non-functional Requirements

The following non-functional requirements were taken into account in the design:

- *Accuracy*: analysis of small vessels and extraction by vascular tracking requires support for performing analysis at sub-voxel accuracy. This implies that calculations must be performed at physical space, allowing to obtain quantitative measurements, such as vesselness functions, at continuous positions not necessarily corresponding to voxel centers. This is achieved by using different types of interpolation strategies.

- *Speed*: the library is designed in such a way that implemented methods perform efficiently, using dedicated numerical schemes where necessary. However, in some cases, speed was sacrificed by providing implementations that were able to provide more insight into the inner mechanisms of vascular analysis algorithms as described next. Moreover, generalization sometimes penalizes speed but allows more consistency, better code reusability and reduces implementation time for new algorithms.

- *Insight*: one of the main objectives for the development of the library is providing insight so as to help to understand the inner mechanisms of existing methods. Some of the current detection and extraction approaches provide dedicated implementations, for example in the Fourier domain (see for example [90]). These implementations tend to be more efficient, but they are difficult to follow in the design stage where it is more important to understand the intermediate calculations. Hence, most of the vascular detection approaches are implemented using local point-based approaches in physical space. A dedicated implementation is more useful when the method is already validated. Still, the idea is also to support these implementations.

- *Integrability*: the software is designed to easily integrate with existing libraries, such as the *Insight Toolkit* [204], for medical image analysis or the *Visualization Toolkit* [159] for advanced visualization, which already integrate with other complementary frameworks. The library is also independent of the graphical user interface library used to develop the final applications. The multi-platform nature

of the library helps also in the integration in different environments. The implementation is also fully compatible with CMake [123], a cross-platform build tool that facilitates the use of a broad range of platforms and compilers, increasing the potential number of users.

- *Reusability*: existing vascular methods are organized and dissectioned according to an object-oriented design, using paradigms such as inheritance and polymorphism that allows code reusability and faster implementations of new approaches.

- *Reproducibility*: the system provides unit tests and examples that allows reproducibility of the experiments.

- *Accessibility*: data structures are designed so as to be readily accessible both for extraction algorithms and for vascular applications that use the relevant extracted information.

This support, combined with the use of abstract techniques of generic programming was decisive for choosing Insight Toolkit as a base library.

B.3 System Modules

The library is divided into several modules or compilable units as follows:

- *Common*: software infrastructure, generic base classes and software design patterns.

- *Detection*: vascular detection algorithms corresponding to vesselness functions.

- *Extraction*: vascular extraction algorithms including components for vascular tracking.

- *I/O*: support input/output operations, mainly to file.

- *ITK*: extension classes of the ITK library.

- *Modelling*: implementation of the *Vessel Knowledge Representation* (VKR) model.

- *Quantification*: support for vascular metrics calculation.

- *Synthetic*: implementation of synthetic vascular models, such as those described in Appendix A.

Next, we describe the most important components in detail.

B.3.1 Modelling Module

The Modelling Module implements the data structures of the VKR information model. Figure B.1 depicts a Unified Modeling Language (UML) diagram of the most important objects in the VKR model. We provide an overview of the main object definitions and their relationships.

According to their function, we can distinguish two main types of objects: data representation objects (left), that describe the vascular structure, and algorithmic objects (right), that implement operations on the data representation objects. As can be seen, there is almost a one-to-one correspondence between data objects and algorithms. This separation between data objects and algorithmic objects provides more flexibility, since it makes easy to define new algorithms without affecting the data representations. Other more straightforward operations are implemented as methods of the corresponding data objects. In Figure B.1 we have set a horizontal line that separates the depth level of the objects: data structures and algorithms above this line correspond to graph level whereas those below operate at underlying modelling levels.

The highest level data structure is the *VesselGraph* which may contain one or several root nodes. All vessel graph nodes are subclasses of the *GraphNode* abstract class, which provides generic node-handling operations and metadata such as node identifiers, and *VesselNode* which is an abstract class specific for nodes of vessel graphs. We chose not to model explicitly the edges of the graph. Thus, the graph consists of nodes, that are connected by virtual links, which are implemented as references (pointers) to the corresponding nodes. *GraphNodes* contain a set of children nodes, as strong references, and a set of parent nodes, as weak references [1].

Due to their importance, we provide a brief description of some salient implemented node types:

- *BranchNode*: is the most important node type, which represents the physical vessel segment that extends between two bifurcations. A *BranchNode* contains a *Centerline.* We decided to implement the centerline as a placeholder of *Section* objects, where the simplest section model is a point that represents the centerline, instead of keeping a list of points on the centerline model itself. This forces a one-to-one mapping and provides the flexibility for a non-explicit centerline definition. Centerline points are thus the centers of *Section* objects, and can be defined with any descriptor that identifies their geometrical position, such as euclidean coordinates, image indexes, chain-codes, etc. The same applies for the points that define the section boundaries. This provides much flexibility in defining the centerline and section for a wide range of applications. In general, this type of flexibility is provided in the VKR model by using *Generic Programming* techniques [45].

- *BifurcationNodes* are more simple in their definition. They explicitly reference confluent branches as parent/child nodes and their use is optional (see Figure 3.2). Algorithms may be devised to operate on bifurcation nodes to take advantage of the direct access to confluent branches.

[1] Strong references imply a composition relationship and weak references an aggregation

- *CompositeNodes* are nodes obtained by wrapping other nodes and exposing the internal links only. The information about internal nodes and links is kept when wrapping is performed, so the situation can be reversed easily. This ability may provide several types of simultaneous representations of the vessel graph, as can be seen in Figure 3.2 (right). One direct application is converting the branch nodes of the same (modified) Strahler order into a single element using the node type *ElementNode*.

- *FeatureNodes* indicate relevant features in vessels and incorporate an optional feature model that describes the corresponding feature such as a stenosis (*StenosisModel*) or aneurysm (*AneurysmModel*). They incorporate a *VesselRegion* structure that indicates the area affected by the feature in corresponding branches.

With respect to the algorithms, those that operate at graph level are subclasses of *GraphNodeVisitor* and *VesselGraphNodeVisitor*. The use of the *Visitor Pattern* [58], allows to separate the node definition from the operations on the graph by decoupling the graph traversal from the node operations. These graph-level algorithms can be classified according to the objects they ultimately operate on. An algorithm may operate at graph level because only graph elements are involved in the corresponding algorithms. An example is calculating the number of nodes in the branch, or computing the (modified) Strahler order of *BranchNodes*. Another possibility is that they encapsulate algorithms that operate at deeper levels (such as the level of centerline or section) but are applied to the corresponding structures on the whole graph and not only locally. In this sense, the level of encapsulation of the data structure finds a correspondence in the level of encapsulation of the algorithms. This makes possible to reuse local algorithms and apply them to the whole graph. An example is the family of *CenterlineAlgorithm* classes, which perform operations on a single centerline. These operations can be performed for all the centerlines of the *BranchNodes* of a vessel graph by defining a specific visitor (*CenterlineAlgorithmVisitor*) which encapsulates the former.

In Figure B.2 we can see a representation of the external operations (we call them "filters" here) that can be performed in order to create the VKR Model and to convert it to other (3D) representations, such as surface meshes or segmentation masks. Objects of type *ImageToVesselGraphAlgorithm* correspond to the vessel extraction algorithms that obtain the output vessel descriptors. Such an extraction scheme, may use the VKR Model as an intermediate representation and then use an algorithm of type *VesselGraphToImageFilter* to obtain the final segmentation or a *VesselGraphToSurfaceFilter* object to obtain a surface mesh.

Finally, most high-level objects, such as filters, nodes, centerlines or sections are implemented using reference counting, so they can be shared by many objects without unnecessary copies and additional overhead.

Needless to say, implementation is an on-going never-ending process, evolving as applications, imaging resources and computational algorithms evolve. Therefore, the description given of current state and trends of our implementation must be assumed as a core implementation aiming at a continuing incremental process incorporating new algorithms, accepting new imaging resources and addressing innovative applications.

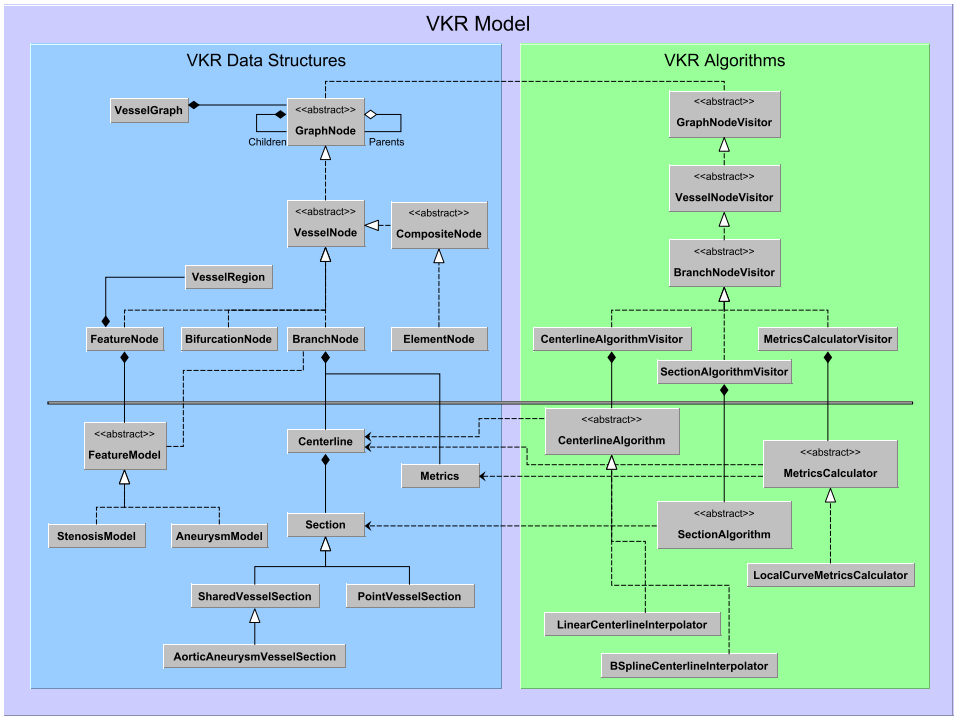

Figure B.1: VKR Model. Internal Implementation

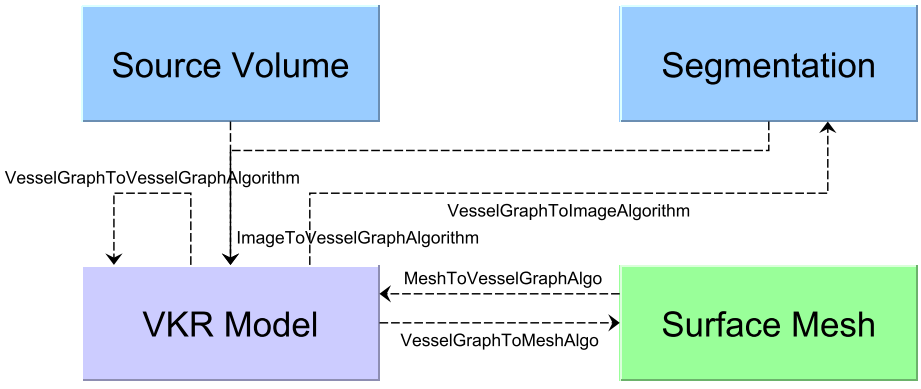

Figure B.2: VKR Model. External Implementation

B.3.2 Detection Module

The *Detection Module* consists mainly of vesselness functions for vascular detection, most of them corresponding to medialness functions enhancing vessel centerlines (see Chapter 5). It implements both central and offset medialness functions and provides support for multi-scale analysis.

Figure B.5 shows the inheritance diagram for the implemented vesselness functions. They take the form of an *ImageFunction*, meaning that they provide a value for every discrete or continuous point in physical space.

A few important base classes are the following:

- *HessianBasedVesselnessImageFunction*: corresponds to vesselness functions that require the calculation of the local Hessian matrix, and possibly its eigenvalues and vectors. The main subclasses are:
  - *HessianOnlyBasedVesselnessImageFunction*: corresponds to the vessselness functions that only require information derived from the Hessian matrix for obtaining the function value. Hence, it corresponds to central medialness approaches which includes, among others, the functions of Sato *et al*. [156] and Frangi *et al*. [54]. The Hessian eigenvalues and eigenvectors may also be obtained directly and may be used for example for vessel section estimation.
  - *OffsetMedialnessImageFunction*: corresponds to the offset medialness of Krissian *et al.* [87].
  - *FluxBasedVesselnessImageFunction*: corresponds to flux-based approaches, and includes the non-linear steerable filter of Koller *et al*. [85] or the approach of Lesage *et al.* in [96].
- *SphereGridBasedImageFunction*: corresponds to vesselness functions that use an sphere grid for calculations. It includes, among others, the Optimally Oriented Flux of Law and Chung [91], the polar profile vesselness measure of Qian *et al*. [149] and a means of directly calculating the eigenvalues and eigenvectors of the oriented flux matrix as in the case of the Hessian matrix.
- *MultiScaleImageFunction*: provides a generic means of converting single-scale image functions into a multi-scale image functions, provided some conditions about the scale representation are met for the target functions. It also provides the ability to specify the way in which scales are integrated.

B.3.3 Extraction Module

The *Extraction Module* contains the algorithms for vessel extraction that obtain a set of vascular descriptors as output. The vesselness functions from the Detection Module may be used in order to determine the vessel (centerline) locations. It implements the *Generalized Vessel Tracking* (GVT) framework (see Chapter 6) as a generic process model for vascular tracking.

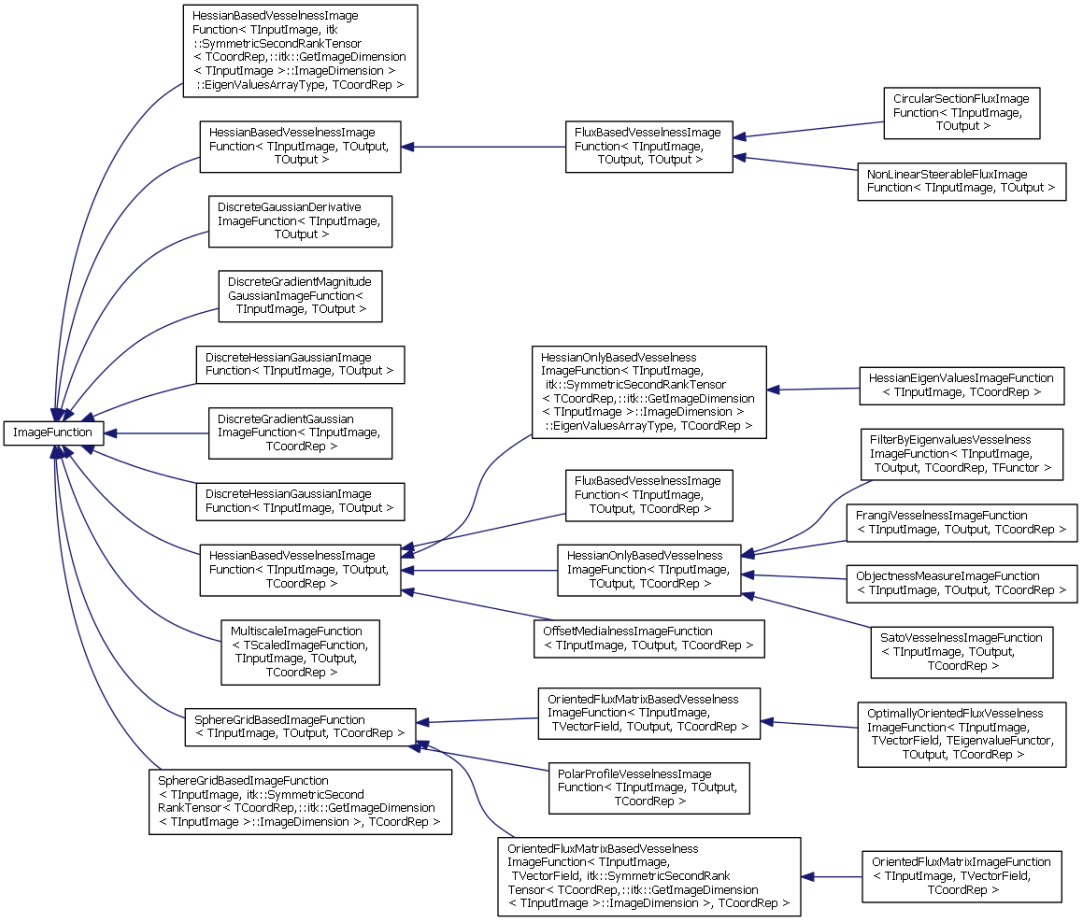

Figure B.3: Inheritance diagram of vesselness functions in the IVAN library.

The main component of the GVT is the *VesselTrackerFilter* class, which inherits *ImageToVesselDataObjectFilter*, which is the base class for the algorithms that take an image as input, and obtain a vessel network descriptor as output, usually in the form of a *VesselGraph* (see Chapter 3).

The collaboration diagram for the *VesselTrackerFilter* class is shown in Figure B.4. The most important component used by this object is the *VesselSectionEstimator*, which computes vessel sections during the *Turn* and *Search* stages of the GVT. The result is stored as a *VesselCenterline* in the current *VesselBranchNode* of the *VesselGraph.* The *VesselTrackerEndCondition*, is the base class that tests the end condition of the algorithms, for example a maximum number of iterations or a minimum value of the medialness.

Most of the algorithmic complexity lies on the *VesselSectionEstimator*, which ultimately determines the centerline path. The following main subclasses are considered:

- *FixedScaleHessianBasedVesselSectionEstimator* / *FixedScaleOOFBasedVesselSectionEstimator*: implements section estimation via eigenvectors of the Hessian and Oriented Flux matrices respectively at a single, user-selected scale.

- *MultiScaleVesselSectionEstimator*: estimates vascular sections at given locations based on image content and at multiple scales. It includes support for estimating the section by eigenvalue analysis of different types of local orientation matrices via the subclass *MultiscaleTensorBasedVesselSectionEstimator*. Two main approaches are implemented, for the Hessian matrix (*MultiScaleHessianBasedVesselSectionEstimator*) and for the Oriented Flux matrix (*MultiScaleOOFBasedVesselSectionEstimator*). Adaptive subclasses of these two estimators automatically select the best scale for estimation based on a medialness metric function.

- *OptimizedVesselSectionEstimator*: implements the novel section estimation with optimization described in Chapter 6. It optimizes a *VesselSectionFitCostFunction* with different possible types of *Optimizer* objects.

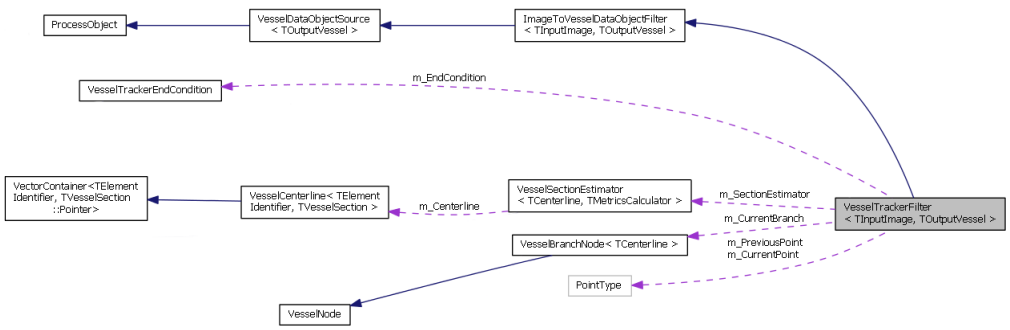

Figure B.4: Collaboration diagram for *VesselTrackerFilter* class.

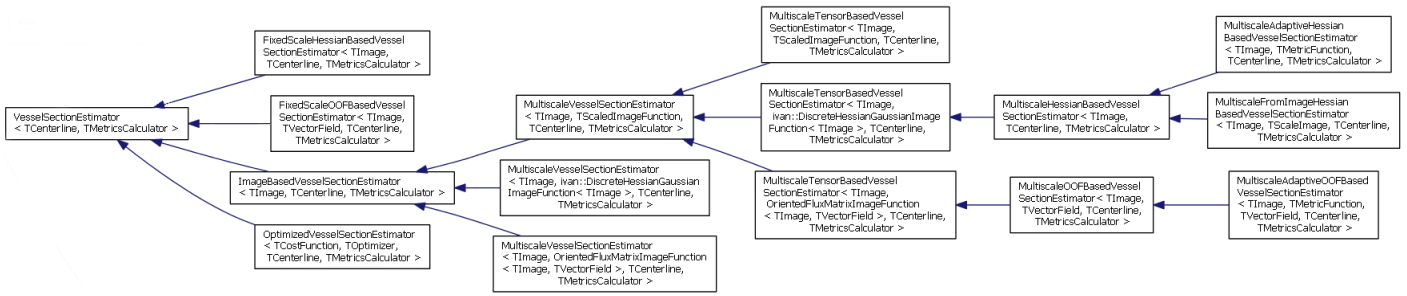

Figure B.5: Inheritance diagram for *SectionEstimator* algorithms in the IVAN library

B.3.4 Synthetic Module

B.3.4.1 Description

The *Synthetic Module* implements ideal image models for vascular analysis as described in Appendix A and other auxiliary objects such as platonic solids as 3D meshes. We can distinguish three main types of objects used for creating the ideal models:

- *Section Generators*: objects which create images of ideal sections with specific shape and intensity profiles. For example, a *CircularFlatSectionGenerator* obtains an image of a circular section with constant/bar intensity profile whereas a *CircularGaussianSectionGenerator* creates an image of a circular section with Gaussian profile of the desired aperture. Several shape or image parameters can be configured, such as the circle radius, or image size, spacing or maximum value.
- *Centerline Generators*: objects which create centerline curves of different shapes. These may be used, among other things, to generate complex volumetric models from these centerlines. For example, a *CircularCenterlineGenerator*, creates a centerline corresponding to a full circumference or a circular arc whereas a *CircularHelixCenterlineGenerator* creates an helix centerline with the desired radius, pitch and height.
- *Volumetric Generators*: objects that create volumetric ideal shape models. These include the cylinder, toroid and helix shape models described in Appendix A. *Section Generators* and *Centerline Generators* may be used to create such models. For example a *CircularFlatTubeGenerator* creates a straight cylinder whose section is a *CircularFlatSectionGenerator*. *GaussianCircularHelixGenerator* creates an helix with Gaussian profile whose centerline is defined by a *CircularHelixCenterlineGenerator*.

B.3.4.2 Implementation of Volumetric Models[2]

Cylinder Model The implementation of the cylinder model is straightforward from the sections obtained from the *Section Generators*. A volumetric image of an ideal cylinder is obtained simply by stacking several 2D section images to create a volume of the desired height. Figure B.6 shows section images corresponding to the bar, convolved-bar and Gaussian ideal section profiles.

Toroid Model In order to create the toroid model, first a discrete centerline is created using *CircularCenterlineGenerator* for a given radius

R and limiting angles θ_{min} and θ_{max} which allow to create a toroid sector instead of a full toroid. In order to obtain adequate precision in the model without leaving gaps, the number of centerline points is chosen as:

$$N = 2\left\lfloor \frac{(\theta_{max} - \theta_{min})R}{\delta} \right\rfloor \quad \{\theta_{min}, \theta_{max}\}\,\varepsilon\,[0, 2\pi] \tag{B.1}$$

[2]See Appendix A for definition of the corresponding volumetric models and intensity profiles.

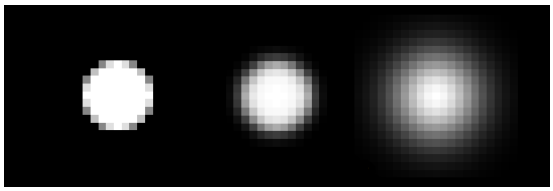

Figure B.6: Section images for the bar (left), bar-convolved ($\sigma = 1.0$) (middle) and Gaussian (right) circular intensity profiles with radius $R = 4.0$ and image spacing $\delta = 1.0$.

where δ is spatial resolution of the volumetric image in which the toroid will lie, assuming the same spacing in all three directions. We choose δ to depend on σ_0 in order to provide and appropriate sampling of the discrete Gaussian functions as follows:

$$\delta = \begin{cases} 0.2\sigma_0 & \sigma_0 \geq 1.25 \\ 0.25 & \text{otherwise} \end{cases} \tag{B.2}$$

Then, an empty volumetric image is created with the spacing δ. Assuming that the toroid is centered on the volume lying on the *xy* plane, the physical dimensions of the image will be approximately:

$$\begin{aligned} S_x^{'} &= S_y^{'} = 2\,(R + 4\sigma_0 + a) \\ S_z^{'} &= 2\,(4\sigma_0 + a) \end{aligned} \tag{B.3}$$

where, a is the desired additional offset. For the calculations of the toroid with Gaussian cross-section we have taken the value $4\sigma_0$ as the external boundary of the Gaussian function, where it is attenuated from respect to the maximum by a factor of 3.3546×10^{-4}which provide enough precision. The resulting image dimensions are:

$$\begin{aligned} N_x &= N_y = \lfloor 2\,(R + 4\sigma_0 + a)/\delta \rfloor \\ N_z &= \lfloor 2\,(4\sigma_0 + a)/\delta \rfloor \end{aligned} \tag{B.4}$$

The resulting final physical dimensions are

$$\begin{aligned} S_x &= S_y = N_x\delta = N_y\delta \\ S_z &= N_z\delta \end{aligned} \tag{B.5}$$

Then, for all image points the following steps are performed:

- Find the closest centerline point.
- Calculate the value of the one-dimensional Gaussian function by taking the distance to the centerline as *r*.
- Set this value if is larger than the current image value.

Figures B.7 and B.8 shows images of toroid models with Gaussian cross-section obtained with the described procedure.

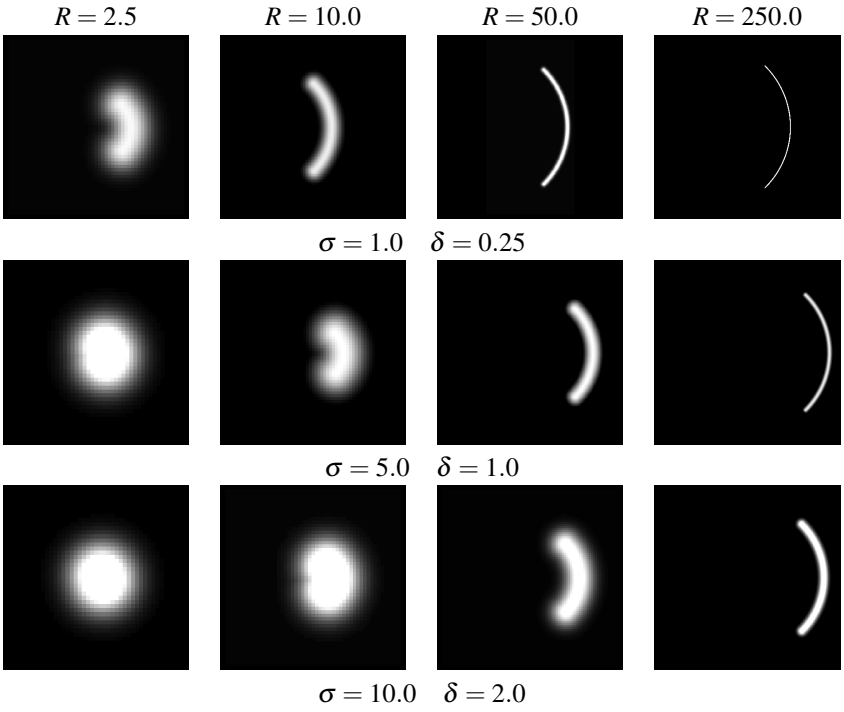

Figure B.7: Discrete volumetric models of toroids with Gaussian cross-section for different values of R and σ_0. Images show axial slices in the xy plane for centerlines with $\theta_{min} = -45°$ and $\theta_{max} = 45°$.

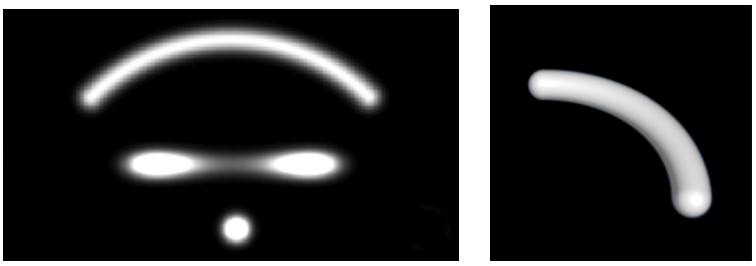

(a) (b)

Figure B.8: Discrete volumetric model of toroids with Gaussian cross-section with $R = 250.0$ and $\sigma_0 = 10.0$. (a) Rotated axial (top), sagittal (middle) and coronal (bottom) slices. (b) 3D volume rendering.

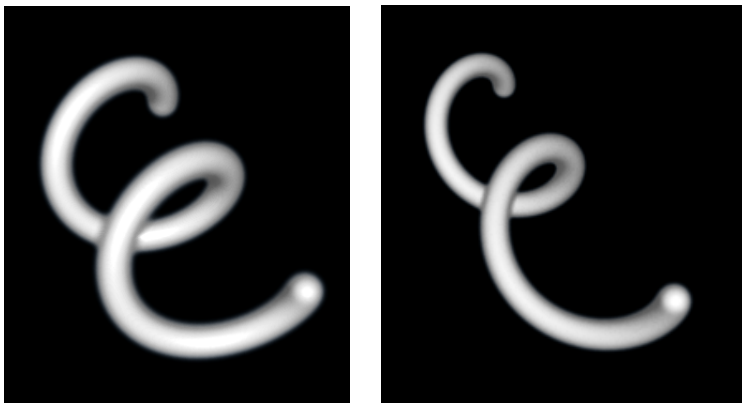

(a) (b)

Figure B.9: 3D volumetric rendering of helix models with Gaussian cross-sections. Both models are obtained with $\sigma_0 = 3.0$, $R = 30.0$ $\theta_{min} = 0º$, and $\theta_{max} = 720º$. (a) $H = 10.0$ (b) $H = 30.0$

Helix Model The generation of the helix model follows the same process as the toroid model, but uses an *HelixCenterlineGenerator* instead. Figure B.9 shows volume rendering of obtained volumetric helices with varying pitch.

Bibliography

[1] H.T. Abada, M.R. Sapoval, J.F. Paul, and J.C. Gaux. Endovascular abdominal aortic aneurysm repair: Is delayed helical ct sufficient? *Radiology*, 231:602–4, 2004.

[2] M. Abramowitz and I.A. Stegun, editors. *Handbook of Mathematical Functions with Formulas, Graphs, and Mathematical Tables*. 1972.

[3] D. Adalsteinsson and J. A. Sethian. A fast level set method for propagating interfaces. *J. Comput. Phys.*, 118(2):269–277, 1995.

[4] G. Agam, S. G. Armato III, and C. Wu. Vessel tree reconstruction in thoracic ct scans with application to nodule detection. *IEEE Trans. Med. Imaging*, 24:486–499, 2005.

[5] G. J. Agin and T. O. Binford. Computer description of curved objects. *IEEE Trans. on Computers*, 25(4):439–449, Apr 1976.

[6] S. Aharinejad, W. Schreiner, and F. Neumann. Morphometry of human coronary arterial trees. *The Anatomical Record*, 251:50–59, 1998.

[7] K. Akitaa and H. Kugaa. A computer method of understanding ocular fundus images. *Pattern Recognition*, 15(6):431–443, 1982.

[8] G. E. Andrews, R. Askey, and R. Roy. *Encyclopedia of Mathematics and its Applications. Vol. 71. Special Functions*. Cambridge University Press, 1999.

[9] L. Antiga, B. Ene-Iordache, and A. Remuzzi. Computational geometry for patient-specific reconstruction and meshing of blood vessels from mr and ct angiography. *Medical Imaging, IEEE Transactions on*, 22(5):674 –684, May 2003.

[10] L. Antiga and D. A. Steinman. Robust and objective decomposition and mapping of bifurcating vessels. *Medical Imaging, IEEE Transactions on*, 23(6):704 –713, june 2004.

[11] S. R. Aylward and E. Bullitt. Initialization, noise, singularities, and scale in height ridge traversal for tubular object centerline extraction. *IEEE Trans. Med. Imaging*, 21(2):61–75, February 2002.

[12] J. Babaud, A. P. Witkin, M. Baudin, and R. O. Duda. Uniqueness of the gaussian kernel for scale-space filtering. *IEEE Trans. Pattern Anal. Machine Intell.*, 8:26–33, 1 1986.

[13] D. Babina, A. Pizuricaa, R. Bellensa, J. De Bocka, Y. Shangb, B. Goossensa, E. Vansteenkistea, and W. Philipsa. Generalized pixel profiling and comparative segmentation with application to arteriovenous malformation segmentation. *Medical Image Analysis*, (online), 2012.

[14] R. Balm, R. Kaatee, J. Blankensteijn, W. Mali, and B. Eikelboom. Ct-angiography of abdominal aortic aneurysms after transfemoral endovascular aneurysm management. *European Journal of Vascular and Endovascular Surgery*, 2:182–188, 1996.

[15] M. Basu. Gaussian-based edge-detection methods - a survey. *IEEE Trans. Systems, Man and Cybernetics*, 32:252–260, 3 2002.

[16] S. Beucher and Ch. Lantuejoul. Use of watersheds in contour detection. In *Int. Workshop on Image Processing, Real-Time Edge and Motion Detection/Estimation*, 1979.

[17] L. Bezold. Coronary artery anomalies, Jan 2010.

[18] K. Bühler, P. Felkel, and A. La Cruz. Geometric methods for vessel visualization and quantification - a survey. In *Geometric Modelling for Scientific Visualization*, pages 399–420. Springer-Verlag, 2002.

[19] H. Blum. A transformation for extracting new descriptors of shape. In Weiant Wathen-Dunn, editor, *Models for the Perception of Speech and Visual Form*, pages 362–380. MIT Press, 1967.

[20] Mohiaddin R. H. Xu X.Y. Borghi A., Wood N.B. 3d geometric reconstruction of thoracic aortic aneurysms. *BioMedical Engineering OnLine*, 5(59), 2006.

[21] T. Boskamp, D. Rinck, F. Link, B. Knmmerlen, G. Stamm, and P. Mildenberger. New vessel analysis tool for morphometric quantification and visualization of vessels in ct and mr imaging datasets. *Radiographics*, 24:287–297, 2004.

[22] S. Bouix, K. Siddiqi, and A. Tannenbaum. Flux driven automatic centerline extraction. *Medical Image Analysis*, 9(3):209–221, June 2005.

[23] R.N. Bracewell. *The Fourier Transform and its Applications, 3rd Ed.* McGraw-Hill, 2000.

[24] U. Brandes, M. Eiglsperger, I. Herman, M. Himsolt, and M. S. Marshall. Graphml progress report: Structural layer proposal. In *Graph drawing. International symposium No9, Vienna, LNCS*, volume 2265, pages 501–512, 2002.

[25] E. Bullitt, S. Aylward, K. Smith, S. Mukherji, M. Jiroutek, and K. Muller. Symbolic description of intracerebral vessels segmented from magnetic resonance angiograms and evaluation by comparison with x-ray angiograms. *Medical Image Analysis*, 5:157–169, 2001.

[26] E. Bullitt, G. Gerig, S. Aylward, S. Joshi, K. Smith, M. Ewend, and W. Lin. Vascular attributes and malignant brain tumors. In *Medical Image Computing and Computer-Assisted Intervention (MICCAI 2003), LNCS*, volume 2878, pages 671–9. Springer, 2003.

[27] E. Bullitt, I. Jung, K. Muller, G. Gerig, S. Aylward, S. Joshi, K. Smith, W. Lin, and M. Ewend. Determining malignancy of brain tumors by analysis of vessel shape. In *Medical Image Computing and Computer-Assisted Intervention (MICCAI 2004), LNCS*, volume 3217, pages 645–653, 2004.

[28] E. Bullitt, K.E. Muller, I. Jung, W. Lin, and S. Aylward. Analyzing attributes of vessel populations. *Medical Image Analysis*, 9:39–49, 2005.

[29] Ali Can, Hong Shen, James N. Turner, Howard L. Tanenbaum, and Badrinath Roysam. Rapid automated tracing and feature extraction from retinal fundus images using direct exploratory algorithms. *IEEE Trans. Inform. Technol. Biomed*, 3:125–138, 1999.

[30] J. Canny. A computational approach to edge detection. *IEEE Trans. Pattern Analysis and Machine Intelligence,*, 8(6):679–698, 1986.

[31] J.F. Carrillo, M. Hernández-Hoyos, E.E. Dávila-Serrano, and M. Orkisz. Recursive tracking of vascular tree axes in 3d medical images. *Int. J. of Computer Assisted Radiology and Surgery*, 1(6):331–9, 2007.

[32] M. Couprie and G. Bertrand. Topological grayscale watershed transform. In *SPIE Vision Geometry VI*, volume 3168, pages 136–146, 1997.

[33] M. A. Creager, T. F. Lüscher, F. Cosentino, and J. A. Beckman. Diabetes and vascular disease: Pathophysiology, clinical consequences, and medical therapy: Part i. *Circulation*, 108:1527–32, 2003.

[34] G. Cumming, L. K. Harding, K. Horsfield, K. Prowse, S. S. Singhal, and M. J. Woldenberg. Morphological aspects of the pulmonary circulation and of the airway. *Fluid Dynamics of Blood Circulation and Respiratory Flow*, 65:230–6, 1970.

[35] P.E. Danielsson. Euclidean distance mapping. *Computer Graphics and Image Processing*, 14:227–248, 1980.

[36] P.E. Danielsson, Q. Lin, and Q.Z. Ye. Efficient detection of second-degree variations in 2d and 3d images. *Journal of Visual Communication and Image Representation*, 12(3):255–305, 2001.

[37] B. Das, Y. Mallya, S. Srikanth, and R. Malladi. Aortic thrombus segmentation using narrow band active contour model. In *In Proc. IEEE Eng. Med. Biol. Soc.*, volume 1, pages 408–11, 2006.

[38] M. de Bruijne, B. van Ginneken, W. J. Niessen, M. Loog, and M. Viergever. Model-based segmentation of abdominal aortic aneurysms in cta images. In *Proc. SPIE Med. Imaging*, volume 5032, pages 1560–71, 2003.

[39] M. de Bruijne, B. van Ginneken, M.A. Viergever, and W.J. Niessen. Interactive segmentation of abdominal aortic aneurysms in cta images. *Medical Image Analysis*, 8:127–138, 2004.

[40] J. Dehmeshki, H. Amin, M. Ebadian-Dehkordi, A. Jouannic, and S. Qanadli. Automatic detection, segmentation and quantification of abdominal aortic aneurysm using computed tomography angiography. In *In Proc. Medical Image Understanding and Analysis*, 2009.

[41] S. Demirci, G. Lejeune, and N. Navab. Hybrid deformable model for aneurysm segmentation. In *IEEE International Symposium on Biomedical Imaging: From Nano to Macro*, Boston, Massachusetts, USA, June/July 2009.

[42] G. Deng and L.W. Cahill. An adaptive gaussian filter for noise reduction and edge detection. *In Proc. IEEE Nucl. Sci. Symp. Med. Im. Conf.*, pages 1615–9, 1994.

[43] T. Deschamps and L. Cohen. Deschamps, t., cohen, l., 2001. fast extraction of minimal paths in 3d images and applications to virtual endoscopy. med. image anal. 5 (4), 281-299. *Medical Image Analysis*, 5(4):281–299, 2001.

[44] E. W. Dijkstra. A note on two problems in connection with graphs. *Numerische Mathematik*, pages 269–271.

[45] G. Dos-Reis and J. Järvi. What is generic programming? In *Proc. of the First International Workshop of Library-Centric Software Design (LCSD'05)*, Oct 2005.

[46] David Eberly. *Ridges in Image and Data Analysis*. Kluwer Academic Publishers, 1996.

[47] M. Erdt, M. Raspe, and M. Suehling. Automatic hepatic vessel segmentation using graphics hardware. In *Proc. 4th Int. Workshop on Medical Imaging and Augmented Reality*, MIAR'08, pages 403–412, Berlin, Heidelberg, 2008. Springer-Verlag.

[48] P. Felkel, A. Kanitsar, A. L. Fuhrmann, and R. Wegenkittl. Surface models of tube trees. In *In Computer Graphics International*, pages 70–77, 2002.

[49] L.M.J. Florack, B. M. Haar Romeny, J.J. Koenderink, and M.A. Viergever. Scale and the differential structure of images. *Image and Vision Computing*, 10(6):376–388, 1992.

[50] J. Folkman. Incipient angiogenesis. *J. Natl. Cancer Inst.*, 92:94–5, 2000.

[51] A. Frangi, W. Niessen, R. Hoogeveen, T. van Walsum, and M. Viergever. Model-based quantitation of 3-d magnetic resonance angiographic images. *IEEE Trans. Medical Imaging*, 18(10):946–956, 1999.

[52] A. Frangi, W. J. Niessen, P. J. Nederkoorn, O. van Elgersma, and M. A. Viergever. Three-dimensional model-based stenosis quantification of the carotid arteries from contrast-enhanced mr angiography. In *IEEE Workshop on Mathematical Methods in Biomedical Image Analysis*, 2000.

[53] A.F. Frangi, W.J. Niessen, K.L. Vincken, and M.A. Viergever. Multiscale vessel enhancement filtering. In *Medical Image Computing and Computer-Assisted Interventation - MICCAI'98*, pages 130–137. Springer-Verlag, 1998.

[54] A.F. Frangi, W.J. Niessen, K.L. Vincken, and M.A. Viergever. Multiscale vessel enhancement filtering. In *Medical Image Computing and Computer-Assisted Interventation (MICCAI)*, pages 130–137. Springer-Verlag, 1998.

[55] W.T. Freeman and E.H. Adelson. The design and use of steerable filters. *IEEE Trans. Pattern Anal. Machine Intell.*, 13:891–906, 9 1991.

[56] I. Fridolin and L. G. Lindberg. Optical non-invasive technique for vessel imaging: I. experimental results. *Phys. Med. Biol.*, 45(12):3765–78, 2000.

[57] G.S.K. Fung, S.K. Lam, SW.K. Cheng, and K.W. Chow. On stent-graft models in thoracic aortic endovascular repair: A computational investigation of the hemodynamic factors. *Computers in Biology and Medicine*, 38(4):484 – 489, 2008.

[58] E. Gamma, R. Helm, R. Johnson, and J. Vlissides. *Design Patterns: Elements of Reusable Object-Oriented Software*. Addison-Wesley, 2000.

[59] G. Gerig, T. Koller, G. Székely, C. Brechbuhler, and O. Kubler. Symbolic description of 3d structures applied to cerebral vessel tree obtained from mr angiography volume data. In *Information Processing in Medical Imaging '93, LNCS 687*, pages 94–111, 1993.

[60] R.C. González and R.E. Woods. *Digital Image Processing, 2nd Ed.* Prentice Hall, 2002.

[61] M. Hernández-Hoyos, P. Orlowski, E. Piatkowska-Janko, P. Bogorodzki, and M. Orkisz. Vascular centerline extraction in 3d mr angiograms for phase contrast mri blood flow measurement. *Int. J. Computer Assisted Radiology and Surgery*, 1(1):51–61, March 2006.

[62] M. Heron, D. L. Hoyert, S. L. Murphy, J. Xu, K. D. Kochanek, and B. Tejada-Vera. Deaths: Final data for 2006. Report, Division of Vital Statistics, U.S. Dep. of Health and Human Services, 2009.

[63] J.A. Hertz, A.S. Krogh, and R.G. Palmer. *Introduction To The Theory Of Neural Computation, Volume I (Santa Fe Institute Studies in the Sciences of Complexity)*. Westview Press, 1991.

[64] J. Holash, P. C. Maisonpierre, D. Compton, P. Boland, C. R. Alexander, D. Zagzag, G. D. Yancopoulos, and S. J. Wiegand. Vessel cooption, regression and growth in tumors mediated by angiopoietins and vegf. *Science*, 284(5422):1994–8, 1999.

[65] R.M. Hoogeveen, C.J. Bakker, and M.A. Viergever. Limits to the accuracy of vessel diameter measurement in mr angiography. *J. Magnetic Resonance Imaging*, 8:1228–35, 6 1998.

[66] K. Horsfield. Morphometry of the small pulmonary arteries in man. *Circulation Research*, 42:593–7, 1978.

[67] K. Horsfield. Diameters, generations, and orders of branches in the bronchial tree. *Journal of Applied Physiology*, 68:457–461, 1990.

[68] K. Horsfield and I. Gorden. Morphometry of pulmonary veins in man. *Lung*, 159:211–8, 1981.

[69] W. Huang, R. T. Yen, M. McLaurine, and G. Bledsoe. Morphometry of the human pulmonary vasculature. *Journal of Applied Physiology*, 81:2123–33, 1996.

[70] Ng L. Cates J. Ibanez L., Schroeder W. *The ITK Software Guide*. Kitware Inc., 2003.

[71] S. Izumiya and N. Takeuchi. Generic properties of helices and bertrand curves. *Journal of Geometry*, 74:97–109, 2002.

[72] M. Jacob and M. Unser. Design of steerable filters for feature detection using canny-like criteria. *IEEE Trans. Pattern Analysis and Machine Intelligence*, 26:1007–19, 8 2004.

[73] R. K. Jain. Normalizing tumor vasculature with anti-angiogenic therapy: a new paradigm for combination therapy. *Nature Med.*, 7:987–998, 2001.

[74] H. Jeong and C.I. Kim. Adaptive determination of filter scales for edge-detection. *IEEE Trans. Pattern Anal. Machine Intell*, 14:579–585, 5 1992.

[75] D. G. Kang, D. C. Suh, and J. B. Ra. Three-dimensional blood vessel quantification via centerline deformation. *IEEE Trans. Medical Imaging*, 28(3):405–414, March 2009.

[76] K. L. Karau, G. S. Krenz, and C. A. Dawson. Branching exponent heterogeneity and wall shear stress distribution in vascular trees. *AJP Heart and Circulatory Physiology*, 280:1256–63, 2001.

[77] G. S. Kassab. Scaling laws of vascular trees: of form and function. *AJP Heart and Circulatory Physiology*, 290:894–903, 2006.

[78] G. S. Kassab, C. A. Rider, N. J. Tang, and Y. C. Fung. Morphometry of pig coronary arterial trees. *Am. J. Physiol.*, 265:350–365, 1993.

[79] C. Kirbas and F. Quek. A review of vessel extraction techniques and algorithms. *ACM Computing Surveys*, 36(2):81–121, June 2004.

[80] A. Klein, W. K. J. Renema, L. J. Oostveen, L. J. Schultze Kool, and C. H. Slump. A segmentation method for stentgrafts in the abdominal aorta from ecg-gated cta data. In X. P. Hu; A. V. Clough, editor, *Proc. SPIE Medical Imaging 2008: Physiology, Function, and Structure from Medical Images*, volume 6916, 2008.

[81] R. Klein, A. Schilling, and W. Strasser. Reconstruction and simplification of surfaces from contours. In *Proc. 7th Pacific Conf. on Comp. Graphics and App.*, 1999.

[82] J.J. Koenderink. The structure of images. *Biological Cybernetics*, 50:363–370, 1984.

[83] A. J. F. Kok and R. van Liere. A multimodal virtual reality interface for 3d interaction with vtk. *Knowledge and Information Systems*, 13(2):197–219, Oct 2007.

[84] T. Koller, G. Gerig, and G. Székely. Object-centered description for analysis and display of the cerebral vascularity. In H.U. Lemke et al., editor, *Computer Assisted Radiology CAR'95*, pages 183–188. Springer-Verlag, 1995.

[85] T. M. Koller, G. Gerig, G. Székely, and D. Dettwiler. Multiscale detection of curvilinear structures in 2-d and 3-d image data. In *In Proc. Fifth International Conference on Computer Vision (ICCV'95)*, pages 864–9. IEEE Computer Society Press, 1995.

[86] K. Krissian, G. Malandain, N. Ayache, R. Vaillant, and Y. Trousset. Model based detection of tubular structures in 3d images. *Computer Vision and Image Understanding*, 80(2):130–171, 2000.

[87] K. Krissian, G. Malandain, N. Ayache, R. Vaillant, and Y. Trousset. Model based detection of tubular structures in 3d images. *Computer Vision and Image Understanding*, 80(2):130–171, 2000.

[88] Harris P.L. Moll F.L. Stelter W.J. Verhoeven E.L.G. Laheij R.J.F., Buth J. Need for secondary interventions after endovascular repair of abdominal aortic aneurysm. intermediate-term follow-up results of a european collaborative registry. *British Journal of Surgery*, 87(12):1666–73, 2002.

[89] T. Lange, S. Eulenstein, M. Huumlnerbein, and P. M. Schlag. Vessel-based non-rigid registration of mr/ct and 3d ultrasound for navigation in liver surgery. *Computer Assisted Surgery*, 8(5):228–240, 2003.

[90] Max W. K. Law and Albert C. S. Chung. Efficient implementation for spherical flux computation and its application to vascular segmentation. *IEEE Trans. on Image Processing*, 18(3):596–612, 2009.

[91] M.W.K. Law and A.C.S. Chung. Three dimensional curvilinear structure detection using optimally oriented flux. In P. Torr D. Forsyth and A. Zisserman, editors, *In Proc. European Conference of Computer Vision (ECCV'08)*, volume LNCS 5305, pages 368–82, 2008.

[92] J. Lee, P. Beighley, E. Ritman, and N. Smith. Automatic segmentation of 3d micro-ct coronary vascular images. *Medical Image Analysis*, 11(6):630–647, 2007.

[93] K. Lee, R.K. Johnson, Y. Yin, A. Wahle, M.E. Olszewski, T.D. Scholz, and M. Sonka. Three-dimensional thrombus segmentation in abdominal aortic aneurysms using graph search based on a triangular mesh. *Computers in Biology and Medicine*, 40(3):271 – 278, 2010.

[94] J. H. Legarreta, F. Boto, I. Macía, J. Maiora, G. García, C. Paloc, M. Graña, and M. de Blas. Hybrid decision support system for endovascular aortic aneurism repair follow-up. In *Proc. of 5th Int. Conf. on Hybrid Artificial Intelligent Systems (HAIS'10)*, page Submitted, 2010.

[95] D. Lesage, E. Angelini, I. Bloch, and G. Funka-Lea. Medial-based bayesian tracking for vascular segmentation: Application to coronary arteries in 3d ct angiography. In *IEEE Int. Symp. Biomed. Imaging (ISBI'08)*, pages 268–271, 2008.

[96] D. Lesage, E.D. Angelini, I. Bloch, and G. Funka-Lea. Design and study of flux-based features for 3d vascular tracking. In *In Proc. of Int. Symposium on Biomedical Imaging (ISBI)*, pages 286–9, 2009.

[97] D. Lesage, E.D. Angelini, I. Bloch, and G. Funka-Lea. A review of 3d vessel lumen segmentation techniques: Models, features and extraction schemes. *Medical Image Analysis*, 13(6):819–845, December 2009.

[98] D. Lesage, E.D. Angelini, I. Bloch, and G. Funka-Lea. A review of 3d vessel lumen segmentation techniques: Models, features and extraction schemes. *Medical Image Analysis*, 13(6):819–845, December 2009.

[99] Q. Lin. *Enhancement, Extraction and Visualization of 3D Volume Data*. PhD thesis, Institute of Technology, Linköpings Universitet, 2003.

[100] T. Lindeberg. Scale-space for discrete signals. *IEEE Trans. Pattern Analysis and Machine Intelligence*, 12:234–254, 3 1990.

[101] T. Lindeberg. Discrete derivative approximations with scale-space properties: A basis for low-level feature extraction. *J. Math. Imaging Vision*, 3:349–376, 4 1993.

[102] T. Lindeberg. Discrete derivative approximations with scale-space properties: A basis for low-level feature extraction. *J. Math. Imaging Vision*, 3:349–376, 1993.

[103] T. Lindeberg. *Scale-space Theory in Computer Vision*. Kluwer Academic Publishers, 1994.

[104] T. Lindeberg. Edge detection and ridge detection with automatic scale selection. *Int. J. of Computer Vision*, 30:465–470, 1996.

[105] T. Lindeberg. Edge detection and ridge detection with automatic scale selection. *Int. J. Comput. Vision*, 30:117–156, 1998.

[106] Tony Lindeberg. Feature detection with automatic scale selection. *International Journal of Computer Vision*, 30:79–116, 1998.

[107] S. Liu, A. H. B. Duffy, R. I. Whitfield, and I. M. Boyle. Integration of decision support systems to improve decision support performance. *Knowledge and Information Systems*, 22(3):261–286, Feb 2009.

[108] W. E. Lorensen and H. E. Cline. Marching cubes: A high resolution 3d surface construction algorithm. *Computer Graphics, Vol. 21, Nr. 4, July 1987*, 21(4):163–9, 1987.

[109] C. Lorenz, I. Carlsen, T. Buzug, C. Fassnacht, and J. Weese. Multi-scale line segmentation with automatic estimation of width, contrast and tangential direction in 2d and 3d medical images. In *CVRMed-MRCAS'97*, pages 233–242, 1997.

[110] L.M. Lorigo, O. Faugeras, W.E.L. Grimson, R. Keriven, R. Kikinis, and C.F. Westin. Co-dimension 2 geodesic active contours for mra segmentation. In *IPMI*, pages 126–139, 1999.

[111] D. Lowe. Object recognition from local scale-invariant features. In *In Proc. Int. Conf. on Computer Vision (ICCV'99)*, 1999.

[112] I. Macía. Generalized computation of gaussian derivatives using itk. *Insight Journal*, 8, Jul-Dec 2007.

[113] I. Macía. Generalized computation of gaussian derivatives using itk. *The Insight Journal*, Dec. 2007.

[114] I. Macía, M. Graña, J. Maiora, C. Paloc, and M. de Blas. Detection of type ii endoleaks in abdominal aortic aneurysms after endovascular repair. *Computers in Medicine and Biology*, 41(10):871–89, Oct 2011.

[115] I. Macía, M. Graña, C. Paloc, and F. Boto. Neural network-based detection of type ii endoleaks in cta images after endovascular repair. *Computers in Biology and Medecine*, page Submitted, 2010.

[116] I. Macía, J. H. Legarreta, C. Paloc, M. Graña, J. Maiora, G. García, and M. de Blas. Segmentation of abdominal aortic aneurysms in ct images using a radial model approach. In E. Corchado; H. Yin, editor, *Proc. Intelligent Data Engineering and Automated Learning, 10th Int. Conference (IDEAL'09)*, volume 5788 of *Lecture Notes in Computer Science (LNCS)*, pages 664–671, Burgos, Spain, Sep 2009. Springer.

[117] I. Macía, D. Wald, and C. Paloc. Extraction and analysis of patient-specific hepatic anatomy from mr images. In *Int. J. of Computer Assisted Radiology and Surgery. Proc. of the 22st Int. Congress and Exhibition (CARS'08)*, volume Suppl. 1, pages 399–401, Barcelona, Spain, Jun 2008.

[118] Iván Macía. Generalized computation of gaussian derivatives using itk. *The Insight Journal*, Dec. 2007.

[119] J. Maiora, G. García, I. Macía, J. H. Legarreta, F. Boto, C. Paloc, M. Graña, and J. Sánchez. Thrombus volume change visualization after endovascular abdominal aortic aneurysm repair. In *Proc. of 5th Int. Conf. on Hybrid Artificial Intelligent Systems (HAIS'10)*, page Submitted, 2010.

[120] J. Maiora, G. García, I. Macía, J. H. Legarreta, C. Paloc, M de Blas, and M. Graña. Thrombus change detection after endovascular abdominal aortic aneurysm repair. In *Proc. of Computer Assisted Radiology and Surgery (CARS'10)*, page In press, 2010.

[121] J. Maiora, G. García, A. Tapia, I. Macía, J. H. Legarreta, C. Paloc, M. Graña, and M. de Blas. Stent graft change detection after endovascular abdominal aortic aneurysm repair. In E. Corchado; H. Yin, editor, *Intelligent Data Engineering and Automated Learning - IDEAL 2009 10th Internationa Conference, Proceedings*, volume 5788 of *Lecture Notes in Computer Science (LNCS)*, page 826, Universidad de Burgos, Burgos, Spain, Sep 2009. Springer.

[122] D. Marr and E. Hildreth. Theory of edge detection. *Proc. of the Royal Society of London. Series B, Biological Sciences.*, 207(1167):187–217, 1980.

[123] K. Martin and B. Hoffman. *Mastering CMake 4th Edition*. Kitware, Inc., USA, 2008.

[124] J. H. Metzena, T. Krögerb, A. Schenk, S. Zidowitz, H. O. Peitgen, and X. Jiang. Matching of anatomical tree structures for registration of medical images. *Image and Vision Computing*, 27(7):923–933, Jun 2009.

[125] J. Mille and L. D. Cohen. Deformable tree models for 2d and 3d branching structures extraction. In *IEEE Conf. on Computer Vision and Pattern Recognition Workshops*, 2009.

[126] R. D. Millán, L. Dempere-Marco, J. M. Pozo, J. R. Cebral, and A. F. Frangi. Morphological characterization of intracranial aneurysms using 3-d moment invariants. *IEEE Trans Med Imaging*, 26(9):1270–82, 2007.

[127] M. Miyazaki, N. Ichinose, S. Sugiura, H. Kanazawa, Y. Machida, and Y. Kassai. A novel mr angiography technique: Speed acquisition using half-fourier rare. *Journal of Magnetic Resonance Imaging*, 8(2):505–7, 2005.

[128] C. Murray. The physiological principle of minimum work, i: the vascular system and the cost of blood volume. *Proc. Natl. Acad. Sci. USA*, 12(3):207–214, 1926.

[129] M. Näf. *3D Voronoi Skeletons: a Semicontinuous Implementation of the 'Symmetric Axis Transform' in 3D Space*. PhD thesis, ETH Zürich, 1996.

[130] O. Nilsson, D. Breen, and K. Museth. Surface reconstruction via contour metamorphosis: An eulerian approach with lagrangian particle tracking. In *In Proc. 16th IEEE Visualization (VIS'05)*, 2005.

[131] D. A. Nordsletten, S. Blackett, M. D. Bentley, E. L. Ritman, and N. P. Smith. Structural morphology of renal vasculature. *AJP Heart and Circulatory Physiology*, 291:296–309, 2006.

[132] T. O'Donnell, T. Boult, X. Fang, and A. Gupta. The extruded generalized cylinder: A deformable model for object recovery. In *Proc. of Computer Vision and Pattern Recognition (CVPR'94)*, pages 174–181, 1994.

[133] S. Oka and M. Nakai. Optimality principle in vascular bifurcation. *Biorheology*, 24(6):737–751, 1987.

[134] S. Olabarriaga, M. Breeuwer, and W. J. Niessen. Minimum cost path algorithm for coronary artery central axis tracking in ct images. In *Med. Image Computing and Computer Assisted Intervention (MICCAI'03)*, 2003.

[135] S.D. Olabarriaga, J.M. Rouet, M. Fradkin, M. Breeuwer, and W.J. Niessen. Segmentation of thrombus in abdominal aortic aneurysms from cta with nonparametric statistical grey level appearance modelling. *IEEE Trans. Med. Imag.*, 24:477– 485, 4 2005.

[136] M. Orkisz, L. Flórez-Valencia, and M. Hernández-Hoyos. Models, algorithms and applications in vascular image segmentation. *Machine Graphics and Vision*, 17(1/2):5–33, 2008.

[137] S. Osher and J. A. Sethian. Fronts propagating with curvature-dependent speed: Algorithms based on hamilton-jacobi formulations. *J. Comput. Phys.*, 79:12–49, 1988.

[138] M.A. Oskoei and H. Hu. A survey on edge detection methods, technical report ces-506. Technical report, University of Essex, 2010.

[139] K. Palágyi, E. Sorantin, E. Balogh, A. Kuba, C. Halmai, B. Erdohelyi, and K. Hausegger. A sequential 3d thinning algorithm and its medical applications. In *Proc. of the 17th Int. Conf. on Information Processing in Medical Imaging (IPMI'01), LNCS*, volume 2082, pages 409–415. Springer Verlag, 2001.

[140] M. Paradowski, H. Kwasnicka, and K. Borysewicz. Capillary blood vessel tortuosity measurement using graph analysis. In *Knowledge-Based and Intelligent Information and Engineering Systems, 13th Int. Conf. (KES 2009)*, 2009.

[141] J. Park and S. Lee. Keyword search in relational databases. *Knowledge and Information Systems*, In print, 2010.

[142] M. Piccinelli, A. Veneziani, D. A. Steinman, A. Remuzzi, and L. Antiga. A framework for geometric analysis of vascular structures: Application to cerebral aneurysms. *Transactions on Medical Imaging*, 28(8):1141 –55, Aug 2009.

[143] S. M. Pizer, D. Eberly, B. S. Morse, and D. S. Fritsch. Zoom-invariant figural shape: The mathematics of cores. *Computer Vision and Image Understanding*, 69:55–71, 1998.

[144] S. M. Pizer, K. Siddiqi, G. Székely, J. N. Damon, and S. W. Zucker. Multi-scale medial loci and their properties. *International Journal of Computer Vision*, 55(2-3):155–179, 2003.

[145] S.M. Pizer, D. Eberly, D. Fritsch, and B.S. Morse. Zoom-invariant vision of figural shape: The mathematics of cores. *Computer Vision and Image Understanding*, 69(1):55–71, 1998.

[146] T. Pock, R. Beichel, and H. Bischof. A novel robust tube detection filter for 3d centerline extraction. In Springer-Verlag, editor, *Proc. 14th Scandinavian Conf. on Im. Analysis, LNCS*, volume 3540.

[147] T. Pock, C. Janko, R. Beichel, and H. Bischof. Multiscale medialness for robust segmentation of 3d tubular structures. In *10th Computer Vision Winter Workshop*, 2005.

[148] A. Puig, D. Tost, and I. Navazo. Hybrid model for vascular tree structures. In Liere R. van Leeuw, W. de, editor, *Data Visualization 2000 : Joint Eurographics and IEEE TCVG Symposium on Visualization, Amsterdam, The Netherlands*, pages 125–135. Springer-Verlag, 2000.

[149] Xiaoning Qian, Matthew P. Brennan, Donald P. Dione, Wawrzyniec L. Dobrucki, Marcel P. Jackowski, Christopher K. Breuer, Albert J. Sinusas, and Xenophon Papademetris. A non-parametric vessel detection method for complex vascular structures. *Medical Image Analysis*, 13(1):49–61, 2009.

[150] F.K.H. Quek and C. Kirbas. Vessel extraction in medical images by wave-propagation and traceback. *IEEE Trans. Med. Imaging*, 20(2):117–131, February 2001.

[151] J. R. Reichenbach, R. Venkatesan, D. J. Schillinger, D. K. Kido, and E. M. Haacke. Small vessels in the human brain: Mr venography with deoxyhemoglobin as an intrinsic contrast agent. *Radiology*, 204:272–7, 1997.

[152] E. L. Ritman. Micro-computed tomography of the lungs and pulmonary-vascular system. *Proc. of the Am. Thoracic Society*, 2:477–480, 2005.

[153] L. M. Sangalli and S. Vantini. Registration of functional data: Aligning inner carotid artery centerlines. In *Proceedings of the XLIV Riunione Scientifica Società Italiana di Statistica*, 2008.

[154] W. P. Santamore and A. A. Bove. Why arteries are the size they are. *Journal of Applied Physiology*, 104:1259, 2008.

[155] Y. Sato, S. Nakajima, N. Shiraga, H. Atsumi, S. Yoshida, T. Koller, G. Gerig, and R. Kikinis. 3d multi-scale line filter for segmentation and visualization of curvilinear structures in medical images. *Medical Image Analysis*, 2(2):143–168, June 1998.

[156] Y. Sato, S. Nakajima, N. Shiraga, H. Atsumi, S. Yoshida, T. Koller, G. Gerig, and R. Kikinis. 3d multi-scale line filter for segmentation and visualization of curvilinear structures in medical images. *Medical Image Analysis*, 2(2):143–168, June 1998.

[157] M. Schaap, C.T. Metz, T. van Walsum, A.G. van der Giessen, A.C. Weustink, N.R. Mollet, C. Bauer, H. Bogunovic, C. Castro, X. Deng, E. Dikici, T. O'Donnell, M. Frenay, O. Friman, M. Hernández Hoyos, P.H. Kitslaar, K. Krissian, C. Kühnel, M.A. Luengo-Oroz, M. Orkisz, Ö. Smedby, M. Styner, A. Szymczak, H. Tek, C. Wang, S.K. Warfield, Y. Zhang, S. Zambal, G.P. Krestin, and W.J. Niessen. Standardized evaluation methodology and reference database for evaluating coronary artery centerline extraction algorithms. *Medical Image Analysis*, 13(5):701–714, 2009.

[158] C. Scharlach. Ridges and the description of image structure. In *In Proc. V Conf. on Diff. Geom. and Vision*, 1992.

[159] W. Schroeder, K. Martin, and B. Lorensen. *The Visualization Toolkit: An Object-Oriented Approach to 3D Graphics*. Kitware, 4th edition edition, 2006.

[160] B. G. Schunck. Edge detection with gaussian filters at multiple scales. *In Proc. IEEE Comp. Soc. Work. Comp. Vis.*, pages 208–210, 1987.

[161] M. Schwarz, M. P. Nguyen, U. Kiencke, C. Heilmann, R. Klemm, C. Benk, F. Beyersdorf, and H. J. Busch. Integration of the circle of willis into avolio's model of the arterial hemodynamics. In *6th IASTED Int. Conf. on Biomedical Engineering*, 2008.

[162] H. P. Schwefel. *Evolution and Optimum Seeking*. Wiley, 1995.

[163] D. Selle, B. Preim, A. Schenk, and H. O. Peitgen. Analysis of vasculature for liver surgical planning. *IEEE Trans. Med. Imaging*, 21:1344–57, 2002.

[164] M. Shah, A. Sood, and R. Jain. Pulse and stair case edge models. *Comput. Vis. Graph. Image Process.*, 34:321–343, 1986.

[165] T. F. Sherman. On connecting large vessels to small: the meaning of murray's law. *Journal of General Physiology*, 78:431–453, 1981.

[166] K. Siddiqi and B. B. Kimia. A shock grammar for recognition. cvpr'96:507-513, san francisco, ca, ieee. In *IEEE Computer Vision and Pattern Recognition (CVPR'96)*, pages 507–13, 1996.

[167] K. Siddiqi and S. Pizer. *Medial Representations: Mathematics, Algorithms and Applications*. Springer, 2008. ISBN 978-1402086571.

[168] S. Singhal, R. Henderson, K. Horsfield, K. Harding, and G. Cumming. Morphometry of the human pulmonary arterial tree. *Circulation Research*, 33:190–7, 1973.

[169] F. M. Sones and E. K. Shirey. Cine coronary arteriography. *Modern Concepts of Cardiovascular Disease*, 31:735–8, 1962.

[170] C. Steger. Extracting curvilinear structures: A differential geometric approach. In *Fourth European Conference on Computer Vision*, pages 630–641. Springer-Verlag, 1996.

[171] C. Steger. Extracting curvilinear structures: A differential geometric approach. In *Proc. 4th European Conference on Computer Vision*, pages 630–641. Springer-Verlag, 1996.

[172] A. N. Strahler. Hypsometric (area-altitude) analysis of erosional topology. *Geological Society of America Bulletin*, 63(11):1117–42, 1952.

[173] Charagundla S.R. Stravopoulos S.W. Imaging techniques for detection and management of endoleaks after endovascular aortic aneurysm repair. *Radiology*, 243(3):641–55, 2007.

[174] M. Styner, C. Brechbuhler, G. Székely, and G. Gerig. Parametric estimate of intensity inhomogeneities applied to mri. *Trans. Med. Imag*, 19(3):153–165, 2000.

[175] M. Subasic, S. Loncaric, and E. Sorantin. 3d image analysis of abdominal aortic aneurysm. In *In Proc. SPIE Med. Imag. Proc.*, volume 4684, pages 1681–9, 2002.

[176] R. Beichel T. Pock, Ch. Janko and H. Bischof. Multiscale medialness for robust segmentation of 3d tubular structures. In *Proc. 10th Computer Vision Winter Workshop (CVWW)*, pages 93–102, 2005.

[177] R. Lamparello P. Rosen R. Macari M. Tolia A.J., Landis. Type ii endoleaks after endovascular repair of abdominal aortic aneurysms: Natural history. *Radiology*, 235:683–6, May 2005.

[178] R. Torii, M. Oshima, T. Kobayashi, K. Takagi, and T. E. Tezduyar. Influence of wall elasticity in patient-specific hemodynamic simulations. *Computers & Fluids*, 36(1):160–8, 2007.

[179] T.A Upchurch G.R., Schaub. Abdominal aortic aneurysm. *Am. Fam. Physician*, 73(7):1198–204, April 2006.

[180] C. van Bemmel, O. Wink, B. Verdonck, M. Viergever, and W. Niessen. Blood pool contrast-enhanced mra: Improved arterial visualization in the steady state. *IEEE Trans. Medical Imaging*, 22(5):645–652, 2003.

[181] I. van Herzeele, R. Aggarwal, and I. Malik. Use of simulators in vascular training. *Heart*, 95:613–4, 2009.

[182] P. M. A. van Ooijen, G. de Jonge, and M. Oudkerk. Coronary fly-through or virtual angioscopy using dual-source mdct data. *Eur Radiol.*, 17(11):2852–59, Nov 2007.

[183] A. Vasilevskiy and K. Siddiqi. Flux maximizing geometric flows. *IEEE Trans. Pattern Anal. Mach. Intell.*, 24(12):1565–78, 2002.

[184] D. Vukadinovic, T. van Walsum, R. Manniesing, S. Rozie, R. Hameeteman, T. T. de Weert, A. van der Lugt, and W. J. Niessen. Segmentation of the outer vessel wall of the common carotid artery in cta. *IEEE Transactions on*, 29(1):65–76, Jan. 2010.

[185] S. Wang, J. Chen, X. Yang, and X. Zhang. Patient-specific hemodynamic analysis for cerebral aneurysm. In *Proc. Bioinformatics and Biomedical Engineering (ICBBE'08), 2nd Int. Conf. on*, 2008.

[186] Z. Weiping and S. Huazhong. Detection of cerebral vessels in mra using 3d steerable filters. In *In Proc. IEEE Engineering in Medicine and Biology, 27th Annual Conference*, pages 3249–52, 2005.

[187] J. Wever, J. Blankensteijn, W. Mali, and B. Eikelboom. Maximal aneurysm diameter follow-up is inadequate after endovascular abdominal aortic aneurysm repair. *European J. of Vasc. and Endovasc. Surg.*, 20:177–182, 2 2000.

[188] Van Rijn J.C. Broeders I.A. Eikelboom B.C. Mali WP Wever J.J., Blankensteijn J.D. Inter- and intraobserver variability of ct measurements obtained after endovascular repair. *American Journal of Roentgenology*, 175:1279–82, 2000.

[189] R.T. Whitaker and X. Xue. Variable-conductance, level-set curvature for image denoising. In *International Conference on Image Processing (ICIP'01)*, volume 3, pages 142–145, 2001.

[190] Waugh R.C. White G.H., May J. Type i and type ii endoleak: A more useful classification for reporting results of endoluminal aaa repair. *Journal of Endovascular Surgery*, 5(4):378–80, 1998.

[191] Waugh R.C. Chaufour X. Yu W. White G.H., May J. Type iii and type iv endoleak: Toward a complete definition of blood flow in the sac after endoluminal aaa repair. *Journal of Endovascular Surgery*, 5(4):305–9, 1998.

[192] C. M. Wilson, K. D. Cocker, M. J. Moseley, C. Paterson, S. T. Clay, W. E. Schulenburg, M. D. Mills, A. L. Ells, K. H. Parker, G. E. Quinn, A. R. Fielder, and J. Ng. Computerized analysis of retinal vessel width and tortuosity in premature infants. *Investigative Ophthalmology and Visual Science*, 49(8):3577–3585, 2008.

[193] O. Wink, W.J. Niessen, and M.A. Viergever. Multiscale vessel tracking. *IEEE Trans. Med. Imaging*, 23(1):130–133, 2004.

[194] T. Wischgoll, S. Choy J, and G. S. Kassab. Extraction of morphometry and branching angles of porcine coronary arterial tree from ct images. *AJP Heart and Circulatory Physiology*, 297:1949–55, 2009.

[195] A.P. Witkin. Scale-space filtering. *Proc. 8th Int. Joint Conf. Art. Intell.*, pages 1019–22, 1983.

[196] N. Witt, T. Y. Wong, A. D. Hughes, N. Chaturvedi, B. E. Klein, R. Evans, M. McNamara, S. A. M. Thom, and R. Klein. Abnormalities of retinal microvascular structure and risk of mortality from ischemic heart disease and stroke. *Hypertension*, 47:975–981, 2006.

[197] I.H. Witten, E. Frank, L. Trigg, M. Hall, G. Holmes, and S.J. Cunningham. Weka: Practical machine learning tools and techniques with java implementations. In Ko K. Kasabov N., editor, *ICONIP/ANZIIS/ANNES'99 Workshop on Emerging Knowledge Engineering and Connectionist-Based Information Systems*, pages 192–196, Dunedin, New Zealand, 1999.

[198] D. A. Woodrum, A. J. Romano, A. Lerman, U. H. Pandya, D. Brash, P. J. Rossman, L. O. Lerman, and R. L. Ehman. Vascular wall elasticity measurement by magnetic resonance imaging. *Magnetic Resonance in Medicine*, 56:593–600, 2006.

[199] S. Worz and K. Rohr. Segmentation and quantification of human vessels using a 3-d cylindrical intensity model. *IEEE Trans. on Image Processing*, 16(8):1994–2004, 2007.

[200] X. Wu, V. Kumar, J. R. Quinlan, J Ghosh, Q. Yang, H. Motoda, G. J. McLachlan, A. Ng, B. Liu, P. S. Yu, Z. H. Zhou, M. Steinbach, D. J. Hand, and D. Steinberg. Top 10 algorithms in data mining. *Knowledge and Information Systems*, 14(1):1–37, 2008.

[201] M. Xu and D. Pycock. A scale-space medialness transform based on boundary concordance voting. *J. of Mathematical Imaging and Vision*, 11(3):277–299, 1999.

[202] J. Yang, L. X. Yu, M. Y. Rennie, J. G. Sled, and R. M. Henkelman. Comparative structural and hemodynamic analysis of vascular trees. *AJP Heart and Circulatory Physiology*, 298:1249–59, 2010.

[203] Q. Yang, J. Liu, S. R. S. Barnes, Z. Wu, K. Li, J. Neelavalli, J. Hu, and E. M. Haacke. Imaging the vessel wall in major peripheral arteries using susceptibility-weighted imaging. *Journal of Magnetic Resonance Imaging*, 30(2):357–365, 2009.

[204] T. S. Yoo, M. J. Ackerman, W. E. Lorensen, W. Schroeder, V. Chalana, S. Aylward, D. Metaxas, and R. Whitaker. Engineering and algorithm design for an image processing api: a technical report on itk - the insight toolkit. *Stud. Health. Technol. Inform.*, 85:586–592, 2002.

[205] T.S. Yoo, M. J. Ackerman, W. E. Lorensen, W. Schroeder, V. Chalana, S. Aylward, D. Metaxas, and R. Whitaker. Engineering and algorithm design for an image processing api: A technical report on itk - the insight toolkit. In J. Westwood, editor, *In Proc. of Medicine Meets Virtual Reality*, pages 586–92, 2002.

[206] A. L. Yuille and T. A. Poggio. Scaling theorems for zero-crossings. *IEEE Trans. Pattern Analysis and Machine Intelligence*, 8:15–25, 1986.

[207] L. Zhou, M. S. Rzeszotarski, L. J. Singerman, and J. M. Chokreff. The detection and quantification of retinopathy using digital angiogram. *IEEE Trans. Med. Imaging*, 13:619–626, 1994.

[208] Y. Zhou, G. S. Kassab, and S. Molloi. On the design of the coronary arterial tree: a generalization of murray's law. *Phys. Med. Biol.*, 44:2929–45, 1999.

[209] F. Zhuge, G.D. Rubin, S. Sun, and S. Napel. An abdominal aortic aneurysm segmentation method: level set with region and statistical information. *Med. Phys.*, 33:1440–53, 5 2006.

[210] C. Zohios, G. Kossioris, and Y. Papaharilaoub. Geometrical methods for level set based abdominal aortic aneurysm thrombus and outer wall 2d image segmentation. *Computer Methods and Programs in Biomedicine*, 107(2):202–217, 2012.